N° d’ordre: 2011-34 **ANNÉE 2011**

THÈSE

présentée devant

L’ÉCOLE CENTRALE DE LYON

pour obtenir

le titre de DOCTEUR
SPÉCIALITÉ ACOUSTIQUE

par

Petr YULDASHEV

Propagation d’ondes de choc dans les milieux aléatoires avec des inhomogénéités distribuées dans l’espace ou dans une couche mince

Nonlinear shock waves propagation in random media with inhomogeneities distributed in space or concentrated in a thin layer

Soutenue le 10 novembre 2011 devant la Commission d’Examen

JURY

Président:	M.	Daniel	Juvé
Examinateurs:	M.	Philippe	Blanc-Benon (Co-Directeur de Thèse)
	Mme.	Vera	Khokhlova (Co-Directeur de Thèse)
	M.	Robin	Cleveland (Rapporteur)
	M.	Vladimir	Preobrazhensky(Rapporteur)
	M.	Valentin	Burov
	M.	Oleg	Sapozhnikov

Laboratoire de Mécanique des Fluides et d’Acoutique, UMR CNRS 5509
Ecole Centrale de Lyon
et
Département d’Acoutique, Faculté de Physique, Université d’État de Moscou

Remerciements

Ce travail de thèse en co-tutelle s'est déroulé au département d'acoustique de la Faculté de Physique de l'Université d'Etat de Moscou de Lomonossov et au Département de Mécanique des Fluides et d'Acoustique de l'École Centrale de Lyon.

Je remercie d'abord le Professeur Oleg Rudenko, Directeur du département d'acoustique de la Faculté de Physique de l'Université d'Etat de Moscou, et le Professeur Michel Lance, Directeur du Laboratoire de Mécanique des Fluides et d'Acoustique à l'École Centrale de Lyon, de m'avoir accueilli au sein de leurs équipes.

J'adresse également mes plus sincères remerciements à l'Ambassade de France en Russie qui m'a permis d'obtenir une bourse du Gouvernement Français pour l'accomplissement de cette thèse en co-tutelle, et qui m'a permis de connaître la France.

J'exprime ma plus profonde gratitude au Daniel Juvé, Directeur du Centre Acoustique, qui m'a accueilli au sein de son équipe de recherche et qui m'a fait l'honneur de présider ce jury. Ma gratitude s'adresse également au Professeur Vladimir Preobrazhensky à l'École Centrale de Lille et au General Physics Institute of Russian Academy of Science A.M. Prokhorov, au Professeur Robin Cleveland à l'Université d'Oxford et au Professeur Valentin Burov à l'Université de Lomonossov qui ont accepté d'être rapporteurs de ce travail et m'ont fait l'honneur d'être membres de mon jury.

J'adresse toutes mes plus vives reconnaissances à mes directeurs de thèse en co-tutelle Vera Khokhlova (Professeur à l'Université d'État de Moscou de Lomonossov) et Philippe Blanc-Benon (École Centrale de Lyon, Directeur de recherche au CNRS). Ils ont beaucoup contribué à cette thèse par leurs conseils, par leurs commentaires et par leurs soutiens. Ils étaient toujours disponibles pour la discussion et ils m'ont toujours aidé à trouver une solution aux questions tant scientifiques que de la vie quotidienne. Et si ma thèse est lisible c'est en partie grâce à leurs lectures attentives.

Toute ma gratitude va de même au Professeur Oleg Sapozhnikov à l'Université de Lomonossov. Ses conseils et ses discussions sur mes résultats expérimentaux et théoriques ont beaucoup contribué à la réalisation de mon travail de thèse. Je remercie tous les autres professeurs de l'équipe acoustique de l'Université d'Etat de Moscou qui m'ont fait découvrir au travers des cours de l'acoustique, la théorie des ondes dans ses diverses aspects.

Je remercie spécialement Sébastien Ollivier, qui a été mon troisième "chef de science" en ce qui concerne les expériences faites à l'École Centrale de Lyon. J'aimerai bien dire un grand merci à Edouard Salze, Emmanuel Jondeau, Jean-Michel Perrin et Nathalie Grosjean pour leur aide dans la réalisation pratique des expériences et Pascale Jeandel pour son aide informatique. Je remercie de même tous les autres membres de l'équipe acoustique pour m'avoir accueilli au centre acoustique.

Je joins à ces remerciements ceux qui j'adresse à Mikhail Averyanov, qui a soutenu avant sa thèse en co-tutelle et avec qui nous avons travaillé ensemble sur certain sujets pendant mes études à l'Université et qui m'a beaucoup aidé au début de ma thèse.

Je remercie aussi tous les étudiants et doctorants avec qui j'ai travaillé pendant l'écriture de ma thèse pour l'ambiance positive et optimiste qu'ils ont créée.

J'exprime ma grande reconnaissance à Anne Zucco pour sa contribution à la collaboration entre MSU et ECL, et en particulier son travail administratif pour l'organisation de cette collaboration. Elle a également pris part à l'organisation de mon séjour en France.

Enfin, je remercie ma famille pour sa confiance et son soutien, lequel m'a toujours permis de choisir les bonnes solutions et m'a donné de l'enthousiasme pendant mon travail de thèse.

Abstract

Propagation of nonlinear acoustic waves in inhomogeneous media is an important problem in many research domains of modern theoretical and applied acoustics. For example, studies on propagation of high amplitude N-waves in turbulent atmosphere are relevant to the sonic boom problem which involves high interest due to development of new civil supersonic aircrafts. In relation to sonic boom problem, many studies on spark-generated N-wave propagation through a turbulent layer were carried out in model laboratory-scale experiments which are more controlled and reproducible than field measurements. Propagation of high intensity focused ultrasound in tissue (HIFU) is intensively studied for medical applications. HIFU is a basis of new surgical devices for noninvasive thermal and mechanical ablation of tumors.

In this thesis, the problem of characterization of high amplitude N-waves generated in air by an electric spark was studied using combined acoustical and optical methods. The fine structure of shocks was deduced from the shadowgraphy images with a resolution that cannot be obtained using condenser microphones. It was shown that the combination of optical and acoustical methods allows complete characterization of the N-waves.

N-wave propagation through a layer of thermal turbulence was further studied in a laboratory experiment. The evolution of statistical distributions and average values of the most important N-wave parameters was investigated at different propagation distances. Experimental results were compared to data obtained in another experiment known in literature, where N-wave was propagated through kinematic turbulence. It was shown that in the case of almost the same widths of the turbulent layers, values of the characteristic scales and rms of refractive index fluctuations, the kinematic turbulence leads to stronger distortions of the peak pressure and the shock rise time of the N-wave and to 2-3 greater probabilities to observe intense focusing in caustics.

Effects of nonlinear propagation and random focusing on the statistics of N-wave amplitude were studied theoretically using the KZK equation and the phase screen model. The phase screen was characterized by the correlation length and the refraction length – the distance where first caustics occur. Probability distributions, mean values and standard deviations of the N-wave peak pressure were obtained from the numerical solutions and were presented as functions of the propagation distance and the nonlinear length. Statistical results from the KZK model were compared with analytical predictions of the nonlinear geometrical acoustics approach (NGA). It was shown, that NGA approach is valid only up to the distance of one third of refraction length of the screen. Strong nonlinear effects were shown to suppress amplitude fluctuations. The effect of the scale of inhomogeneities on amplitude statistics was also investigated.

The problem of focusing of ultrasound beam through inhomogeneous medium is important for medical diagnostics and nondestructive testing problems. The inhomogeneities of biological tissue or of industrial materials can destroy beam focusing. In the thesis, distortions of a weakly nonlinear diagnostic beam focused through a phase layer of special configuration were considered experimentally and theoretically. Feasibility of selective destruction of focusing of different harmonics in the beam was predicted in the modeling and confirmed in experiment.

The most modern HIFU devices rely on using two-dimensional multi-element phased arrays with elements randomly distributed over a segment of a spherical surface. Numerical experiment is an important tool to characterize pressure fields created by HIFU radiators. Intensity levels at the focus of HIFU radiators can reach several tens of thousands of $\mathrm{W/cm^2}$, causing nonlinear propagation effects and formation of shocks. In the thesis, a numerical solution was obtained for the first time for the nonlinear field of a therapeutic array including high amplitude shocks in the focus. An effective algorithm was developed, making it possible to perform such calculations on SMP computers.

Keywords: Weak shock waves, nonlinear acoustics, shadowgraphy, sonic boom, turbulence, phase screen, ultrasound, HIFU, therapeutic arrays

Contents

Introduction

Relevance of the research

Propagation of nonlinear waves in randomly inhomogeneous media is an important problem in many modern applications of theoretical and applied acoustics such as diagnostic and therapeutic ultrasound (Hill *et al.*, 2002), long range propagation of sound in atmospheric acoustics (Tatarskii, 1971, Krasilnikov, 1998, Plotkin, 2002), propagation of waves from explosive sources in ocean (Brekhovskikh, 1974). Inhomogeneities of sound speed in the propagation medium distort the wavefront of the incident wave and lead to a redistribution of the acoustic field parameters in space, formation of random focusing and regions of defocusing. Nonlinear effects combined with diffraction also strongly affect acoustic field characteristics. For example, a relative diffraction shift between nonlinearly generated harmonics in a focused ultrasonic beam gives an increase in the focusing gain for the positive peak pressure (Bessonova *et al.*, 2009). On the other hand, in the case of very intense beams, formation of shocks and strong nonlinear absorption at the shock fronts smooths the focal peaks. If propagation of single pulses is considered, then the nonlinear refraction plays an important role in reducing pressure amplitudes in the foci (Rudenko & Sapozhnikov, 2004, Musatov *et al.*, 1992). Due to the complexity of the general propagation problem, which can not be described analytically, in most important cases many of its aspects are not studied yet. In some situations, even numerical approaches to solve direct problems of nonlinear propagation in inhomogeneous medium cannot be applied. At the same time, the problems from different domains in aeroacoustic or medical acoustics are close in terms of the similar theoretical approaches employed. Same simplifications, such as parabolic equation or phase screen model, can be used to model nonlinear wave propagation both in air and biological-type medium.

Generation and propagation of noise from subsonic and supersonic aircrafts is an important problem in modern aeroacoustics (Plotkin, 2002). Prediction of the noise level of the sonic boom on the ground is of special attention due to development of new civil supersonic aircrafts (Krasilnikov, 1998). Due to nonlinear effects, a multi-shock wave transforms to the N-wave at some distance from the airplane and propagates through the inhomogeneities of the atmosphere boundary layer (Tatarskii, 1971), which leads to random redistribution of the acoustic field on the ground (Maglieri *et al.*, 1992, Plotkin, 2002). The noise level on the ground is therefore a random variable which depends on the statistical characteristics of the given atmospheric conditions. Random variations of the wave amplitude and the shock rise time can be very significant (Elmer & Joshi, 1994). Subjective loudness depends on the amplitude of the N-wave and, in particular, on the shock rise time, therefore it is important to predict the effect of turbulence on statistical characteristics of these parameters (Fidell *et al.*, 2002, Leatherwood & Sullivan, 1992, Leatherwood *et al.*, 2002, Niedzwiecki & Ribner, 1978).

The problem of N-wave propagation in a turbulent atmosphere has been studied using both theoretical and experimental methods. Theoretical studies were based on models of varying complexity. The simplest approach was to use the approximation of linear (Candel, 1977, Blanc-Benon *et al.*, 1995) and nonlinear geometrical acoustics (Gainville, 2008, Coulouvrat, 2002). In this approach, some analytical solutions can be obtained, including statistical distributions for the N-wave amplitude behind the phase screen (Dubrovskii *et al.*, 1996, Rudenko & Enflo, 2000, Gusev & Rudenko, 2006). However, the approximation of geometrical acoustics does not take into account several important effects such as diffraction and nonlinear refraction. Moreover, acoustic field can be correctly described only up to the distances of the first caustics formation. In this regard, in many others studies a number of models based on nonlinear KZK equation were developed, which additionally takes into account the effects associated with the presence of stratification of the atmosphere, inhomogeneities of longitudinal and transverse components of the wind, temperature fluctuations, the influence of the ground surface, as well as relaxation absorption of sound in the atmosphere (Averiyanov, 2008, Averiyanov *et al.*, 2006, Blanc-Benon *et al.*, 2002, Dallois, 2000, Coulouvrat, 2008, Cotté & Blanc-Benon, 2009, Leissing, 2009). Recently, more sophisticated methods were developed to simulate propagation of nonlinear waves based on Euler equations and using finite volume numerical solver (Alauzet & Loseille, 2010). However, the statistical properties of the N-wave amplitude after propagation through a turbulent layer, depending on various factors as nonlinearity and the size of inhomogeneities, were not well studied within the framework of these models. Therefore, a more detailed study of statistics of the N-wave amplitude in a random medium is of undoubted interest. In particular, the main effects of random focusing can be described using the phase screen model to simulate random medium and the parabolic KZK nonlinear equation.

Experimental studies of sonic boom problem based on field measurements of sonic booms are not numerous because they are technically difficult and very expensive projects (Lee & Downing, 1991, Maglieri *et al.*, 1992, Elmer & Joshi, 1994, Hilton *et al.*, 1964). Disadvantages of the field measurements are the lack of control on atmosphere conditions; poor knowledge of turbulence along propagation paths of waves; difficulties to acquire sufficiently large statistical database (Elmer & Joshi, 1994, Willshire & Devilbiss, 1992). These inherent drawbacks complicate analysis of influence of different physical effects on statistics of N-wave distortions. As an alternative to field measurements, laboratory scale experiments are often used to model N-wave propagation through a turbulent layer (Lipkens & Blackstock, 1998a, Lipkens, 1993, Ollivier & Blanc-Benon, 2004, Averiyanov, 2008). In such model experiments, most of important characteristic parameters of outdoor propagation can be downscaled and, as a rule, the turbulence, the source of shock waves, and the geometry of propagation are well controlled.

In the currently known laboratory experiments with a spark source the turbulence is most often generated in a jet expanding from the rectangular nozzle and creating a turbulence of vector type (Lipkens & Blackstock, 1998a, Ollivier & Blanc-Benon, 2004, Averiyanov, 2008). Randomly oriented flows of air, varying from point to point and in time, lead to variations of the "effective" sound speed (Blokhintsev, 1981). In the atmosphere there are also exist inhomogeneities of scalar type, forming in an upward flow of heated air from the ground surface. Variations of the sound speed are the result of temperature fluctuations. Homogeneous isotropic turbulence fields of scalar and vector types have different spectra and properties (Comte-Bellot & Bailly, 2003). Therefore, according to the theoretical analysis of linear wave propagation (Ostashev, 1997, Ostashev, 1994, Blanc-Benon *et al.*, 1995) done using approximation of geometrical acoustic, this difference in spectra leads to different impact of turbulence on the statistics of the wave distortions. However, simulations of nonlinear propagation of the N-wave in 3D geometry using more realistic models such as parabolic equation are not available up to date. It is interesting therefore to study experimentally the influence of the turbulence type (vector or scalar) on statistics of the N-wave distortions. The reliable experimental comparative data are not yet reported in the literature, except some preliminary results reported (Ollivier & Blanc-Benon, 2004). In the recent study (Averiyanov, 2008) the case of the N-wave propagation in kinematic turbulence for different intensities of the turbulent fluctuations was thoroughly considered experimentally. The data of this study will be used as a reference in the comparison with the results on the N-wave propagation through thermal turbulence performed in this thesis.

To model the outdoor propagation at laboratory scale, both the propagation distance, the size of the turbulent inhomogeneities, and the wavelength of the acoustic pulse should be downscaled. Short shock pulses with 30-50 microseconds duration, generated by a spark source (Wright, 1983), can be used to represent sonic boom N-waves with the scaling factor of 1:1000. In the measurement of such pulses with the help of modern commercially available condenser microphones there are significant difficulties associated with limited frequency response of these microphones in the upper frequency range (Yuldashev *et al.*, 2008b). While the peak pressure and duration of the pulse can be accurately measured, the shock rise time is strongly overestimated (Yuldashev *et al.*, 2011). In this regard, the development of new methods to measure the acoustic shock waves, e.g. optical methods, is of great interest. The application of shadowgraphy to measure the shock width and rise time of the N-wave will be discussed in the thesis.

Propagation of a finite amplitude ultrasound beam through randomly inhomogeneous medium is an important problem for numerous applications in biomedicine (Hill *et al.*, 2002, Bailey *et al.*, 2003, Rudenko, 2006, Rudenko, 2007) and nondestructive testing (Brysev *et al.*, 2004). For example, in ultrasound hyperthermia and surgery, the inhomogeneities of fat and skin layers, connective tissues, and bones may appear on the path of an intense beam. The inhomogeneities distort the beam focusing implemented by classical methods, thereby degrading the useful effect and causing unwanted side effects by injuring healthy tissues (Bobkova *et al.*, 2010, Li *et al.*, 2006). In diagnostic ultrasound, the distortion of the focusing by the inhomogeneities reduces the resolution and sensitivity of equipment and increases its measurement errors (Hill *et al.*, 2002).

In modern medical diagnostics, ultrasound devices that employ operation modes utilizing nonlinearity of the propagation medium are being widely used. A characteristic example is scanning with the use of the second harmonic, when wave propagation in tissue is accompanied by generation of higher order harmonics (Averkiou *et al.*, 1997, Khokhlova *et al.*, 2006) (Tissue Harmonic Imaging, THI). The second harmonic scanning increases resolution, decreases noise and improves overall quality of diagnostic images (Rudenko, 2007). Investigation of physical mechanisms of the image quality enhancement and technical progress of the devices are important tasks up to date (Wojcik *et al.*, 1998, Varslot & Masoy, 2006, Jing & Cleveland, 2007, Varslot *et al.*, 2007, Christopher, 2009).

Results of many of studies (Christopher, 1997, Yan, 2004, Brysev *et al.*, 2004, Brysev *et al.*, 2005) allow to suppose that, under certain conditions, focusing of a harmonic in the inhomogeneous medium can have advantages over the conventional focusing of the beam emitted at the frequency of the harmonic. In other words, the same inhomogeneity can defocus the beam at a frequency f stronger than the n-th harmonic of the frequency, f/n, generated in the beam. Clarifying conditions when better focusing of harmonics occurs for one or another type of inhomogeneities is an important theoretical problem. For example, second-harmonic focusing through random inhomogeneities with gaussian spectrum was considered in study (Yan, 2004), and through more realistic inhomogeneities which were based on real tissue specimens – in (Wojcik *et al.*, 1998).

On the other hand, the problems of ultrasonic beam propagation through artificial inhomogeneities are of great interest. For example, in the experimental study (Zhang *et al.*, 2009) a beam was focused using a plate of acoustic metamaterial consisting of a network of Helmholtz resonators. Another example, that has long been discussed in nonlinear acoustics of nondispersive media, is the problem of controlling cascade processes of harmonics generation that result in an increased nonlinear absorption of acoustic waves. This problem is important for ultrasound application, especially in biomedical applications where it is necessary to deliver high acoustic power to a particular spatial region. Such a control can be implemented, for example, by introducing resonant absorption of the chosen harmonics (Andreev *et al.*, 1985, Khokhlova *et al.*, 2000). For the same goal, it was also proposed to introduce a phase shift between the harmonics (waveform precorrection) (Couture *et al.*, 2008, Sarvazyan *et al.*, 1998). By analogy with the second method, the use of a specially chosen phase screen that selectively dephases a desired harmonic may be of interest as one more promising method to control the process of generating harmonics.

In therapeutic applications of acoustics the use of high intensity focused ultrasound (HIFU) for noninvasive surgery is one of the most rapidly developing research topic (Bailey *et al.*, 2003). HIFU is used to achieve non-invasive thermal destruction of tumors (ter Haar, 2001, Crum & Hynynen, 1996), to stop internal bleedings (Vaezy *et al.*, 2001), to targeted delivery of drugs (Hoff, 2002), and to produce other biological effects (Burov *et al.*, 2002). In recent years, a new class of HIFU transducers – ultrasound therapeutic arrays – is actively studied and introduced in prototypes of clinical devices (Pernot *et al.*, 2003, Hynynen *et al.*, 2006, Quesson *et al.*, 2006, Hand *et al.*, 2009). Arrays consist of many radiating elements, located on a segment of a spherical surface. Each element of such arrays is controlled independently, allowing to steer the focus electronically, to create complex configuration of the field in the form of multiple foci (Gavrilov & Hand, 2000b, Gavrilov, 2003), and to minimize heating of acoustic obstacles (for example, ribs), while maintaining the therapeutical efficiency in the focus (Bobkova *et al.*, 2010). The abilities of arrays can also be utilized to improve the quality of focusing in inhomogeneous tissue using time reversal methods, as well as to trace the region of treatment, which shifts due to respiration (Pernot *et al.*, 2003, Pernot *et al.*, 2004).

Numerical experiment is an important tool in characterizing pressure fields created by HIFU radiators, in developing exposure protocols, and in predicting corresponding HIFU-induced biological effects in tissue (Canney *et al.*, 2008, Bessonova *et al.*, 2009). The numerical experiment can be useful also at the design stage of manufacturing process to choose optimal parameters of the device. Intensity levels at the focus of HIFU radiators can reach several tens of thousands of $\mathrm{W/cm^2}$, causing nonlinear propagation effects. Nonlinear effects can result in formation of weak shocks in the ultrasound waveform, which fundamentally changes the efficiency of ultrasound thermal action on tissue and can lead to new biological effects of a non-thermal nature (Burov *et al.*, 2002, Canney *et al.*, 2010).

Until now, no results have been reported yet on modeling nonlinear effects in three-dimensional fields of multi-element HIFU arrays with account for the formation of shocks. Several difficulties are combined at once in this problem: the complex diffraction structure of the near field and large focusing angles requiring the use of accurate diffraction models and a fine spatial numerical grid. In addition, strong nonlinear effects require large number of harmonics to be included in the simulations or a fine temporal grid. For simulation in a three-dimensional geometry with allowance for generation of shock fronts, in general, significant resources of RAM and computer time are required, which exceed the capabilities of modern SMP computers, i.e., multiprocessor computers with shared memory. Thus, developing of new algorithms allowing to model nonlinear acoustic field of such arrays is a very important problem.

Aims of the dissertation

The general aim of the dissertation is an experimental and theoretical study of propagation of nonlinear pulsed and periodic ultrasound signals in media with random inhomogeneities distributed in space or concentrated in a narrow layer in the context of aeroacoustic problems and problems of diagnostic and therapeutic medical ultrasound. According to this aim, the following tasks can be outlined:

1. Determination of accuracy of optical shadowgraphy method in measurement of the rise time of the shock in a pressure N-wave used in the model downscaled sonic boom experiment. Demonstration of limitations of commercial condenser microphones in measurements of acoustic shock fronts.
2. Investigation of statistical characteristic of acoustic field of the N-wave propagated through a layer of thermal turbulence in a laboratory scale experiment. Comparison of N-wave peak pressure and rise time statistics obtained in the experiments with thermal and with kinematic turbulence.

3. Development of two-dimensional numerical model based on the KZK equation to study nonlinear and diffraction effects in the problem of N-wave propagation behind a random phase screen taking into account the propagation through caustics. Investigation of influence of nonlinear effects and the characteristic scale of inhomogeneities of the phase screen on statistical distributions of the N-wave amplitude. Comparison between simulation results and analytical solutions obtained in the approximation of nonlinear geometrical acoustics.
4. Investigation of selective destruction of the harmonics fields in a finite amplitude weakly focused beam after propagation through a random phase layer of special configuration.
5. Development of a new numerical algorithm based on the Westervelt equation to simulate three-dimensional nonlinear fields of strongly focused multi-element transducers – therapeutic arrays – taking into account formation of shocks in the focal region.
6. Development of method of an axially symmetric equivalent source to accelerate simulations of nonlinear fields of therapeutic arrays using two-dimensional axially symmetric numerical models based on either the KZK or the Westervelt equation.

Dissertation scientific novelty

1. It is shown that application of shadowgraphy method to accurately measure the shock rise time of an N-wave is possible only if shadowgrams are quantitatively interpreted by simulating diffraction effects in the light propagation through optical inhomogeneities of the shock front.
2. Nonlinear propagation of spherical N-wave through a layer of thermal turbulence was investigated in the laboratory scale experiment with well-controlled parameters. Experimental results demonstrated significant quantitative difference between distortions of the N-wave amplitude and shock rise time in thermal turbulence and in a turbulent air flow.
3. A numerical model based on the KZK equation was developed to describe statistical properties of nonlinear pulse parameters after propagation behind a random phase screen. Unlike previous models based on approximation of nonlinear geometrical acoustics, in the developed approach the combined effects of nonlinearity, diffraction and dissipation, and propagation through caustics were taken into account significantly increasing the applicability scope of the model.
4. It is shown theoretically and confirmed experimentally that a phase layer of special configuration can selectively affect the focusing quality of different harmonics in a finite amplitude weakly focused beam.
5. A new numerical algorithm was developed which is able to calculate the three-dimensional nonlinear field of therapeutic ultrasound array in conditions of shock fronts formation in the focal region. It is shown that the intensity levels used in modern therapeutic arrays are sufficient to produce shock fronts in the focus.
6. Feasibility of using the model of an axially symmetric equivalent transducer for simplified calculations of the nonlinear field of therapeutic array in the focal region was shown.

Reliability of the results presented in dissertation is verified by the benchmark numerical and physical experiments, and by the agreement of the results of these experiments to *a priory* known information, to the theoretical data, and numerical simulations, obtained in the papers of other authors.

Dissertation scientific and practical statements

1. Smoothing of the shock fronts in the measurements of shock waves using condenser microphones is important for interpreting the results of model aeroacoustic experiments.
2. Comparison of experimental data of the N-wave propagation in thermal turbulence with the known data obtained in the turbulent air flow shows a significant difference in distortion of the N-wave statistics in turbulent fields with different spatial spectra.
3. The developed model and numerical experiment on nonlinear pulse propagation behind a random phase screen can be used to estimate statistics of acoustic field depending on three parameters: the nonlinear length, the refraction length of the phase screen, and the characteristic size of the phase inhomogeneities.
4. A phase layer of special configuration can be used to filter some harmonics from nonlinear interactions in a finite amplitude focused beam.
5. Numerical algorithm based on the Westervelt equation allows to simulate ultrasound fields with shocks generated by transducers with complex geometry, including multi-element two-dimensional arrays of modern ultrasonic surgical devices.
6. Model of equivalent axially symmetric source can be used to simplify simulations of nonlinear fields of therapeutic arrays in the focal region in a wide range of transducer parameters and acoustic intensity. The calculations can be used to optimize configuration of arrays at the development stage and to estimate nonlinear effects in the focus.

Main results

1. Shadowgraphy method combined with interpretation of shadowgrams based on simulations of light diffraction on the shock front allows to measure the shocks with rise time of 0.15 μs. This time resolution is one order greater than the resolution which can be obtained using modern wide-band condenser microphones.
2. In the case when the main parameters and intensity level of sound speed fluctuations in kinematic and in thermal turbulence are the same, the latter leads to weaker distortions of the statistics of the propagated N-wave. Equal level of distortions is achieved if intensity of the sound speed fluctuations in a kinematic turbulence is 2-3 times smaller than in a thermal turbulence.
3. Developed numerical model allows to describe statistical characteristics of the N-wave behind a random phase screen taking into account the propagation trough caustics. Distortion of statistical distributions of acoustic field behind the screen is determined by the amplitude of the wave, the refraction length, and by the scale of phase inhomogeneities. Approximation of the non-

linear geometrical acoustics is valid for propagation distances up to one third of the refraction length.

4. Using a special ”resonant” phase layer it is possible to destroy focusing of some spectral components of the focused nonlinear beam and to preserve focusing of other components.
5. The new numerical algorithm allows to simulate three-dimensional nonlinear ultrasound fields with localized formation of shocks. For intensity levels achieved in the modern therapeutic arrays, shock fronts with amplitudes up to 80 MPa can be formed in the focus.
6. The model of an axially symmetric equivalent source allows to simulate nonlinear effects in the focal region of transducers with complex geometry with high accuracy ($2 - 3$ %), including the multi-element phased arrays with random distribution of elements.

Presentations and conferences

The results included into the dissertation have been presented at the following Russian and international conferences: at the meetings of Acoustical Society of America (Honolulu, USA, November-December 2006 and Seattle, Washington, May 2011), at the conference ”Waves-2006” (Zvenigorod, Russia, May 2006), at the XVIII, XIX and XXII Sessions of Russian Acoustical Society (Taganrog, 2006, Nizhniy Novgorod, 2007, and Moscow, 2010), at the 19th International Congress on Acoustics (Madrid, Spain, September 2007), at the joint meeting of Acoustical Society of America and European Association of Acoustics ”Acoustics’08” (France, Paris, June-July 2008), at the 10-th Congress of French Acoustical Society ”CFA10” (France, Lyon, 2010), at the 2nd International Symposium ”Current and future applications of MR-guided focused ultrasound 2010” (Washington DC, USA, October 2010), at the trilateral conference ”Computational Experiment in Aeroacoustics”, CEAA (Svetlogorsk, September 2010), at the conference ”Advanced Metrology for Ultrasound in Medicine”, (Teddington, UK, May 2010), at 11th International Symposium on Therapeutic Ultrasound, (New York, April 2011), at International Congress on Ultrasonics, (Gdansk, Poland, September 2011). All the obtained results have been also discussed at the scientific seminars of the Department of Acoustics of the Moscow State University, at the seminar of Prokhorov General Physics Institute of Russian Academy of Sciences (April 2009), and at the seminar of the N.N. Andreev Acoustical Institute (October 2011).

This work was partially supported by the grant of the president of the Russian Federation no. Scientific School-4449.2006.2, by the grants RFBR no. 10-02-91062-CNRS and no. 09-02-01530, by GPI RAS’s Fundamentals of Acoustic Diagnostics of Artificial and Natural Media programs, ISTC (project no. 3691) and NIH (project no. R01EB007643), by the grant INTAS no. 7841, by Projet International de Coopération Scientifique (PICS RFBR 10-02-91062/CNRS 5603) grants, by the international student award of the Acoustical Society of America, and by special stipend of the French Government for the preparation of the dissertation under the co-supervision in the frame of the agreement between École Centrale de Lyon, France and Physics Faculty of the Moscow State University, Russia. Computational resources were provided by Supercomputer Center of MSU and by LMFA.

Publications

Main results of the dissertation are published in 21 papers, 5 of which are pre-reviewed articles in journals, 10 are articles in conference proceedings and 6 are abstracts of conferences.

Author's personal contribution

The author took part in all the steps of the research presented in the dissertation. Investigation consisted of the development of the theoretical and numerical models and conduction of the experiments. Experimental data presented in the dissertation were obtained personally by the author in collaboration with the team of LMFA, Ecole Centrale de Lyon (Sébastien Ollivier, Edouard Salze, Emmanuel Jondeau, Jean-Michel Perrin, Nathalie Grosjean) and with LEMAC laboratory of A.M. Prokhorov General Physics Institute of Russian Academy of Sciences (Leonid Krutyansky and Andrey Brysev).

Structure and volume of the dissertation

The dissertation consists of the introduction, five chapters, conclusions, four appendixes, and list of references. Each chapter, in addition to the original material, contains an introduction with literature review and conclusions. The references list contains 150 articles on 10 pages; the total volume of the dissertation is 170 pages, including 85 figures and 5 tables.

Figures and formulas in the dissertation are referred as (5.3) where the first number is the chapter number and the second number is the number of the formula or the figure in this chapter.

Dissertation content

The first chapter is devoted to measurements of short duration and high amplitude shock pulses using acoustical and optical methods. In §1.1 a review on the use of spark sources in model aeroacoustic experiments to generate N-pulses with a narrow shock front is presented. The problem of measuring such pulses using condenser microphones is discussed. The possibility to use optical shadowgraphy methods to improve time resolution in measurements of the shock front is proposed. In §1.2 the experimental setup for optical and acoustic measurements of the spherical N-wave in homogeneous air is described. The N-wave propagation is analyzed in §1.3 using numerical simulation of the Burgers equation. In §1.4 the results of acoustic measurements of the N-wave are shown and the method for determination of the wave parameters from these data is described. A comparison of the experiment with theory showed good agreement in amplitude and duration, but not for the shock rise time. In §1.5 optical measurements of the shock rise time using shadowgraphy method are described. Shadowgrams are interpreted by modeling light propagation through inhomogeneities of the refraction index at the shock. The results of optical measurements are shown to be in excellent agreement with the theory based on the Burgers equation. In §1.6 conclusions of chapter 1 are given.

The second chapter of the thesis is devoted to experimental study of the spherical N-wave propagation in thermal turbulence. In §2.1 a review of laboratory-scaled experiments used to investigate the propagation of N-pulses in a boundary turbulent layer of atmosphere is given. The problem to study quantitative differences in the statistics of N-wave after propagation through turbulence layer of different types – either thermal (scalar type) or kinematic (vector type) turbulence – is posed. In §2.2 the particular features of the spectra of the vector and scalar turbulent fields which have influence on distortions of acoustic waves are discussed. §2.3 describes an experimental setup built at the Graduate Engineering School of Lyon (ECL), which allows to investigate the N-wave propagation through thermal turbulence generated by a heating grid. In §2.4 experimental characterization of the turbulent field using thermal probe is reported. In §2.5 statistical distributions of various parameters of the N-wave (amplitude, duration, shock rise time) obtained at different distances from the source in series of acoustic measurements are presented. In §2.6 the experimental data are compared with the statistics of the N-wave propagated in kinematic turbulence (Averiyanov, 2008). It is shown, that if other conditions are the same, the kinematic turbulence is 2-3 times more efficient than thermal turbulence in terms of probability to observe strong focusing. In §2.7 conclusions of chapter 2 are given.

In the third chapter the theoretical model which allows to describe the statistics of N-wave acoustic field after propagation in random medium is considered. The model is based on the two-dimensional KZK equation and on the phase screen model. In §3.1 a review on the application of phase screen models in problems of wave propagation in random inhomogeneous media is presented. Studies where statistics the N-wave amplitude was investigated in the approximation of nonlinear geometrical acoustics (NGA) are discussed. Limitations of the NGA approach are noted and advantages of parabolic equation which takes into account diffraction effects are emphasized. Numerical method for solving the KZK equation is described in §3.2. The phase screen model with a Gaussian spectrum is presented in §3.3. Phase screen is determined by the correlation length which corresponds to the characteristic size of phase inhomogeneities and by the refraction length – characteristic distance where first caustics occur. In §3.4 the typical spatial patterns of the peak positive pressure and distorted N-waveforms in the regions of random focusing and defocusing are shown. Qualitative impact of nonlinear effects and the size of inhomogeneities is discussed. In §3.5 the probability distribution functions of the N-wave amplitude are presented which were obtained from the simulations with long phase screen realizations. Parametric study of the effects of the size of inhomogeneities and nonlinearity on the broadening of the distribution functions is performed for different propagation distances. A comparison with analytical results of the NGA is provided. The applicability of the NGA is found only up to distances of one third of the refraction length. Twofold effect of nonlinearity, which lead either to broadening (weak nonlinearity) or narrowing (strong nonlinearity) of the distribution functions is discussed. In §3.6 conclusions of chapter 3 are given.

The fourth chapter is devoted to theoretical and experimental study of nonlinear beam focusing through a physically realizable phase screen (phase layer) of a special configuration. In §4.1 the problem of beam focusing through randomly inhomogeneous medium is discussed in the context of medical diagnostic ultrasound and nondestructive testing. A possible better focusing of the beam on frequency of higher harmonics is noted. A problem of control the focusing of different harmonics in the beam using the resonant phase distortion introduced by a special phase layer is posed. In §4.2 theoretical model to simulate the propagation of nonlinear beam, based on the Westervelt equation, is described. The focusing quality criterion for harmonics is introduced and theoretical model of the phase layer which consists of a great number of identical circular regions with fixed phase shift and randomly distributed in a plane is presented. In §4.3-4.4 the simulation results for different harmonics in two special cases of 180° and 90° phase shifts for fundamental frequency component on layer inhomogeneities are discussed. The possibility to selectively destroy the focusing of the fundamental frequency and odd harmonics in the case of 180° phase layer is shown. The destruction of the second harmonic in the case of 90° layer located close to the focus is demonstrated. When the 90° phase layer is placed close to the source the better focusing of the higher harmonics is shown. In §4.5 the experimental setup which was used to measure the ultrasound field of the focused transducer is described. The experiment was done in LEMAC laboratory in GPI of A.M. Prokhorov. Physical realizations of 180° and 90° phase layers are presented. The experimental results are shown to qualitatively confirm the results of simulations . In §4.6 conclusions of chapter 4 are given.

The fifth chapter deals with the problem of modeling three-dimensional high intensity focused ultrasound fields generated by 2D therapeutic arrays with account for the formation of shocks in the focus. In §5.1 a review of perspective and applications of therapeutic arrays is done. The importance of modeling of their nonlinear acoustic fields is discussed. The main constraints and problems associated with numerical methods and computing resources are identified. In §5.2 a theoretical model based on the equation Westervelt is described, and the boundary conditions for the numerical algorithm are provided. Various optimization and parallelization of the algorithm are discussed, which are necessary due to the high numerical burden of the problem both in computation time and memory. In §5.3 the results of tests which confirmed accuracy of the algorithm are presented. In §5.4 the results of the pressure field simulations for an 256-element therapeutic array in a wide range of intensities of ultrasound are presented. Formation of a shocked waveform in the focus is shown at intensity levels that can be achieved in modern devices. In §5.5 a method of an axially symmetric equivalent transducer which allows to accelerate calculations of the fields of therapeutic arrays in the focal region is discussed. In §5.6 conclusions of chapter 5 are given.

In the general conclusions, the main results are briefly summarized.

Chapter 1

Measurements of the N-wave front shock rise time in air using microphones and shadowgraphy optical method

§1.1 Introduction

Pressure N-waves with durations of the order of tens of microseconds can be generated in air by electric sparks or focused laser beams (Wright, 1983, Qin & Attenborough, 2004). Close to the source, the amplitude of the initial spark-generated N-wave can be quite high ($>$ 1000 Pa) and nonlinear propagation effects are of importance not only in the close vicinity of the spark (where they are the reason for N-wave formation), but also at some distance from the origin (Yuldashev *et al.*, 2008b). Such experimental conditions that provide nonlinearly propagating N-wave have been used in downscaled laboratory experiments on sonic boom propagation in order to study the distortion of N-waves by atmosphere inhomogeneities (Davy & Blackstock, 1971, Lipkens, 1993, Lipkens & Blackstock, 1998a, Lipkens & Blackstock, 1998b, Lipkens, 2002, Ollivier & Blanc-Benon, 2004, Averiyanov, 2008, Blanc-Benon *et al.*, 2005). Short duration N-waves are also used in laboratory experiments to simulate problems of architectural acoustics, (Picaut & Simon, 2001) street acoustics, (Grillon *et al.*, 1996, Picaut *et al.*, 2005) and outdoor sound propagation, (Almgren, 1986) where wide bandwidth and high frequencies of pressure waves are desirable.

The validity of experimental data analysis and the validity of comparison between experimental and theoretical data strongly depend on the accurate knowledge of the initial N-wave parameters such as peak pressure, duration, and shock rise time. It is thus of utmost importance to accurately measure and model the propagation of N-waves in homogeneous air before investigating more complex configurations. However, it has been shown that it is technically difficult to resolve the fine structure of the shocks that have rise times less than one microsecond, mainly because of the limited frequency bandwidth of commercially available microphones (Loubeau *et al.*, 2006, Yuldashev *et al.*, 2008b). This complicates experimental validation of the theoretical predictions of shock fine structure and high frequency spectrum.

Propagation of spark-generated N-waves in homogeneous atmosphere has been studied experimentally by several authors, in particular by W. Wright and co-workers (Wright, 1983, Wright & McKittrick, 1967, Wright & Medendorp, 1968). Recently, the relative roles of nonlinear effects, thermoviscous absorption, and molecular (oxygen and nitrogen) relaxation in N-waveform distortion were studied both experimentally and theoretically (Yuldashev *et al.*, 2008b, Averiyanov *et al.*, 2007). A numerical model based on the generalized Burgers equation was developed and the ability of the model to predict peak pressures and duration of the wave was established. However, strong discrepancies between modeling and measurement were observed in estimation of the front shock rise time which was attributed to the limited bandwidth of the microphone. Better resolution was achieved using handmade microphones, but overestimated values of the shock rise time were still recorded (Wright, 1983, Wright & McKittrick, 1967, Wright & Medendorp, 1968, Lipkens & Blackstock, 1998a). More accurate experimental techniques are therefore necessary to measure frequencies above 150 kHz and to resolve fine shock structure. This problem is of particular importance for sonic boom propagation studies because shock rise time is one of the important parameters responsible for the boom annoyance (Fidell *et al.*, 2002, Leatherwood & Sullivan, 1992).

An alternative approach to measure pressure shocks in a laboratory environment is to use optical methods instead of acoustic microphones. Measurement of shock thickness using optical methods has been widely treated in literature (Mach & Salcher, 1887, Settles, 2001, Merzkirch, 1974, Yuldashev *et al.*, 2008a, Yuldashev *et al.*, 2010b, Cowan & Hornig, 1950, Greene *et al.*, 1951, Panda & Adamovsky, 1995, Panda, 1995). However, although weak shocks have been addressed, (Settles, 2001) most of the effort was generally focused on measuring strong shocks created by supersonic flows; the thickness of strong shocks was usually estimated using indirect methods based on the shock speed measurements (Hargather & Settles, 2007,Panda & Adamovsky, 1995, Panda, 1995). It was also shown that a laser interferometer can be used to measure spark generated pressure waves, but no quantitative analysis has yet been done (Smeets, 1977).

The goal of this work is to demonstrate that the combination of optical and acoustical methods allows complete characterization of short duration and high amplitude N-waves, including rise time measurements. An N-wave is recorded by a microphone along the propagation path from a spark source. The fine structure of the shock is also deduced from the shadowgraphy images with a resolution that cannot be obtained via acoustic measurements (Settles, 2001, Merzkirch, 1974). The distributions of light intensity in the measured images are compared to the results of modeling of light propagation through inhomogeneities of refraction index caused by the presence of the shock. To reveal whether diffraction of light has to be considered in simulations, two models are built. The first model is based on the geometrical optics approximation, (Kravtsov & Orlov, 1990) while the second one is based on scalar diffraction theory (Goodman, 1996). Experimental data for N-wave parameters are compared with the results of acoustic modeling, where spherical spreading, thermoviscous dissipation, oxygen and nitrogen relaxation, and nonlinear propagation are included (Yuldashev *et al.*, 2008b).

§1.2 Experimental setup for acoustical and optical measurements

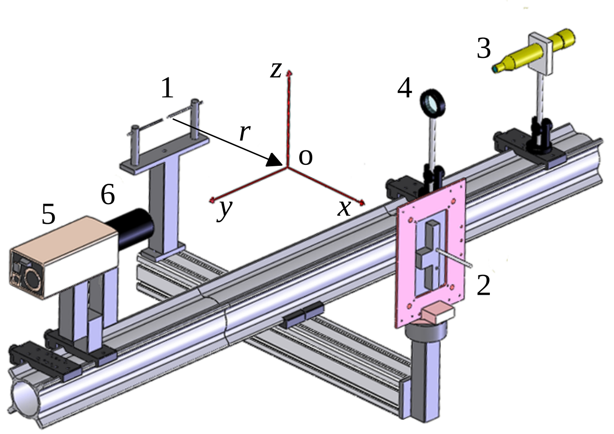

Figure 1.1: Experimental setup: 1-spark source, 2-microphone in a baffle, 3-Nanolight flash lamp, 4-focusing lens, 5-camera, 6-lens.

The experimental setup designed for acoustical and optical measurements of spark-generated N-waves in homogeneous air is presented in Fig. 1.1. High amplitude pressure pulses are produced by a 15 kV spark source (1) with 16 mm gap between tungsten electrodes. The repetition rate is of the order of 1 Hz. Spherically diverging pulses are measured along the x coordinate with a broadband microphone (Brüel & Kjær, 1/8” diameter, type 4138) coupled with an adapted preamplifier (B&K 2670) and amplifier (B&K Nexus amplifier with extended bandwidth -3 dB at 200 kHz). The microphone is mounted into a baffle (2) in order to avoid diffraction effects on its edge. The recorded signal is digitized (12 bit, 5 MHz) using a data acquisition card (National Instruments PCI 6610). The sensitivity of the microphone is defined using the calibration method presented in (Yuldashev *et al.*, 2008b, Averiyanov, 2008, Averiyanov *et al.*, 2007) and is equal to 1.46 mV/Pa at low frequencies. The measurements are performed at increasing source-microphone distances from 16 cm to 105 cm.

Optical equipment includes a flash-lamp (3) (Nanolite KL–L model, 3.5 kV tension), light filter, lens (4) (4 cm diameter, 16 cm focal length), a digital CCD camera (5) (Dantec dynamics, FlowSense 2M) with acquisition system, Nikon lens (6) with 60 mm focal length, and calibration grid. Optical equipment is mounted on a rail and aligned coaxially. The flash-lamp generates short duration (20 ns) light flashes that allow to have a good resolution of the front shock shadow. According to theoretical estimations, the minimum rise time expected in experiments is as small as $0.1\,\mu$s, that is 5 times longer than the flash duration. Longer light flash duration would result in long signal integration times, so that the shock image would be blurred. The focusing lens is used to collimate the flash light in order to have a parallel light beam. The dimension of the CCD camera is 1600 pixels along the horizontal coordinate and 1186 pixels along the vertical coordinate. The lens is used to focus the camera at a given observation plane perpendicular to the optical axis. Before each optical measurement, the CCD camera and lens are calibrated by capturing an image of a calibration grid placed at the chosen observation plane. Light source and camera are triggered by electromagnetic pulse of the spark.

Choosing $t = 0$ as the time when a spark is generated, photographs are taken at the instant t when the front shock position is tangent to the optical axis. At this time, a local coordinate system shown in Fig. 1.1 is defined in the following way: y is the coordinate along the optical axis, which is the light propagation direction from the optical source to the camera; x is the axis in the acoustic source-microphone direction, perpendicular to the optical axis; z is the axis perpendicular to the xy plane. The origin O thus corresponds to the point where the light beam grazes the front shock of the N-wave. The acoustic source coordinates are $(x_S, y_S = 0, z_S = 0)$, with $x_S < 0$. The coordinate r corresponds to the radial distance from the acoustic source, it is related to the local cartesian coordinates by: $r = \sqrt{(x-x_S)^2 + y^2 + z^2}$. The wavefront radius at the observation time t is named R; with this definition $R = |x_S|$. Optical measurements of the shock front are performed for different distances from 16 to 66 cm between the spark source and the optical axis.

§1.3 Theoretical background: propagation of a spherical N-wave in air

In this section, the propagation of a high amplitude pulse is studied theoretically, simulating the experimental conditions of spark-generated N-waves in air. The propagation model is first reviewed, (Yuldashev *et al.*, 2008b) then the effects of thermoviscous absorption, nonlinear propagation and relaxation on distortion of the N-wave parameters are discussed.

1.3.1 Sound propagation model

Consider a point source that generates high amplitude spherically divergent pulsed waves. To model the propagation of the pulse in the relaxing homogeneous atmosphere a generalized Burgers equation (Rudenko & Soluyan, 1977, Yuldashev *et al.*, 2008b) is used:

$$\frac{\partial p}{\partial r} + \frac{p}{r} = \frac{\beta}{\rho_0 c_0^3} p \frac{\partial p}{\partial \tau} + \frac{b}{2\rho_0 c_0^3} \frac{\partial^2 p}{\partial \tau^2} + \sum_{\nu=1}^{2} d_\nu \frac{\partial}{\partial \tau} \int_{-\infty}^{\tau} \exp\left(-\frac{\tau - \tau'}{\tau_\nu}\right) \frac{\partial p}{\partial \tau'} \mathrm{d}\tau' \tag{1.1}$$

Here p is the acoustic pressure, r is the radial propagation coordinate with the origin at the source, $\tau = t - (r - r_0)/c_0$ is the retarded time, c_0 is the ambient sound speed at low frequencies, r_0 is the reference distance to set boundary conditions, ρ_0 is the density, β is the coefficient of nonlinearity, and b is the coefficient of viscosity in the air. Each relaxation process ν is characterized by two parameters: relaxation time τ_ν and coefficient $d_\nu = (c_\infty^\nu - c_0)/c_0^2 = c_\nu/c_0^2$, where c_∞^ν is the so-called frozen sound speed of an acoustic signal propagation through the medium with relaxation time much longer than the effective duration of the signal $T_s << \tau_\nu$. The second term on the left-hand side of Eq. (1.1) accounts for the spherical divergence of the wavefront, while the right-hand side accounts for nonlinear effects (first term), dissipation due to thermoviscous absorption (second term), and relaxation processes associated with the excitation of oscillatory energy levels of oxygen O_2 and nitrogen N_2 in the air (last term) (Rudenko & Soluyan, 1977, Cleveland *et al.*, 1996, Pierce, 1981). Equation (1.1) is valid if $\lambda/r << 1$, where λ is the wavelength associated with the length of the N-wave. This condition is satisfied in the current laboratory-scaled experiments ($\lambda \sim$ 1.5 cm, $r >$ 15 cm).

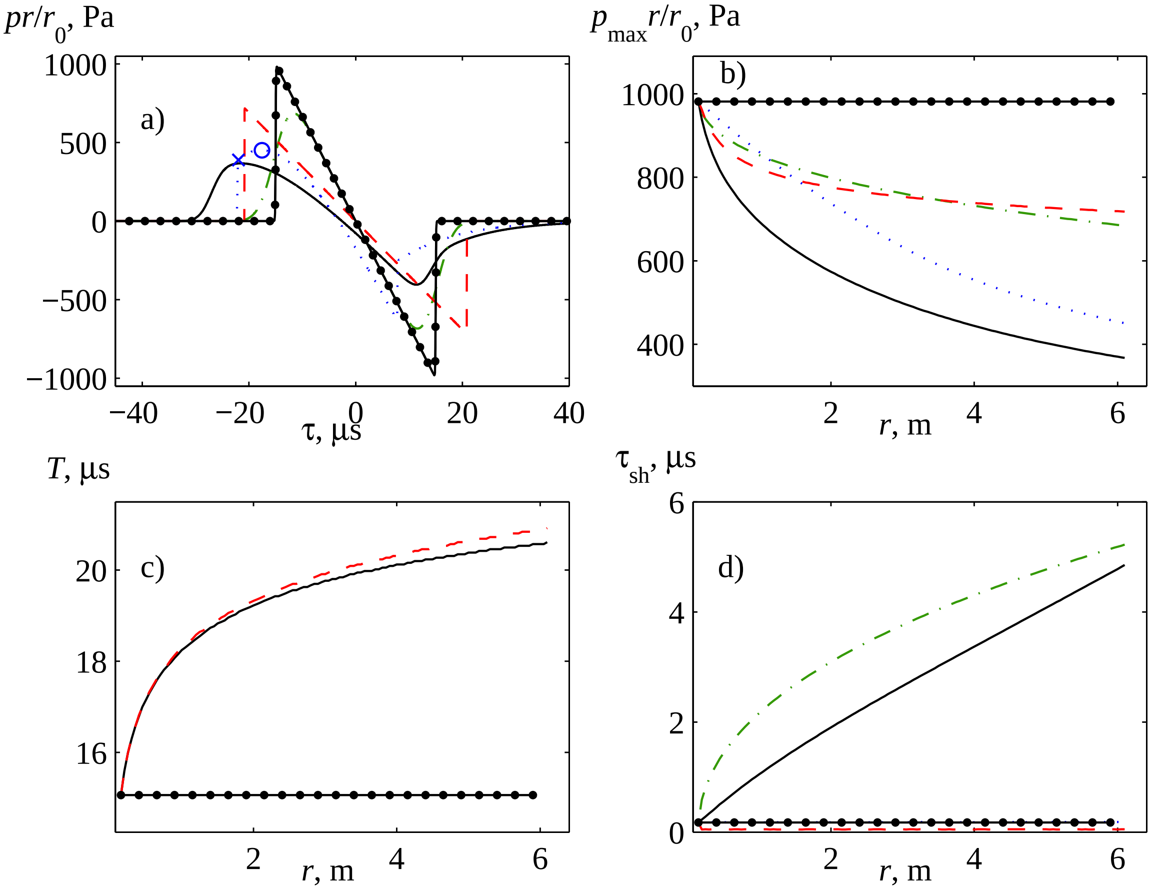

Figure 1.2: Relative effects of nonlinearity, thermoviscous absorption, and molecular relaxation on N-wave propagation: (a) simulated waveforms at the distance $r = 6$ m, (b) peak positive pressure, (c) duration, and (d) rise time along the propagation path.

Equation (1.1) is solved numerically in finite differences using a previously developed algorithm (Yuldashev *et al.*, 2008b). The initial waveform is set at the distance r_0 from the source in the form of an ideal N-wave with thin shocks that are smoothed according to the quasi-stationary solution of the classic Burgers equation. The initial rise time of the shock is thus defined by the balance of the nonlinear and dissipation effects, which better approximates the experimental conditions. The equation (1.1) is solved using a method of fractional steps with an operator splitting procedure of the first order (Ames, 1992). At each step in the propagation distance the calculations of the nonlinear term are performed in the time domain using the central flux-conservative Godunov-type algorithm (Kurganov & Tadmor, 2000); thermoviscous absorption and relaxation terms are calculated in the frequency domain using the exact solution for each spectral component; spherical divergence of the wave is taken into account by introducing specific dimensionless variables in the Eq. (1.1). Both oxygen and nitrogen relaxation effects are included in further simulations presented in the chapter.

1.3.2 Effect of nonlinearity, thermoviscous absorption, and relaxation on N-wave propagation

In order to evaluate the relative roles of acoustic nonlinearity, thermoviscous absorption, and relaxation on the distortion of the spherically diverging N-wave in air, numerical simulations based on Eq. (1.1) are performed with alternative inclusion of each term, responsible for the corresponding effect. The parameters used to model the propagation medium correspond to the experimental conditions: β = 1.2, $b = 4.86 \cdot 10^{-5}$ Pa·s, ρ_0 = 1.19 kg/m^3, $c_0 = 343.8$ m/s. For a relative humidity of 34 $\%$, a temperature of 293 K, and an ambient pressure level of 1 atmosphere, the parameters c_ν and τ_ν of oxygen and nitrogen relaxation processes are calculated using empirical expressions: c_1 = 0.11 m/s, τ_1 = 6.0 μs (O_2) , c_2 = 0.023 m/s, τ_2 = 531 μs (N_2) (Pierce, 1981). The amplitude of the initial N-wave is p_0 = 1000 Pa and the half-duration is T_0 = 15 μs, which corresponds to the typical values measured at r_0 = 15 cm from the acoustic source. The shock rise time of the initial N-wave, defined here as the time during which the acoustic pressure increases from 0.1 to 0.9 level of the peak positive pressure, (Lipkens & Blackstock, 1998a) is chosen according to the quasi-stationary solution of the Burgers equation as $\tau_{\text{sh0}} = 0.18$ μs.

A summary of the results of modeling N-wave propagation is presented in Fig. 1.2. Shown in Fig. 1.2a are the waveforms obtained at the distance $r = 6$ m from the source. This distance is chosen because it is sufficiently long to distinguish clearly the changes in the waveform due to all the effects discussed above. The waveforms are multiplied by the ratio r/r_0 in order to compensate for spherical divergence of the wave that dominates over other physical effects. The solid curve with bold circles is obtained if the right-hand side of the Eq. (1.1) is set to zero, i.e. if only spherical divergence is considered. In this case, the waveform compensated by r/r_0 remains identical to the initial waveform at r_0. Other physical effects are further accounted separately: nonlinear effects (dashed curve), thermoviscous absorption (dash-dotted curve), and oxygen and nitrogen relaxation (dotted curve). Finally, all the mentioned effects are accounted together (black solid curve).

In accordance to the weak shock theory, the presence of nonlinear effects only (dashed curve) results in increased duration and decreased peak pressure level of the wave (Rudenko & Soluyan, 1977,Pierce, 1981). Linear thermoviscous absorption (dash-dotted curve) has no effect on the wave duration measured between half peak pressure levels but increases the rise time and attenuates the peak pressures. Relaxation phenomena (dotted curve) have negligible effects on the rise time of the shocks and pulse duration, but they attenuate the peak pressures and distort the waveform that becomes asymmetric; the front and rear shock fronts are shifted equally in time because of faster propagation of high frequencies in a relaxing medium. All effects except molecular relaxation keep the wave symmetric. When all effects are included together in the propagation model (black solid curve), the duration and the rise time increase while the peak pressure decreases and the waveform becomes asymmetric. Note, however, that for propagation distances shorter than $r = 1$ m the waveform retains its symmetric shape almost unchanged (not shown here) in contrast to the waveform calculated at 6 m from the source.

Propagation curves for the peak positive pressure $p_{\max}$ and half-duration T of the wave are presented in Fig. 1.2b-c. The peak positive pressure depends on both nonlinear effects, relaxation, and thermoviscous absorption (Fig. 1.2b). No pulse lengthening is observed when only thermoviscous absorption or relaxation are present (dotted and dash-dotted curves coincide with the solid curve with bold circles); it is mainly determined by the nonlinear effects (Fig. 1.2c). The difference between the black solid curve (all effects) and the dashed curve (nonlinear effects only) at propagation distances longer than one meter comes from the fact that molecular relaxation and thermoviscous absorption attenuate the pressure level, which in turn weakens the nonlinear effects. For distances up to one meter, pulse lengthening can be estimated by accounting only for nonlinear propagation effects, as relaxation and thermoviscous absorption have little influence. This justifies the method proposed by Wright (Wright, 1983) to estimate the sensitivity of microphones from the pulse lengthening. However, for propagation distances longer than one meter the effect of molecular relaxation cannot be neglected.

The dependence of the front shock rise time τ_{sh} (the time needed to pressure rise from 0.1 to 0.9 of the peak positive pressure) on the propagation distance is presented in Fig. 1.2d. If the relaxation effects are taken into account, the rise time is calculated by considering the front shock amplitude (from zero pressure up to the cross marker in Fig. 1.2a) rather than using the maximum pressure of the wave (circle marker). Using this definition the rise time coincides with the rise time of the initial wave. However the amplitude of the shock decreases due to relaxation effects. On the contrary, the thermoviscous absorption significantly increases the rise time. If nonlinear effects only are considered (dashed curve), the rise time tends to decrease to zero, as described by the weak shock theory (Rudenko & Soluyan, 1977). However, the minimum rise time of $0.05\ \mu\text{s}$ is achieved in numerical simulations due to internal viscosity of the numerical algorithm. This internal viscosity is much weaker than the real air viscosity and hence does not introduce significant error to the results of simulations. Finally, if all the effects are taken into account (black solid curve), the shock front rise time is governed by the competition between the nonlinear and absorption effects. In this competition, the role of nonlinear effects diminishes with the propagation distance because the pressure level decreases. In the next section, theoretical predictions obtained from the model that include all previously mentioned effects are compared to experimental data measured using a 1/8 inch condenser microphone.

§1.4 Acoustical measurements of N-wave waveforms

The goal of this section is to compare, for increasing propagation distances, theoretical predictions to pressure measurements using a microphone. Accurate characterization of the N-wave which is used as an input to the model is a critical point. First the method how the duration and the peak pressure of the measured wave can be determined despite the microphone-induced distortion of the waveform is detailed. Simulations and acoustic measurements of the peak pressure, N-wave duration, and shock rise time are then compared along the propagation path. In the next sections the accuracy of the rise time measurements is improved using optical methods.

1.4.1 Characterization of the N-wave parameters in experiment

Estimation of the N-wave duration from measurement

The straightforward definition of the N-wave duration in the modeling is taken as the time between the points of the half peak positive and negative pressure values. However, in the measurements, the waveform is distorted due to the limited bandwidth of the microphone, therefore the definition is not so obvious. This section details how the duration of the N-wave can be accurately estimated from the spectrum of the measured waveform even if it is filtered by the microphone. Accurate estimation of the N-wave duration is critical since this parameter is used to determine the sensitivity of the microphone by analyzing the pulse lengthening due to nonlinear propagation effects (Wright, 1983).

The pressure waveforms obtained from the microphone output are typically different from an N-wave: they have a much more complex and asymmetric shape with oscillations (Yuldashev *et al.*, 2008b, Qin & Attenborough, 2004). This distortion is due to the limited frequency response of the microphone and amplifier, and also due to the diffraction effects on the edge of the residual small gap between the microphone and the baffle (Wright, 1983). Even if an ideal pressure N-wave is incident on the membrane of the microphone, the output voltage from the amplifier $v(t)$ is not a symmetric N-wave. Consequently, the estimation of the pulse duration is significantly influenced by the frequency response of the measuring system. In contrast to other papers, (Wright, 1983, Lipkens & Blackstock, 1998a) the duration of the pulse is estimated here from the spectrum of the wave rather than from the waveform itself.

The definition of pulse duration in the frequency domain is based on the analysis of the frequencies where the amplitude of the spectrum is minimum (close to zero) (Yuldashev *et al.*, 2008b). If the microphone response and diffraction effects can be represented in the frequency domain as a smooth transfer function, the frequencies of the spectrum minima (which are zeros for an ideal N-wave) should be the same for the N-wave spectrum and for the corresponding output voltage from the microphone. If $\widehat{p}(f)$ is the spectrum of the pressure N-wave incident on the microphone (in Pa), and $\widehat{H}_M(f)$ is the measurement chain frequency response (in Volts/Pa), then the spectrum of the output voltage from the amplifier is $\widehat{v} = \widehat{p}\widehat{H}_M$. If the high frequency cutoff of the response $\widehat{H}_M$ is above the frequency of several first minima in the spectrum $\widehat{p}$, these first minima of the N-wave spectrum $\widehat{p}$ and of the measured spectrum $\widehat{v}$ will be the same and well detectable. If the incident pressure wave is close to an ideal N-wave, then its duration can be deduced, for example, from the frequencies f_1 and f_2 of the first two minima in the spectrum $\widehat{v}$. For an ideal N-wave, its half duration T is related to f_1 and f_2 by $T = 0.718/f_1$ and $T = 1.226/f_2$. In this work, it is assumed that pressure waveforms are close to ideal N-waves. The duration of the measured wave $v(t)$ is therefore considered to be equal to that of the ideal N-wave whose frequencies of the

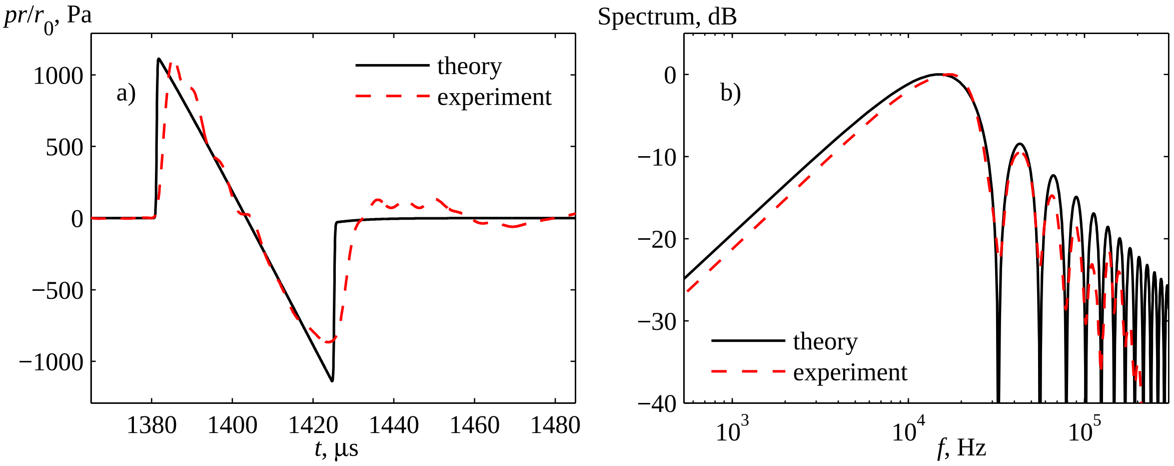

Figure 1.3: Measured (dashed) and calculated (solid) waveforms at the distance r = 49 cm from the source (a); corresponding normalized amplitude spectra (maximum at 0 dB) (b).

first two minima in the amplitude spectrum $\widehat{p}$ match the frequencies of the first two minima in the spectrum $\widehat{v}$ of the measured signal.

Setting initial peak pressure and duration of the N-wave in the modeling

To proceed with the numerical modeling, not only duration, but also the peak pressure (amplitude) of the N-wave should be set at the initial distance $r_0 = 16$ cm from the source. The peak pressure at r_0 is determined according to the following method proposed in the earlier papers (Wright, 1983, Lipkens & Blackstock, 1998a, Yuldashev *et al.*, 2008b). As it was shown in Fig. 1.2 the effects of nonlinear propagation are dominant close to the source ($r < 1$ m), thus it is assumed that the lengthening of the N-wave with the propagation distance r is linked to the initial peak pressure according to the weak shock theory (Pierce, 1981). The mean half duration of the experimental wave is estimated at different distances from the source and the linear dependence of T^2 on $\ln(r/r_0)$ is then fitted to find the initial peak pressure of the wave. The following values are obtained: peak pressure $p_{\max} = 1400 \pm 80$ Pa and half duration $T_0 = 19.0 \pm 0.1$ μs.

1.4.2 Comparison of simulation data with experimental results

In this section the results of the microphone measurement of the pressure waveform, peak pressure, half-duration, and rise time of the front shock at different distances are compared to the theoretical data obtained with medium and initial wave parameters identical to that in the experiment (temperature = 291 K, relative humidity = 34%, $r_0 = 16$ cm, $p_{\max}(r_0) = 1400$ Pa, $T_0(r_0) = 19.0$ μs).

Waveform and spectrum

The pressure waveform obtained from the microphone output voltage at 49 cm from the source and the corresponding amplitude spectrum (dashed curves) are compared in Fig.1.3 to the results of numerical simulations (solid curves). The experimental and the calculated waveforms are quite

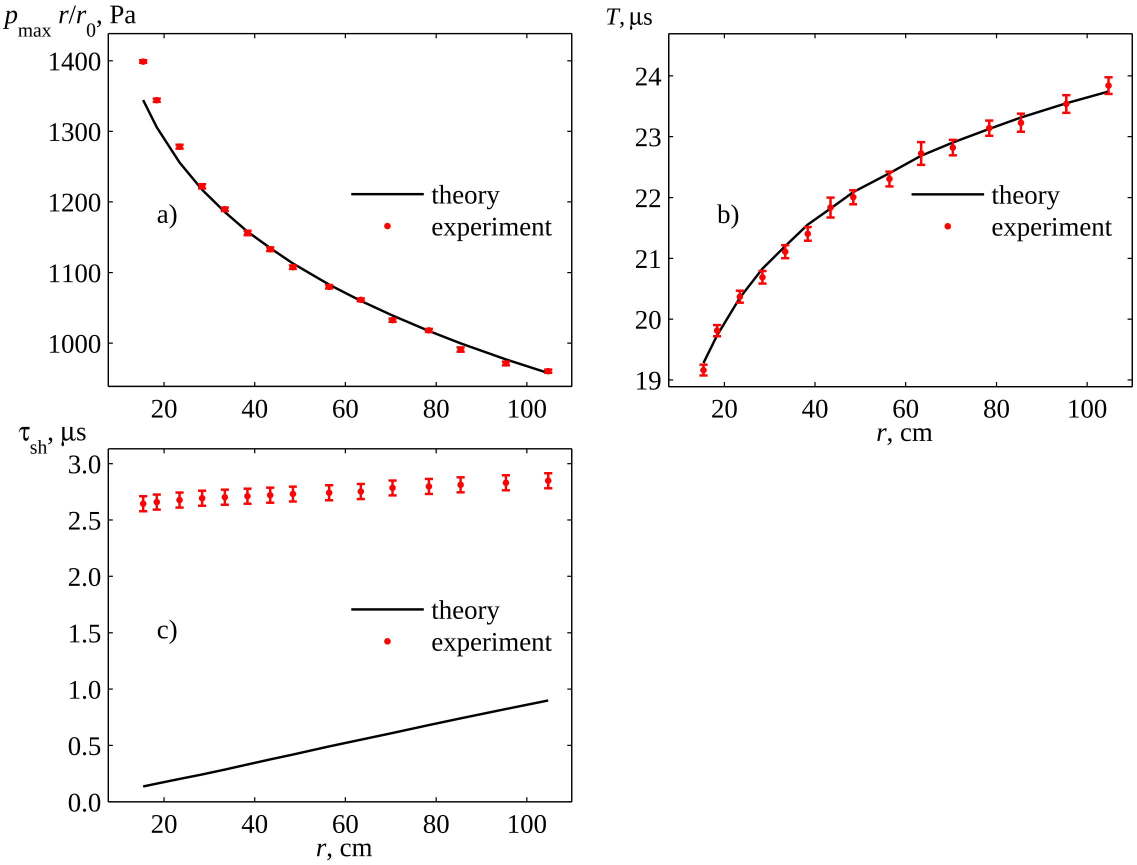

Figure 1.4: Theoretical (solid line) and experimental (markers with error bars) data for peak positive pressure (a), half duration (b), and rise time (c) of the wave.

different. The shape of the calculated waveform is almost symmetric which confirms that oxygen and nitrogen relaxation has little effect at short propagation distances (Fig. 1.2). Contrary to that, the measured waveform is much less symmetric, has oscillations on the back slope, and the rise time of both shocks is much longer. Concerning the amplitude spectrum (Fig.1.3b), at frequencies less than 80 kHz the measured spectrum (dashed curve) is very close to the calculated one (solid curve) both in its shape and amplitude. At frequencies higher than 80 kHz the amplitude of the measured spectrum decreases with much higher rate than the calculated one. These differences, that are due to the limited frequency response of the measurement system, explain the fact that the rise time of the measured waveform is much longer than that of the calculated one. A good agreement between the positions of spectrum minima is achieved at all ranges of frequencies, that validates the method of estimating pulse duration from the spectrum minima. Note, that the values of half-duration T calculated using only the first f_1 or only the second f_2 minima agree within an interval of 3%.

Peak pressure, duration, and rise time

Measured and modeled propagation curves of (a) the peak pressure, (b) the duration, and (c) the rise time are compared in Figs. 1.4a-c. Similar to the results shown in Fig. 1.2, the peak pressure in Fig. 1.4a is multiplied by the ratio r/r_0 in order to compensate for the decrease of the pressure amplitude due to the spherical divergence of the wavefront. The error bars in Fig. 1.4 are deduced from statistical processing of 100 measured waveforms. The experimental and theoretical decrease of the peak pressure with the propagation distance are in accordance within an interval of 4%. Concerning the N-wave duration, experimental and theoretical data are also in good agreement, within an interval of 2% (Fig. 1.4b). On the contrary, it is clear from Fig. 1.4c that there is no agreement between the rise time of the shock front estimated from the output voltage of the microphone and the rise time deduced from the model. The huge overestimation of the rise time in the experimental signal is due to the limited frequency response of the measurement chain (microphone and amplifier) at high frequencies (Averiyanov *et al.*, 2007). Note that some authors used handmade microphones with higher frequency cutoff, (Wright, 1983, Lipkens & Blackstock, 1998a) however they were still limited in frequency to accurately measure the shock front.

Very good agreement between the experimental and theoretical data for the peak pressure and duration tends to show that the model is very accurate, but the ability of the model to predict shock structure has to be confirmed. Since microphones are not able to measure correctly high frequencies, optical measurements based on shadowgraphy have been performed to measure the fine structure of the front shock with higher accuracy.

§1.5 Measurement of the front shock rise time using shadowgraphy

Using optical methods it is possible to reconstruct the spatial variation of the pressure wave with a good resolution (Settles, 2001). The rise time of the shock front can then be calculated from the pressure rise in space (shock width). Among numerous visualization methods for compressible flows (schlieren, interferometry, etc.), the shadowgraphy technique (Settles, 2001, Merzkirch, 1974) is chosen here because it is relatively simple in design but still sufficiently sensitive to obtain images of the acoustic shock wavefront. According to this method the distribution of light intensity in space is photographed and then analyzed. The pattern of the light intensity is formed due to the light refraction on inhomogeneities of the refraction index caused by variations of medium density. In our case, spatial density variations are produced by the acoustic wave.

The shadowgraphy technique has been used in literature to capture hydrodynamic shocks in supersonic flows (Mach number > 1.1), but it was reported to be unsuitable for the direct measurement of shock thickness (Panda & Adamovsky, 1995). The difficulty is related to strong diffraction effects (shock thickness $\delta x \sim 0.5$ μm was close to light wavelength), (Panda, 1995) which dominate light focusing and complicate interpretation of light intensity patterns (Merzkirch, 1974). However, it was detected that the width of the central dark stripe in the shadow depends on a jump in refraction index across the shock, but this information was not correlated with the shock thickness. To assess the shock amplitude and shock structure of such strong shocks, other meth-

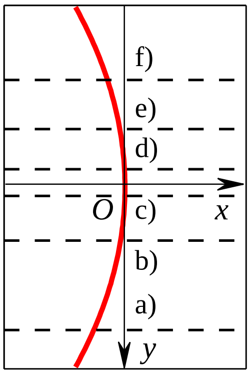

Figure 1.5: Positions of the camera observation plane along the y axis that correspond to the shadowgrams given in Fig. 1.6: 32 mm (a), 12 mm (b), 2 mm (c), -4 mm (d), -13 mm (e), and -24 mm (f). Shock wavefront is plotted schematically as a red solid curve.

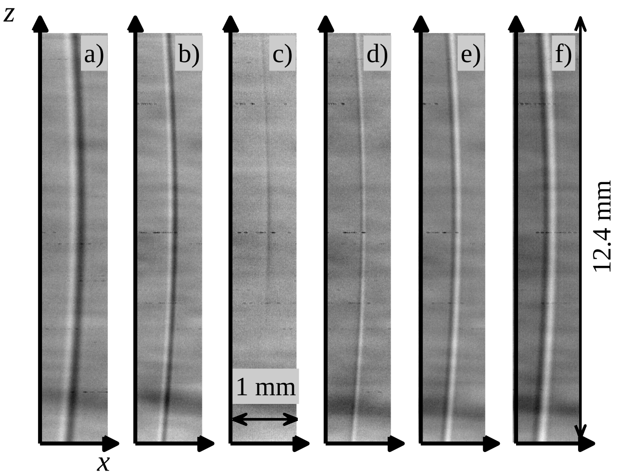

Figure 1.6: Shadowgrams captured at different positions of observation plane along the light propagation path y = 32 mm (a), 12 mm (b), 2 mm (c), -4 mm (d), -13 mm (e), and -24 mm (f).

ods based on measurements of light reflection coefficient have been proposed (Cowan & Hornig, 1950, Greene *et al.*, 1951).

The shocks investigated in the present work are very weak in comparison with those studied in (Panda & Adamovsky, 1995, Panda, 1995) : typically, a measured acoustic wave has a peak pressure $p_{max} < 1500$ Pa, i.e. an acoustical Mach number $M_a < 0.01$, and the theoretically estimated shock thickness is greater than 30 μm. In this case a "focused" shadowgraphy technique can be used. Shadow images called *shadowgrams* are captured by a camera at some distance from the shock wave by changing the position of the objective focal plane. Shadowgrams are interpreted by comparison with simulation of light propagation through the inhomogeneity of the refraction index induced by the front shock of the N-wave. In this way, the front shock thickness and its rise time can be obtained. Modeling of light propagation and the analysis of the shadowgrams are detailed in the next sections.

1.5.1 Measurement and processing of shadowgrams

For example, in this section shadowgram analysis is given for one series of measurements, taken at distance $|x_S| = 16$ cm between the source and optical axis (Fig. 1.1). For this acoustic source-optical axis distance shadowgrams of the shock were recorded for six different positions of the focal plane of the camera on the y-axis (Fig. 1.5): y = 32 (a), 12 (b), 2 (c), -4 (d), -13 (e), -24 (f) mm. The position of the focal plane was changed by moving the camera along the light propagation direction y while keeping the focal distance of the camera fixed. The shadowgrams are shown in Fig. 1.6a-f; the dimensions of each image are 1 mm (97 pixels) in x direction and 12.4 mm (1186 pixels) in z direction; image horizontal scale is 0.0104 mm per pixel. The shadows induced by the front shock have a spherical curvature with a radius of 15.2 ± 1.3 cm, which is in good agreement with the given acoustic source-optical axis distance $|x_S| = 16$ cm.

Each image contains one dark and one bright stripe that represent a shadow of the shock front. The bright stripe is formed by converging and the dark stripe by diverging light, due to bending of the light while passing through the shock front. It can be seen in Fig. 1.6 that the bright and dark stripes are inverted if the focal plane of the camera is set upstream ($y < 0$ for Fig. 1.6d-f) or downstream ($y > 0$ for Fig. 1.6a-b) the grazing point O. The images recorded with the camera focused downstream the grazing point ($y > 0$) are *real* or *normal* shadowgrams formed at the observation plane, while images recorded with the focus upstream the grazing point ($y < 0$) are so-called *imaginary* or *virtual* shadowgrams, which are inverted as if one looks across a diverging lens (Settles, 2001, Merzkirch, 1974). The inversion of the position of the dark and bright stripes in *real* and *virtual* shadowgrams will be illustrated in more details later in the paper.

The shock shadows in the images that are taken close to the position $y = 0$ (Fig. 1.6c) are thinner and the contrast between the dark and bright stripes is lower; the shadows become wider when the focal plane is moved away from the origin. To quantify the width of the shadow of the front shock, the following image processing is applied: 1) spherical curvature of the shock shadow is compensated in order to obtain straight vertical stripes, 2) 2D images with vertical stripes are averaged along the z direction to obtain the variation of light intensity along the x-axis, 3) background noise intensity is estimated and subtracted from the signal.

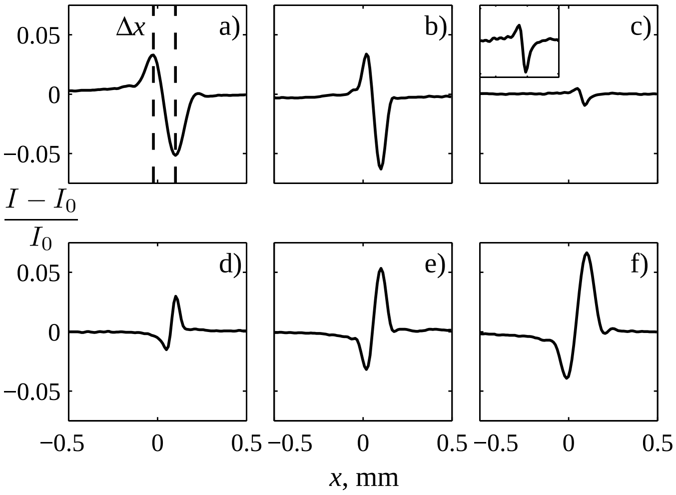

Figure 1.7: Normalized intensity distributions $(I - I_0)/I_0$ along the x-axis obtained from shadowgrams given in Fig. 1.6. I_0 is the background intensity. In the subplot (c) a zoom is plotted.

The resulting one dimensional intensity distributions calculated from the 2D images are presented in Figs. 1.7a-f. To increase the signal to noise ratio, 15 shadowgrams are recorded at each y position, and the average intensity is computed after compensation of small random shifts in the shock arrival time due to small variations of spark position. The width of the front shock shadow is further referred as the *shadow width*, and is defined as the distance Δx between maximum and minimum values of the light intensity distribution (Fig. 1.7a).

1.5.2 Calculation of the rise time from shadowgrams

The shadow width Δx (Fig. 1.7a) is related to the front shock thickness, which is equal to $c_0 \tau_{sh}$, and thus is also related to the rise time τ_{sh}. In order to establish the relation between the shadow width Δx and the shock thickness $c_0 \tau_{sh}$, propagation of light through the inhomogeneity of refraction index induced by the pressure shock is simulated. Two models that govern light propagation through the shock are built and compared. The first model is based on the geometrical optics approximation (Kravtsov & Orlov, 1990). This approximation is very often used to explain image properties in optical methods (Hargather & Settles, 2007). However, diffraction effects were reported to have strong influence on shadowgraphy images (Panda & Adamovsky, 1995). In order to reveal the effect of light diffraction on image formation in a given experiment, a second model based on the parabolic diffraction equation is built (Goodman, 1996) and the results obtained using these two models are compared.

Inhomogeneity of refraction index induced by the front shock

Acoustic pressure p can be related to the perturbations of the refraction index n of the light. The relationship between the refraction index and air density $\rho_0 + \rho$ is linear: $n = 1 + k(\rho_0 + \rho)$, where $k = 0.00023\ \mathrm{m}^3/\mathrm{kg}$ is Gladstone-Dale constant, (Merzkirch, 1974) $\rho_0 = 1.19\ \mathrm{kg/m}^3$ is the ambient density, and ρ is the density perturbation caused by the acoustic wave. Under given experimental condition, the density perturbation can be regarded as a linear function of acoustic pressure p: $\rho = p/c_0^2$; higher order terms can be neglected as the acoustic pressure is small compared to the ambient atmospheric pressure: $p_{max}/p_{\mathrm{atm}} \sim 0.01$. Hence, the refraction index can be expressed as:

$$n = 1 + k\left(\rho_0 + \frac{p}{c_0^2}\right). \tag{1.2}$$

Let consider that shadowgrams are recorded at the time t when the front shock grazes the optical axes (Fig. 1.1). At this time, the radius of curvature of the spherically diverging front shock is $R = |x_S|$, where x_S is the acoustic source position on the x-axis. Since the radius of front shock curvature R is much greater than both shock thickness $c_0\tau_{sh}$ and the shadow width Δx, no significant gradient in distribution of the refraction index is expected along the vertical z-axis and it can be neglected. The deflection of light therefore will mainly occur in the plane $(x, y, z = 0)$ and simplified 2D geometry can be used in simulating light propagation in the $z = 0$ plane.

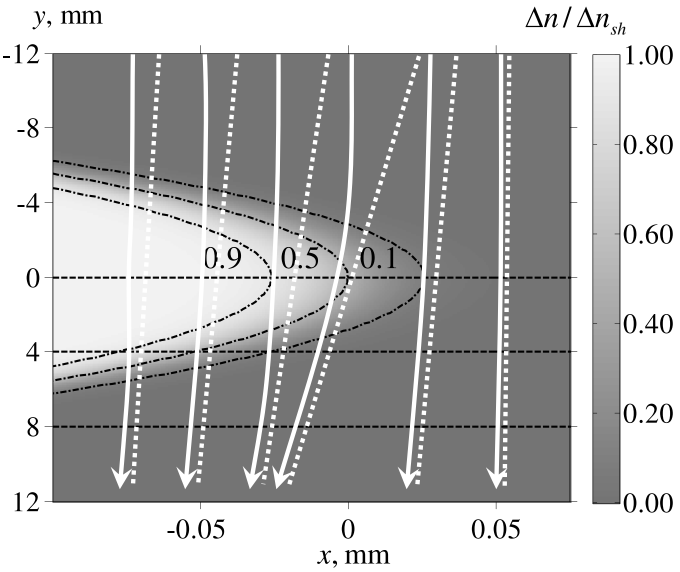

Figure 1.8: Formation of shadows. Spatial variations of refraction index caused by the acoustic shock front in the xOy plane. Contour dash-dot lines show refraction index levels corresponding to values $0.1\Delta n_{\mathrm{sh}}$, $0.5\Delta n_{\mathrm{sh}}$ $0.9\Delta n_{\mathrm{sh}}$. Refraction of optic rays is schematically shown by arrows (solid lines), back propagation of rays is shown by dashed lines.

As mentioned in sec. 1.3.1, the front shock of the acoustic wave in homogeneous air is well described by the quasi stationary solution of the classical Burgers equation. The shock has the form of hyperbolic tangent and the rise time is determined by the shock amplitude and thermoviscous absorption in the medium (Rudenko & Soluyan, 1977). The refraction index induced by the N-wave thus can be written as:

$$n = n_0 + \frac{\Delta n_{sh}(r - R + d)}{2d}\left[\tanh\left(\frac{r - R}{c_0\tau_{\mathrm{sh}}/2.2}\right) - \tanh\left(\frac{r - R + 2d}{c_0\tau_{\mathrm{sh}}/2.2}\right)\right]. \tag{1.3}$$

Here $r = r(x, y) = \sqrt{(x - x_S)^2 + y^2}$, $n_0 = 1 + k\rho_0$ is the refraction index of ambient air, $\Delta n_{sh} = kp_{\max}/c_0^2$ is the magnitude of the refraction index variations, and $d = c_0T$ is the half length of the acoustic pulse.

Spatial variations of the refraction index $(n - n_0)/\Delta n_{sh}$ around the front shock of the acoustic wave, defined by Eq. (1.3), are plotted in Fig. 1.8. This picture is calculated using the parameters of the shock pulse modeled at $R = 16\ \mathrm{cm}$ from the spark (Fig. 1.4): peak pressure $p_{\max} =$ 1400 Pa, half duration $T = 19\ \mu$s, and rise time $\tau_{\mathrm{sh}} = 0.15\ \mu$s. Dark-gray color ($n - n_0 = 0$) corresponds to the ambient refraction index; light deflection on the refraction index inhomogeneity is schematically shown with white arrows. Black dashed contours correspond to the levels of 0.9, 0.5, and 0.1 (from left to right) of the jump in the refraction index at the shock front.

Light refraction model based on geometrical optics

Light refraction on the shock front (refraction index inhomogeneity shown in Fig. 1.8) is first calculated based on the geometrical optics approximation using a Hamilton-Jacobi type system of equations (Kravtsov & Orlov, 1990):

$$\frac{d\mathbf{s}}{d\theta} = \mathbf{k}\,; \qquad \frac{d\mathbf{k}}{d\theta} = \frac{1}{2}\nabla n^2 \tag{1.4}$$

Here vector $\mathbf{k}$ is the wave vector of the light, $\mathbf{s}(x, y)$ is the ray trajectory, θ is the propagation path along the ray, $n = n(x, y)$ is the refraction index. Initial conditions correspond to the parallel beam incident from the negative direction of the y axis (Fig. 1.8a). The system of equations (1.4) is solved numerically using a fourth order accurate Runge-Kutta algorithm. The light intensity in the observation plane is inversely proportional to the cross-sectional area of the light ray tubes.

Light diffraction model based on the parabolic approximation

A second light propagation model is built to account for diffraction effects. This model is based on the parabolic approximation of scalar diffraction theory (Goodman, 1996). For the harmonic wave propagation the equation has the form:

$$\frac{\partial E}{\partial y} = \frac{i}{2k_0}\frac{\partial^2 E}{\partial x^2} + \frac{i\Delta n(x, y)}{n_0}k_0 E \tag{1.5}$$

Here $\Delta n(x, y) = n(x, y) - n_0$ is the variation of the refraction index, E is the electric component of the light, $k_0 = 2\pi/\lambda$ is the wave number, λ is the light wavelength, i is the imaginary unit. Equation (1.5) is solved in finite differences using the method of fractional steps with the operator splitting of the first order (Ames, 1992). At each grid step in the propagation direction y the diffraction operator (first term of the right hand side in Eq. 1.5) is calculated using the Crank-Nicholson algorithm. Variations of the refraction index (second term of the right hand side in Eq. 1.5) are taken into account using the exact solution.

To model the white light flash used in the experiment, a set of wavelengths in the range from 370 to 780 nm is superposed. Light propagation of 15 wavelengths uniformly distributed in the given range is calculated based on the Eq. (1.5). The initial condition remains the same for each light wavelength and is given by $E(x, y = y_0) = 1$. It is verified that a greater number of wavelengths does not significantly affect the modeling results. The light intensities are calculated for each wavelength as proportional to $|E|^2$ and then superposed to obtain the total intensity distribution.

Shadow width predicted with two light propagation models

To determine if light diffraction is important in formation of shock shadows, light propagation through the refraction index distribution (Fig. 1.8) is simulated using the geometrical and the parabolic models. Intensity distributions are then calculated along the horizontal dashed lines in Fig. 1.8a ($y = 0, 4$ and 8 mm) and presented in Fig. 1.9.

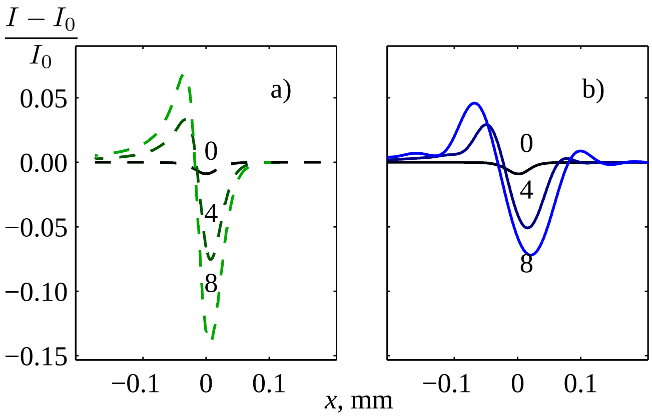

Figure 1.9: Intensity distributions calculated along the x-axis for three observation positions $y = [0, 4, 8]$ mm using (a) geometrical optics model and (b) parabolic equation model.

The results of both models show good qualitative agreement with the intensity distributions obtained from the shadowgrams (Fig. 1.7). At the $y = 0$ position, the contrast is very low, the bright component of the shadow is not well pronounced, and the shadow width Δx cannot be measured. With increasing distance of the observation plane ($y = 4$ and 8 mm) from the origin $y = 0$ the bright component in the image and the contrast increase. The quantitative agreement between the two models is however not so good in both maximum intensity level and in the shadow width. In particular, significant broadening of the shadow for increasing distances y is observed only if diffraction is accounted for. This disagreement is more evident at longer distances y.

The summary of the modeling results for the shadow width Δx versus the position of the observation plane y is shown in Fig. 1.10. Simulations are performed for different rise times τ_{sh} of the shock front, i.e. for different variations of refraction index obtained using Eq. (1.3). Dashed curves are obtained with the geometrical optics model (Eq. 1.4), and solid curves – with the diffraction model (Eq. 1.5). Pairs of curves (dashed and solid) correspond to the values of the shock rise time τ_{sh} varying over the range from 0.1 to 0.3 μs. The contrast of both set of curves curves varies from dark to light when the rise time increases.

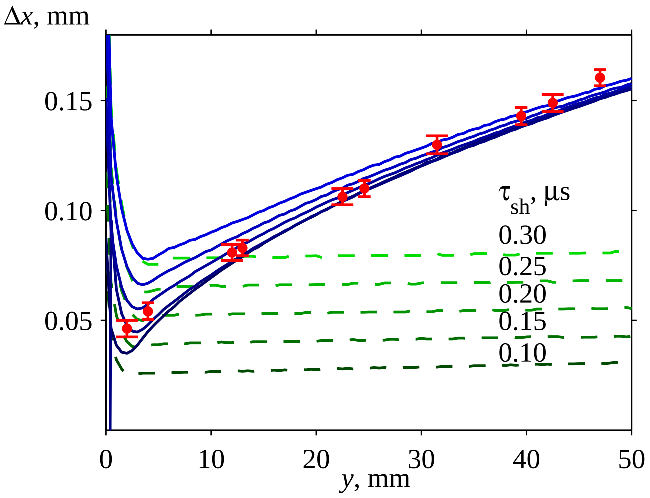

Figure 1.10: Shadow width modeled for images taken at different positions y of the camera focus. Dashed curves are obtained using the geometrical optics model and solid curves - using the parabolic equation. The change of the contrast in both sets of curves from dark to light corresponds to increasing shock rise time in the modeling. Points with vertical bars are shadow widths and corresponding standard deviations measured from experimental shadowgrams.

If the observation plane is too close to the position $y = 0$ where the light just grazes the front shock, the light intensity variation is too small to estimate the shadow width and both models give erroneous estimations. Away from the position $y = 0$, the comparison of dashed and solid curves in Fig. 1.10 shows that the results obtained using geometrical optics or the parabolic approximation differ strongly. According to geometrical optics, the shadow width Δx does not increase when the observation plane is moved away from $y = 0$, while the parabolic approximation model predicts an increase of the shadow width by a factor of roughly 3 at $y = 50$ mm in this particular case. This difference outlines that diffraction effects can not be neglected in the analysis of shadowgrams.

In order to discuss the ability of the two models to predict experimental data, shadow widths obtained from shadowgrams measured at different observation plane positions y are plotted in Fig. 1.10 with dots. Error bars indicate standard deviations on the estimation of Δx. Sources of error are mainly finite pixel size and small variations of the shadow width from one shot to another. The comparison of the modeling and experimental data confirms that light diffraction cannot be neglected: at observation positions $y > 2$ mm, the shadow width obtained in the parabolic approximation modeling grows in a similar way as in experiment, while the geometrical optics results strongly differ from the experimental data. The only region where geometrical optics could be used is the region within 2 mm near the $y = 0$ position where diffraction effects are not important, but even in this region geometrical optics overestimates Δx. At longer distances y a geometrical optics propagation model is not appropriate to predict the shadow width Δx. Consequently, only results of the parabolic approximation modeling will be further used to deduce shock rise time from shadowgraphy images.

However, the difference between the shadow widths calculated for different shock rise times depends on where the observation plane is positioned. If the coordinate of the observation plane is beyond $y = 10$ mm, the difference between shadow widths obtained for different rise times $\tau_{\rm sh}$ decreases significantly and becomes almost negligible beyond the distance $y = 20$ mm. Shadowgrams taken at these positions therefore would lead to strong uncertainty in the estimation of the rise time $\tau_{\rm sh}$.

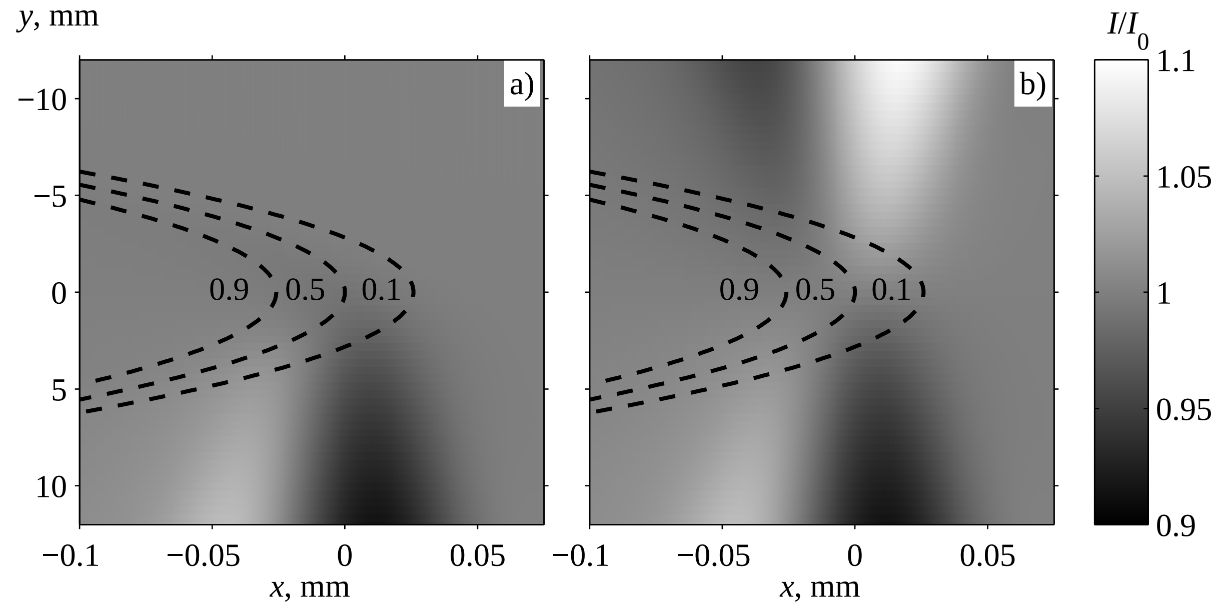

Figure 1.11: Light intensity distribution on real shadows (a) and real and imaginary shadows (b).

A diffraction propagation model is also used to explain inverted patterns of *real* and *virtual* shadows. First, consider a light intensity field of parallel beams passed through the shock, Fig. 1.11a. The shock configuration is the same as in Fig. 1.8. The intensity of *real* shadows is uniform upstream the grazing point. Nevertheless, the optical system focused upstream this point perceives the image formed by the light propagated backward through *homogeneous* air. The intensity field of backward propagated light is shown in Fig. 1.11b. It indicates inversion of the shadow's pattern between upstream and downstream areas that is in accord with experimental results (Fig. 1.6).

Estimation of the shock rise time from shadowgrams

Shock rise time is deduced from the measured shadowgrams based on the comparison between shadow widths Δx in the recorded image and in the results of the light diffraction modeling. As the shadow width can be modeled for any given front shock rise time τ_{sh} and observation plane position y (Fig. 1.10), it is possible to find which rise time of the shock in simulations corresponds to a measured shadow width.

Optimal observation plane positions y, at which comparison and estimate the rise time were done, are chosen using the modeling results (Fig. 1.10). At observation planes too close to $y = 0$, the contrast of theoretical shadowgrams is too low. At observation planes positioned beyond $y = 10$ mm the difference between the theoretical Δx obtained for different rise times τ_{sh} is smaller than experimental error bars. A wide range of rise times could thus be associated to a small range of measured shadow width, which would lead to a huge uncertainty in rise time estimation. The shadow width is most sensitive to τ_{sh} at positions $2\ \mathrm{mm} < y < 5\ \mathrm{mm}$. For example, among shadowgrams given in Fig. 1.6, only shadowgrams c) and d) can be used.

The front shock rise time thus is obtained by fitting the rise time in the model to produce the same shadow width Δx as in the corresponding measured shadowgram, with the condition that the observation plane position y is in the range [2 mm, 5 mm]. The virtual shadowgrams with focus at positions $y \in$ [-5 mm, -2 mm] can be also used. Note also that the shadow width theoretical prediction is not sensitive to fluctuations in peak pressure: possible error in the shock width estimation due to peak pressure uncertainty is less than 1% (only shadow contrast is affected, lower $p_{\max}$ produces lower contrast). An interval of confidence of $\tau_{\rm sh}$ can be obtained by determining the rise times that correspond to the higher and lower values of the Δx error bars.

Using this method with the spark source positioned at 16 cm from the optical axis, the analysis of shadowgrams measured with the camera focused at the $y = 2$ mm (Fig. 1.6c) gives an estimation of the rise time $\tau_{\rm sh} = 0.15 \pm 0.03$ μs. This value agrees very well with the result predicted by the acoustic propagation model and is about 17 times smaller than deduced from the microphone output waveform.

1.5.3 Shock rise time in acoustic modeling and optical measurements

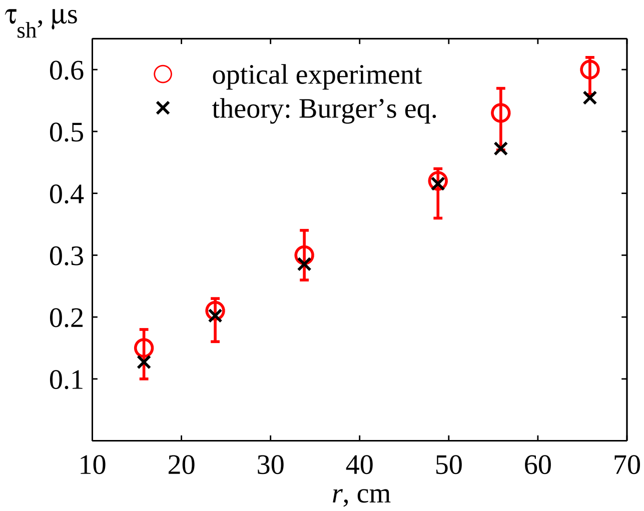

Figure 1.12: Comparison between the optically measured rise time (circles) and the rise time predicted by using the acoustic wave propagation (crosses, Eq. 1.1) at different distances from the spark source.

In order to test the ability of the sound propagation model to predict the increase of the front shock rise time $\tau_{\rm sh}$ with the sound propagation distance r (Fig. 1.2d), shadowgrams are recorded for increasing spark source - optical axis distances $|x_S|$ over the interval [16 cm, 66 cm]. The rise time of the front shock is deduced from the images by fitting the shadow width in the image and in the results of the diffraction model. Note, that at distances longer than 66 cm the shadowgrams contrast was not sufficient to allow accurate analysis. A first reason is the spherical divergence of the wave that induces amplitude decreases, that itself leads to the lowering of image contrast. A second reason is the front shock rise time increase with the distance, which also decreases the contrast of the image.

In Fig. 1.12, the front shock rise time deduced from the optical method and the prediction using the wave propagation model (Eq. 1.1) are compared. There is a very good agreement between the results obtained in acoustic modeling and measured optically. The rise times deduced from the experiments are slightly higher than those predicted by the Burgers equation, but the relative error does not exceed 10 %. This result confirms that the rise time of the front shock is much smaller than it could be deduced on the basis of the microphone output waveform.

Note that, successfully applied to measure the front shock, shadowgraphy appeared to be not sufficiently sensitive to detect the rear shock of the acoustic pulse. One explanation could be that the rear shock is smoother than the front shock due to relaxation effects and diffraction on the spark source electrodes. To measure the rear shock with precision using optical methods, a more sensitive experimental setup should be developed; laser interferometry could be a possible technique (Smeets, 1977, Yuldashev *et al.*, 2010b).

§1.6 Conclusions

In this chapter the propagation of nonlinear N-waves in homogenous relaxing air was studied theoretically and experimentally. The main attention was paid to measurements and calculations of the front shock rise time. Amplitude and half duration data are also reported. Numerical simulations were performed based on a Burgers-type equation generalized to describe spherically divergent nonlinear sound waves in a medium with thermoviscous absorption and oxygen and nitrogen relaxation. Simulation results showed that the rise time lengthening is mainly determined by the thermoviscous absorption.

Numerical results were compared to the results of acoustical and optical experiments. The initial wave parameters for simulations were deduced from the acoustical experiment data obtained using a condenser microphone. Comparison of numerical simulation results with microphone pressure measurements showed quite good agreement for peak positive pressure values and duration of the pulse. However, the rise time of the front shock deduced from the microphone output was largely overestimated because of the limitations in the frequency response of the measuring system.

In order to estimate the rise time of the shock front more accurately, optical measurements based on a focused shadowgraphy technique were performed. Shock front shadowgrams were captured and analyzed. To interpret shadowgrams, the refraction index inhomogeneity produced by the shock was modeled and two light propagation models were tested: the first is based on the geometrical optics approach, and the second is based on the scalar diffraction theory and the parabolic approximation. It is shown that geometrical optics cannot accurately predict the shadow intensity pattern and results in overestimation of the acoustic shock rise time. The rise times deduced from shadowgrams using the parabolic model are in a very good agreement with the acoustic modeling, thus validating the acoustic wave propagation model (Eq. 1.1). However, the optical method has limitations due to diffraction effects: only shadow images captured close to the point where the light grazes the front shock are useful for the rise time estimation.

Consequently, the results from measurements of short duration N-waves by microphones should be analyzed with care because the response of the measurement system has a great influence on shock rise time estimation. Only the combination of modeling, acoustical and optical measurements provides accurate characterization of high amplitude shock pulses in laboratory experiments in air. Reported results should be taken into account in comparison between theoretical and experimental data of more complex problems, for example, in studying N-wave propagation through the turbulence (Lipkens, 1993, Blanc-Benon *et al.*, 2005, Averiyanov, 2008).

Chapter 2

Propagation of spherically diverging nonlinear N-wave in a thermal turbulence

§2.1 Introduction

In the general introduction it was mentioned that studies on N-wave propagation in atmosphere are important due to high interest in development of civil supersonic aircrafts and inherent sonic boom problem. Field measurements of sonic booms are not numerous because they are complex and very expensive projects (Lee & Downing, 1991, Maglieri *et al.*, 1992, Elmer & Joshi, 1994, Hilton *et al.*, 1964). The main advantage of the outdoor experiments is that the sonic boom problem is studied in its natural conditions. However, the field measurements have important disadvantages: a lack of control on atmosphere conditions; a poor knowledge of turbulence along propagation path of the N-wave; difficulties to acquire sufficiently large statistical database (Elmer & Joshi, 1994, Willshire & Devilbiss, 1992). These inherent drawbacks complicate the analysis of the influence of different physical effects on the statistics of N-wave distortions. As an alternative to outdoor measurements, the study of N-wave propagation through turbulent media can be carried out using laboratory-scale experiments (Lipkens & Blackstock, 1998a, Lipkens, 1993, Ollivier & Blanc-Benon, 2004, Averiyanov, 2008). In the model experiments, characteristic scales of the real atmosphere are downscaled to fit laboratory scale. For example, in a study (Lipkens & Blackstock, 1998a) the downscaling factor 1:10000 was reported, and in the most recent work (Averiyanov, 2008) the factor was 1:1000. In such experiments, the turbulence, the acoustic source and the geometry are well controlled.

Some model experiments have also been done in water, which provide downscaling coefficient of 1:100000 if ultrasound frequencies about 1 MHz are used (Ganjehi *et al.*, 2008, Marchiano *et al.*, 2007). Experiments in water have numerous advantages, such as the small size of the experimental setup, the good reproducibility of the emitted signal, a smooth adjustment of signal amplitude, and the ability to scan the pressure field with good spatial resolution. However, it is difficult to produce turbulence in water. Moreover, there is a great difference in waveform signatures: ultrasound sources usually generate narrow-band impulse signal, whereas the N-wave is a broadband single pulse. Thus, the experiments in water are more suitable for the analysis of nonlinear wave propagation through static artificial inhomogeneities (Jing & Cleveland, 2007, Yuldashev *et al.*, 2010a). The model experiments in air are more conventional to study N-wave propagation through turbulence.

Laboratory downscaled experiments in air also do not fully coincide with the conditions of the full-scale outdoor propagation environment. For example, the geometry of wave propagation is different – a spherical wave generated by stationary spark source in a laboratory (Averiyanov, 2008,Lipkens & Blackstock, 1998a,Ollivier & Blanc-Benon, 2004) and a conical wave front (Mach cone), diverging from a moving airplane. Also, because of the need to reduce the wavelength while keeping the same propagation medium, the dominant mechanism of absorption is changing: thermoviscous processes are more important in laboratory scaled experiments (Yuldashev *et al.*, 2011), while in outdoor full-scale experiment it is molecular relaxation (Bass *et al.*, 2002). In this regard, the main purpose of the laboratory experiments of this type is still not an exact reproduction of outdoor N-waves propagation in the atmosphere, but the study of certain key aspects of the propagation of nonlinear pulses in turbulent media. The experimental data can be used to test and refine theories and numerical models, which then will be applied to study the N-wave propagation in real environment. Of great importance, therefore, become well-posed laboratory experiments in which the largest number of parameters needed for theoretical description of the problem are known.

Currently, because of the limited computing resources, it is not possible to provide numerical simulations of nonlinear pulse propagation in turbulent media in the three-dimensional geometry, even using propagation model based on parabolic equations, similar to those developed in the precedent studies of different authors (Averiyanov *et al.*, 2011,Jing & Cleveland, 2007). Therefore, until now the comparison of experiments was carried out only with the results of simulations based on several two-dimensional parabolic models (Averiyanov, 2008, Averiyanov *et al.*, 2011, Blanc-Benon *et al.*, 2002). However, it is clear that the efficiency of focusing should increase in three dimensions compared with two-dimensional. On the other hand, the nonlinear effects in these two cases (2D/3D) should appear in different degree due to the different geometrical decays of the wave amplitude with the increasing propagation distance. Thus, the comparison with 2D-models can be only qualitative. However, in some cases fairly good quantitative agreement between simulation and the experiment was found (Averiyanov, 2008). This agreement, probably, can be explained by the fact that in the simulations, the initial plane wave was used instead of the wave with curved wavefront to represent the origin from the point source. So, the random focusing effects in 2D simulations were stronger and closer to the 3D case. The numerous models based on geometric acoustics (Karweit *et al.*, 1991, Blanc-Benon *et al.*, 1991, Blanc-Benon *et al.*, 1995), which can be realized in 3D, are not suitable for quantitative analysis of experimental data. This is due to the known fact that geometrical acoustics models can not properly describe acoustic field at distances where the first caustics occur (Blanc-Benon *et al.*, 2002, Averiyanov *et al.*, 2011). This limitation of the model will be also shown for the statistics of the N-wave amplitude in chapter 3. However, while the theoretical description of the problem may not be available in full, one can make comparative analysis of the available experiments that differ in some parameter. For example, it is interesting to study the influence of turbulent inhomogeneities type (vectorial or scalar) on the statistics of N-wave distortions. In the framework of geometrical acoustics, this issue was largely studied (Blanc-Benon *et al.*, 1991,Karweit & Blanc-Benon, 1993,Blanc-Benon *et al.*, 1995,Blanc-Benon *et al.*, 2002), but the experimental comparative data for N-wave propagation in vectorial (kinematic) and scalar (thermal) turbulence are not yet reported in the literature.

In the currently known laboratory experiments which use spark sources, the turbulence was most often created expanding a jet from a rectangular nozzle, and this turbulence was of vector type (Blokhintsev, 1981,Lipkens & Blackstock, 1998a,Averiyanov, 2008,Ollivier & Blanc-Benon, 2004). Randomly oriented flows of air, varying from point to point and in time, lead to random variations of the "effective" sound speed (Blokhintsev, 1981). This turbulence is called also as kinematic turbulence. In the atmosphere there are also inhomogeneities of scalar type, appearing in upward flow of heated air lifting from ground surface. Fluctuations of the sound speed are the result of temperature fluctuations, so the corresponding turbulence is also called as thermal. Homogeneous isotropic turbulence fields of scalar and vector types have different spectra and properties (Comte-Bellot & Bailly, 2003). Therefore, according to the theoretical analysis of linear wave propagation (Ostashev, 1997,Ostashev, 1994,Blanc-Benon *et al.*, 1995), this difference in spectra leads to different impact on the statistics of the wave distortions. In particular, it is important for the wave propagation that, even in the case of homogeneous and isotropic vector turbulence, the longitudinal and transverse correlation functions and corresponding spectra are different (Karweit & Blanc-Benon, 1993,Tatarskii, 1971,Comte-Bellot & Bailly, 2003). In the scalar homogeneous and isotropic turbulence, the correlation function, in contrast, is the same in all directions. This difference of spectra properties leads to different rate of random distortions of the wavefront and hence to quantitatively different statistics of the amplitude, arrival time, and other parameters of propagating wave.

The case of N-wave propagation in kinematic turbulence has been thoroughly considered in the recent study (Averiyanov, 2008) for different levels of the turbulent fluctuations, both from experimental and theoretical points of view. This chapter presents new results on the propagation of the N-wave in thermal turbulence with fixed intensity of refraction index fluctuations. In the following of the chapter, the main properties of vectorial and scalar turbulence will be discussed and essential difference in its spectra for the acoustic waves propagation will be outlined in the §2.2. The experimental setup and measurements technics will be described in §2.3. Results on characterization of the thermal turbulent field will be presented in §2.4. Statistics of the most important parameters of the distorted N-wave propagated through the layer of scalar turbulence will be analyzed in §2.5. The presented experiment and the reported in the study (Averiyanov, 2008) are close in terms of source parameters, propagation distance path inside the turbulent layers and of the characteristic sizes of turbulent inhomogeneities, so it is possible to compare the N-wave statistics obtained in both experiments under various values of the mean-square of the refractive index fluctuations. The comparison is done in §2.6 and the main results are summarized in §2.7.

§2.2 Parameters of vector and scalar turbulent fields

In studies about pulse propagation through turbulent medium it is commonly accepted that the latter can be represented as a static random spatial field. This approach is valid due to the fact that, during the pulse travel time, the distribution of turbulent inhomogeneities does not change significantly. In theory and in numerical simulations a model of homogeneous isotropic turbulence is often used (Batchelor, 1999, Tatarskii, 1971). In model experiments it is also preferable to keep the wave propagation path inside the zone of well-developed homogeneous isotropic turbulence (Averiyanov, 2008). In this case, the spectrum of the turbulent field can be described by a modified von Kármán spectrum, which in the inertial region satisfies the Kolmogorov law $k^{-5/3}$ (Batchelor, 1999). The literature distinguishes the energy spectrum $G(k)$ and the spatial spectrum of random scalar field $\Phi_{3D}(k)$ which are related as:

$$\Phi_{3D}(k) = \frac{G(k)}{4\pi k^2}, \tag{2.1}$$

where $k = |\vec{k}| = \sqrt{k_x^2 + k_y^2 + k_z^2}$. In the case of vector turbulence the spectral tensor $\Phi_{ij}(k)$ is introduced, which for an incompressible flow can be expressed through the spectrum of kinetic energy $E(k)$ by the following equation (Comte-Bellot & Bailly, 2003):

$$\Phi_{ij}(k_1, k_2, k_3) = \frac{E(k)}{4\pi k^2}\left[\delta_{ij} - \frac{k_i k_j}{k^2}\right]. \tag{2.2}$$

The modified von Kármán energy spectra of the scalar $G(k)$ and vector $E(k)$ turbulence are presented below in Eq. (2.3) and Eq. (2.4), respectively:

$$G(k) = C <\mu_{\text{sc}}^2> \frac{k^2}{L_{0\text{sc}}^{2/3}} \frac{\exp\left(-k^2/k_m^2\right)}{(k^2 + k_{0\text{sc}}^2)^{11/6}}, \tag{2.3}$$

$$E(k) = C\frac{11}{6} <\mu_{\text{vec}}^2> \frac{k^4}{L_{0\text{vec}}^{2/3}} \frac{\exp\left(-k^2/k_m^2\right)}{(k^2 + k_{0\text{vec}}^2)^{17/6}}. \tag{2.4}$$

Here the spectra are already written in terms of refraction index fluctuations μ

$$\mu = -\frac{T'}{2T_0} - \frac{u_x}{c_0}, \tag{2.5}$$

which in physical nature correspond either to temperature fluctuations $T' = T - T_0$ or flow velocity fluctuations $\vec{u}$. In the first case $<\mu_{\text{sc}}^2> = <T'^2>/4T_0^2$, and in the second – $<\mu_{\text{vec}}^2> = <u_x^2>/c_0^2$. When the turbulence of vector-type in the posed problem is considered, the only one component of the velocity is of the main interest, denoted, for example, as u_x, whose direction coincides with the propagation direction of the acoustic wave. The transverse components u_y and u_z of velocity vector have only some minor influence on the distortion of the acoustic field (Averiyanov, 2008, Averiyanov *et al.*, 2011), so at first approximation their contributions can be ignored. In addition to the mean square refractive index fluctuations $<\mu^2>$, the spectra of turbulence highlight two

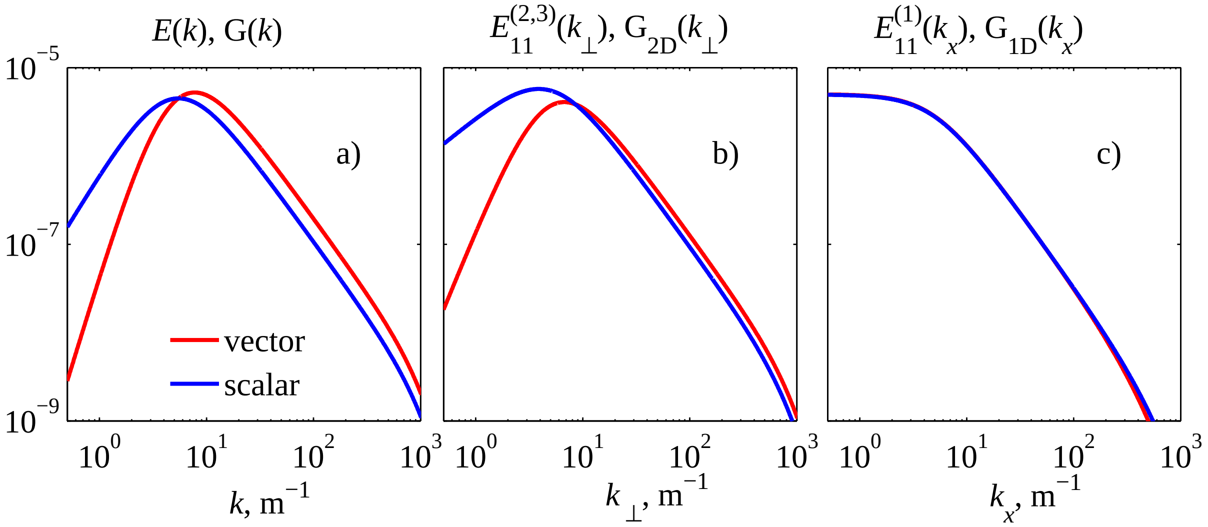

Figure 2.1: Different types of spectra of vector and scalar turbulent fields. (a) – three-dimensional energy spectra as a function of the modulus of the spatial wave number $|\vec{k}| = k$, (b) – the two-dimensional spectra as a function of the transverse wavenumber $k_\perp = \sqrt{k_y^2 + k_z^2}$, (c) – one-dimensional spectra as a function of longitudinal wave number k_x. For the vector field the spectra presented in (b, c) correspond to the velocity component u_x, chosen as the longitudinal. Spectra parameters are: $L_0 = 20$ cm, $l_0 = 5$ mm, and $\sqrt{<\mu^2>} = 1\%$.

scaling parameters: $k_0 = 1/L_0$ and $k_m = 5.92/l_0$. The parameter L_0 is called as the "outer scale" of turbulence and represents the characteristic size of the largest fluctuations, and the parameter l_0 is the "inner scale" which indicates smallest inhomogeneities and is a characteristic scale where energy of turbulent fluctuations dissipates. Value of the normalization constant C, which appears in the formulae (2.3) and (2.4), can be found in Appendix C.

Spectra of vector and scalar turbulence are essentially different in their properties which lead to different impacts on statistics of distortions of propagating acoustic wave. For example, the spectrum of homogeneous isotropic turbulence of scalar type $\Phi_{3D}(k)$ depends only on the modulus of k-space vector $k = |\vec{k}|$, while the spectrum of a single component of an incompressible kinematic homogeneous isotropic turbulence $\Phi_{11}(k)$ depends on k_x, k_y and k_z anisotropically (Comte-Bellot & Bailly, 2003). The difference in the distribution of the intensity of refractive index fluctuations over inhomogeneities scales is also noticeable. Fig. 2.1 shows the graphs of vector and scalar spectra with the same values of parameters $\sqrt{<\mu^2>} = 10^{-2}$, $L_{0sc} = L_{0vec} = 20$ cm, and $l_0 = 5$ mm. The chosen parameters of spectra are consistent with the experimental measurements discussed below in sec. 2.4.3 and with spectra parameters provided in the Aver'yanov's study. In Fig. 2.1a the three-dimensional energy spectra are shown, which indicate that the scalar-type spectrum dominates at low spatial frequencies, i.e. for the largest inhomogeneities, whereas in the inertial range between k_0 and k_m the energy of the vector-type turbulence fluctuations is higher by 11/6 times. However, it should be noted that the energy spectrum of the kinematic turbulence contains the energy of all three components of the velocity. Therefore, to provide the reasonable comparison with the thermal turbulence, the spectrum of only one component, in this case, the longitudinal

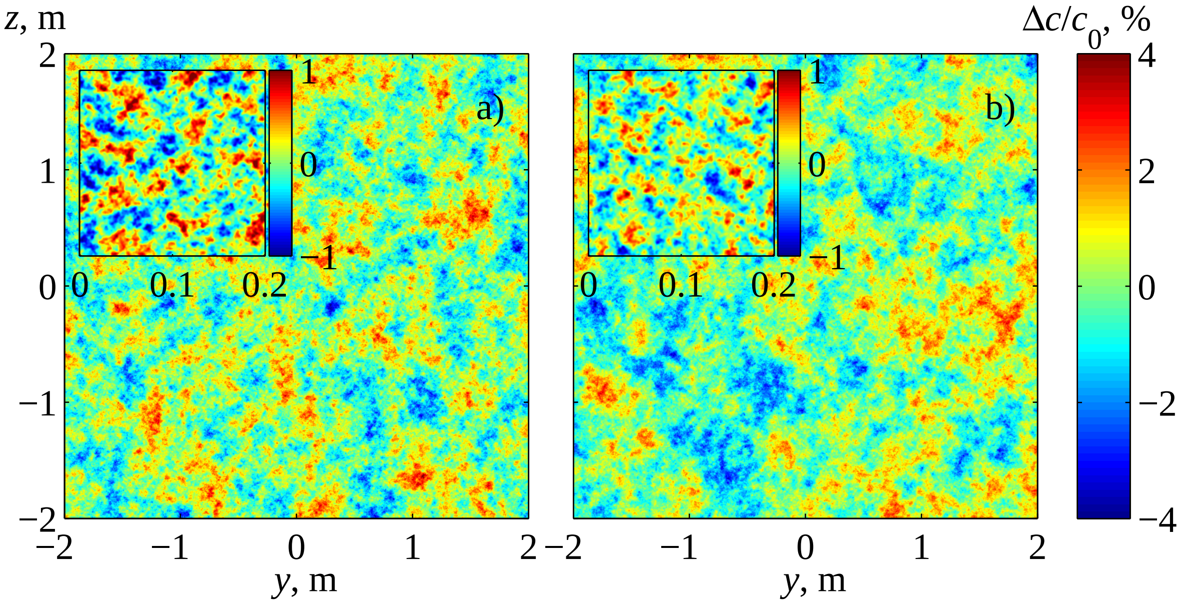

Figure 2.2: Realizations of the turbulent fields, constructed on the basis of the von Karman spectrum of vector (a) and scalar (b) types. In the tabs, given the increased 10-fold with filtered low-frequency field components.

component u_x, should be considered:

$$\Phi_{11} = \frac{E(k)}{4\pi k^2}\left[1 - \frac{k_1^2}{k^2}\right]. \tag{2.6}$$

As a consequence of anisotropy, the spectrum of this component can not be represented as a function of the k modulus. Therefore, in Fig. 2.1b a two-dimensional spectrum as a function of the transverse k-space component $k_\perp = \sqrt{k_y^2 + k_z^2}$ is shown. The mathematical definition of this spectrum can be found in Appendix C, Eq. (C.10). For the scalar turbulence the corresponding spectrum is given by Eq. (C.5). Graphs of the two-dimensional spectra for both types of turbulence indicate that the spectrum of vector fluctuations prevails over the spectrum of scalar fluctuations in the inertial range by 1.33 times. At the same time, the longitudinal one-dimensional spectra of thermal (Eq. C.2) and kinematic (Eq. C.8) turbulence as functions of the coordinate k_x are almost identical (Fig. 2.1c). So, the essential difference between the two spectra is observed in transversal plane of k-space that corresponds to transversal plane in physical space.

Realizations of the turbulent fields of vector-type (a) and of scalar-type (b) in the transversal plane (y, z) are demonstrated in Fig. 2.2. The realizations were constructed using the method of summation of random Fourier modes (Karweit *et al.*, 1991, Dallois, 2000, Blanc-Benon *et al.*, 2002, Averiyanov, 2008). At the corner tabs, 10 times smaller areas are shown in which large-scale fluctuations in spectral range $k < 2\pi/0.1\ \mathrm{m}^{-1}$ were filtered. One can note that in the realization of the scalar field (b) there are large-scale, but more rare fluctuations of the refractive index, in comparison with the realization of u_x of the vector-type field (a). Comparing smaller-scale fluctuations in the inertial range it is clear that they are much more intense in the vector-type turbulence than in the case of the scalar-type field (b) (see zoomed and filtered areas in the tabs).

The difference between the fluctuation level in the transversal plane in the inertial range of scales leads to different rates of accumulation of the wavefront distortions with increasing propagation distance. Hence, random focusing distortions of the acoustic field are produced faster and first focusing zones – caustics, are occurred closer to the acoustic source. For example, in Blanc-Benon *et al.* (1995) probability density functions of appearance of the first caustic were calculated using the geometrical acoustics approximation. Also, formulae of the most probable distance of appearance of the first caustic were determined in the cases of vector and scalar random fields: x^{vec}_{caust} and x^{sc}_{caust}, respectively. The resulting expressions indicate that the vector random field leads to formation of caustics at shorter distance. In the particular case of calculations done using modified von Kármán spectra, it was found that

$$x^{sc}_{\text{caust}} - x^{vec}_{\text{caust}} = x^{sc}_{\text{caust}} \left[1 - \left(\frac{< \mu^2_{sc} >}{11/6 < \mu^2_{vec} >} \right)^{1/3} \right]. \tag{2.7}$$

In the case of equality of the mean-square values $< \mu^2_{sc} >$ and $< \mu^2_{vec} >$ the difference between distances of the most probable formation of the first caustic is of $0.183 x^{sc}_{caust}$. However, this estimation of caustics formation distance is only approximative. For now, systematic comparative studies on the discussed impact of turbulence type on the nonlinear N-wave distortions involving more realistic models such as the parabolic approximation, as far as the author knows, does not exist. Exceptions are theoretical study (Blanc-Benon *et al.*, 2002, Hugon-Jeanin, 1992) and an experimental work (Ollivier & Blanc-Benon, 2004), which nevertheless, does not provide clear and definitive results.

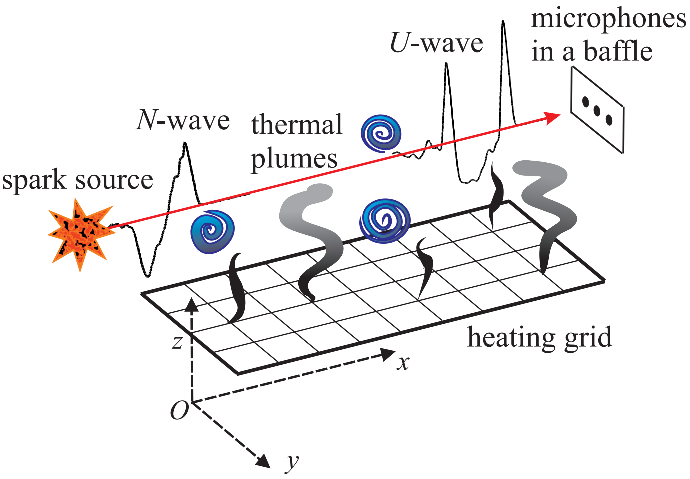

Figure 2.3: Schematic view of the experiment on the propagation of a spherical N-wave generated by a spark source in a thermal turbulence.

In the following sections, laboratory scale experimental setup which was developed to study the propagation of nonlinear N-wave in thermal turbulence will be presented. Characteristics of the measured turbulent field such as intensity fluctuations, spectra and correlation functions will be analyzed in detail. Then statistical results for the most important parameters of the acoustic pulse will be reported.

§2.3 Experimental setup

The schema of the experiment is shown in Fig. 2.3. A spherical N-wave generated by a spark source propagates over the field of thermal turbulence created by a special heating grid. The signal is recorded with microphones mounted in a baffle and located on the same height as the source at

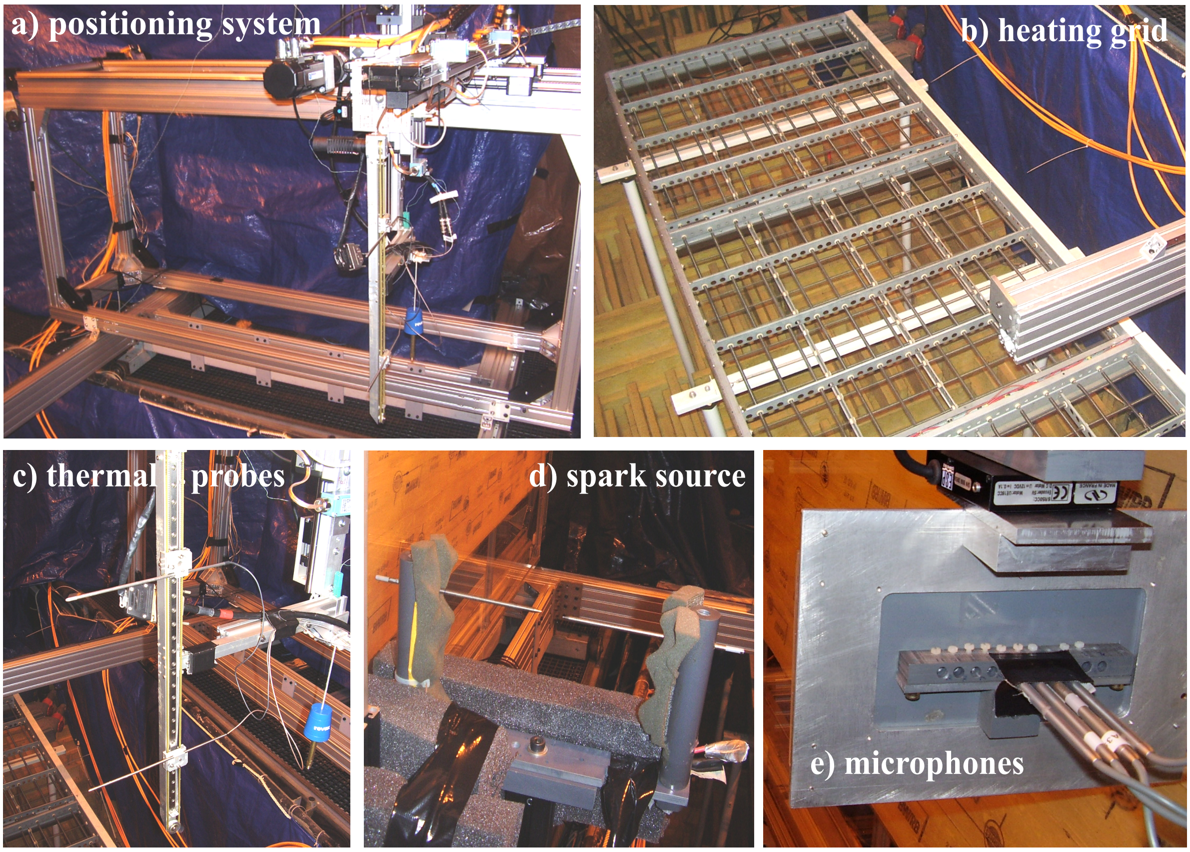

Figure 2.4: Photographs of different components of the experimental setup.

the distance r from it. As a result of the propagation through the inhomogeneous medium the initial N-shaped wave is distorted. For example, in the focusing zone (caustics) a U-shaped waveform is formed, and in defocusing zone – low amplitude and long duration wave.

The experimental setup was placed in the anechoic chamber of the Acoustic Center of the Laboratory of Fluid Mechanics and Acoustics (LMFA) in the Graduate Engineering School of Lyon (ECL). The experimental setup was equipped by a three-dimensional positioning system with an additional turn table to provide rotation around the vertical axis (Fig. 2.4a). The positioning system allowed to move the sensors in the range of 2 m and 0.8 m in the horizontal plane and 1.0 m vertically. Sensors (thermal probes Fig. 2.4c or microphones Fig. 2.4e) were mounted at the lower end of the vertical axis. The thermal turbulence was generated using a heating grid of resistors (Fig. 2.4b). The dimensions of the grid, which was located at height of 1.2 m above the floor and consisted of four sections, were 4.4×1.1 m^2 in the horizontal plane. The heating resistive elements were placed in two layers, separated by 3 cm in height. A square grid of heating elements with a mesh size of 9×9 cm^2 was formed using perpendicular alignement of the elements between the two layers. The total power of the grid was 64 kW. The space around the grid was surrounded by curtains in order to eliminate possible side winds, which could lead to instability of the turbulent field and its strong distortions due to convection.

To measure the temperature a thermocouple of type K (chromel-alumel) and 2 thermal probes Dantec type $55\mathrm{P}31$ (Fig. 2.4c) were used. The thermal probes are made on the basis of a platinum wire of diameter 1 $\mu\mathrm{m}$ and of length 0.5 mm, and have electric resistance of 52 ohm at 20 °C. The control and power unit Dantec $56C20$ was used together with the thermal probes. The sensors were preliminarily calibrated in a temperature controlled chamber using the thermocouple as a reference. The sensitivities of 13.7 and 12.8 °C/V were obtained for the first and second probes. Before the beginning of each measurement series, the thermocouple was used to verify the calibration of the thermal probes. Signals from the thermal probes were recorded during 30 sec for most measurement points. At some points the duration of records was increased up to 3 minutes, in order to estimate more accurately the spectrum of the turbulence.

For the acoustic measurements, 1/8 inch broadband condenser microphones (Brüel & Kjær, model 4138) were connected to preamplifiers (Brüel & Kjær type 2670) and 4-channel amplifier (Brüel & Kjær Nexus with extended up to 200 kHz bandwidth). As described in chapter 1, microphones were mounted in a rectangular baffle (Fig. 2.4e). Signals were digitized using a National Instruments digital acquisition card (PXI 1033) with a sampling rate of 10 MHz and a digitization of 12 bits. Four microphones were used in the measurements, but only two of them were fully operational. Calibration of microphones was carried out according to the method described in section 1.4 of the chapter 1. As a result of the calibration, low-frequency (range 10 Hz – 10 kHz) sensitivity values for the two fully operational microphones were 1.40 ± 0.08 mV/Pa and 1.11 ± 0.06 mV/Pa, respectively. The microphones were separated by an interval of 2 cm along the direction perpendicular to the source-receiver line.

During measurements, the following meteorological data were recorded: temperature, barometric pressure, and relative humidity. The measurements were carried out in winter, the ambient temperature was low enough to yield beneficial effect on the intensity of temperature fluctuations. Due to functioning of the heating grid the temperature in the chamber increased with time, thus the measurements were carried out in cycles of 45 min. The ambient temperature was cooled down by opening the door of the anechoic chamber for 10-15 minutes. As a result of compliance with this regime, the air temperature outside the volume, surrounded by curtains, did not fall below 20 °C and did not rise above 25 °C. Processing of relative humidity data showed that the absolute partial pressure of water vapor remained practically unchanged during the experiment and was $p_{\mathrm{w}} = 710 \pm 50$ Pa. Using this value it is possible to estimate the approximate relative humidity inside the volume of turbulent heated air. The atmospheric pressure during the experiment was equal to 97900 Pa.

§2.4 Characteristics of the thermal turbulence

2.4.1 Cartography of statistical moments of the temperature fluctuations

The turbulent temperature field was characterized using two thermal probes separated by a horizontal distance of 156 mm, allowing the measurements of temperature fluctuations at two points at the same time. First, a scanning was carried out in the horizontal plane (x, y), located at the height $z = 1644$ mm above the grid in order to determine the optimal propagation path of the N-wave. Scans were performed on different days in three areas, numbering a total of 182 measuring points;

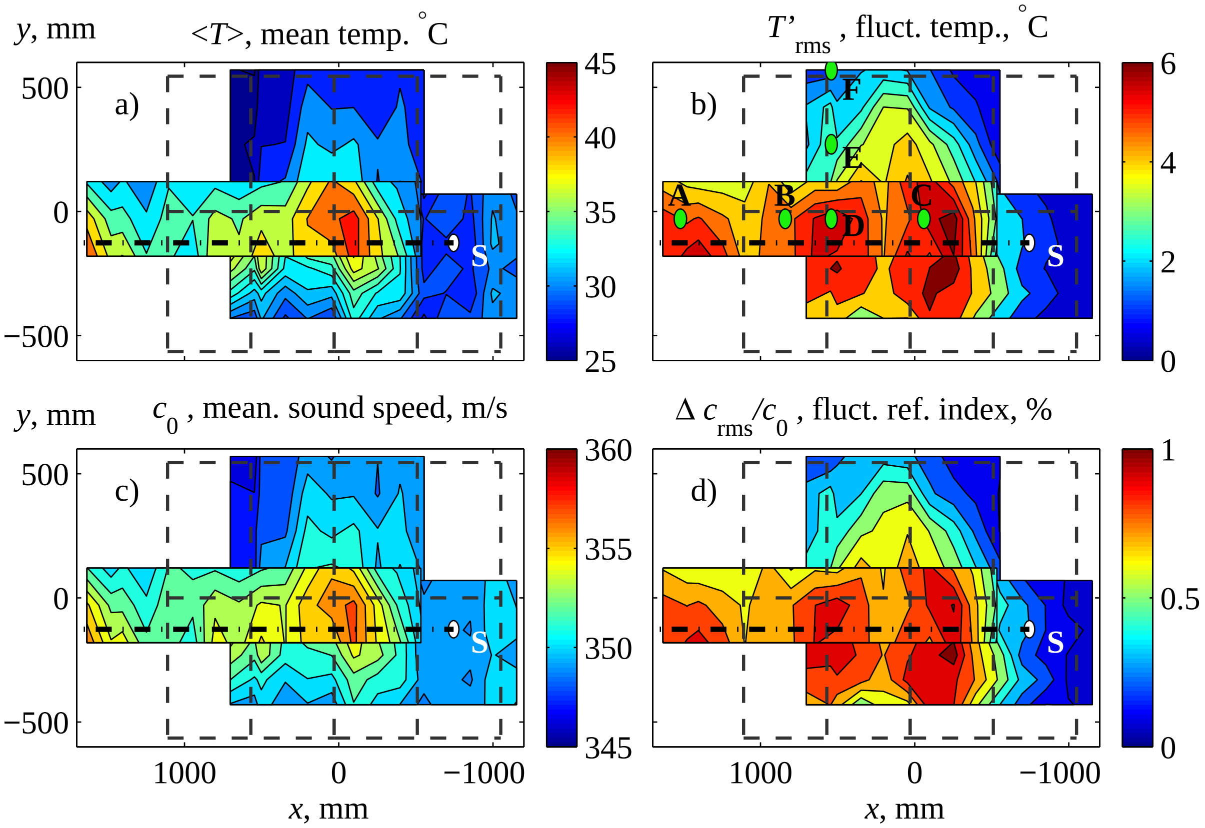

Figure 2.5: Parameters of the turbulent field in the horizontal plane $(x, y, z = 1644\ \mathrm{mm})$: the average temperature of $<T>$ (a), the rms of temperature fluctuations T'_{rms} (b), the average sound speed c_0 (c) and the rms of the refractive index fluctuations $\mu_{\mathrm{rms}} = \sqrt{<\mu^2>} = \Delta c_{\mathrm{rms}}/c_0$ (d). Contours of the grid are shown by fine dashed lines. Also marked the lines passing through the centers of the respective sections of the grid. The source position is shown by a white dot next to the letter S. The propagation path of the N-wave from the source to the microphones is marked by a thick dash-dot line. Green dots and black letters A-F next to them (b) correspond to places where turbulence spectra presented in Fig. 2.10 (a-f) were measured.

the obtained data were then concatenated into a single map. The mean temperature and its rms fluctuation are shown in Fig. 2.5a and Fig. 2.5b, respectively. Contours of two sections of the grid are marked by thin dashed lines. On the map of the mean temperature one can notice that the grid efficiently heats the air only in the central region where the temperature $<T>= 45$ °C was reached. On the edge of the grid, due to the inflow of cold air, the temperature remains quite low ($<T>= [25, 30]$ °C). It is also seen that at the junction of the adjacent sections of the grid near $x = 1000$ mm the temperature is lowered due to lack of heating elements here. The relative humidity in the heated zone was calculated as $H = 6\%$ at $<T>= 45$ °C, and $H = 11\%$ at $<T>= 35$ °C, so the air was very dry.

The rms value of temperature fluctuations T'_{rms} is distributed in the plane (x, y) much more evenly (Fig. 2.5b) than the mean temperature. The rms value reaches 6 °C in the central region and smoothly decreases towards the edges of the grid. The mean sound speed and mean-square $\mu_{\mathrm{rms}} = \sqrt{<\mu^2>} = \Delta c_{\mathrm{rms}}/c_0$ of the refractive index fluctuations corresponding to the measured temperature data are shown in Fig. 2.5c and Fig. 2.5d, respectively. The rms of the refractive index

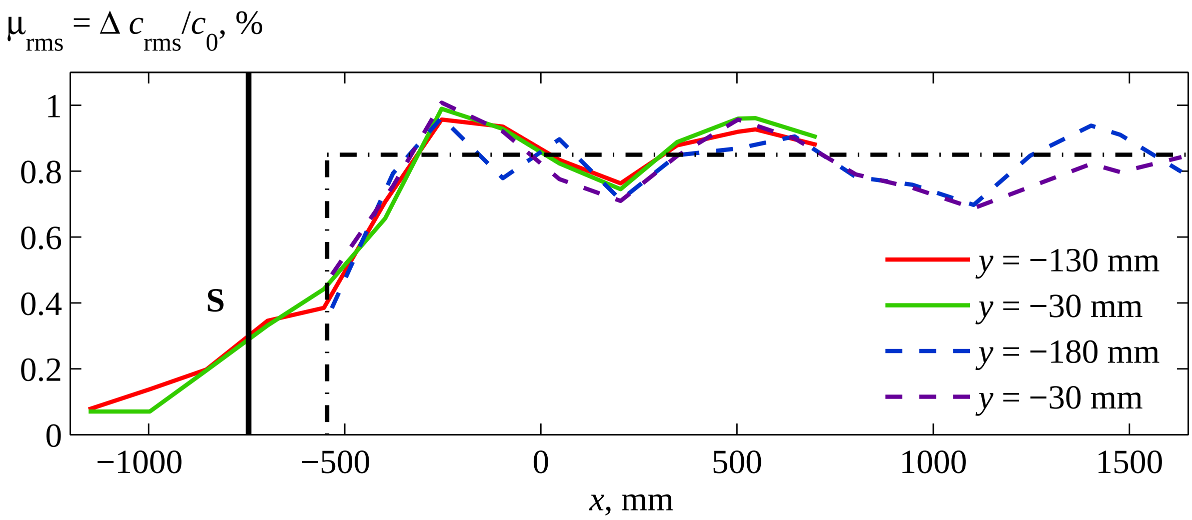

Figure 2.6: Plots of the rms of the refractive index fluctuations $\mu_{\mathrm{rms}} = \Delta c_{\mathrm{rms}}/c_0$ along x coordinate for several values of y coordinates chosen near of the propagation path of the N-wave ($y = -126$ mm). The first series of measurements: $y = -130$ mm (red line) and $y = -30$ mm (green line). Second series: $y = -180$ mm (blue line) and $y = -30$ mm (purple line). Source position on the axis x is marker by a vertical solid line. Effective medium with a constant value of the rms $\Delta c_{\mathrm{rms}}/c_0 = 0.85\%$ and starting at a distance of 200 mm from the source, is shown by black dot-dashed lines.

fluctuation $\Delta c_{\mathrm{rms}}/c_0$ in some measurement points reaches 1% value, although in most areas, where turbulence is intense, $\Delta c_{\mathrm{rms}}/c_0$ is ranging from 0.75% to 0.95%.

Accordingly to the maps of the mean sound speed and refraction index fluctuations, the spark source was placed in the point with coordinates $(-745, -126, 1470)$ mm, which is marked by a white circle (next to the letter S). This point is located in the transition zone between the low (blue color) and high (red color) levels of turbulent fluctuations (Fig. 2.5d). The rms of the refractive index fluctuations near the source was about 0.25%. This source location was chosen in order to have an acoustic "source-receiver" path in the zone where the fluctuations of the refractive index are more intensive. The chosen propagation path of the N-wave is marked in Fig. 2.5 by a thick dash-dotted line. It is seen, that a high level of the refractive index fluctuations is retained also in vicinity of the path. A small difference in height between the actual path and the horizontal plane mapping of turbulence (1470 mm versus 1644 mm) is explained by necessity of additional space for mounting of microphones in the baffle on the vertical axis of the positioning system, which was not foreseen in advance. As it was shown by measurements in the vertical plane (x, z), this difference of heights is negligible in terms of turbulence fluctuation level.

Fig. 2.6 plots the mean-square of the refractive index fluctuations $\mu_{\mathrm{rms}} = \sqrt{<\mu>^2} = \Delta c_{\mathrm{rms}}/c_0$ along the x coordinate for several values of the y coordinates chosen in the vicinity the acoustic path ($y = -126$ mm). The red and green solid curves were obtained in one series of measurements, and the blue and purple dashed lines – in another. It is seen that the results of different series are in good agreement. The rms value of the refractive index fluctuations increases with increasing the distance between the source and the thermal probe location. It reaches a maximum of 1% and then gradually changes with the distance in the range between 0.75% and 0.95%. To carry out the theoretical estimates or to compare the data with other experimental studies, it is convenient

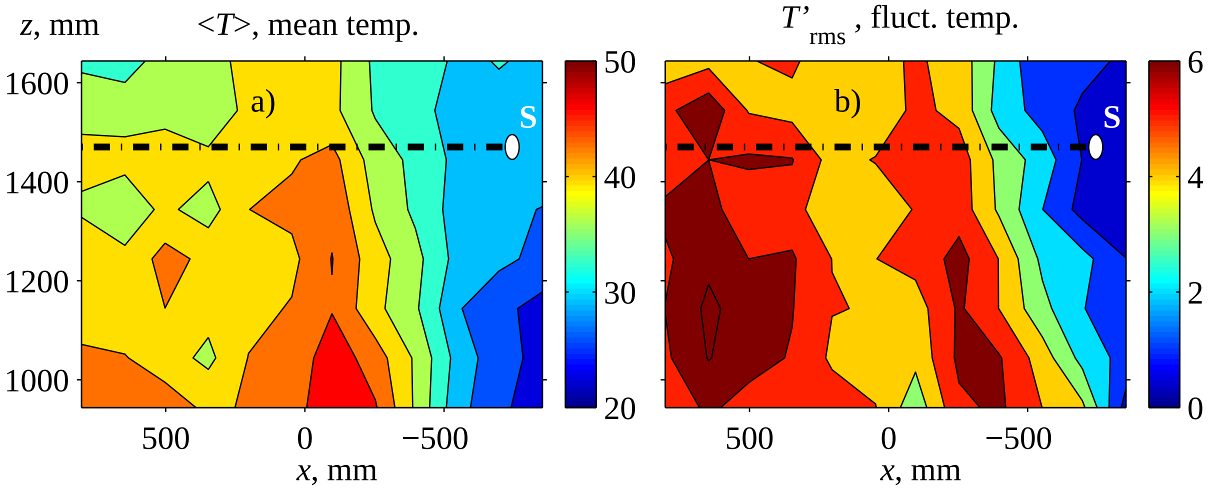

Figure 2.7: The parameters of the turbulent field in the vertical plane $(x, y = -30\ mm, z)$: the average temperature of $<T>$ (a), the rms fluctuation ΔT_{rms} (b). Source position is shown by with a white dot next to the letter S. Propagation path of the N-wave is marked by a thick dash-dot line.

to replace the real turbulent medium by an effective one with a fixed average value of the rms fluctuations μ_{rms}. It is reasonable to choose the starting edge of the effective medium close to the source because it will be convenient for modeling. Here the origin has been chosen at the 200 mm from the source, i.e. at $x = -545$ mm. The effective average μ_{rms} was determined from the equality of the integral of this quantity under the experimental curves and under the rectangle shown in Fig. 2.6 by black dot-dashed lines. Thus one can assume that the N-wave propagation took place in a layer of homogeneous isotropic turbulence, starting at the distance of 200 mm from the source and which have constant level of mean-square of the refractive index fluctuations equal to 0.85%.

In addition, measurements of the temperature field in the vertical plane (x, z) at $y = -30$ mm were done. Along the x axis there were 12 measurement points and along the z axis – 8, i.e. 96 points at all. The results for the mean temperature and the rms value of temperature fluctuations are shown in Fig. 2.7. It is seen that the average temperature only slightly increases when approaching the probe to the grid in the measured altitude range. Temperature fluctuations at the bottom in some places become more intense than at the top by $1 - 2$ °C about. Processing the experimental data as previously for the Fig. 2.6, one can obtain the values of μ_{rms} for the "effective" turbulent boundary layer equal respectively to 0.73%, 0.76%, and 0.87% at altitudes 1644 mm, 1544 mm and 1444 mm, which are consistent with the measurements in the plane (x, y). It should be noted that different measurements were made in different days, and, because of the changing of ambient temperature and other conditions, the turbulence intensity could vary slightly (10%).

2.4.2 Correlation measurements

The thermal turbulence generated in the experiment is considered as a fixed scalar field from the point of view of acoustics. However, in fact, the turbulence is convecting at low speed. The average value of a convecting speed U_{vert} of turbulent structures is necessary to know, for modeling of the spatial spectrum of the turbulence. Indeed, the thermal probe gives a signal in time, and accordingly, the spectrum is a function of the frequency f in Hz, while in the theory of random fields, one operates with the spectrum derived as a function of spatial frequencies, expressed in m^{-1}. To find the convection velocity, vertical correlations were measured, i.e. thermal probes were placed one above another as it is shown in Fig. 2.4c. Convecting speed U_{vert} can be obtained as the ratio of the distance between the probes to the shifting time interval between the two signals, which gives their maximum correlation. The method assumes a Taylor hypothesis of "frozen turbulence", which states that the turbulent structures are preserved moving along the flow with an average speed $T(x,t) = T(x - U_{\mathrm{vert}}t, 0)$.

Vertical correlations were measured at two points with coordinates $(175, -30, 1644)$ mm and $(725, -30, 1644)$ mm; length of the recorded signals was 90 seconds. Fig. 2.8 shows the measured shifting time interval between the signals at which the maximum correlation is reached (red markers), depending on the distance Δz between the probes. The slope of the best linear fit (black solid line) gives the magnitude of the lifting speed U_{vert} equal to 1.14 ± 0.01 m/s at the point with $x = 175$ mm and to 1.07 ± 0.02 m/s at the point with $x = 725$ mm. As it is seen from the data, the convecting speed of the turbulent structures is small, contribution to the change of the refractive index is smaller than 0.3%. In addition, the direction of the convection is perpendicular to the direction of the selected propagation path, so influence of this flow on distortions of the acoustic field can be neglected. The only possible effect is a transversal drift of the acoustic field by approximately rU_{vert}/c_0 as the wave propagates over a distance r. For $r = 2$ m the drift would be 6 mm, which is negligible since the experiment was done with a spherical source, rather than with a narrow beam. So no matter what part of the wavefront reaches the microphones – this one passed along the line of sight from the source, or a few millimeters sideways.

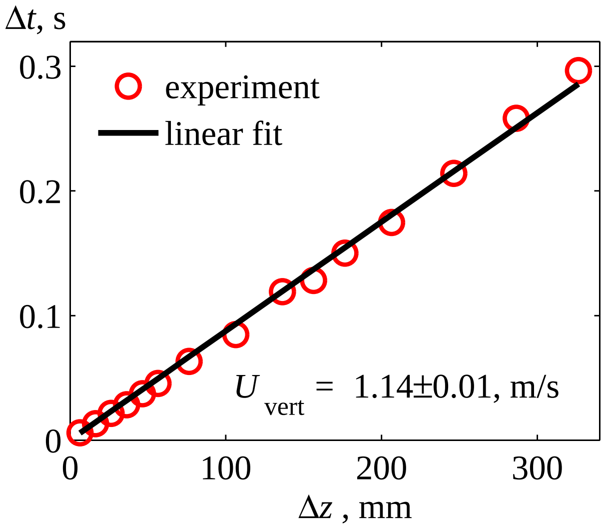

Figure 2.8: Determination of the average lifting speed of the turbulent structures U_{vert} using dependence of the time shifting interval between the two signals of the probes, at which the maximum correlation is reached, from the distance between them. Measurements were made at the point $(175, -30, 1644)$ mm. The experiment – red circular markers, linear approximation $\Delta z = U_{\mathrm{vert}}\Delta t$ – black line.

The next step in the characterization of turbulence is the determination of the outer scale L_0 (Eq. 2.3). For this purpose, correlation measurements were carried out in a horizontal direction along the axis x near the point with coordinates $(175, -30, 1644)$ mm. The selected point is inside the area of most intense fluctuations and the thermal probes do not leave it out if the separation between them increases. The correlation function, $B(\Delta x)$, is defined as:

$$B(\Delta x) = \frac{< T_1'(x + \Delta x) T_2'(x) >}{T_{1rms}' T_{2rms}'}, \tag{2.8}$$

where T_i' is a signal of the i-th probe with subtracted average value and T_{irms}' is the mean square of temperature fluctuations. The time average in the Eq. (2.8) was carried over the signals with 90 seconds duration. The results of correlation measurements are shown in Fig. 2.9 (a) with blue markers. If it would be possible to measure the correlation in a whole range of distances between the probes starting from $\Delta x = 0$ up to few characteristic outer scales L_0, then this value could be calculated using the formula (Comte-Bellot & Bailly, 2003)

$$L_0 = 1.339 L_x = 1.339 \int_0^\infty B(r) dr, \tag{2.9}$$

where L_x, by definition, is called as the integral correlation length (Rytov *et al.*, 1978). The estimation of L_0 by the formula (2.9), with a correction due to the fact that the integration was carried out only up to the separation distance of $\Delta x = 400$ mm, gives a value of 17 cm. However, in this study L_0 was determined from the best fit of the experimental data with the theoretical correlation curve, calculated from the modified Kármán spectrum (black line in Fig. 2.9, see equation C.6), in smaller range of separation distance values Δx between the probes (up to L_0). As a result, the value of $L_0 = 20$ cm was obtained, which is considered hereafter as an estimate of the outer scale. Despite the differences between theory and experiment for large Δx (Fig. 2.9), it must be kept in mind that these data points are less reliable than the points with a small separation distance between the thermal probes. Note, that the resulting value $L_0 = 20$ cm is not consistent with an estimation $L_0 = 15$ cm obtained using the Eq. (2.9) in previous measurements of the correlations at height of 1.9 m above the same heating grid, realized in other experimental studies (Wasier, 1999). Nevertheless, the measurements done in the current study were letted to have priority. In addition, purple triangular markers shows a set of correlation data for a fixed value of $\Delta x = 156$ mm, obtained in a scanning measurement series along the axis x for $y = -30$ mm (Fig. 2.5). The most of the data are grouped close to the theoretical estimation of the correlation for the given Δx and the measurement results from the first series.

Finally, experimental data for the vertical correlation, obtained from measurements of the lifting speed U_{vert} are shown in Fig. 2.9b. Here, in contrast to Fig. 2.8, in the processing of the data of temperature probes, the signals were averaged without shifting one relative to another. Measurements are presented for the point $(175, -30, 1644)$ mm by red diamond markers and for the point $(725, -30, 1644)$ mm by green squares. The theoretical correlation curve here is the same as in Fig. 2.9a and marked by a black line. It can be seen that at small Δx the agreement between experiment and theory is quite good. However, starting from $\Delta x = 200$ mm, there are significant differences that indicate possible greater correlation between large turbulent structures in the vertical direction than in the horizontal direction. Thus, the turbulent field is slightly anisotropic in (x, z) and (y, z) vertical planes.

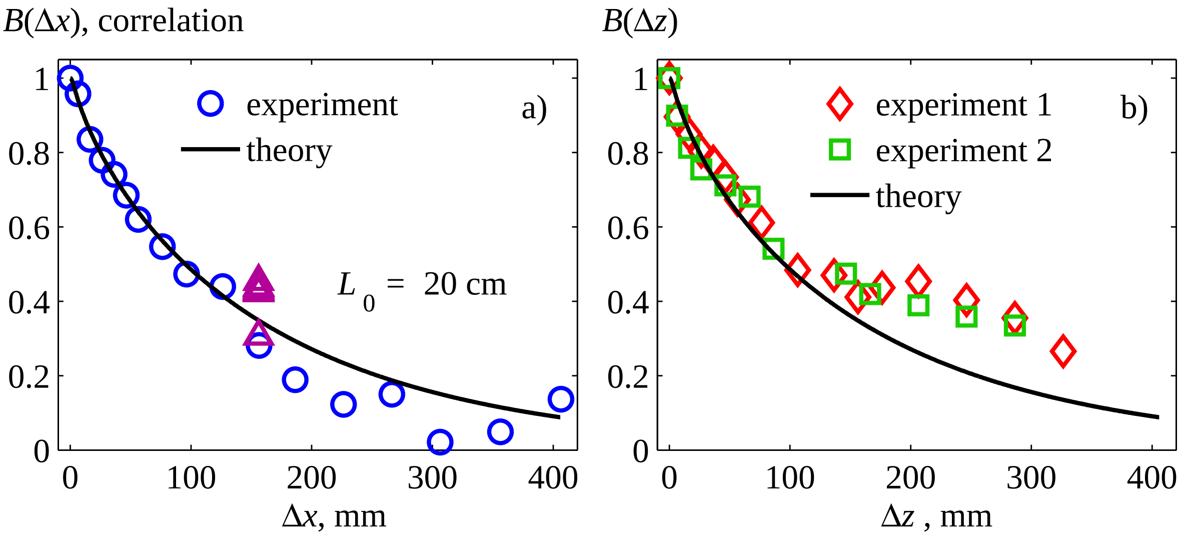

Figure 2.9: Horizontal correlation near the point with coordinates $(175, -30, 1644)$ along the x axis (blue circles) (a), the vertical correlation in the points $(175, -30, 1644)$ (red diamond markers) and $(725, -30, 1644)$ (green squares) (b). Purple marker denotes the dataset obtained in the mapping measurements (Fig. 2.5) along the line $y = -30$ $(\Delta x = 156$ mm). The theoretical correlation function associated with the von Karman spectrum with parameters $L_0 = 20$ cm and $l_0 = 5$ mm is shows by a black solid line.

2.4.3 One-dimensional spectra of refraction index fluctuations

Theoretical one-dimensional spectrum of homogeneous isotropic turbulence is defined as one-dimensional Fourier transform of the correlation function (Rytov *et al.*, 1978) $B(z)$:

$$G_{1D}(k) = \frac{1}{2\pi} \int_{-\infty}^{+\infty} B(z) e^{-ikz} dz. \tag{2.10}$$

It is known that one-dimensional and three-dimensional spectra of the turbulence are related together by the following integral relation (Comte-Bellot & Bailly, 2003):

$$G_{1D}(k) = \frac{1}{2} \int_{k}^{+\infty} \frac{G(k')}{k'} dk' \tag{2.11}$$

The power spectrum can be obtained from the experimental data by averaging the spectra of individual realizations. The power spectrum $W(f)$ expressed as a function of the frequency f in Hz is defined as:

$$W(f) = \lim_{T\to\infty} \frac{2\pi}{T} < |\widehat{f}_T(f)|^2 >, \tag{2.12}$$

where f_T is a spectrum of one random realization of duration T. To deduce the wavenumber spectrum from the frequency spectrum the Taylor hypothesis of frozen ”turbulence” was used. This hypothesis leads to the following replacement of the arguments: $\Phi^{1D}_{exp}(k) = W(f = kU_{\text{vert}}/2\pi)$. It is also necessary to replace the duration T by the length $X = U_{\text{vert}}T$ in Eq. (2.12). The method of signal processing and calculation of the experimental power spectra is detailed in Appendix C.

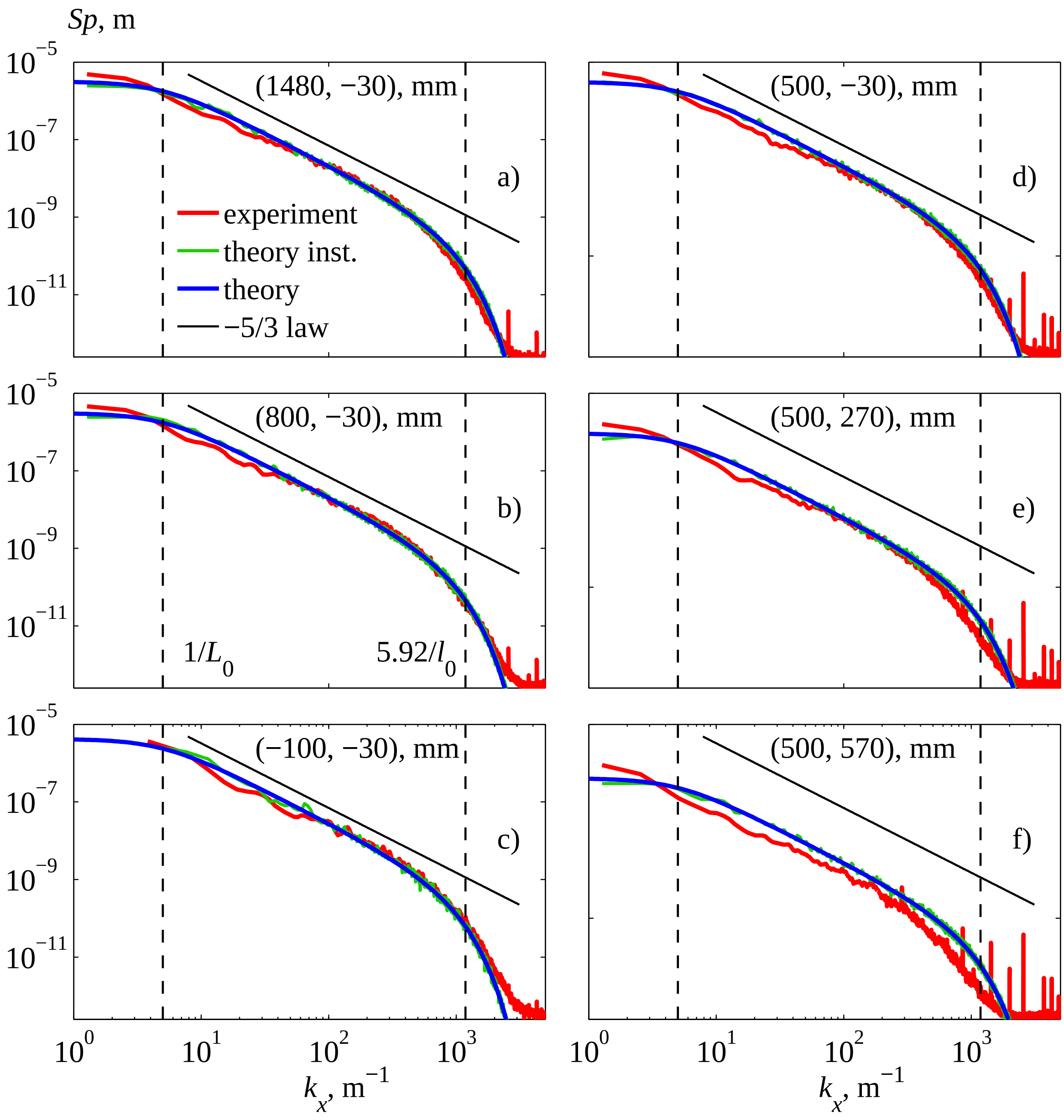

Figure 2.10: One-dimensional spectra of fluctuations of the refractive index obtained experimentally (red line) and by the von Karman model spectrum with the parameters of $L_0 = 20$ cm, $l_0 = 5$ mm (blue line). The green line shows a spectrum obtained by processing the artificial realization with the von Kármán spectrum using the same methodology (see Appenix. C), as in the processing of experimental spectra. Black line corresponds to the law $k^{-5/3}$.

Fig. 2.10 shows the experimental spectra of refractive index (red line) in comparison with theoretical spectra (blue line). For the theoretical spectrum, the parameters $L_0 = 20$ cm and $l_0 = 5$ mm were set. The mean-square $<\mu^2>$ for each of the theoretical spectrum is taken from the corresponding experimental data. In addition, to be sure that the processing of the experimental data does not introduce significant errors, the spectra based on artificial random realizations constructed with theoretical spectrum, are shown by the green line. The artificially calculated spectrum showed that the treatment of the thermal probe signals does not introduce significant errors in the experimental spectrum. Finally, the black line corresponds to the Kolmogorov law $k^{-5/3}$ which describes very well the decrease of experimental spectra in the inertial range. Spectra (a - d) were captured at the points located in a line along the x axis near the propagation path of the N-wave (green circles from A to D in Fig. 2.5b). Spectra (e - f) were measured at points along the y axis, where there is a transition zone to the ”weak” turbulence (circles E and F in Fig. 2.5b).

According to the results obtained in the area of intense turbulence, experimental and theoretical spectra fairly well correspond with each other in the inertial range (spectra from a to d). However, in a segment of spatial frequencies between $k \approx 5\ \mathrm{m}^{-1}$ and $k \approx 60\ \mathrm{m}^{-1}$, the experimental spectra are sometimes $1.3 - 2.0$ times lower in comparison to the theoretical spectrum. The relevant inhomogeneous structure scales ($l = \pi/k$) are in the range from 60 cm to 5 cm. In Appendix C further examples of spectra measured in the zone of intense turbulence, in which the lower values of the experimental spectrum in the given range are almost absent, are given. The lower values of the experimental spectrum in Fig. 2.10 in the mentioned range of scales are compensated by higher values of the spectral density at very large inhomogeneities ($k < 5\ \mathrm{m}^{-1}$, $l > 60$ cm). Since the size of the turbulent field is of the order of one meter along each direction, the low-frequency fluctuations observed in the spectrum are not associated with the presence of inhomogeneities of that size but rather to slow variations of the whole turbulent field. These variations may be caused by several poorly controlled factors, such as a slow movement of the curtain or sidewinds. For smaller scales ($l < 5$ cm, $k > 60\ \mathrm{m}^{-1}$), the agreement between theory and experiment in most cases is excellent. Also the decay of the spectrum at the smallest scales $k > 5.92/l_0 \approx 1200\ \mathrm{m}^{-1}$, due to the dissipation of turbulent fluctuations, corresponds well to the theory. On the contrary, the spectra measured in the zone where the turbulence level is low are much more different from the theoretical spectra (Fig. 2.10 e and f). There is significant decrease of fluctuations intensity across the inertial range and very high intensities of low-frequency fluctuations in comparison with theory. This may be due to significant influence of air currents arriving at the edge of the grid from the surrounding area, since the curtains did not provide a complete isolation of the turbulent field.

In conclusions to this section following the detailed measurement results on can note that the scalar turbulent field produced by the heating grid is sufficiently homogeneous and isotropic in central zone above the heating grid. The value of the mean square of refractive index fluctuations in this region is $\sqrt{<\mu^2>} = 0.85\,\%$ on average. The N-wave was propagated in the turbulent layer which starts at 200 mm from the spark source. Experimental turbulence spectra were found to be well described by the modified von Kármán spectrum with the outer and the internal scales equal to $L_0 = 20$ cm and $l_0 = 5$ mm, correspondingly. In the next section, results of acoustical measurements of N-waveforms will be presented and analyzed.

§2.5 Acoustical measurement results

2.5.1 Propagation of the N-wave in still air

Parameters of the N-wave in homogeneous air were determined according to the method described in chapter 1. Processing of one measurement series gave the amplitude $p_0 = 1080 \pm 40$ Pa and the half-duration $T_0 = 19.8 \pm 0.2$ μs at distance $r = 19$ cm from the source. Thus, the parameters of nonlinear pulse used in this chapter are similar to the parameters of the pulse which was used in chapter 1 and which characteristics were $p_0 = 1400 \pm 80$ Pa and $T_0 = 19.0 \pm 0.1$ μs at a distance of 16 cm from the source, and $p_0 = 1090 \pm 60$ Pa and $T_0 = 20.1 \pm 0.1$ μs at a distance $r = 19$ cm, respectively.

In the second measurement series in homogenous air, locations of microphones were the same as in measurements in the presence of turbulence. Thus, it was possible to study the statistical distributions of various parameters of the N-wave, which are normalized to the corresponding values in homogeneous media. There were 9 source-microphones distances in the range from $r = 41$ cm up to $r = 201$ cm with an increments of 20 cm. In Fig. 2.11 are presented peak positive (a) and negative (b) pressures, half-duration (c) and the front shock risetime (d) as functions of the propagation distance. The parameters of the N-wave at a distance $r = 41$ cm from the source were $p_0 = 430 \pm 25$ Pa and $T_0 = 21.8 \pm 0.2$ μs, which are consistent with the data of the first

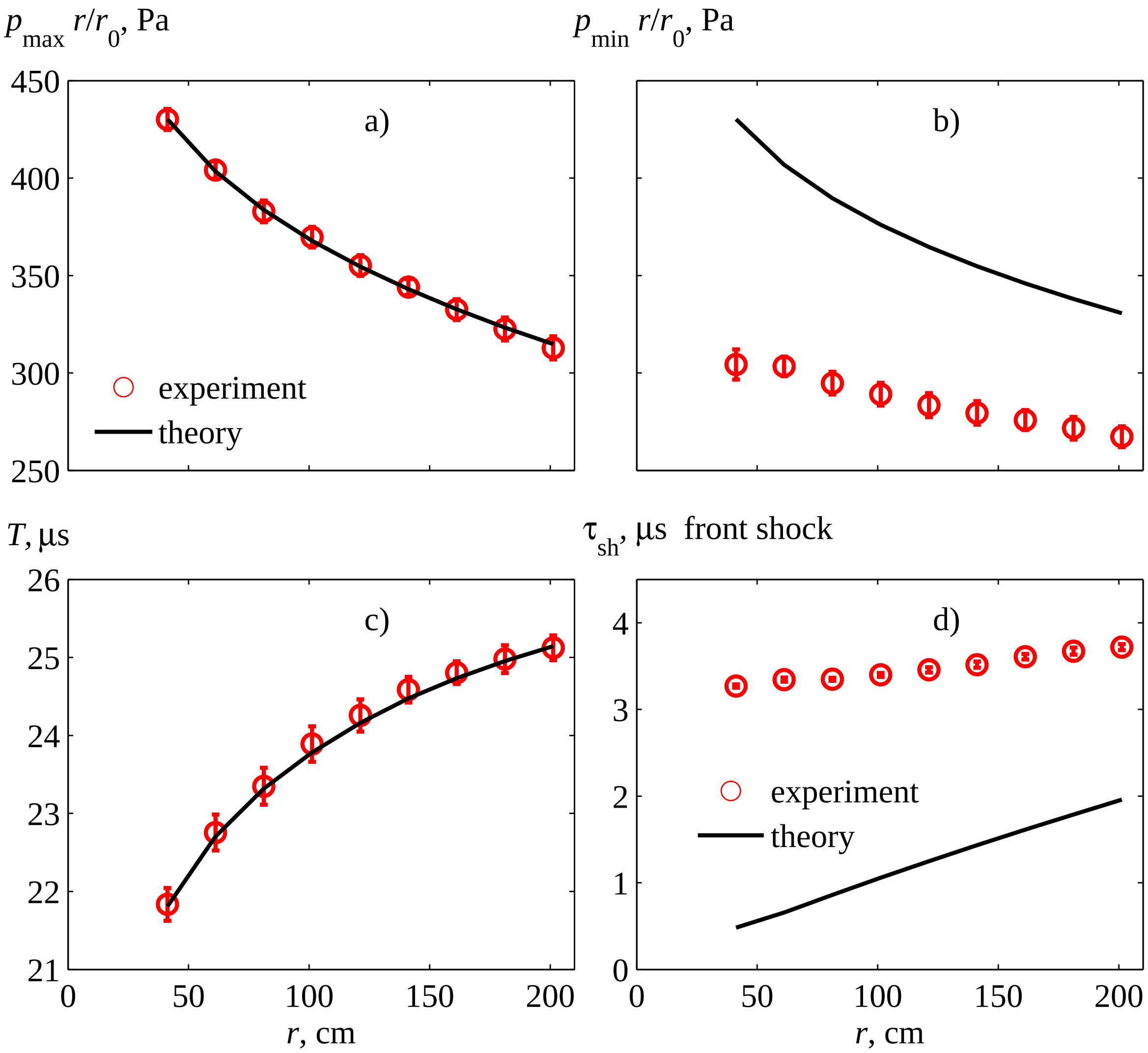

Figure 2.11: Main parameters of the N-wave, measured in a homogeneous air. The positive peak pressure (a), the negative peak pressure (b), half-duration (c), the front shock risetime (d). Black line shows the results of numerical simulation, red markers – the results of the experiment. Atmospheric conditions were the following: $p_{\text{atm}} = 97900$ Pa, $T_{\text{atm}} = 14.5$ °C, humidity 35%.

series. The following Tab. 2.1 summarizes the data from the graphs in Fig. 2.11. Amplitude values of $p_{\max}$ and $p_{\min}$ are given without multiplication by the spherical spreading compensation factor r/r_0. Here and below the variable $p_{\min}$ refers to the module of the negative peak pressure. The values indicated in the table are obtained by an averaging of 200 measured waveforms at each given distance r.

r, cm	41	61	81	101	121	141	161	181	201
$p_{\max}$, Pa	430	272	194	150	121	100	85	73	64
$p_{\min}$, Pa	304	204	150	118	96	82	70	62	55
T, μs	21.8	22.7	23.3	23.9	24.3	24.6	24.8	25.0	25.1
τ_{sh}, μs, exp.	3.26	3.33	3.32	3.36	3.41	3.46	3.52	3.56	3.59
τ_{sh}, μs, theory	0.48	0.65	0.85	1.05	1.24	1.43	1.62	1.80	1.97

Table 2.1: Main parameters of the N-wave, measured in homogeneous medium in the range of distances r from 41 cm to 201 cm. The risetime of the front shock τ_{sh} is defined here using the peak of the derivative of the waveform. The risetime obtained using this definition coincides with the values defined using the waveform as a time of pressure rise on the shock between 5% and 95% levels of the peak positive pressure $p_{\max}$.

In chapter 1, the definition of the shock risetime as a time needed to to pressure to rise from 0.1 to 0.9 of the peak positive pressure was used. In this chapter the definition of the front shock risetime was changed. Due to the fact that it is necessary to analyze highly distorted waveforms (Fig. 2.12), the usual definition of the shock risetime based on the waveform is no longer applicable. More meaningful in this case is to use another definition, based on the width of the peak of the waveform derivative (Averiyanov, 2008). Using the new definition, it is necessary that in a homogeneous medium the risetime, obtained under the two methods would be consistent. This can be achieved by setting the appropriate threshold level, over which the width of the derivative peak is calculated. Thus, in the case of experimental data, the level of $e^{-0.57}$ yields results that coincide with the definition of "0.1-0.9" thresholds in the waveform method. However, in the study (Averiyanov, 2008) author introduced a threshold level equal to e^{-1}, which, in the case of experimental data meets the "0.05-0.95" thresholds in the waveform definition. Since in the §2.6 the present data will be compared with experimental data from the cited study, here the latter definition was chosen.

The pulses produced by the spark source have small fluctuations from on shot to another. For example, the standard deviation of the peak positive pressure $p_{\max}$ is in a range from 1% to 2% at different distances r. The standard deviation of the peak negative pressure $p_{\min}$ is from 1.5% to 2.5%, half-duration – from 0.5% to 1%, the front shock risetime – not larger than 0.1 μs, and the pulse arrival time – from 1 μs to 1.3 μs. It will be shown, that after propagation through inhomogeneous turbulent media, fluctuations of the listed parameters are significantly bigger than in quiet air.

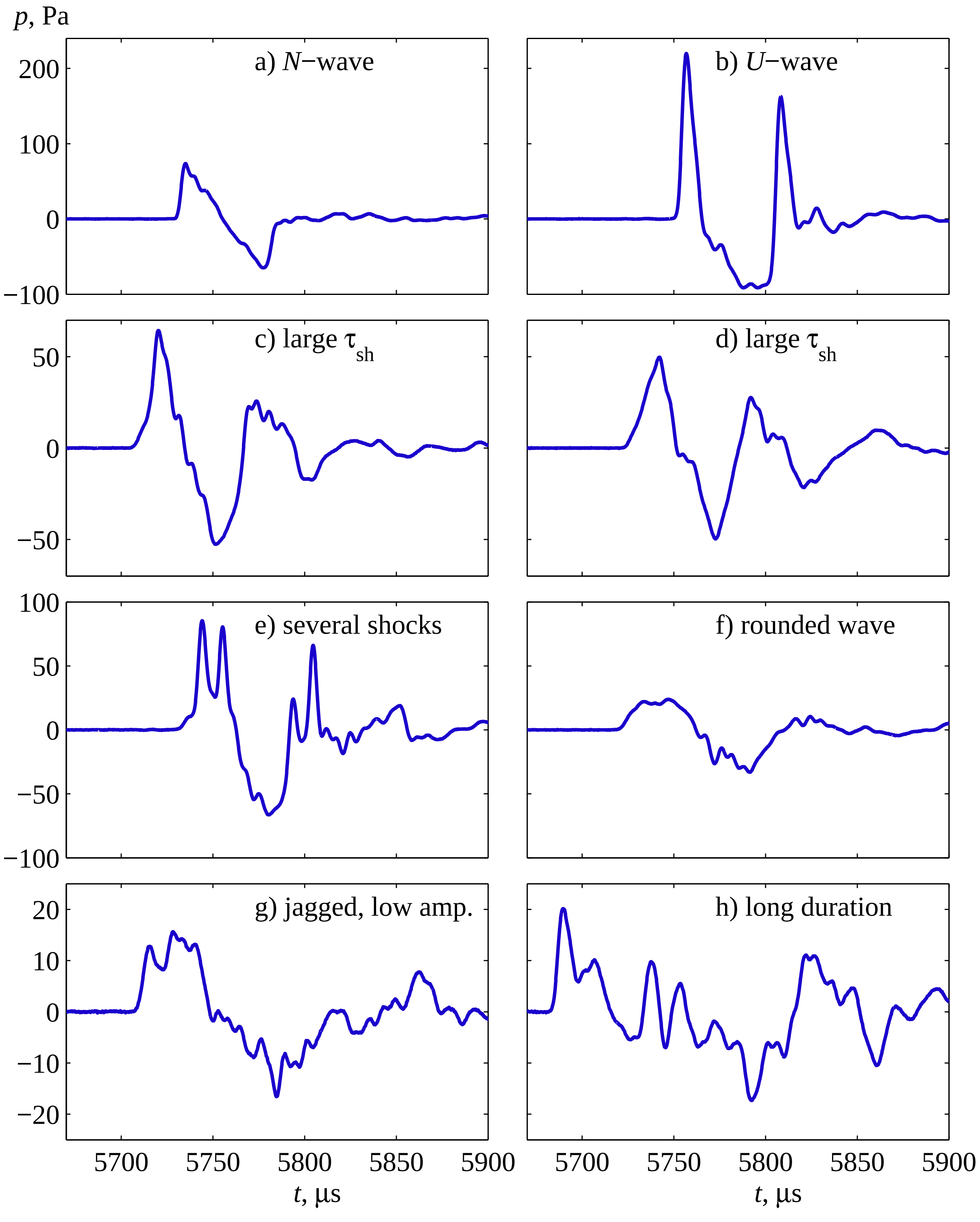

Figure 2.12: Typical distorted waveforms measured at a distance $r = 201$ cm from the source after propagation through a turbulent layer. The scales of the vertical axes in different rows of the figure are different.

2.5.2 Propagation of the N-wave through thermal turbulence

Typical examples of distorted waveforms measured after propagation through a turbulent layer are shown in Fig. 2.12. Although the given examples are the most typical, they does not cover the all variety of possible distortions of the initial N-wave. The obtained waveforms are in good agreement with sonic booms, measured in the atmosphere (Lee & Downing, 1991) and distorted

N-waves measured in other model experiments (Lipkens & Blackstock, 1998a, Averiyanov, 2008). For example, even after the large distance ($r = 2$ m) of propagation through the turbulence the classical N-waveform can be maintained (Fig. 2.12a). When crossing a caustic a U-wave is formed with amplitude more than 3 times bigger than the amplitude of the N-wave in homogeneous medium (Fig. 2.12b). Scattering by inhomogeneities increases the risetime of the shock up to $10 - 15$ μs (c and d), although the waveform at the same time remains sufficiently coherent. In some cases, there are several shocks in the waveform, which is likely due to summation of waves with different arrival times acquired after passing two strong inhomogeneities (e). In defocusing areas, smoothed waveforms (f) can be detected as well as jagged waves of small amplitude (g) or waves with very long duration (h).

Results of statistical analysis of the waveforms, measured with two microphones, are presented in the following subsections. The total number of waveforms involved in the analysis was 1000 for the distance $r = 41$ cm, 2000 for the distances from $r = 61$ cm to $r = 121$ cm and 4000 from $r = 141$ cm to $r = 201$. The results are presented as histograms and graphs of the two first statistical moments: the mean value and the standard deviation. The maximum and minimum peak values observed in measured samples are also presented.

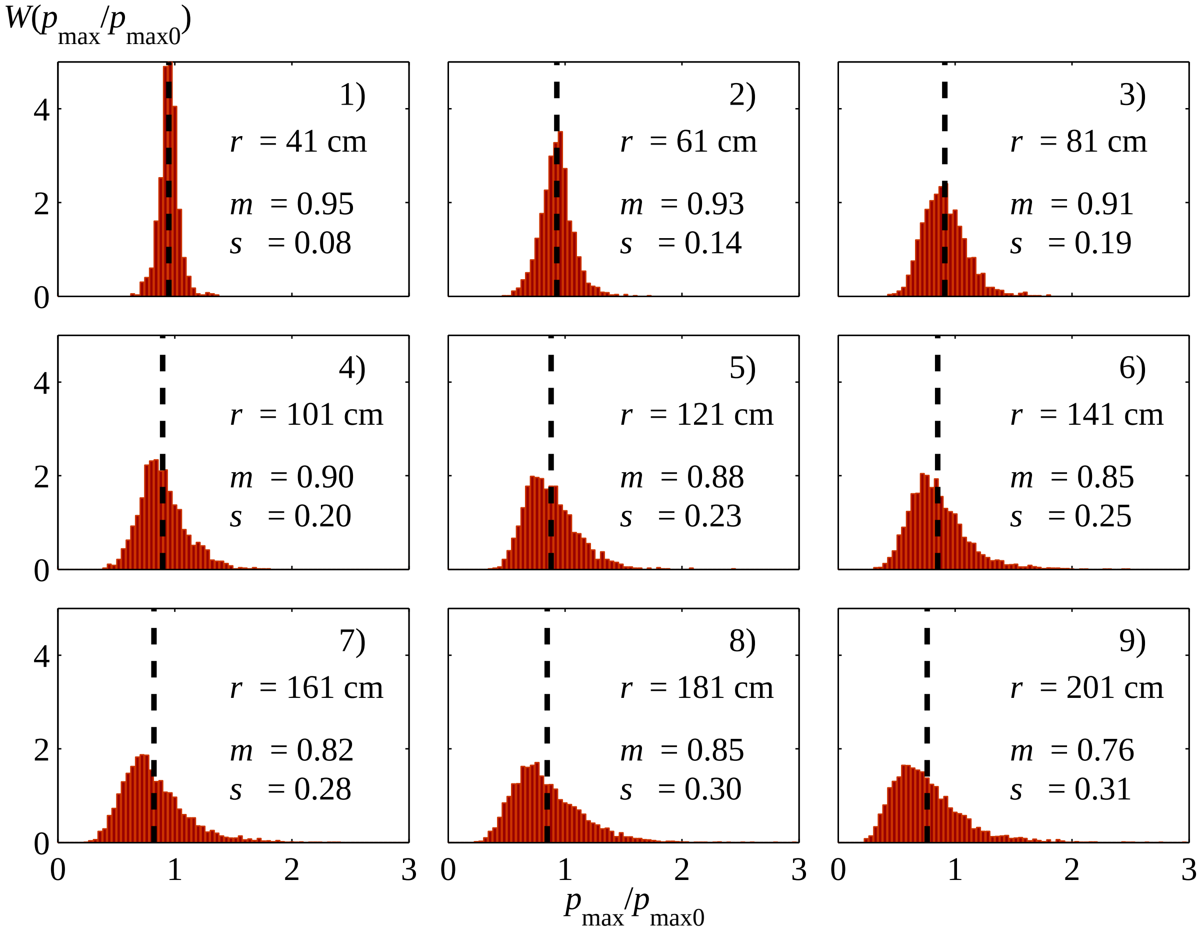

Figure 2.13: Histograms of the statistical distributions of the peak positive pressure, normalized to the corresponding values in a homogeneous medium, $p_{\max}/p_{\max 0}$. Black dashed line shows the average value of each distribution. Values for the source-microphones distance r, the mean m and standard deviation s are given on the graphs. Class size is 0.04.

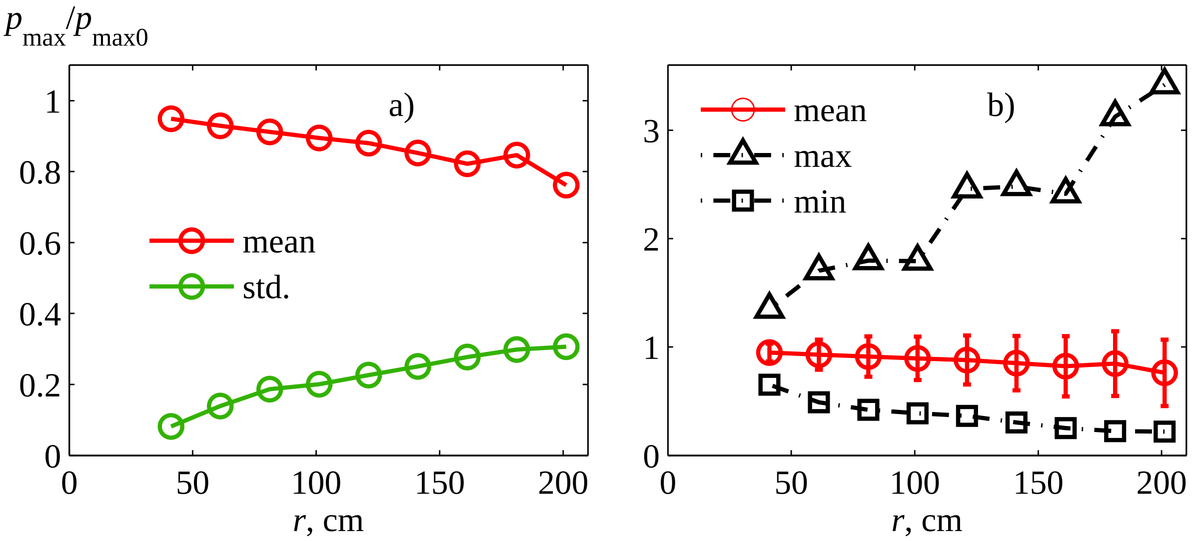

Figure 2.14: Average characteristics of the peak positive pressure, normalized to values in a homogeneous medium $p_{\max}/p_{\max 0}$. The graph shows the mean value (red line) and the standard deviation (green line) (a), as well as maximum (triangle markers) and minimum (square markers) values observed in the sample (b).

Peak positive and negative pressures $p_{\max}$ and $p_{\min}$.

One of the most important characteristics of the N-wave that determines its noise impact, is peak positive pressure $p_{\max}$ (Fidell *et al.*, 2002). Additionally, due to nonlinear effects, the bigger $p_{\max}$ leads to smaller risetime of the shock front. The decreasing of the risetime was found to strongly increase the noise effect of the N-wave (Fidell *et al.*, 2002). Fig. 2.13 shows the histograms of the peak positive pressure, normalized to the values measured in homogeneous medium, $p_{\max}/p_{\max 0}$. Nine histograms correspond to different distances r from the source to microphones. The closest distance to the source $r = 41$ cm is in the top left corner and the last distance $r = 201$ cm is in bottom right. The same order of histograms will be used when plotting data of other parameters of the wave. On each histogram the mean value m and standard deviation s are given. Histograms shows conventional broadening of the statistical distribution with increasing distances r, accompanied by an increase of the standard deviation and a decrease of the mean value. At close distances, the distributions are almost symmetrical, but far from the source the maximum of the distribution is shifted to lower values of the amplitudes and at high amplitudes a long ”tail” is formed. As it will be shown in the next chapter 3, the main features of the evolution of the statistical distributions observed in the experiment can be described using a phase screen as a simple model to represent random inhomogeneous layer.

Fig. 2.14a shows the mean value m and standard deviation s as functions of the distance r, and in Fig. 2.14b the maximum (triangle markers) and minimum (square markers) values are also marked. One can see that at large distances ($181-201$ cm) pulses with amplitude 3-3.5 times higher than the measured in homogeneous media are observed. At the same time, the minimum amplitude observed at the same distances is 4-5 times less than in quiet air. This behavior of the statistical distributions of $p_{\max}$ is qualitatively similar to that observed in the experiment on propagation of an

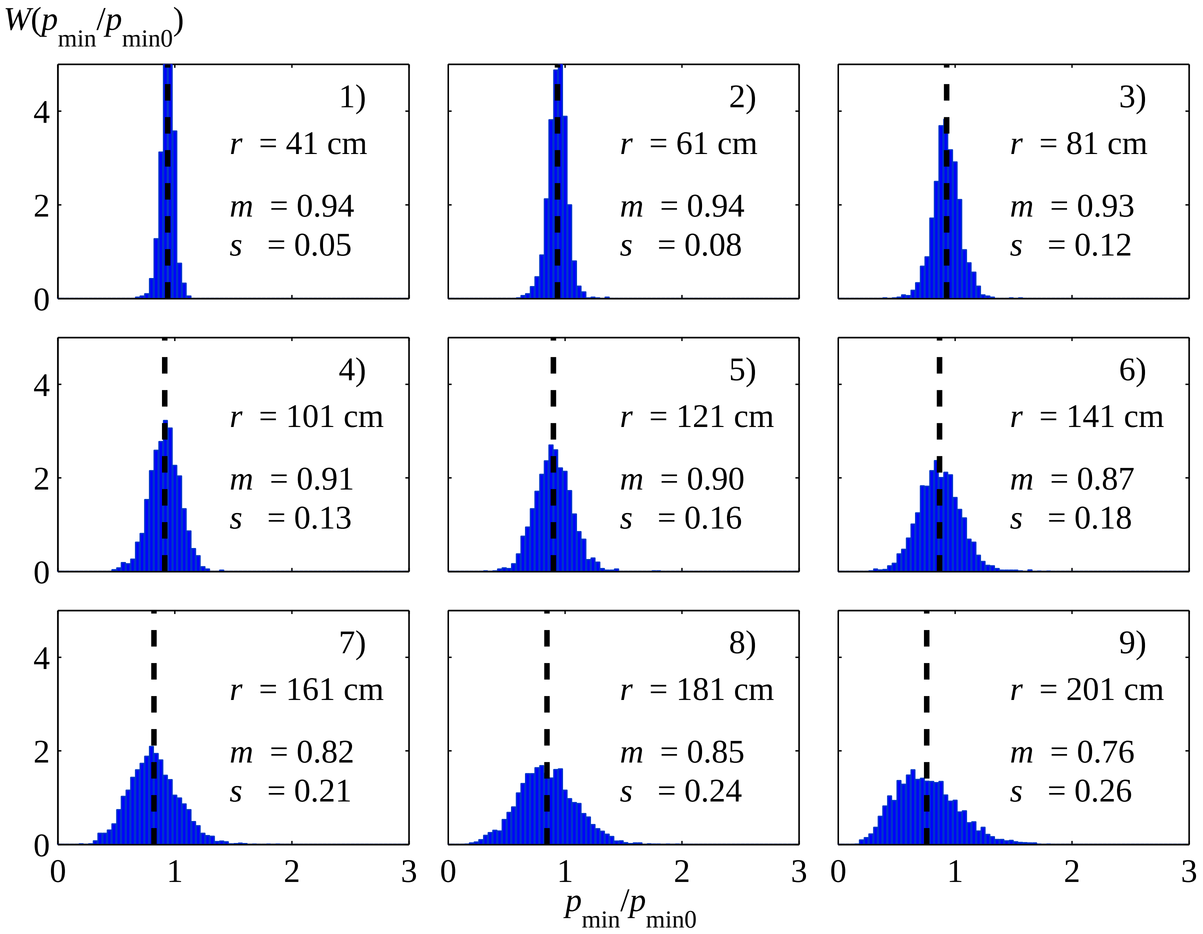

Figure 2.15: Histograms of the statistical distributions of the peak negative pressure, normalized to the corresponding values in a homogeneous medium, $p_{\mathrm{min}}/p_{\mathrm{min0}}$. Black dashed line shows the average value of each distribution. Values for the source-microphones distance r, the mean m and standard deviation s are given on the graphs. Class size is 0.04.

N-wave in the kinematic turbulence (Averiyanov, 2008, Lipkens & Blackstock, 1998a). However, as it will be shown in the last section of this chapter, there are important quantitative differences between these two cases.

Statistical distributions of the peak negative pressure p_{min} (Fig. 2.15) behave similarly to the distributions of p_{max}, but differ in some details. The distributions of p_{min} at almost all distances, except for the last one, are symmetrical around the mean value without appearance of spikes at high amplitudes. It is seen most clearly from Fig. 2.16b that the maximum observed values of the peak negative pressure in absolute value do not rise higher than 2 times of the p_{min} of the N-wave propagated in the homogeneous medium. On the other hand the minimum observed values are 5-6 times less than in the case of homogeneous air. Accordingly to the described features of statistical distributions, the standard deviation of p_{min} (Fig. 2.16a, blue line, squares) is less by 0.05-0.07 than the standard deviation of p_{max} (Fig. 2.16a, red line, squares). At the same time, the mean value of p_{min} (blue line, circles) decreases as function of the distance r quantitatively similarly to the mean value of p_{max} (red line, circles). The observed differences of p_{max} and p_{min} statistics are explained by the conventional asymmetry of the distorted pulse in focal zones (Fig. 2.12b). While the peak positive pressure of the focused pulse significantly increases, p_{min} is not reaching

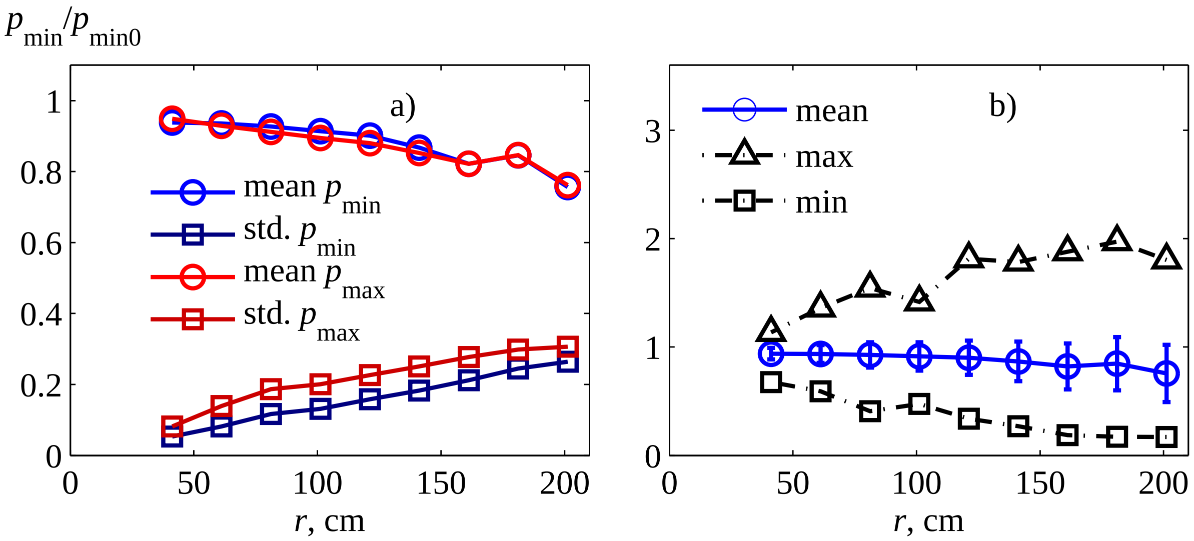

Figure 2.16: Average characteristics of the peak negative pressure, normalized to values in a homogeneous medium $p_{\min}/p_{\min 0}$. The graph shows the mean value (blue line, circle markers) and the standard deviation (blue line, square markers) (a), as well as maximum (triangle markers) and minimum (square markers) values observed in the sample (b). The comparison with normalized peak positive which data are shown by red line is also provided.

high values. Thus, statistically, appearance of large $p_{\min}$ values is not expected. It should be reminded also, that even in homogeneous air the description of the negative peak pressure of the N-waves remains a problem (see chapter 1). In more detail, the choice of an initial waveform for the model which could correctly take into account slight asymmetry of the real N-wave waveform (Fig. 2.11b) is a challenge. So theoretical analysis of the behavior of $p_{\min}$ statistics in the case of turbulent propagation medium should be taken with care.

Pulse half-duration

In chapter 1 the estimation of half-duration based on the N-wave spectrum was proposed. It was appeared to provide good results when compared to theoretical predictions. However, the N-wave propagated through a layer of turbulence is so heavily distorted that this definition of the half-duration can not be successfully applied. To somehow characterize the duration of distorted N-wave, it is necessary to introduce another definition that can be applied both in homogeneous and inhomogeneous propagation cases. It is necessary, that the half-duration obtained according to the old and new definitions for the wave propagating in homogeneous air will be the same.

To estimate half-duration of a pulse a definition based on the evaluation of the temporal moments of the signal can be introduced. If the temporal moments of the signal $p(t)$ are defined as following:

$$M_n = \int_{-\infty}^{+\infty} (t - t_0)^n p^2(t) dt, \tag{2.13}$$

where $n = 0, 1 \ldots \infty$, then the moment M_0 is equal to the energy of the pulse $p(t)$ with a scaling coefficient. The ratio of the first and zeroth moments is called as the arrival time of "center of mass" of the signal: $t_0 = M_1/M_0$. For an ideal N-wave this quantity coincides with the time

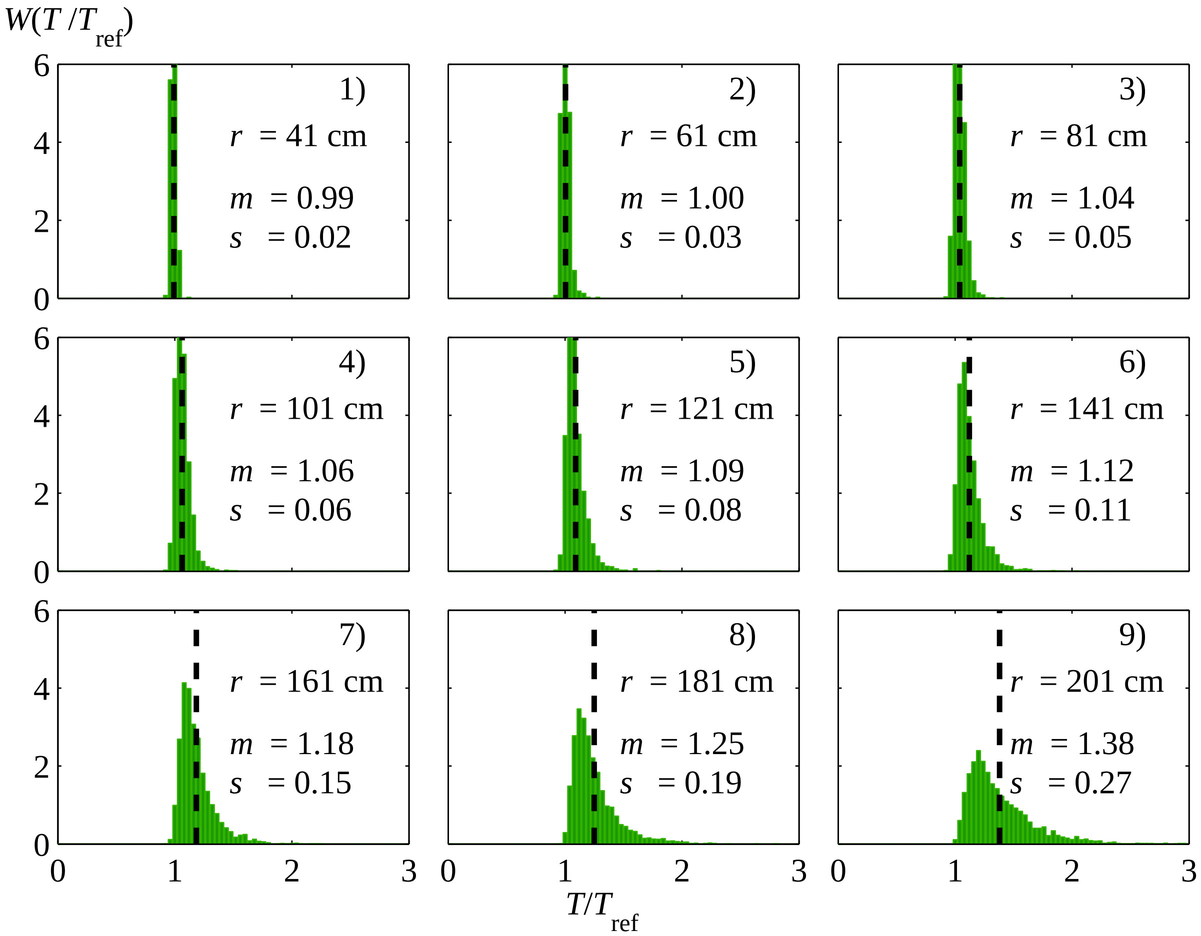

Figure 2.17: Histograms of the statistical distributions of the N-wave duration derived from temporal moments (Eq. 2.13) and normalized to the corresponding values in a homogeneous medium, T/T_{ref}. Black dashed line shows the average value of each distribution. Values for the source-microphones distance r, the mean m and standard deviation s are given on the graphs. Class size is 0.04.

when the signal passes through zero at the back slope. Half-duration of the signal can be determined on the basis of the second moment as $T_2 = \sqrt{M_2/M_0}$. To obtain the half-duration that coincides with the definition based on the waveform or on the spectrum, in the case of the ideal N-wave it is necessary to introduce a correction coefficient: $T = \sqrt{5/3}T_2 = \sqrt{5/3}\sqrt{M_2/M_0}$. However, since the experimental waveforms are somewhat different from the ideal N-wave, better results were obtained using the coefficient 1.33 instead of $\sqrt{5/3} \approx 1.29$. Thus, the half-duration is defined here as $T = 1.33\sqrt{M_2/M_0}$. Note that the analysis of half-duration of distorted waveforms based on temporal moments was not carried out earlier in the laboratory-scale experimental studies (Averiyanov, 2008, Lipkens & Blackstock, 1998a, Ollivier & Blanc-Benon, 2004).

Fig. 2.17 shows the histograms of statistical distributions of the halfduration T, normalized to the corresponding values measured in homogeneous medium, T_{ref}. Thus, the nonlinear lengthening of the pulse is compensated and primarily the effect of the turbulence on the statistical distributions is demonstrated. It is seen from the histogram that the turbulence mainly increase the pulse duration. Short pulses are almost not observed – the minimum measured value is only 0.92 from the pulse half-duration measured in homogeneous medium (Fig. 2.18b). At large propagation distances, pulses such as in Fig. 2.12h can be observed, whose duration is 2-3 times larger than the

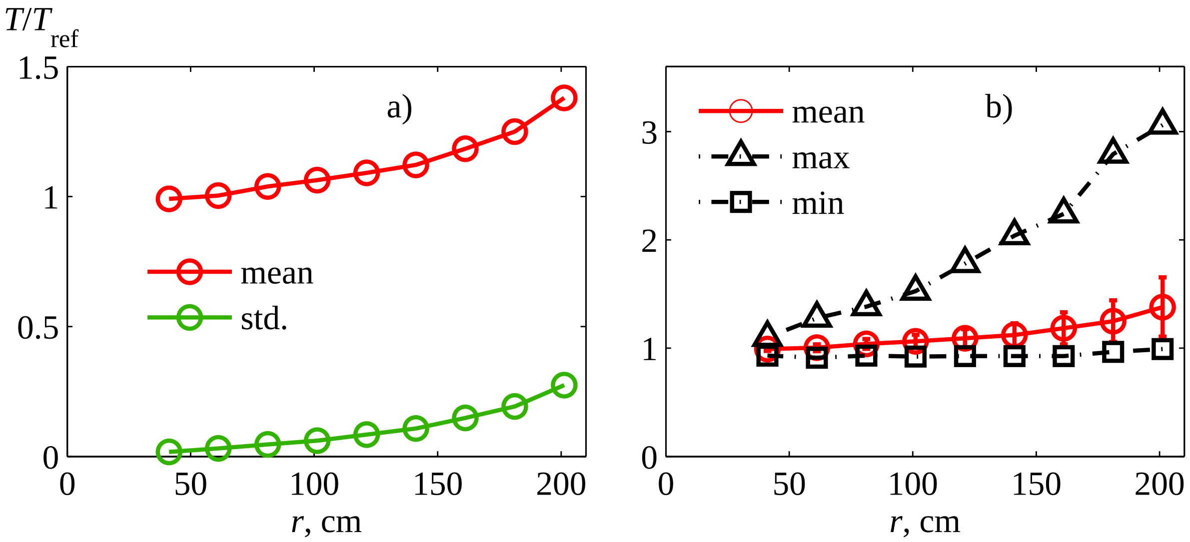

Figure 2.18: Average characteristics of the N-wave duration derived from temporal moments (Eq. 2.13) and normalized to values in a homogeneous medium $T/T_{\rm ref}$. The graph shows the mean value (red line) and the standard deviation (green line) (a), as well as maximum (triangle markers) and minimum (square markers) values observed in the sample (b).

duration of the N-wave in homogeneous medium (Fig. 2.18b). However, the mean duration at the maximum studied distance increased only by 40%. The mean and the standard deviation of the duration tend to grow faster with increasing distance r (Fig. 2.18a), indicating the strengthening of the destructive role of the turbulent medium on the propagating N-wave.

The shock risetime $\tau_{\rm sh}$

As mentioned above, to estimate the risetime of shocks, a method based on the width of the peak of the waveform derivative was used in the current chapter. Since the microphone smooths out shock fronts which have risetime less than 3 μs as shown in chapter 1, then it is useless to normalize the measured risetime on the values obtained in homogeneous media. So the histograms of the risetime are given directly in microseconds (Fig. 2.19). Similarly as in other studies, in which microphones Brüel&Kjær 4138 were used, shocks with risetime less than 2.7 μs are not observed (Averiyanov, 2008). Several spikes with risetime of order of $1-2$ μs at distances $r = 181$ and 201 cm, are related to the noisy waveforms which were not processed correctly. The mean value of the risetime and its standard deviation increase with the propagation distance r (Fig. 2.20a). At $r = 201$ cm the values of the mean 5.5 μs and standard deviation 2.0 μs are found. At larger propagation distances the maximum observed risetime is of 15-20 μs, which is consistent with results obtained in another study where the same risetime definition was used (Averiyanov, 2008). A significant increase of the shock risetime of great part of the strongly distorted waveforms is very important in terms of noise effects of the sonic boom, since the wave with more smooth shock front causes less discomfort (Fidell *et al.*, 2002). Also as for the peak positive pressure, the quantitative difference of the risetime statistics between the two cases of turbulence of different types will be discussed in §2.6.

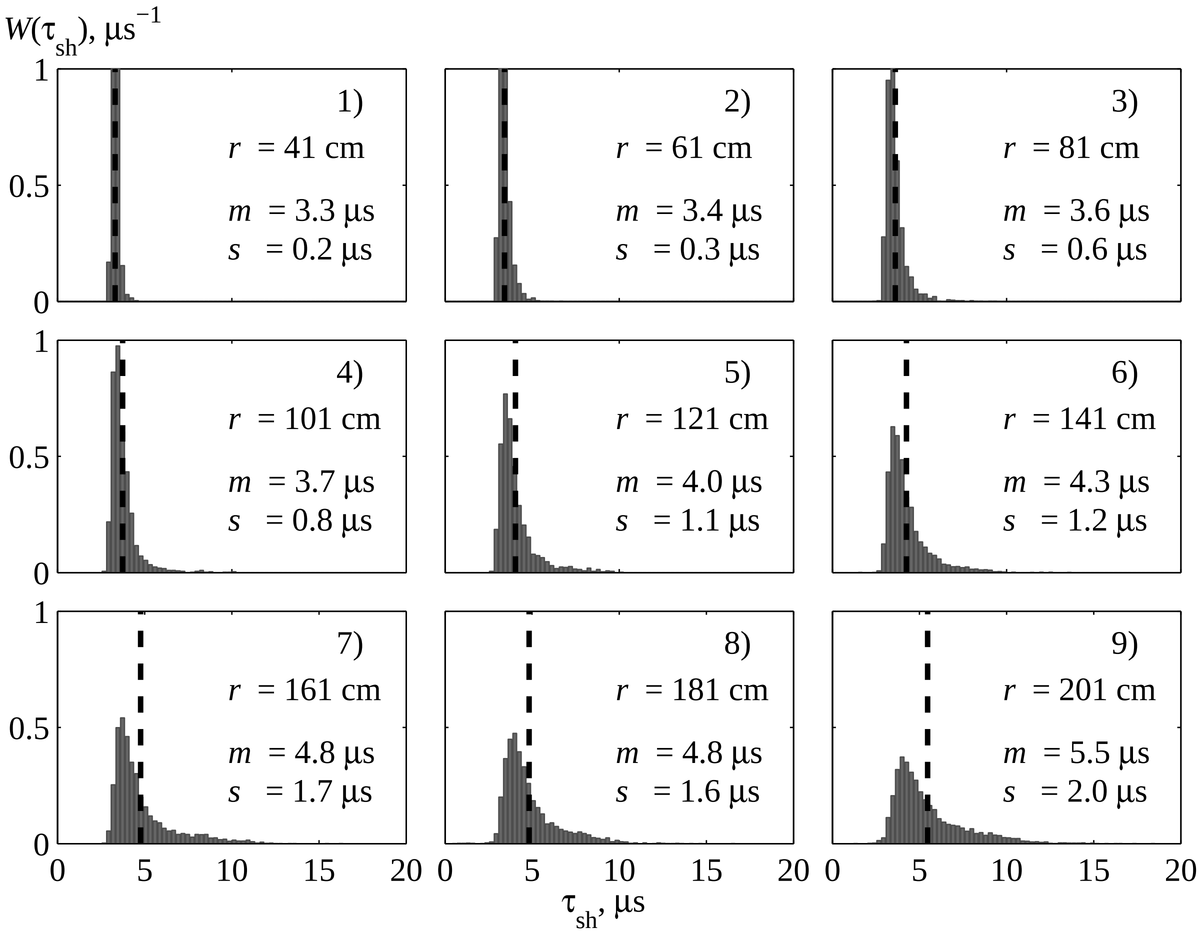

Figure 2.19: Histograms of the statistical distributions of the shock risetime, defined using a peak of the waveform derivative. The data are given in microseconds. Black dashed line shows the average value of each distribution. Values for the source-microphones distance r, the mean m and standard deviation s are given on the graphs. Class size is 0.267 μs.

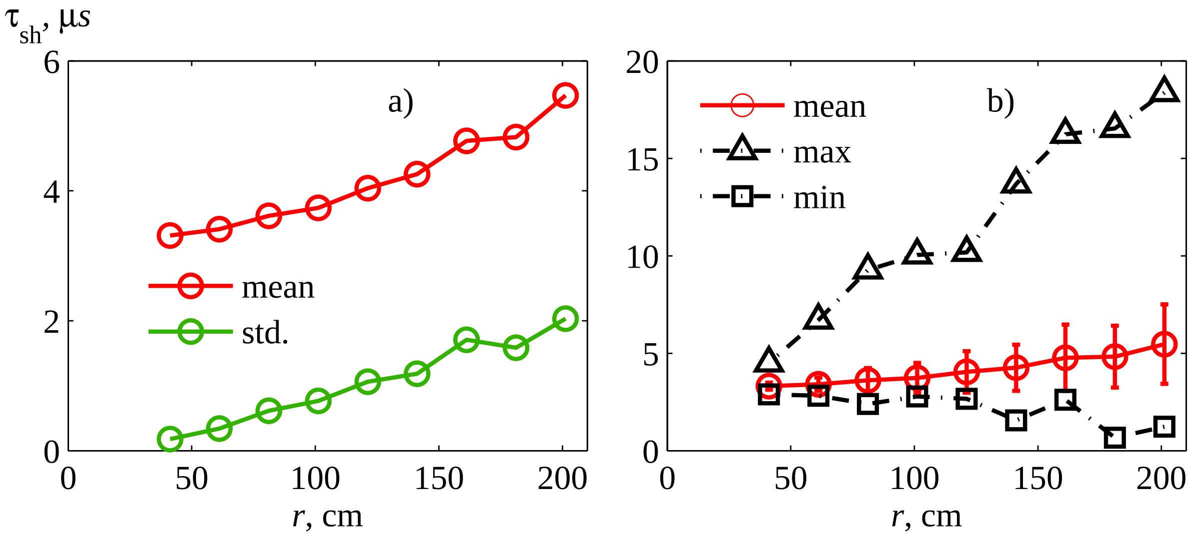

Figure 2.20: Average characteristics of the shock risetime, defined using a peak of the waveform derivative. The graph shows the mean value (red line) and the standard deviation (green line) (a), as well as maximum (triangle markers) and minimum (square markers) values observed in the sample (b).

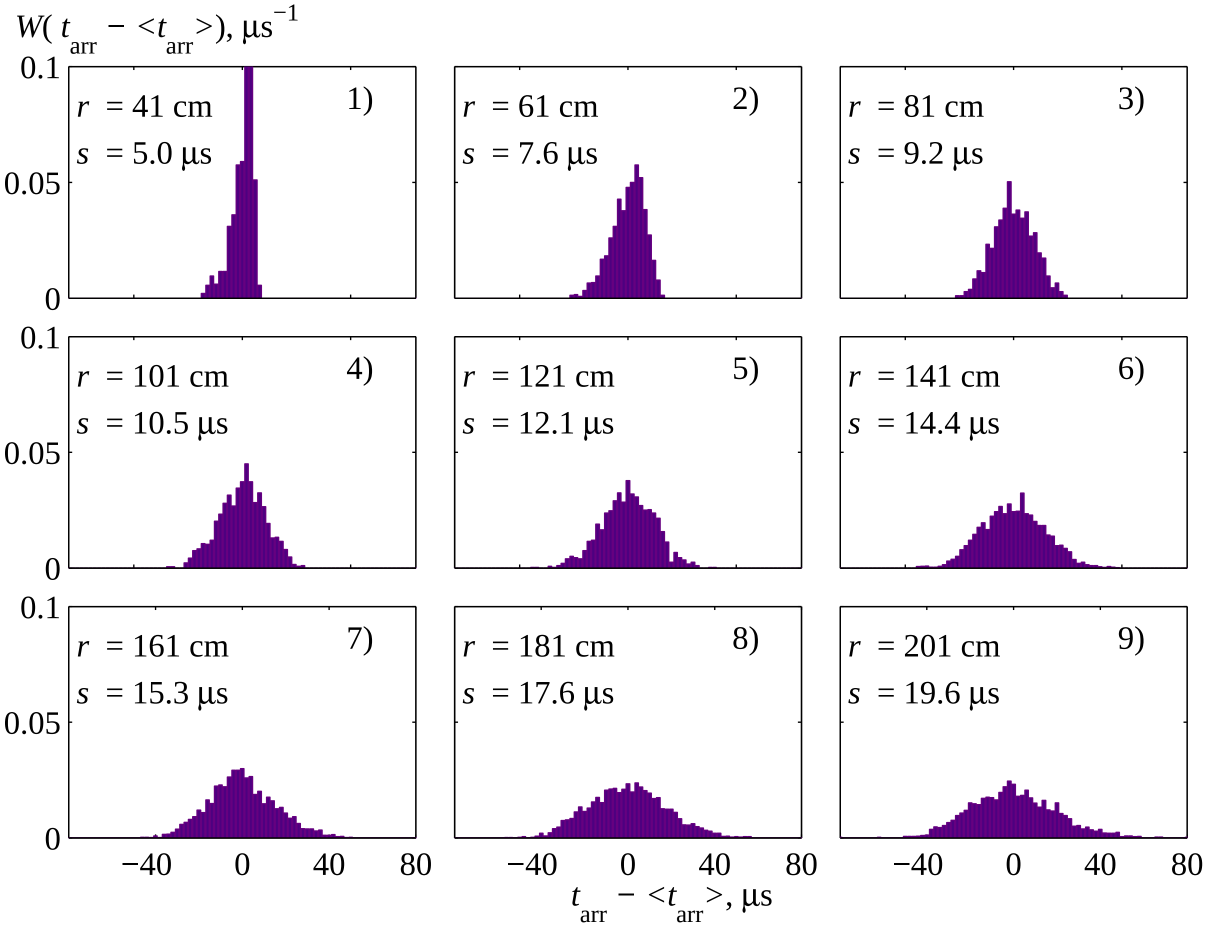

Figure 2.21: Histograms of the statistical distributions of the pulse arrival time with subtracted mean value. The data are given in microseconds. Values for the source-microphones distance r and standard deviation s are given on the graphs. Class size is 2 μs.

Pulse arrival time

In addition to the characteristics that concern the shape of the pulse, it is of interest to pay attention to the arrival time of the pulse. Statistics of the arrival time is a measure of the turbulence impact on the acoustic pulse in the longitudinal direction. Here, the arrival time was defined as the instant when the waveform for the first time crosses the level 5% of the magnitude of the peak positive pressure $p_{\max}$. In the study (Averiyanov, 2008) the difference between statistics of the arrival times obtained in turbulent and homogeneous media was investigated. Since the temperature in the turbulent flow did not change significantly in comparison to the homogeneous medium, corrections were easily taken into account. It was shown that, in the turbulent medium, on the average the pulse arrives earlier than in homogeneous air. In the study presented in this chapter the average sound speed in the turbulence was very different from the sound speed in homogeneous medium and it was non-uniformly distributed in space (Fig. 2.5c). Therefore, it is not useful to compare the difference in arrival times between turbulent and quiet air. For example, in Tab. 2.2 the differences of mean values of arrival times for all distances r are listed, which shows that in the presence of turbulence, due to overall heating of air, the pulse arrives much faster than in homogeneous environment. The observed difference of arrival times of the pulse in uniform and turbulent

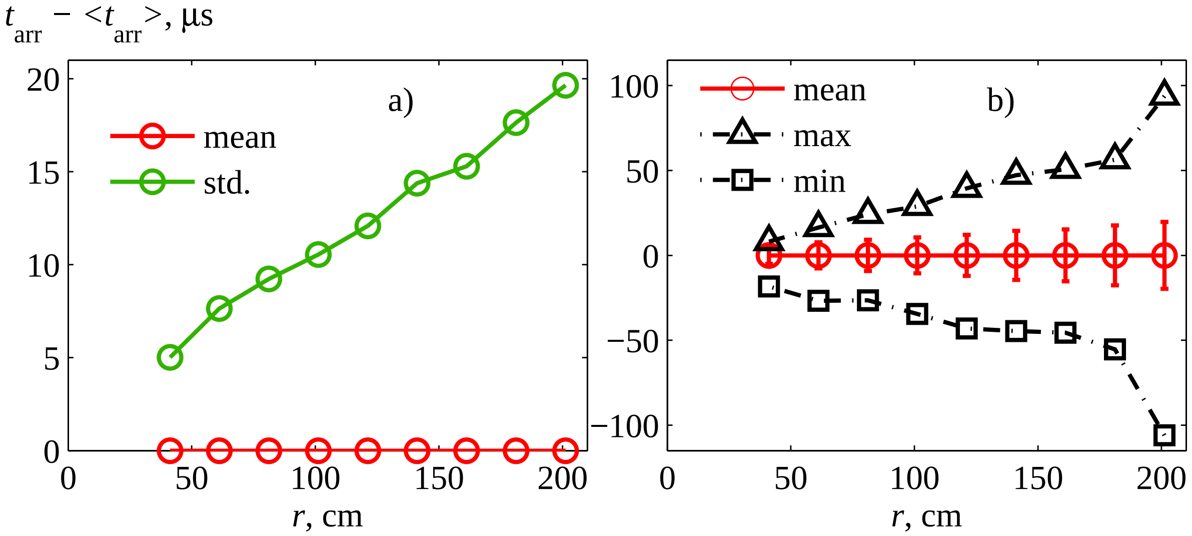

Figure 2.22: Average characteristics of the arrival time. The graph shows the mean value (red line) and the standard deviation (green line) (a), as well as maximum (triangle markers) and minimum (square markers) values observed in the sample (b).

environments greatly exceeds the effect of early arrival of the wave caused only by turbulent inhomogeneities (Averiyanov, 2008). Consequently, histograms in Fig. 2.21 show the arrival time with subtracted mean value: $t_{\mathrm{arr}} - < t_{\mathrm{arr}} >$. Statistical distributions of the arrival time are symmetrical about zero and maximum and minimum observed values symmetrically scattered around zero (Fig. 2.22b). Standard deviation increases with distance almost linearly (Fig. 2.22a) demonstrating gradual accumulation of random distortions. It may be noted that the form of the given distribution functions is close to a Gaussian distribution. This is confirmed by the calculation of the kurtosis which gives values close to 3. In this case, the Gaussian distribution is the consequence of the fact that the random arrival time at the given distance r is a result of large number of random time shifts acquired on each small section of the propagation path. Following the central limit theorem, the resulting arrival time has s Gaussian probability distribution (Rytov *et al.*, 1978).

r, cm	41	61	81	101	121	141	161	181	201
$<t_{\mathrm{arr}}> - <t_{\mathrm{arr0}}>$, μs	-31	-49	-74	-94	-119	-149	-174	-165	-173

Table 2.2: Difference between the arrival time in turbulent and in homogeneous air $<t_{\mathrm{arr}}> - <t_{\mathrm{arr0}}>$.

§2.6 Statistical distributions of N-wave parameters in thermal and in kinematic turbulence

In the previous paragraphs, detailed description of the statistical distributions of various parameters of the N-wave obtained in the experiment with thermal turbulence was presented. The author of the study (Averiyanov, 2008) provided the database of the experiment on the propagation of an N-wave in kinematic turbulence (Fig. 2.23a). In this experiment, measurements were made at

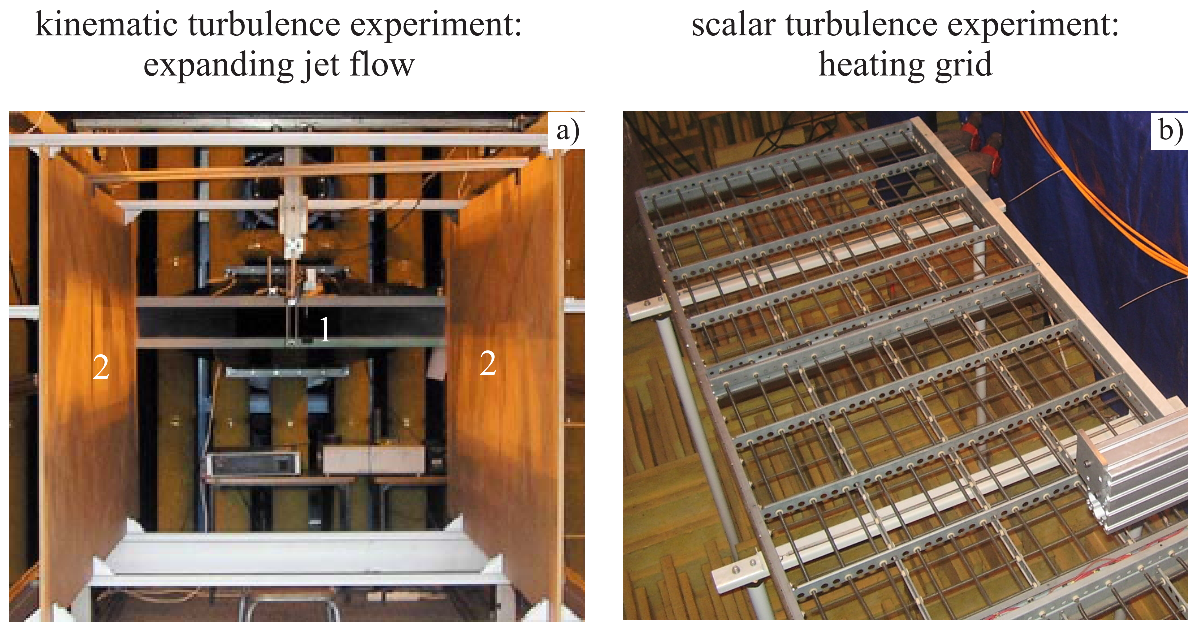

Figure 2.23: Two experiments on N-wave propagation through turbulent media: experiment with jet flow (1) expanded between two wooden baffles (2) – kinematic turbulence case, (a), and experiment with heating grid – scalar turbulence case, (b).

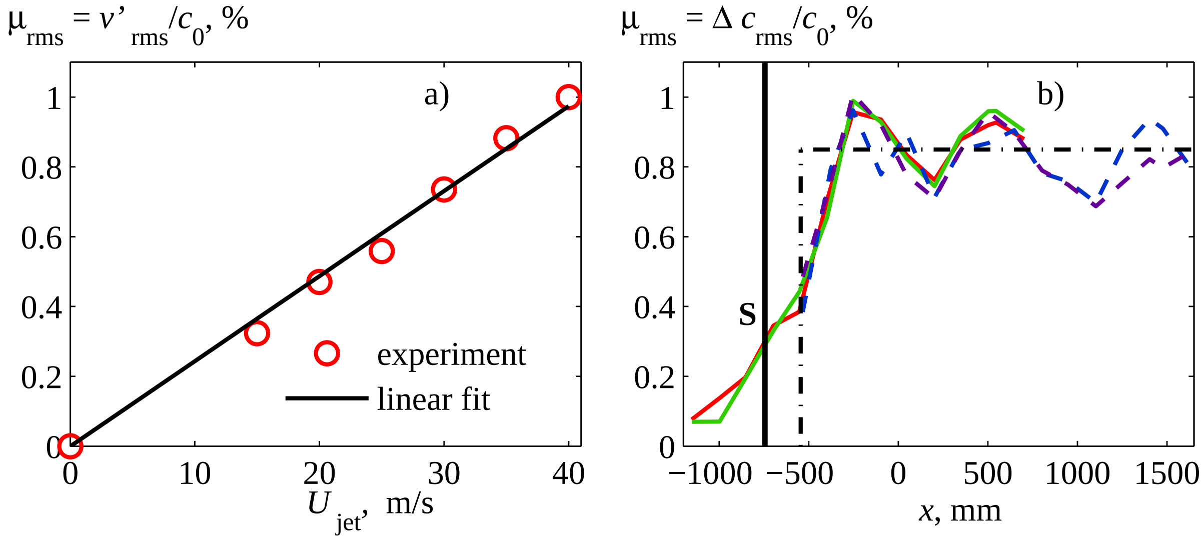

Figure 2.24: The rms fluctuations of the refraction index measured in the experiment with the jet (Fig. 2.23a, U_{jet} is flow velocity at the exit of the jet) and along the N-wave propagation path in the experiment with heating grid (Fig. 2.23b).

different levels of turbulent fluctuations of the refraction index, namely at $\mu_{\mathrm{rms}} = \sqrt{<\mu^2>} = 0.33$, 0.47, 0.56, 0.74, 0.89 and 1% (Fig. 2.24a), in contrast to the experiment presented in this chapter where the turbulence level was fixed (Fig. 2.24b). In the main series of measurements, microphones were placed at a distance of 2.2 m from the spark source, and the width of the fully developed turbulence layer was 1.4 m (Fig. 2.25). The layer was placed in such manner that before and after its edges there were propagation path sections where refraction index fluctuations were equal to zero. The distance from the spark source to the beginning of the turbulent layer was equal to 0.36 m, including $0.10-0.15$ m of transition zone where turbulent fluctuations grow from zero to constant level determined by initial velocity of the jet – U_{jet}. After crossing the turbulent layer the N-wave propagated over 0.43 m before reaching the microphones. In this last part of the propagation path, focusing and defocusing effects continue to modify the pulse waveform due to the distortions of the wavefront, accumulated in the turbulent layer. This effect will be theoretically shown using the phase screen model in chapter 3. Therefore, one can effectively include this last part of the propagation path in overall distance where the N-wave accumulate the waveform distortions. The sum of the turbulent layer width and the length of the last part of the propagation path gives a layer with an "effective" width of 1.8 m. Thus, in both experiments the width of the turbulent layers was approximately the same – 1.8 m, which makes it easy to compare the measurement results obtained in one and in another experiment.

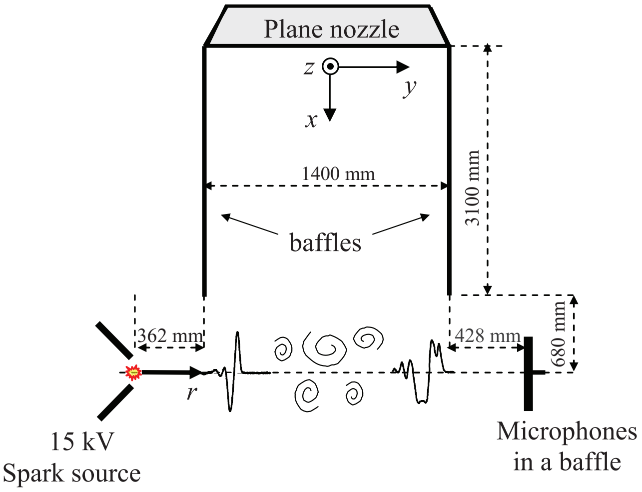

Figure 2.25: Schematic view of the experimental setup of the N-wave propagation experiment through kinematic turbulence.

For the first, the differences and similarities of two turbulent fields are clarified in Fig. 2.26. The one-dimensional spectra expressed in terms of fluctuations of the refraction index μ, measured in these two experiments, are compared in Fig. 2.26a. The experimental data of the spectra are shown with solid lines, and theoretical spectra with dashed lines. Red color corresponds to the kinematic turbulence (vector type) and blue color to the thermal turbulence (scalar type). In the case of kinematic turbulence the spectrum of μ was calculated from the spectrum of the transver-

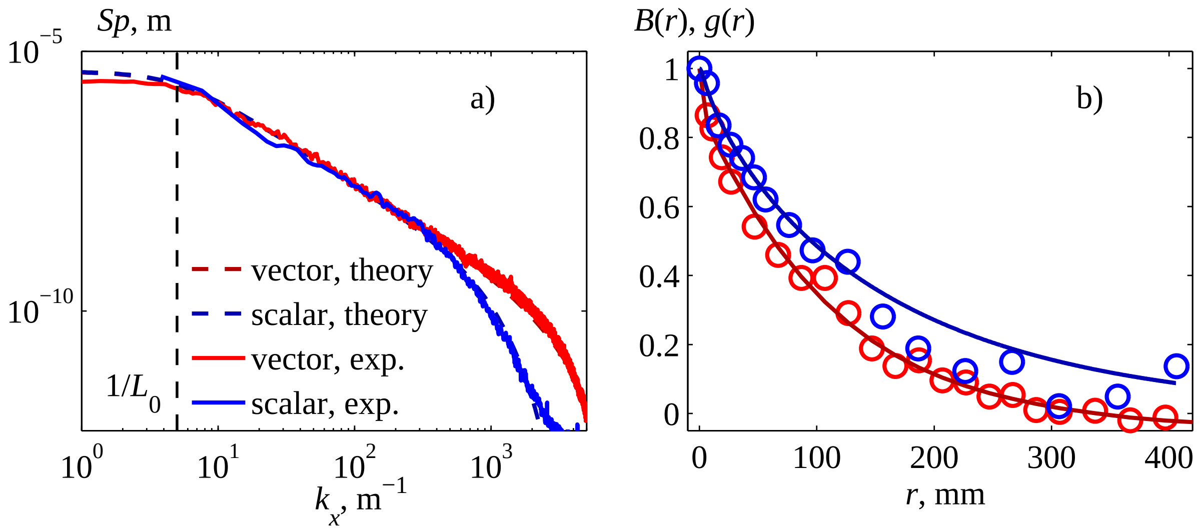

Figure 2.26: Comparison of one-dimensional spectra of vector (red lines) and scalar turbulence (blue lines) (a). Measured spectra are shown by solid lines, and theoretical by dashed lines. Spectrum of kinematic turbulence is normalized to have the same rms as the spectrum of thermal turbulence. Comparison of transversal correlation function of kinematic turbulence with correlation function of thermal turbulence (b).

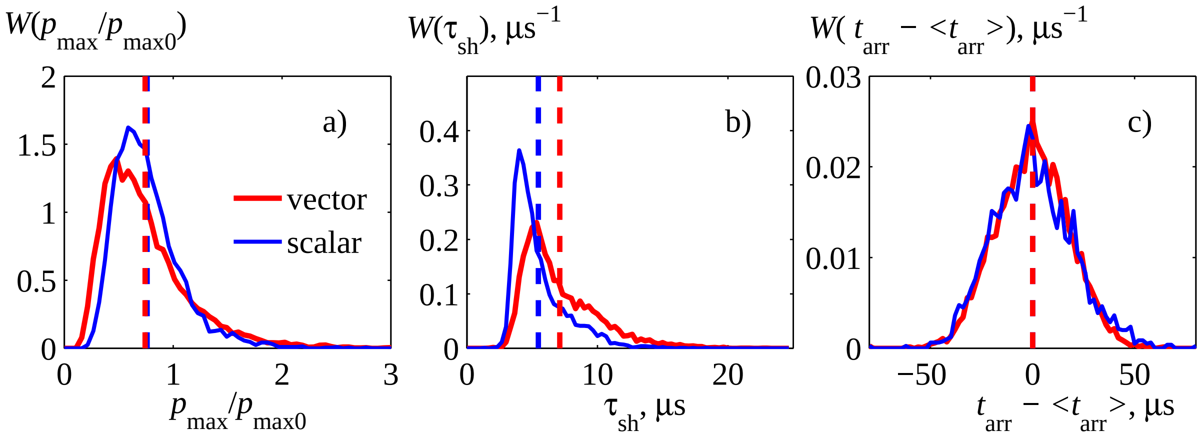

Figure 2.27: Comparison of the probability distributions of the normalized peak positive pressure $P_+ = p_{\max}/p_{\max 0}$ (a), the shock risetime τ_{sh} (b) and the arrival time $t_{\mathrm{arr}} - <t_{\mathrm{arr}0}>$ (c) between the cases of the N-wave propagation in turbulent air flow (red line) and in thermal turbulence (blue line) in the conditions of similar values of the mean-square of the refraction index and length of the propagation path inside the turbulent layer ($\mu_{\mathrm{rms}} = 0.89\%$ and 0.85%, respectively, $r = 1.8$ m).

sal to the mean flow velocity component which was aligned along with the propagation direction of acoustic wave. The presented spectrum data was measured in the case of the rms $\mu_{\mathrm{rms}} = 1\%$ and was normalized in Fig. 2.26a in order to have the same μ_{rms} as the thermal turbulence spectrum, which was 0.9% for the given measurement point. It is seen from the figure, that the two 1D spectra are close inside inertial range of scales and both are in good agreement with modified von Kármán model spectra (either scalar or vector types) with the outer scale $L_0 = 20$ cm. The inner scales of the spectra are different: 5 mm for the thermal turbulence and 1.3 mm for the kinematic turbulence. However, this difference of inner scales is not critical, since the amplitude of the corresponding inhomogeneities is very small in comparison to the most important large-scale inhomogeneities of the scale L_0. The ratio of characteristic amplitudes of these inhomogeneities is about 0.01. Moreover, such small inhomogeneities cannot produce efficient focusing of the used N-wave which has the typical wavelength of about 15-20 mm.

Experimental evidence of different structure of the turbulent fields in the plane transversal to the propagation path is demonstrated in Fig. 2.26b. In this figure the measured (circles) and theoretical (solid line) transversal correlation functions of the kinematic turbulence are shown by red color and are compared with the the thermal turbulence correlation function shown in blue. It should be reminded that for isotropy scalar turbulence its correlation function is the same in longitudinal and transversal directions. It is seen, that the kinematic turbulence has shorter transversal correlation, which is in agreement with theory, discussed previously in §2.2.

Let us first consider series of measurements, where the rms values of the refractive index fluctuations μ_{rms} in both experiments are approximately the same (0.85% and 0.89%). For this case, in Fig. 2.27, the statistical distribution functions for the normalized peak pressure $P_+ = p_{\max}/p_{\max 0}$ (a), the shock risetime τ_{sh} (b) and the arrival time $t_{\mathrm{arr}} - <t_{\mathrm{arr}}>$ (c) are compared. Additionally, in Tab. 2.3 the mean and standard deviation for these variables, as well as the probability of exceeding thresholds of the normalized peak pressure equal to 1, 1.5 and 2 are presented. From the results it is evident that for the same average value, the distribution function of the peak positive pressure in the case of kinematic turbulence is wider (Fig. 2.27a) and has higher standard deviation (compare lines no. 1 and no. 2 in Tab. 2.3). The most important differences can be noted by comparing the probability of exceeding the thresholds specified above for the peak pressure. For example, the probability of exceeding the amplitude in homogeneous medium, $P_{+,1}$, is about the same (17.8% and 20.1%). However, for higher thresholds 1.5 and 2 the kinematic turbulence gives a 2-3 times greater probability (see $P_{+,1.5}$ and $P_{+,2}$) than the thermal turbulence. Thus, kinematic turbulence is much more effective in terms of the appearance of intense focusing. The probability of doubling the amplitude in this case is more than 1%. Meanwhile the kinematic turbulence also leads to more efficient smoothening of the shock front (Fig. 2.27b). The corresponding distribution function (red line) is shifted toward larger values of τ_{sh}, has larger mean value and standard deviation than the distribution function in the case of the thermal turbulence (blue line). It is interesting that the distribution functions of the arrival time are almost identical (Fig. 2.27c) and their standard deviation differs by only 10%. This means that in the longitudinal direction, the influence of both turbulent fields in these two cases was roughly the same. In line no. 3 of Tab. 2.3 the data for slightly lower level of vector fluctuations ($\mu_{\text{rms}} = 0.74\%$) confirm the conclusion.

turb. type, μ_{rms}	$<P_+>$	δP_+	$<\tau_{\text{sh}}>$	$\delta\tau_{\text{sh}}$	δt_{arr}	$P_{+,1}$, %	$P_{+,1.5}$, %	$P_{+,2}$, %
1 scalar, 0.85% ○	0.762	0.31	5.5	2.0	19.6	17.8	2.9	0.4
2 vector, 0.89% ○	0.743	0.40	7.1	2.8	17.9	20.1	5.1	1.3
3 vector, 0.74% ○	0.790	0.40	6.9	2.7	15.4	23.6	6.1	1.5
4 vector, 0.33% ○	0.965	0.31	5.6	1.8	8.3	38.5	5.8	0.7

Table 2.3: Comparison of the main characteristics of statistical distributions of the normalized peak positive pressure $P_+ = p_{\text{max}}/p_{\text{max0}}$, the shock risetime τ_{sh} and the arrival time $t_{\text{arr}} - < t_{\text{arr0}} >$. Cumulative probability $W(P_+ > \alpha)$ of exceeding some value α was denoted here as $P_{+,\alpha}$

.

The available results also allow us to consider cases with comparable degree of distortion of the N-wave characteristics in turbulence fields of two different types. For example, in Fig. 2.28, similar to the Fig. 2.27, the distribution functions obtained in the case of the thermal turbulence (blue line) are compared with the functions in a case of kinematic turbulence at $\mu_{\text{rms}} = 0.33\%$ (green line), i.e. with 2.6 times smaller intensity of turbulent fluctuations. In Tab. 2.3 relevant data are shown in line no. 4. Although the average peak pressure differs, the width of the distributions, defined by the standard deviation, is the same ($\delta P_+ = 0.31$). Nevertheless, as in the previous case, the probabilities of observing N-waves with large amplitudes, $P_{+,1.5}$ and $P_{+,2}$, in the kinematic turbulence case are 2 times greater than in the scalar turbulence case. For the shock risetime, the distribution functions were found to be very close each to another (Fig. 2.28b). The effect of turbulence in the longitudinal direction quantified by the standard deviation of the arrival time for the considered case of kinematic turbulence is 2.4 times smaller than in the thermal turbulence case. Thus, comparable level of distortions of the N-wave propagating in the kinematic turbulence is achieved at significantly lower rms values μ_{rms} of the refractive index fluctuations than in thermal turbulence (by 2-3 times).

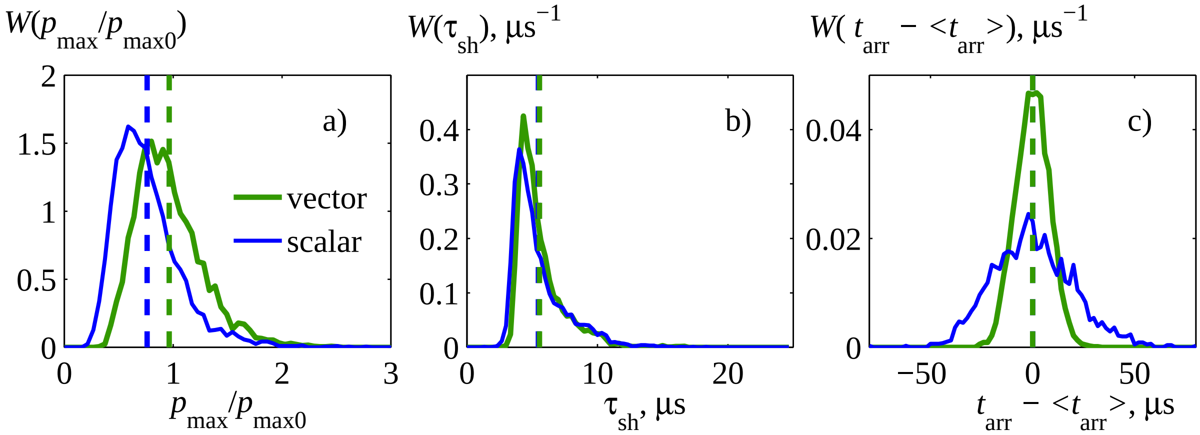

Figure 2.28: Comparison of the probability distributions of the normalized peak positive pressure $P_+ = p_{\rm max}/p_{\rm max0}$ (a), the shock risetime $\tau_{\rm sh}$ (b) and the arrival time $t_{\rm arr} - < t_{\rm arr0} >$ (c) between the cases of the N-wave propagation in turbulent air flow (green line) and in thermal turbulence (blue line) in the conditions of similar degree of statistical distortions of P_+ and $\tau_{\rm sh}$. For the vector turbulence case the results of measurement series with $\mu_{\rm rms} = 0.33\%$ are shown.

§2.7 Conclusions

Propagation of high amplitude and short duration N-pulses (40 μs duration and amplitude of 1100 Pa at 20 cm from the source) with spherical wavefront was investigated experimentally in thermal turbulence produced by a heating grid. Mapping of the turbulent field both in the horizontal and vertical planes near the source-microphones path was carried out and the main parameters of temperature fluctuations were determined. It is shown that in the zone of fully developed turbulence the measured spectra of refraction index fluctuations are well described by the von Kármán model spectrum with the following parameters: outer scale $L_0 = 20$ cm, inner scale $l_0 = 5$ mm, and mean-square fluctuation of the refractive index $\mu_{\rm rms} = 0.85\%$. Statistical distributions and average values of the most important parameters of the N-wave were investigated as functions of increasing propagation distance from the source to the microphones in the range from 0.4 m to 2 m, which corresponds to the width of the turbulent layer from 0.2 m and up to 1.8 m. A method to determine the duration of the distorted N-waves based on computing time integral moments of the pulse was proposed. Classical effects of broadening the probability distributions of the N-wave parameters (peak pressures, shock rise time, and arrival time) and trends for the mean and standard deviation with increasing propagation distance were demonstrated (Lipkens & Blackstock, 1998a, Blanc-Benon *et al.*, 2002, Averiyanov *et al.*, 2011, Yuldashev *et al.*, 2010c). For the new investigated parameter, i.e. for the pulse duration, the possibility of an increase by 2-3 times in comparison with corresponding values in homogeneous medium was shown. The appearance of strong focusing in the caustics, where the amplitude of the pulse is more than 3 times greater than the amplitude in homogeneous media, and the waveform is U-shaped was also noted.

The results of the present experiment were compared to the previously reported results on statistical distortions in the experiment on N-wave propagation in kinematic turbulence (Averiyanov, 2008). For similar conditions in terms of acoustic source and turbulence parameters (characteristic scales, turbulence levels μ_{rms} and spectra, propagation distance in the turbulence) it is shown that kinematic turbulence leads to much stronger distortions of the peak pressure and the shock rise time of the N-wave. In addition, the kinematic turbulence was shown to be much more efficient in terms of appearance of strong focusing: in comparison to the case of thermal turbulence, it produces 2-3 times greater cumulative probability for the peak positive pressure to exceed two times the amplitude of the N-wave propagated in homogeneous air. Kinematic turbulence also leads to stronger smearing of the shock front. Comparable distortions of the peak pressure and the shock rise time are achieved in the kinematic turbulence at much lower values of the refraction index rms μ_{rms} (2.5 times lower) than in the thermal turbulence. In perspective, the obtained results of comparison between two experiments should be validated using numerical modeling of N-wave propagation at least in 2D geometry.

Chapter 3

Statistical properties of nonlinear diffracting N-wave behind a random phase screen

§3.1 Introduction

A model of an infinitely thin random phase screen has been widely used as a simplified approach to study various problems of linear and nonlinear wave propagation in random inhomogeneous media (Dubrovskii *et al.*, 1996, Gusev & Rudenko, 2006, Rudenko & Enflo, 2000, Martin & Flatte, 1988, Shlenov & Kandidov, 2004). Contrary to the continuous inhomogeneous medium the phase screen model incorporates only initial distortion of the phase front of the wave. However, this model includes basic effects of nonlinear propagation and random focusing that lead to distortion of statistical characteristics of the wave field in randomly inhomogeneous medium. Propagation of high intensity noise through turbulent layers in the atmosphere is an example of where the phase screen model may be implemented. An ideal symmetrical N-wave is often used as an initial waveform of noise wave generated by the supersonic aircraft (Blanc-Benon *et al.*, 2002, Averiyanov, 2008, Lipkens & Blackstock, 1998a).

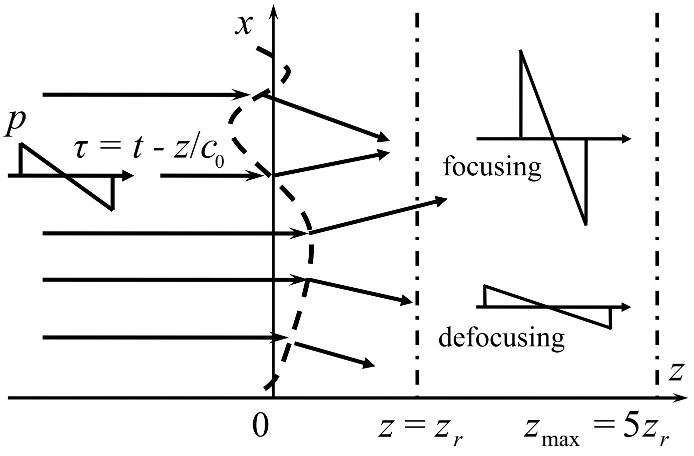

Figure 3.1: Propagation of initially plane N-wave through infinitely thin phase screen (dashed line) located at $z = 0$. Arrows illustrate focusing and defocusing effects behind the screen. The refraction length is denoted as z_r, maximum propagation distance in numerical simulations is $z_{\max} = 5z_r$.

Until now, the statistical properties of nonlinear N-waves behind a random phase screen were studied in detail using nonlinear geometrical acoustics (NGA) approximation (Dubrovskii *et al.*, 1996, Gusev & Rudenko, 2006, Rudenko & Enflo, 2000). The geometry of the problem in case of a one-dimensional screen is illustrated in Fig. 3.1. Initially plane N-wave propagates along the coordinate z perpendicular to the screen located at $z = 0$ (Dubrovskii *et al.*, 1996). At each transverse coordinate x the phase screen introduces a random time delay that leads to the distortion of the wave front. In NGA approach the spatial fluctuations of the time delay define areas of converging and diverging rays, i.e. focusing and defocusing of the wave (Fig. 3.1). Ray convergence corresponds to focusing, i.e. to the increase of the wave amplitude, and ray divergence corresponds to defocusing, i.e. decrease of the wave amplitude.

In NGA approximation the statistical properties of acoustic field behind the screen depend on the probability distribution function of ray convergence after passing the screen and the initial wave amplitude that determines nonlinear propagation effects. Analytic solutions have been obtained for probability distributions and mean values of the amplitude and duration of an N-wave after passing through one-dimensional phase screen having either broadband or narrowband Gaussian probability distribution of ray convergence (Dubrovskii *et al.*, 1996). The problem was further extended and analytic solutions were obtained for non-perpendicular angle of incidence of a wave on the phase screen and for two-dimensional phase screens (Gusev & Rudenko, 2006, Rudenko & Enflo, 2000). The advantage of the NGA approach to this problem is that analytic solutions are available and basic physical effects can be clearly seen. However, some restrictions of the solutions call for developing of more general approaches. Here some of them are listed. The NGA solutions are valid only at the distances before first caustics occur, i.e. some of the ray tube areas vanish to zero. Nonlinear amplitude dependence of the propagation speed of the N-wave shock front leads to additional distortions of the wave front in space; this effect may be considered within the NGA formulation, but the exact solution has not yet been obtained. The effects of diffraction are not included and therefore the wave keeps the N-waveform, although more variability of distorted waveforms like U-wave or double peaked and rounded waves may be expected (Lipkens & Blackstock, 1998a, Averiyanov, 2008). Spatial pattern of the acoustic field behind the screen depends not only on the ray convergence probability function, but also on the characteristic size of the phase variations introduced by the screen. For small size random variations of the phase, focusing will occur from smaller spatial areas of the screen surface and for bigger size variations - from bigger apertures. If diffraction effects are of concern, for the same ray convergence, i.e. focal length to the caustics, the focusing gain in these two cases will be higher for bigger scale fluctuations. More statistical properties of the screen, in addition to the ray convergence distribution, therefore are necessary to adequately account for the diffraction effects while propagating through caustics.

In this chapter, a model based on the numerical solution of the Khokhlov-Zabolotskaya-Kuznezov (KZK) equation is considered. This model accounts for the combined nonlinear and diffraction effects and makes it possible to consider wave propagation through and beyond caustics. Extended form of this equation is widely used in applications to the atmosphere acoustics to study propagation of finite amplitude acoustic waves in inhomogeneous media with continuous variations in space (Averiyanov *et al.*, 2006). Here, numerical simulations of N-wave propagation behind random realizations of one-dimensional screen are performed up to large distances further than the distance of occurrence of first caustics. Statistical properties of the phase screen are characterized by the phase probability distribution and by the spatial correlation function. The results of modeling are statistically analyzed and compared, where it is possible, with those calculated in nonlinear geometrical acoustics approximation (Dubrovskii *et al.*, 1996, Rudenko & Enflo, 2000).

§3.2 Numerical model of N-wave propagation through caustics

The phase screen model is used here only to set initial time delays of the N-wave. The KZK equation for the wave propagation behind the screen in the homogeneous medium can be written in dimensionless form as follows:

$$\frac{\partial}{\partial \theta}\left[\frac{\partial P}{\partial Z} - NP\frac{\partial P}{\partial \theta} - A\frac{\partial^2 P}{\partial \theta^2}\right] = \frac{1}{4\pi}\frac{\partial^2 P}{\partial X^2}. \tag{3.1}$$

Here $P = p/p_0$ – is the acoustic pressure, normalized by the N-wave initial amplitude p_0, $Z = z/\lambda$ – is the propagation distance, and $X = x/\lambda$ – the transverse spatial coordinate normalized by the N-wave length $\lambda = c_0 T_0$, c_0 – is the ambient sound speed, $\theta = 2\pi\tau/T_0$ – the dimensionless time, normalized by the initial duration of the N-wave T_0, $\tau = t - z/c_0$ – is the retarded time. Fluctuations of the time delay are introduced at $z = 0$. Dimensionless parameters in Eq. (3.1) are introduced as $N = 2\pi\varepsilon p_0/c_0^2\rho_0 = \pi\lambda/z_n$ – nonlinear parameter, where $z_n = T_0 c_0^3\rho_0/2\varepsilon p_0$ is the characteristic nonlinear distance at which the amplitude of the plane N-wave decreases by a factor of $\sqrt{2}$, ε is the nonlinearity coefficient of the propagation medium, $A = 2\pi^2\delta/T_0 c_0^2 = \lambda/z_a << 1$ – is the thermoviscous dissipation parameter, where δ – is the coefficient of the diffusivity of sound and $z_a = c_0^3 T_0^2/2\pi^2\delta$ is the characteristic absorption distance.

Single N-wave with a random time delay $2\pi\Psi$ at each transverse coordinate is considered as a boundary condition, i.e. $P(Z = 0, \theta, X) = P_0(\theta - 2\pi\Psi)$, where $P_0(\theta)$ is the N-wave of the duration equal to 2π. Phase shift $\Psi(X)$ in each simulation is a one particular random realization of the phase screen. Since weak dissipation is taken into account in the modeling, shock front of the N-wave is not infinitely thin. The rise time of initial N-wave is defined here similarly as in the Chapter 1 – it is the time required for the pressure to increase from 10% to 90% of the maximum peak pressure. Defining the function $P_0(\theta)$ as

$$P_0(\theta) = \frac{\theta}{2\pi}\left[\tanh\alpha(\theta - \pi) - \tanh\alpha(\theta + \pi)\right], \tag{3.2}$$

where $\alpha = N/4A$, the N-wave with the rise time $\theta_{\text{sh}} \approx 11A/N$ corresponding to the quasi-stationary solution of the Burgers equation is produced automatically. As a result of shocks smoothing, peak pressures in the initial N-wave are slightly smaller than that of the ideal one. However, this difference does not exceed 8% for the simulation parameters used in this work.

Numerical solutions to the Eq. (3.1) are obtained using an algorithm developed previously in a study (Averiyanov *et al.*, 2006). This numerical time domain algorithm is based on the method of fractional steps with a first-order operator-splitting procedure, so that nonlinear, absorption, and diffraction effects are applied sequentially over a grid step in the propagation coordinate. Diffraction and absorption operator are solved using Crank-Nicolson finite difference method and nonlinear operator – using conservative Godunov-type algorithm (Averiyanov, 2008, Kurganov & Tadmor, 2000). A boundary condition at the edges of the transverse spatial grid $X = 0$ and $X = L$, where L is the length of the screen, is chosen as $\partial P/\partial X = 0$ (rigid wall). To control reflections from the boundaries the fluctuations introduced by the phase screen at $z = 0$ are smoothed to zero in the vicinity of the boundaries, so that the N-wave has a plane wave front in the regions $[0\ L_0]$ and $[L - L_0\ L]$, where $L_0 << L$ is a size of transition zone. The computational domain in the transverse coordinate is chosen large enough in order, fist, to avoid undesirable reflections from the boundaries at the propagation distances considered and, second, to have sufficiently large working region for computation of statistical distributions with acceptable error.

Typically, numerical simulations are performed for a random phase screen with the length equal to 1000λ and up to the distances of several nonlinear lengths, the time window changes from $\theta = -16$ to $\theta = 38$, which yields approximately 8.5 periods of the initial N-wave. Numerical steps are chosen according to the considered dimensionless parameters in the Eq. (3.1). In the case of absorption parameter equal to $A = 1.5 \times 10^{-4}$ and nonlinearity parameter equal to $N = 0.05$, the numerical step along the transverse coordinate is equal to $h_X = 0.0125$, time step is equal to $h_\theta = 0.007$ and numerical step in the propagation direction is equal to $h_Z = 0.025$. The dissipation parameter A is chosen in the way to resolve the shock front for the range of nonlinear parameters N considered here and the given time step. Physically, the chosen value of the dissipation parameter A corresponds to the propagation of N-waves with $50\ \mu$s duration produced by the spark source and described in two previous chapters.

§3.3 Phase screen model with different scales of inhomogeneities

Statistical properties of continuous randomly inhomogeneous media depend on a spatial power spectrum of fluctuations. The spatial power spectrum of the phase screen is usually derived from the spectrum of continuous random medium thus retaining its characteristic properties. To model the atmospheric turbulence the von Karman, Kolmogorov, and Gaussian power spectra are commonly used (Rytov *et al.*, 1978, Tatarskii, 1971). Kolmogorov energy spectrum describes turbulent energy distribution inside the inertial interval enclosed between outer and inner scales, but does not give information about spectrum distribution outside this region. A more realistic model is the von Karman model. It is a two scale model that, in addition to the inertial interval, describes turbulent energy behavior at small wave numbers and its dissipation at large wave numbers. For atmospheric turbulence, the ratio between the internal and external scales is very small (order of 10^{-4}) (Lipkens & Blackstock, 1998a, Vorontsov *et al.*, 2008) and this impose some restrictions to the wave propagation modeling. The small turbulent structures in the Kolmogorov or von Karman spectra which are smaller than the acoustic wavelength produce backward scattering which is not taken into account in the KZK equation. In the modeling using parabolic equation, therefore, a spectrum should be used, in which small scale fluctuations, less than the wave amplitude, are suppressed.

Spatial energy spectrum of the Gaussian shape describes fluctuations of one characteristic scale. If this scale is chosen equal to the outer scale of a real turbulence, small scale inhomogeneities are suppressed, thus retaining the validity of the parabolic approximation. Although Gaussian spectrum does not exactly correspond to a realistic atmospheric turbulence, it is very a convenient and is widely used model (Shlenov & Kandidov, 2004, Martin & Flatte, 1988, Blanc-Benon *et al.*, 2002). In this work the scope of research was also restricted by Gaussian spectrum, which is sufficient for the aim to investigate the effect of the inhomogeneity scale on the N-wave propagation regardless multiple scales phenomena.

Random realizations of the phase screen were obtained using well-known method of filtering white Gaussian noise to fit the second-order statistics of the random phase (Shlenov & Kandidov, 2004, Martin & Flatte, 1988, Vorontsov *et al.*, 2008). In this method the amplitude of each harmonic of the discrete Fourier spectrum of the function $\Psi(X)$ is taken as δ-correlated pseudorandom normally distributed complex number, multiplied by the spectrum factor $\sqrt{G(k = n\Delta k)\Delta k}$, where

$$G(k) = G_0 \exp\left(-k^2 l^2/2\right) \tag{3.3}$$

is the Gaussian power spectrum density of the screen $\Psi(X)$, G_0 is the amplitude of the spectrum, l is the correlation length of the screen or the characteristic spatial scale of phase inhomogeneities, n - the number of discrete spatial harmonic, Δk – the discretization step between the harmonics. Then the inverse discrete Fourier transform is performed and yields two statistically independent realizations of the phase screen, which are the real and imaginary parts of the transformation result. The phase fluctuations $\Psi(X)$ have Gaussian statistics with zero average value and standard deviation D_0:

$$W(\Psi) = \frac{1}{\sqrt{2\pi D_0^2}} \exp\left(-\frac{\Psi^2}{2D_0^2}\right) \tag{3.4}$$

The second spatial derivative of the phase, $\partial^2\Psi/\partial X^2$, determines the convergence of the ray tube at each transverse coordinate X and also has Gaussian distribution law (Dubrovskii *et al.*, 1996):

$$W(\Psi'' = \partial^2\Psi/\partial X^2) = \frac{1}{\sqrt{2\pi D_2^2}} \exp\left(-\frac{\Psi''^2}{2D_2^2}\right) \tag{3.5}$$

The inverse value of the standard deviation D_2 of the distribution, Eq. (3.5), is the characteristic refraction length, $Z_r = 1/D_2$, which is the distance from the phase screen where most of the first caustics occur. Since the KZK equation well describes only paraxial wave propagation and small angles of diffraction (Tjotta *et al.*, 1991), the refraction length in simulations is chosen sufficiently large in comparison to the N-wave wavelength and the correlation length: $Z_r = z_r/\lambda = 63$.

In the solutions, obtained using NGA approach, all statistical properties of nonlinear acoustical field at a chosen distance from the screen depend only on the ratio between characteristic refraction Z_r and nonlinear $Z_n = z_n/\lambda$ lengths (Dubrovskii *et al.*, 1996, Gusev & Rudenko, 2006). If diffraction effects are taken into account, additional parameter, especially the ratio of the N-wave length and the correlation length of the phase screen is of importance. Gaussian power spectrum density, Eq. (3.3), is characterized by two independent parameters: the amplitude G_0 and the correlation length l. According to the basic properties of Gaussian processes, the characteristic refraction length Z_r is related to the chosen parameters G_0 and l as:

$$Z_r^2 = \frac{l^5}{3\sqrt{2\pi}G_0} \tag{3.6}$$

Two typical phase screen realizations with the same characteristic refraction length Z_r but different correlation lengths are presented on the left side in Fig. 3.2. Correlation lengths are normalized by the length of an initial N-wave. The realization, Fig. 3.2a, has the correlation length $l = 3$, and the realization, Fig. 3.2b, has twice bigger spatial scale, $l = 6$. The choice of the spatial scales of fluctuations corresponds to the experimental data for the real atmosphere (Lipkens & Blackstock, 1998a). It is seen that the phase fluctuations of the second screen (Fig. 3.2b) with larger spatial variations are bigger in amplitude than those of the screen with smaller scale variations (Fig. 3.2a). It can be easily explained using the basic properties of the Gaussian processes. The amplitude of phase fluctuations is proportional to the dispersion D_0, Eq. (3.4), which satisfies the relation $D_0 = \sqrt{2\pi}G_0/l$ in the case of the Gaussian spectrum Eq. (3.3). Substituting this relation into the Eq. (3.6) and eliminating the spectrum amplitude G_0, it can be obtained that $D_0 = l^2/Z_r\sqrt{3}$, i.e. the dispersion of phase fluctuations is proportional to the square of the correlation length. Phase fluctuations from the second screen are therefore 4 times intensive than those from the first one, which is observed in Fig. 3.2. In the NGA approach these two phase screens of the same refraction length are equivalent in statistical sense and produce equivalent statistical solutions for the N-wave amplitude. However, if diffraction effects are considered, the solutions will be different. For example, phase fluctuations that are spatially bigger should produce stronger focusing in caustics.

§3.4 Typical spatial distributions of N-wave amplitude and waveform distortions behind a phase screen

3.4.1 Random patterns of N-wave amplitude behind the screen

In this work, the probability distribution functions of acoustic field were calculated from a few realizations of the phase screen sufficiently wide in the x-direction. According to the hypothesis of ergodicity, this is equivalent to the average over a large number of realizations in one spatial point. For each value of nonlinear parameter N, acoustic field modeling was performed using two statistically independent realizations of the phase screen. The length of each realization was equal to 800λ excluding boundary zones. This screen length contains approximately 520, 260 or 130 characteristic scales of phase fluctuations for the screens with $l = 1.5$, $l = 3$ or $l = 6$,

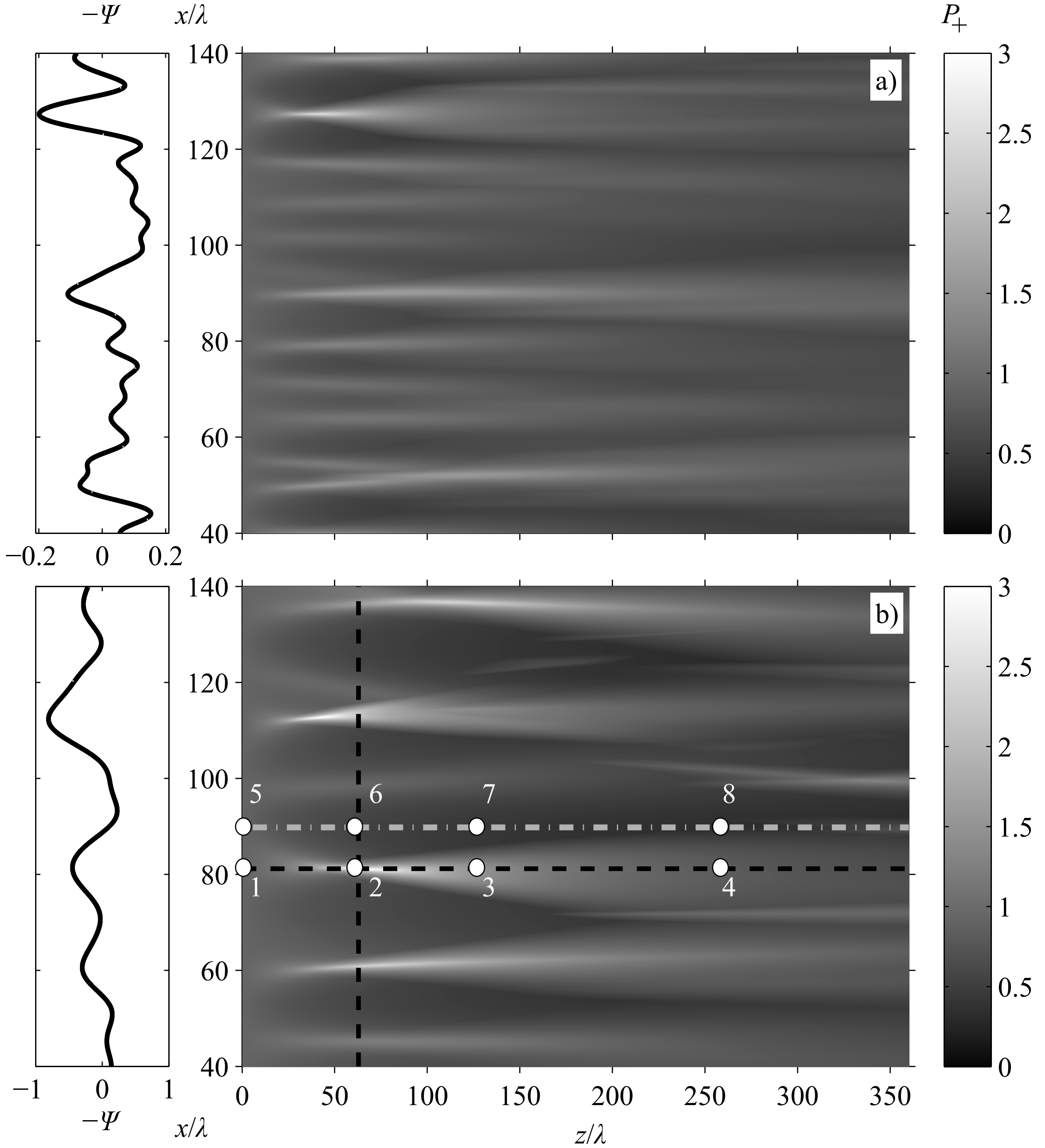

Figure 3.2: Spatial distributions of the peak positive pressure for initially plane N-wave propagating behind two different random phase screens $\Psi(x)$ shown as solid curves on the left. Correlation length of the screens is a) $l = 3$ and b) $l = 6$. Nonlinear length $z_n = 8z_r$, refraction length $z_r/\lambda = 63$. N-waveforms calculated along the horizontal dash line (through focusing zone) at points 1-4 are shown in Fig. 3.4a and calculated along the horizontal dash-dot line (through defocusing zone) at points 5-8 are shown in Fig. 3.4b. Peak pressure along vertical dashed line is presented in Fig. 3.3b

respectively. Comparison between statistical distributions of the acoustic field modeled with these two independent phase screens showed a good agreement and justify that the chosen length of phase screens was long enough for statistical analysis.

Typical spatial patterns of the N-wave peak positive pressure, $P_+ = p_+/p_0$, calculated behind two phase screens of the same refraction length but smaller or bigger correlation lengths, are illustrated in Fig. 3.2a and Fig. 3.2b. Phase screens are presented on the same figure as an initial phase shift of the acoustic wave. For a better visualization of the process, the width of the regions shown in the figure is much smaller than the real computational domain. Nonlinear length equal to $z_n = 8z_r$ and refraction length equal to $z_r/\lambda = 63$ were used to calculate both patterns. Dimensionless correlation lengths of the screens were $l = 3$ (Fig. 3.2a) and $l = 6$ (Fig. 3.2b). Complex spatial structure of the acoustic field is observed; focal zones form at different distances from the phase screen and have different focusing gains, depending on the size and strength of the particular phase inhomogeneity of the screen. The first high amplitude focusing regions (in general - caustics) are located at the distance approximately equal to the refraction length $z = z_r$. This distance is shown with the vertical dashed line in Fig 3.2b. At distances greater than the refraction length, formation of random foci is observed as well as the result of focusing produced by large scale phase fluctuations, that are present in realization since the spectrum have the finite non zero value at low spatial frequencies. On average, the amplitude of the N-wave in these foci is smaller than in the first ones mainly due to nonlinear dissipation effect, but also due to the thermoviscous absorption. Also, strong foci can appear at close distances from the screen, for example, see the caustic at $z/\lambda = 50$, $x/\lambda = 115$ in Fig. 3.2b. Comparison of Fig. 3.2a and Fig. 3.2b, shows that focusing effects are more pronounced for the phase screen with fluctuations of larger spatial correlation scale. For example, the maximum dimensionless pressure in the first acoustic pattern is equal to $P_+ = 2.5$ and in the second one – to $P_+ = 3.8$. However, less number of foci is observed behind the screen with a large correlation length. Smaller scale phase modulation of the wave front thus result in bigger number of random foci of less peak pressure as compared to larger scale phase modulation of the same refraction length.

Focusing gain in caustics is strongly affected by nonlinear effects. Linear N-wave propagation is considered here as a reference case. If nonlinear effects are sufficiently strong, they lead to strong nonlinear dissipation at the wave shock front and the N-wave amplitude decays rapidly during its propagation from the phase screen to the caustic. Also, the focusing gain in caustics is decreasing by nonlinear refraction effect (Musatov *et al.*, 1992) (see below). On the other hand, nonlinear steepening of the shock front at high amplitude field regions enhances focusing, since the acoustic wave differentiates in the caustic (with some correction on the absorption and nonlinear effects). This nonlinear enhancement of focusing will dominate over the nonlinear dissipation for the moderate initial N-wave amplitudes. Inversely, if initial amplitude is very high, the effect of focusing will be weaker for nonlinear propagation than for the linear one. The efficacy of focusing in the caustic therefore is a nonmonotonic function of the initial wave amplitude if refraction length is fixed.

This nonmonotonic behavior of the focusing gain is illustrated in Fig. 3.3. The distributions of the peak positive pressure along the line passing through a caustic are shown in Fig. 3.3a. The chosen trajectory is shown in Fig. 3.2b by horizontal dashed line ($x/\lambda = 56.7$). Shown in Fig. 3.3b are the peak pressure distributions along the transverse coordinate x/λ at the distance of refraction length $z = z_r$ as marked in Fig. 3.2b with the vertical dashed line. Linear propagation and four nonlinear regimes are considered. Black dashed curve (0 in the legend) corresponds to the linear regime and the nonlinear regimes have the following characteristic nonlinear lengths: $z_n = 8z_r$

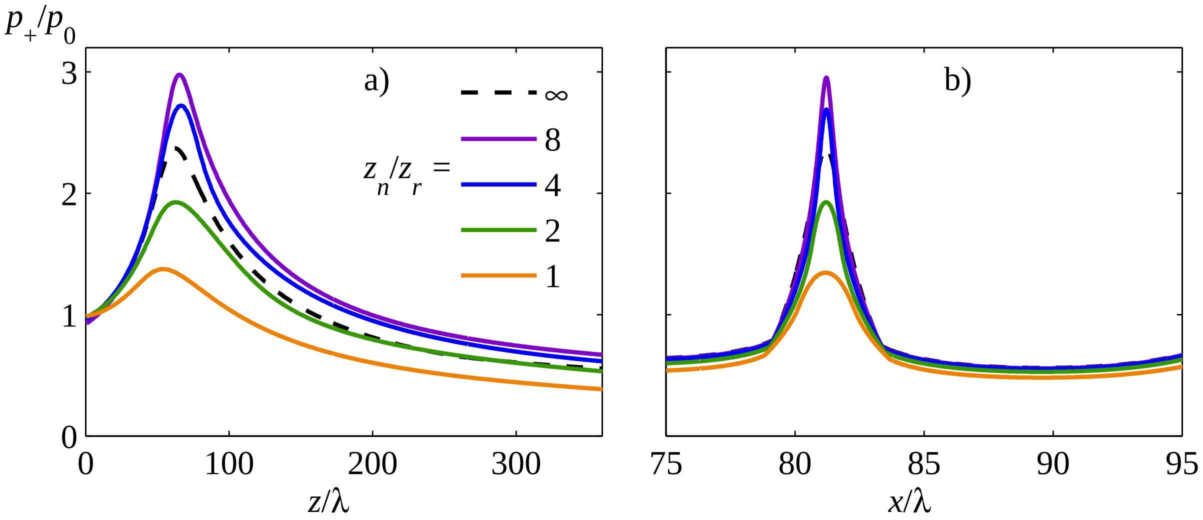

Figure 3.3: The peak positive pressure along the horizontal (through focusing zone) a) and vertical b) dashed lines in Fig. 3.2b for different nonlinear lengths: black dashed line – linear propagation (0), $z_n = 8z_r$ (8), $z_n = 4z_r$ (4), $z_n = 2z_r$ (2) and $z_n = z_r$ (1). Corresponding z_n/z_r ratio is marked as a number in the legend. Purple curve (8) corresponds to the pattern shown in Fig. 3.2b.

– purple line (8), $z_n = 4z_r$ – blue line (4), $z_n = 2z_r$ – green line (2) and $z_n = z_r$ – orange line (1). In each nonlinear case the initial waveform is defined according to the quasi-stationary solution as discussed above. In the case of linear propagation the initial waveform is identical to the waveform in the case of lowest amplitude nonlinear propagation, $z_n = 8z_r$. It is seen that for weak nonlinearity case $z_n = 8z_r$, (8), the peak pressure in the focus exceeds the linear one approximately by 25%. Focusing enhancement is observed also in $z_n = 4z_r$ case, but with less maximum of P_+. In the cases (2) and (1) nonlinear effects are too strong, nonlinear absorption at the shocks dominates over nonlinear enhancement of focusing, peak pressure is lower than in the linear case and decreases when nonlinear effects increase. A conventional shift of the peak pressure maximum toward the phase screen for smaller nonlinear lengths is observed. Also, in a case of weak nonlinearity the focal zone is sharpening in the transversal direction, and, inversely, for strong nonlinearity it become smooth (Fig. 3.3b).

3.4.2 Characteristic examples of N-wave distortions behind the screen

Distortion of the initial N-shape of the wave due to the combined effect of diffraction, nonlinearity, and random focusing is illustrated in Fig. 3.4 and Fig. 3.5. The waveforms were calculated at different propagation distances from the screen along two horizontal lines shown in Fig. 3.2b. The dashed line passes through a random caustic and dash-dotted line passes through the low amplitude defocusing zone. Particular points on the lines at which waveforms are grasped are marked by white circles and numeration of circles corresponds to numeration of waveforms in Fig. 3.4 and Fig. 3.5. The initial N-wave is plotted as black dashed curves (1) and (5). Typical waveform modifications observed while propagating through the caustic are shown in Fig. 3.4a: in the focal zone ($z = z_r$) the waveform tends to take asymmetric U-shape (2, red curve) with higher peak positive pressure; at longer distance ($z = 2z_r$), the waveform (3, green curve) has

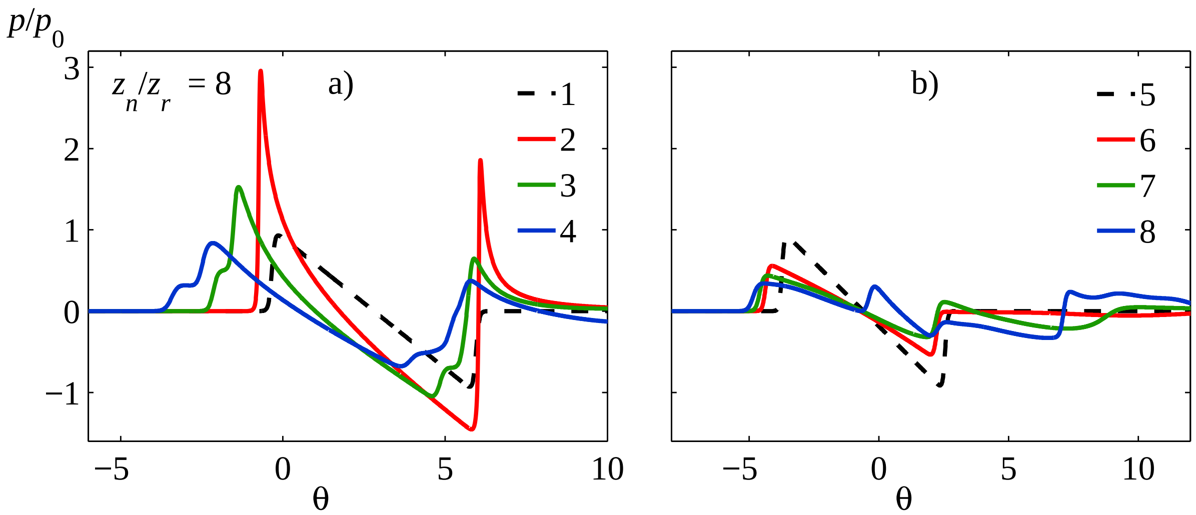

Figure 3.4: Initial and distorted N-waveforms modeled at points 1-4 and 5-8 along the horizontal dashed (a) and dash-dot (b) lines shown in Fig. 3.2b. The distances where waveforms were picked are the following: $z = 0$ (1 and 5), $z = z_r$ (2 and 6), $z = 2z_r$ (3 and 7), $z = 4z_r$, (4 and 8). Weak nonlinearity case is considered: $z_n/z_r = 8$.

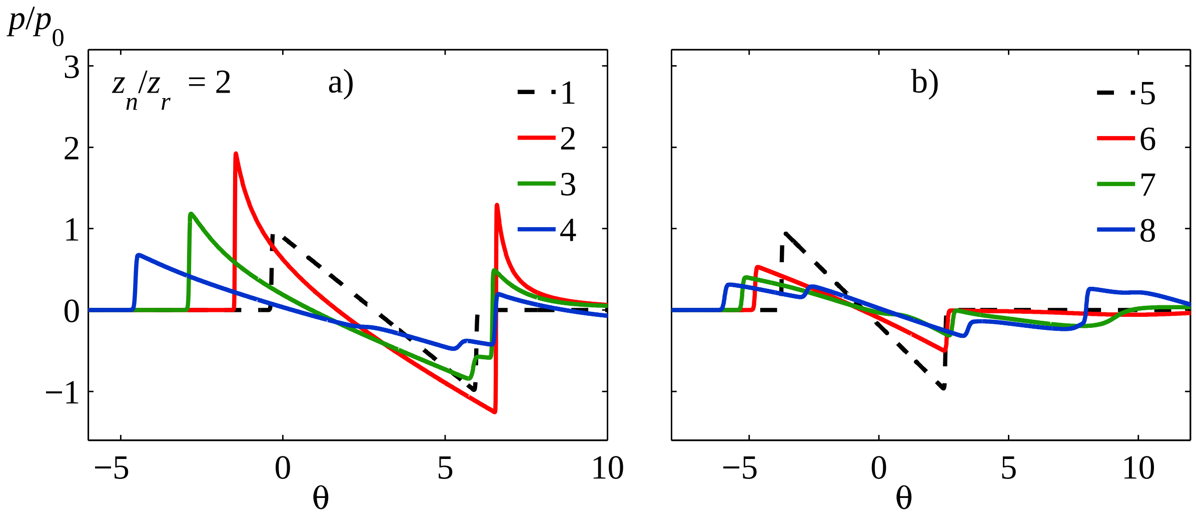

Figure 3.5: N-waveforms in the same points as shown in Fig. 3.4, but using stronger nonlinearity in calculations: $z_n/z_r = 2$. Nonlinear absorption and nonlinear lengthening effects are clearly seen. Fusion of two shocks into the one shock is also observed.

lower amplitude and longer duration due to nonlinear effects, the second shock also appears. For further distances from the screen ($z = 4z_r$) the second shock is more pronounced (4, blue line). Waveform distortion when propagating through the defocusing zone is shown in Fig. 3.4b: double peaked (8, blue curve, $z = 4z_r$) and rounded (7, green curve, $z = 2z_r$) waveforms are observed due to the interference of waves having different arrival times. Close to the screen the N-waveform is almost unchanged in this particular case (6, red curve, $z = z_r$). Results of calculations with four times stronger nonlinearity ($z_n = 2z_r$) are shown in Fig. 3.5. In general, these waveforms are longer and have smaller amplitude in comparison to the previous case due to nonlinear effects. The wave front advancing in the caustic due to the nonlinear lengthening – nonlinear refraction, leads to defocusing and decreasing of the amplitude in addition to nonlinear absorption (Musatov *et al.*, 1992). Moreover, comparing Fig. 3.4a and Fig. 3.5a, it can be observed, that two shocks (curves 3 and 4) are transformed into one shock in the strong nonlinearity case. Thus, not only amplitude and duration are affected by nonlinear effects, but also the complex pattern of two or more shocks, created in a case of the interference of waves having different arrival times.

§3.5 Probability distributions and mean values of the N-wave amplitude behind the phase screen; comparison with nonlinear geometrical acoustics approximation

3.5.1 Probability distributions as functions of propagation distance

Statistical properties of the N-wave field behind the screen are presented here by probability distribution function of the peak positive pressure, P_+. To compute statistical distributions the results of acoustic field modeling behind two independent realizations of random phase screen were used. For each step in propagation distance z from the screen, the probability $W(P_+)dP_+$ was calculated proportionally to the number of points with amplitudes fitting the interval from P_+ to $P_+ + dP_+$. The results of calculations are shown in Fig. 3.6 (a-f) for the distances $z = 0.125z_r$ (a), $z = 0.25z_r$ (b), $z = 0.5z_r$ (c), $z = z_r$ (d), $z = 2z_r$ (e) and $z = 4z_r$ (f) from the phase screen in a case of $z_n = 4z_r$ (each next distance is a double of the previous). Color lines correspond to the results obtained using KZK equation for the phase screens with following correlation lengths: $l = 6$ – red line, $l = 3$ – green line and $l = 1.5$ – blue line. For comparison, analytic solutions (black curves) for the pressure amplitude distributions obtained using the NGA approximation are also shown (Dubrovskii *et al.*, 1996). Note that these solutions are only valid for distances shorter than the refraction length. N-wave amplitudes in case of nonlinear plane wave propagation, without any initial phase modulation, are shown as vertical dashed lines.

Fig. 3.6 shows that the initial δ-function distribution of the N-wave amplitude is broadening due to phase modulations. It is seen that at short distances from the phase screen ($z = 0.125z_r$ and $z = 0.25z_r$, Fig. 3.6a and Fig. 3.6b) probability distributions obtained with NGA approach and KZK modeling for all screens are very similar: in prefocal zone the effect of diffraction and of the correlation length is almost negligible. At longer distances ($z = 0.5z_r$ and $z = z_r$, Fig. 3.6c and Fig. 3.6d), the results of NGA and KZK modeling become different. Note that only large scale phase screen results (red curve) are still close to the predictions of the NGA approach. The distributions at low amplitudes that correspond to the divergent zones of the field (Fig. 3.2b), agree reasonably well. This means that the waveforms in these regions predicted with and without account for diffraction effects are surprisingly close in amplitude. Small number of high amplitude focal zones occupy spatially small portion of the transverse cross section of the field (Fig. 3.2b and Fig. 3.3b) and thus give small contribution to the probability density. This part of the distribution of high amplitudes is long but relatively small in both models.

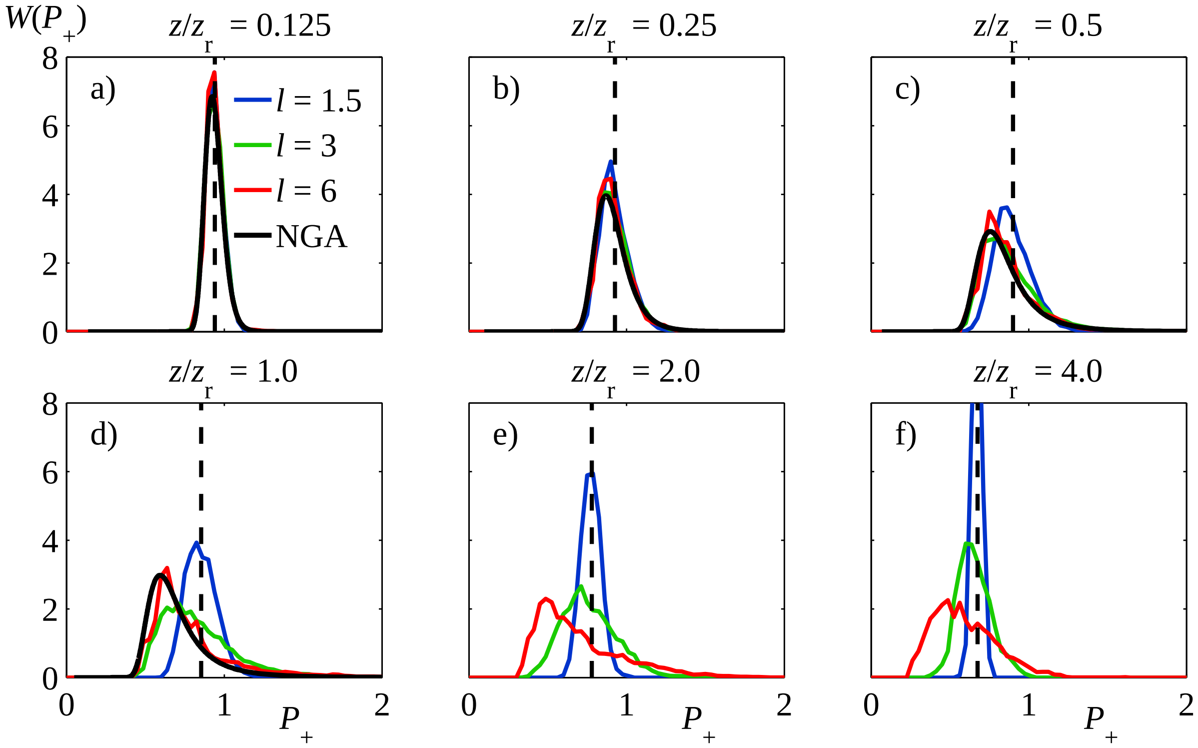

Figure 3.6: Comparison between probability distributions of the N-wave peak pressure P_+ obtained using the KZK model (color curves) and analytical solutions in the NGA approach(black curves). Red line corresponds to the phase screen with correlation length $l = 6$, green – $l = 3$, blue – $l = 1.5$. Dashed lines show the amplitude of plane N-wave. The distributions are presented for six propagation distances $z = 0.125z_r$ (a), $z = 0.25z_r$ (b), $z = 0.5z_r$ (c), $z = 1.0z_r$ (d), $z = 2.0z_r$ (e) and $z = 4.0z_r$ (f). Nonlinear and refraction lengths are in ratio $z_n = 4z_r$.

In NGA analytical solutions there is a problem of probability function normalization. This is due to the fact that the NGA approximation neglects already converged ray tubes. As the phase screen has a random nature some of the caustics appear at short distances than the refraction length z_r. Ray tubes converged to these caustics are excluded from calculations, total number of rays taken into account decreases, the probability density becomes relatively higher and looses its normalization with propagation distance. To compensate this effect, a renormalization of $W(P_+)$ functions can be done as:

$$\tilde{W}(P_+) = W(P_+) / \int_0^\infty W(P_+) dP_+. \tag{3.7}$$

Actually, the renormalized probability functions are shown in Fig. 3.6.

In the case of small-scale inhomogeneities (Fig. 3.6d, green and blue curves) the diffraction effects act much stronger at the distance equal to refraction length $z = z_r$. No strong focusing occurs (Fig. 3.2a), so the probability to observe very high amplitudes is smaller than for the large scale focusing (Fig. 3.2b). On the other hand, the number of random foci is bigger, and defocusing zones between them are narrower and have less decay of the amplitude. So the probability function is almost symmetrical around the regular value that corresponds to the nonlinear plane N-wave propagation. Small scale phase modulations therefore results in less shift of the distribution towards smaller amplitudes as compared to the large scale modulation. This difference of the

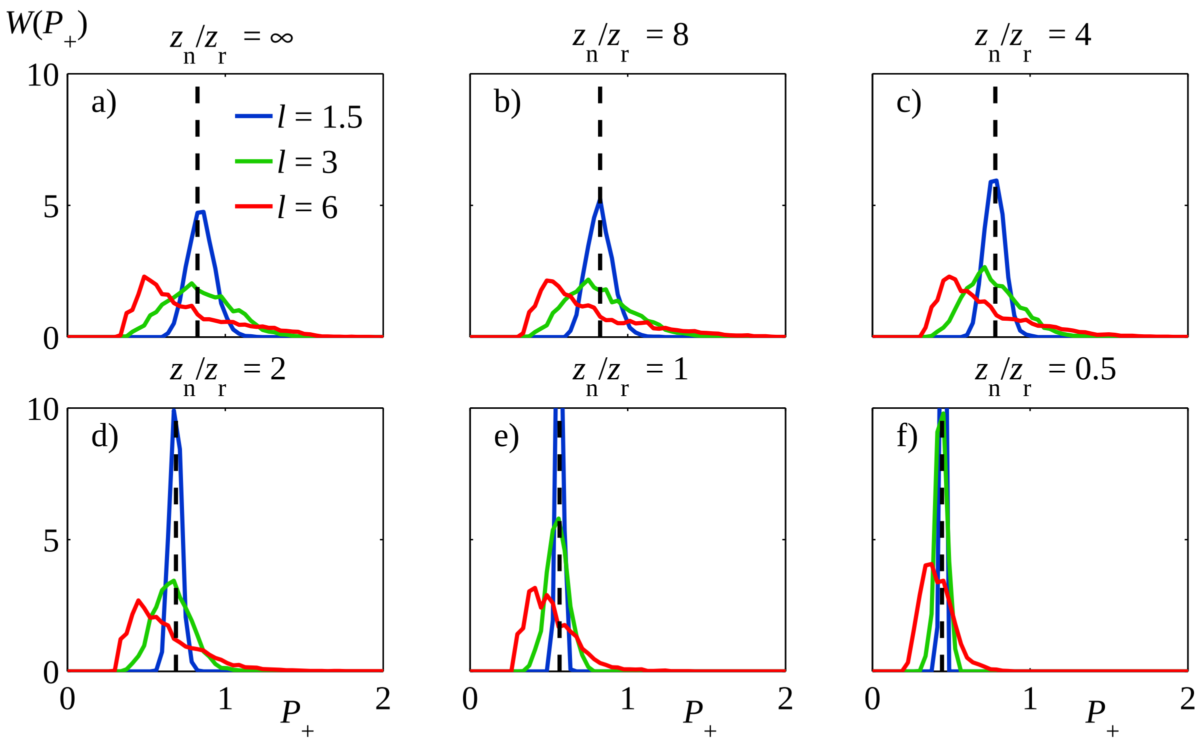

Figure 3.7: Comparison between probability distribution functions of the N-wave peak positive pressure obtained at the distance $z = 2z_r$ for various nonlinear lengths z_n: linear (a), $z_n = 8z_r$ (b), $z_n = 4z_r$ (c), $z_n = 2z_r$ (d), $z_n = z_r$ (e) and $z_n = 0.5z_r$ (f). Correlation lengths of the screens are: $l = 6$ (red curve), $l = 3$ (green curve), $l = 1.5$ (blue curve).

effect of inhomogeneities of either large of small size is even better seen at longer distances from the screen as shown in Fig. 3.6e and Fig. 3.6f ($z = 2z_r$ and $z = 4z_r$). Here the NGA solution is no longer valid and the results are presented only for the KZK equation modeling. Again, large-scale phase screen results in relatively high probability to observe high peak pressures and the maximum of probability density is shifted towards low amplitude values. The probability distributions, produced by the small-scale phase screen, become more narrower and keep centering around the plane wave amplitude. Also, smaller scales of phase screen fluctuations yield narrower probability distributions (compare blue and green curves).

3.5.2 Effect of nonlinearity on probability distribution functions

The effect of nonlinearity on statistical distributions of the peak pressure is illustrated in Fig. 3.7. Linear wave propagation (Fig. 3.7a), and five nonlinear propagation regimes with $z_n = 8z_r$ (b), $z_n = 4z_r$ (c), $z_n = 2z_r$ (d), $z_n = z_r$ (e) and $z_n = 0.5z_r$ (f) are considered at the distance of two refraction lengths, $z = 2z_r$, from the screen. Correlation lengths of the screens and colors of curves are the same as in Fig. 3.6. It is seen that stronger nonlinearity leads to substantial narrowing of the statistical distributions, that is more pronounced in a case of small-scale phase screens. Only for weak nonlinearity ($z_n = 8z_r$ and $z_n = 4z_r$) the statistical distributions can be wider than in linear propagation case. Quantitatively it will be clear from second statistical moment – standard deviation, discussed below. Nonlinear effects thus suppress fluctuations of acoustic field induced by the initial distortion of wave front. This is the result of increased nonlinear absorption in focusing zones that leads to faster amplitude decay and thus to faster quieting of high amplitudes. The nonlinear refraction also limits high pressure peaks in the foci.

3.5.3 Mean value and standard deviation of N-wave amplitude

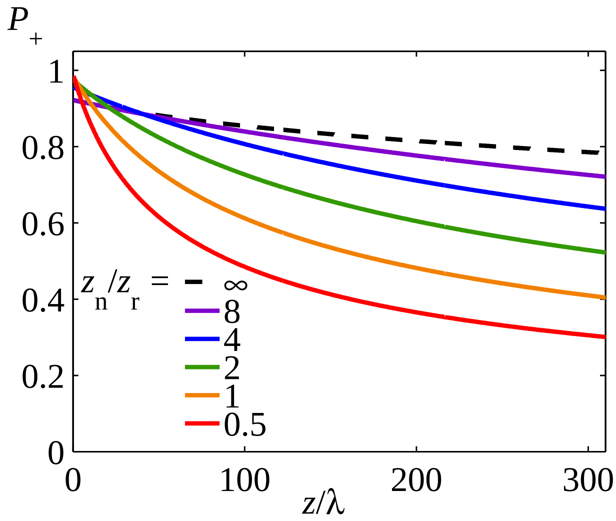

Figure 3.8: The amplitude of the plane N-wave as a function of distance z for different nonlinear lengths: black dashed line ($z_n/z_r = \infty$) – linear propagation, purple line $z_n = 8z_r$, blue line $z_n = 4z_r$, green line $z_n = 2z_r$, orange line $z = z_r$ and red line $z_n = 0.5z_r$. The curves correspond to $a_0/\sqrt{(1+z/z_n)}$ law in nonlinear propagation cases. If linear propagation is considered ($z_n/z_r = \infty$) – the amplitude decrease due to thermoviscous absorption.

Quantitatively, the combined effects of nonlinearity and random focusing can be analyzed by comparing first two statistical momentums: mean value and standard deviation of the peak pressure. Results will be normalized on the amplitude of the plane wave. In Fig. 3.8 the curves of the plane wave amplitude $P_{+,\text{pl.wave}}$ are shown, corresponding to the well known law $a_0/\sqrt{(1+z/z_n)}$ where a_0 is the initial wave amplitude (Rudenko & Soluyan, 1977). Different colors mark different nonlinear lengths, chosen for calculations: black dashed line – linear propagation ($z_n = \infty$), purple line $z_n = 8z_r$, blue line $z_n = 4z_r$, green line $z_n = 2z_r$, orange line $z = z_r$ and red line $z_n = 0.5z_r$. In the linear propagation case the amplitude is decreasing due to termoviscous absorption. At the maximal distance $z = 5z_r = 314\lambda$, considered here, the decrease is 15% only.

First, the normalized mean value $< P_+ > /P_{+,\text{pl.wave}}$ will be considered as a function of distance z for different nonlinear lengths. In Fig. 3.9 the mean value is presented for three phase screens with different correlation lengths (a, b, c), using the same colors and z_n as in Fig. 3.8. It is seen, that the wave front modulations have the substantial effect on the mean value only if phase fluctuations are of large-scale (Fig. 3.9c). In this case, the mean amplitude behind the phase screen is smaller than the plane wave amplitude. However, for the maximal considered distance $z = 5z_r = 314\lambda$ the lowest normalized mean amplitude is 0.8 ($z_n/z_r = \infty$) only. The decrease of the mean amplitude due to random focusing is more important for linear propagation case and diminishes if the nonlinearity increases. This effect is due to strong nonlinear absorption and nonlinear refraction as it was discussed in Fig. 3.3, Fig. 3.5 and Fig. 3.7. The phase screens with small-scale phase fluctuation have negligible impact on the mean amplitude for all nonlinear cases (Fig. 3.9 a and b). For example, the ratio $< P_+ > /P_{+,\text{pl.wave}}$ is not lower than 0.99 for $l = 1.5$ and is not lower than 0.96 for $l = 3$. However, for linear and weak nonlinearity cases small maximum of the mean $< P_+ > /P_{+,\text{pl.wave}}$ is observed between $z = z_r$ and $z = 3z_r$. If the mean value without normalization is considered, $< P_+ >$, weak nonlinearity leads to slightly higher mean

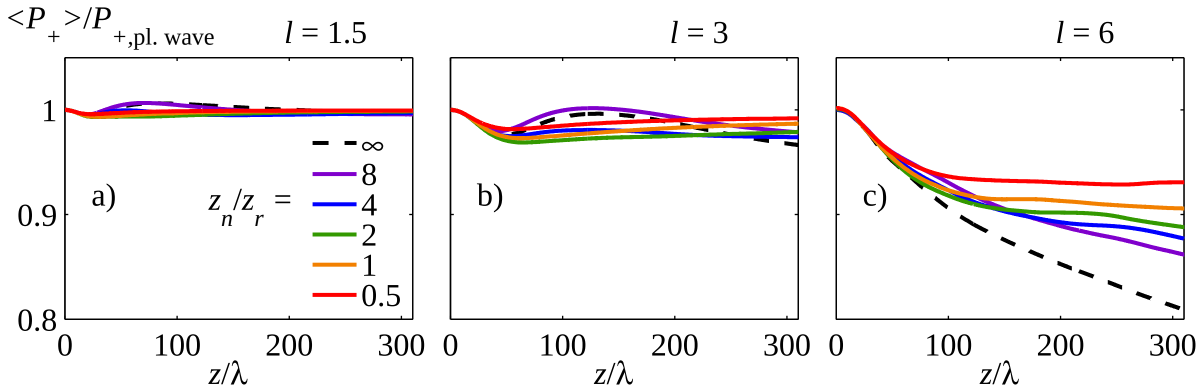

Figure 3.9: Mean peak positive pressure normalized to the plane wave amplitude as a function of propagation distance for various nonlinear lengths z_n: dashed line $z_n/z_r = \infty$ – linear propagation, purple line $z_n = 8z_r$, blue line $z_n = 4z_r$, green line $z_n = 2z_r$, orange line $z = z_r$ and red line $z_n = 0.5z_r$. From left to right – results for the phase screens with correlation length equal to $l = 1.5$ (a), $l = 3$ (b) and $l = 6$ (c).

amplitudes of randomly modulated wave than in the case of its linear propagation. However, this effect, explained by nonlinear enhancement of focusing is small and is not illustrated here.

After the mean value, the normalized standard deviation $\delta P_+/P_{+,\text{pl.wave}}$ is considered as a function of distance z and nonlinear length z_n. The results are collected in Fig. 3.10 using the same notations as in the previous figure. Note, that all curves are more or less similar; the difference is almost quantitative. Therefore, only one case – for the phase screen with large-scale phase fluctuations $l = 6$ will be discussed in detail (Fig. 3.10c). The behavior of the standard deviation with propagation distance is non-monotonic. At first, standard deviation grows linearly from its zero value at $z = 0$. This linear growth is the same for all nonlinear lengths, that is consistent with the asymptotic solution, derived using NGA approximation: $\delta P_+ = 0.5z/z_r$, if $z << z_r$ (Rudenko & Enflo, 2000). The standard deviation has a maximum at the distance approximately equal to the refraction length z_r. In fact most intensive focusing is observed at this length and thus broadening of the probability distribution. Further the standard deviation decreases slowly with increasing of the

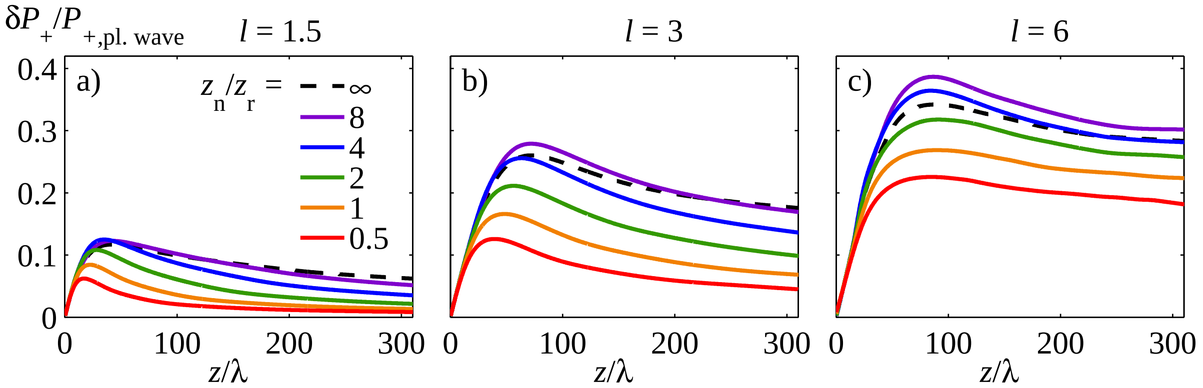

Figure 3.10: Standard deviation of peak positive pressure normalized to the plane wave amplitude as a function of propagation distance for various nonlinear lengths z_n: dashed line $z_n/z_r = \infty$ – linear propagation, purple line $z_n = 8z_r$, blue line $z_n = 4z_r$, green line $z_n = 2z_r$, orange line $z = z_r$ and red line $z_n = 0.5z_r$. From left to right – results for the phase screens with correlation length equal to $l = 1.5$ (a), $l = 3$ (b) and $l = 6$ (c).

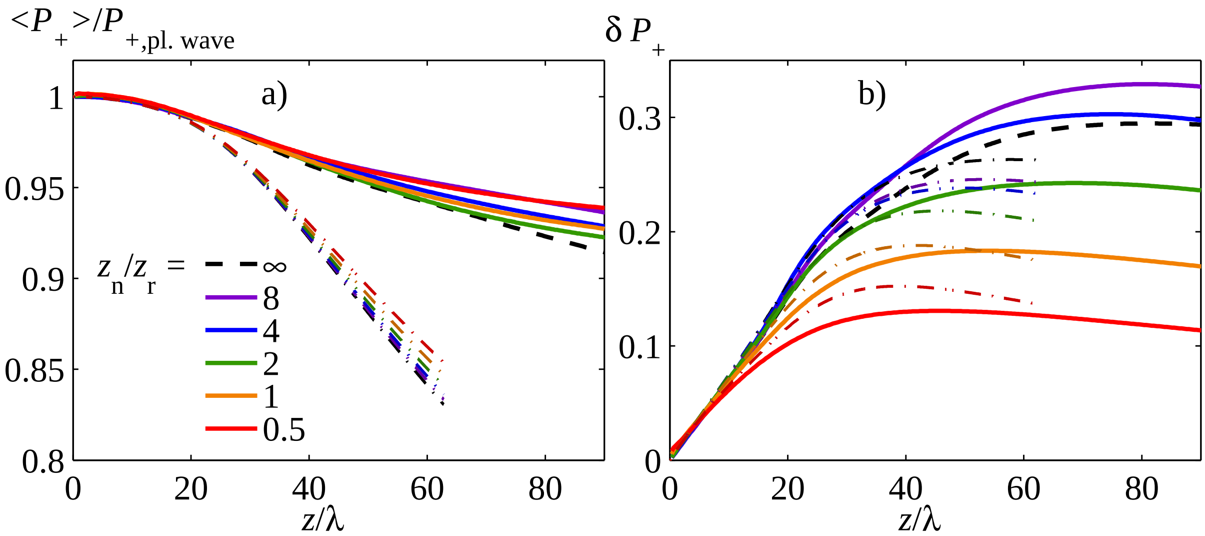

Figure 3.11: Comparison of mean value (a) and standard deviation (b) of peak positive pressure obtained in NGA approach (dashed lines) and in parabolic equation model (solid lines). The results for the phase screen with correlation length $l = 6$ are presented. Line color have the same meaning as in Fig. 3.9 and Fig. 3.10.

propagation distance z. Maximum value of standard deviation is non-monotonic function of nonlinear length. Weak nonlinearity ($z_n/z_r = 8$ and $z_n/z_r = 4$) results in slightly greater maximum than in the linear case ($z_n/z_r = \infty$) due to nonlinear enhancement of focusing. Strong nonlinearity significantly decreases the maxima and the overall level of standard deviation ($z_n/z_r = 2$ and the rest) as it was also seen in Fig. 3.7. Thus, the fluctuations of peak positive pressure in a random field are suppressed for high amplitude waves due to nonlinear effects.

The standard deviation curves, obtained after N-wave propagation behind phase screens with small-scale phase fluctuation are similar to curves discussed above, but some quantitative differences exist. It is seen from Fig. 3.10a and Fig. 3.10b that for linear regime ($z_n/z_r = \infty$) and weak nonlinearity ($z_n/z_r = 8$) the maxima of standard deviations are located very close to the distance of one refraction length from the screen. Stronger nonlinearity results in a shift of the maximum towards the phase screen due to the mechanisms of nonlinear absorption and nonlinear refraction, which suppress high amplitudes. The maximum of standard deviation decrease if the correlation length l decreases for all nonlinear lengths. For example, comparing $l = 6$ and $l = 3$, the maximum is 1.5 times smaller on average, and comparing $l = 3$ and $l = 1.5$ – 2 times, for lowest correlation length in each pair. Additionally, the curves decay faster at large z distances, especially in strong nonlinear cases. Thus, the mean fluctuation level is almost proportional to the scale of phase fluctuations in considered range of correlation lengths.

It is interesting to compare the mean values and standard deviations of the amplitude obtained either from the KZK modeling or from the analytic solutions of the NGA approach. The comparison in Fig. 3.11 is done in the case of large-scale phase fluctuations for different nonlinear lengths ($l = 6$, solid curves). Analytical solutions are traced by dashed color lines. Note that the comparison here is provided for renormalized probability densities of the NGA solution (3.7). It is seen, that after the distance of $z_r/3$ the curves calculated in NGA approximation become significantly different from the KZK solution. If renormalization to keep the integral of the probability density equal to unit is not applied, the difference become noticeable after the distance of $0.25z_r$. For longer distances, closer to refraction length, the NGA solution is no longer valid and becomes quite different from the diffraction model. For example, the mean $< P_+/P_{+,\text{pl.wave}} >$ at distance $z = z_r$ obtained in NGA solution is 15% lower than in KZK modeling. The standard deviations δP_+ are close to KZK results for strong nonlinearities, however, for weak nonlinear and linear cases, the standard deviation is $20 - 30\%$ lower in comparison to parabolic equation model.

§3.6 Conclusions

The combined effects of nonlinearity, random focusing, and diffraction on N-wave propagation behind a random phase screen are investigated using the KZK equation. Probability distributions, mean values, and standard deviations of the N-wave amplitude are obtained from the numerical solutions of the KZK equation and are presented as functions of propagation distance and nonlinear length. The effect of the spatial size of phase fluctuations on statistical distributions is considered. Results obtained from the KZK diffraction model are compared with analytical predictions of the NGA approach. It is shown that close to the screen, or quantitatively up to the distances of $z = z_r/3$, the results of the diffraction and geometric approaches agree very well. At longer distances, statistical properties of the random acoustic field can be accurately described only if diffraction effects are taken into account. First major focusing zones (caustics) form on average at one refraction distance z_r. This distance fully characterizes the focusing properties of the screen in the NGA approach. However, the KZK diffraction model shows that phase screens of the same refraction length but different spatial scales of the phase fluctuations, statistically the same for the NGA approach, produce random acoustic fields with quite different statistical properties. For example, large-scale phase fluctuations produce stronger focusing zones, probability distribution functions are very wide, the probability of observation of high amplitude waves is noticeable. The mean amplitude is smaller than the plane wave amplitude. The amplitude field behind the small-scale phase screens is characterized by weaker focusing effects, probability distributions are narrow and are centered around the mean value that is close to the amplitude of the plane wave. Contrary to the NGA model that maintains the N-waveform everywhere, the diffraction model predicts more realistic waveforms that are characteristic for N-wave propagation in inhomogeneous media. For example, U-shape waves occur in the caustics, rounded and double peaked waves – in the defocusing zones. The effect of nonlinearity on the amplitude statistics is twofold. Weak nonlinearity leads to a slight enhancement of focusing effects resulting in higher probability of high amplitude waves. Standard deviation increases in these cases. Strong nonlinear effects suppress amplitude fluctuations and lead to narrower probability distributions and smaller standard deviations. The mean values approach the value of the plane wave amplitude when nonlinearity increases.

Chapter 4

Distortion of the focused finite amplitude ultrasound beam behind the random phase layer

§4.1 Introduction

Propagation of finite amplitude ultrasound beams through a randomly inhomogeneous medium is a problem of interest both for the general wave theory and for numerous applications in biomedicine (Hill *et al.*, 2002, Bailey *et al.*, 2003, Rudenko, 2007), diagnostic ultrasound (Rudenko, 2007, Rudenko, 2006), nondestructive testing (Rudenko, 2006, Brysev *et al.*, 2004), *etc*. For example, in ultrasound hyperthermia and surgery, strong inhomogeneities – fat and skin layers, connective tissues, and bones may appear on the path of an intense beam. The inhomogeneities distort the beam focusing implemented by classical methods, thereby degrading the useful effect and causing unwanted side effects by injuring healthy tissues (Bobkova *et al.*, 2010, Li *et al.*, 2006). In diagnostic ultrasound, the distortion of the focusing by the inhomogeneities reduces the resolution and sensitivity of such equipment and increases its measurement errors (Hill *et al.*, 2002).

A random phase screen model is widely used in studies of diagnostic ultrasound propagation in randomly inhomogeneous media (Hill *et al.*, 2002, Uscinski, 1977). For example, in order to improve diagnostic images, correction algorithms were developed using a phase screen model and simplified models of linear wave propagation (Liu & Waag, 1994, Hirama *et al.*, 1982, Nock *et al.*, 1989, Rachlin, 1990). Increasing power of computers and improved numerical methods permitted to solve full-wave linear equation for a motionless inhomogeneous media. Realistic maps of density and sound speed, obtained from tissue specimens, were used in these studies (Tabei *et al.*, 2003, Tabei *et al.*, 2002, Mast *et al.*, 1997). However, the simulations were limited to 2D geometry due to complexity and a numerical burden of the algorithm. Recently, similar 3D full-wave equation model was reported (Tillett *et al.*, 2009), but it is still very expensive concerning computer resources. Therefore, replacement of continuous inhomogeneous media by a phase screen and simplified wave propagation models are of current importance up to date in case of 3D geometry, especially if the finite amplitude beam is the object of interest.

In modern medical diagnostics, ultrasound devices that employ operation modes utilizing nonlinearity of the propagation medium are being widely used. A characteristic example is scanning with the use of the second harmonic, when wave propagation in tissue is accompanied by generation of higher order harmonics (Averkiou *et al.*, 1997, Khokhlova *et al.*, 2006) (Tissue Harmonic Imaging, THI). The second harmonic scanning increases resolution, decreases noise and improves overall quality of diagnostic images (Rudenko, 2007). Investigation of physical mechanisms of the image quality enhancement and technical progress of the devices are important tasks up to date (Jing & Cleveland, 2007, Varslot & Taraldsen, 2005, Varslot & Masoy, 2006, Varslot *et al.*, 2007, Wojcik *et al.*, 1998, Christopher, 2009). In the research work both the continuous inhomogeneous media (Jing & Cleveland, 2007, Varslot & Masoy, 2006) and the phase screen model are used (Christopher, 1997, Yan & Hamilton, n.d.). Propagation of nonlinear beams through the phase screen was studied primarily using numerical methods (Christopher, 1997, Christopher, 2009). Recently, the first works on analytical description of the nonlinear beam behind the phase screen (Yan & Hamilton, n.d., Yan, 2004) and experiments on propagation of the nonlinear beams through the inhomogeneous phase layer were performed (Brysev *et al.*, 2005, Yan, 2004, Brysev *et al.*, 2004). The results of these studies allow us to suppose that, under certain conditions, focusing of harmonics nonlinearly generated in the inhomogeneous medium can have advantages over the usual focusing of the beam emitted at the frequency of the harmonic. In other words, the same inhomogeneity can defocus the beam at a frequency f stronger than the n-th harmonic of the frequency, f/n, generated in the beam.

At the same time, the problem of controlling cascade processes of harmonics generation, which result in an increased nonlinear absorption of acoustic waves, has long been discussed in nonlinear acoustics of nondispersive media. This problem is typical for ultrasound techniques, especially in biomedical applications where it is necessary to deliver a high acoustic power to a particular spatial region. Such a control can be implemented, for example, by introducing resonant absorption of the chosen harmonics (Andreev *et al.*, 1985, Khokhlova *et al.*, 2000). For the same goal, it was also proposed to introduce a phase shift between the harmonics (waveform precorrection) (Couture *et al.*, 2008, Sarvazyan *et al.*, 1998). By analogy with the second method, the use of a specially chosen phase screen that selectively dephases a desired harmonic may be of interest as another promising method to control the process of generating harmonics.

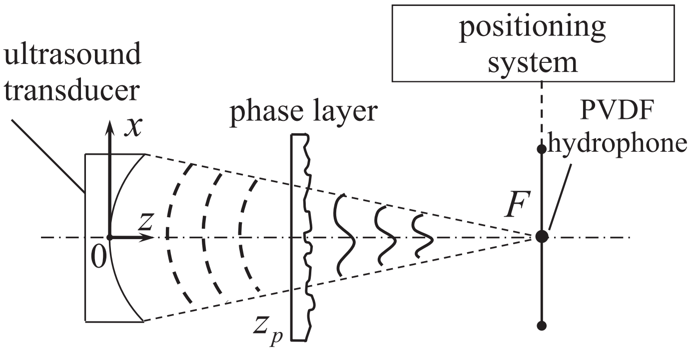

Figure 4.1: Schematic illustration of the problem and a diagram of the experimental setup.

Geometry of the problem is illustrated in Fig. 4.1. The finite amplitude focused beam, emitted by a transducer of focal distance F, propagates through the phase screen, placed at distance the $z = z_\mathrm{p}$. The phase screen introduces the wave front distortions and after that the beam propagates in the homogeneous media. Main interest in the described problem are distortions of the acoustic field in the focal plane $z = F$. The phase screen considered in this chapter will be called the phase layer, since its physical realization of finite thickness will be presented later in the experimental part of the work.

In the modeling part of this work, a phase layer is substituted as an infinitely thin phase screen consisting of a great number of identical circular regions randomly distributed on a plane. The phase shift within the circular regions is fixed. A similar model was used in the study (Yan, 2004) to experimentally validate theoretical findings based on the model of a phase layer with a smooth phase variations. The situation was analyzed for quasilinear beam propagation with allowance for only second harmonic generation and weak phase modulation. The primary attention in the comparison between the theory and experiment was to analyze the effect of the correlation length of the layer on focusing of the nonlinear beam. However, from a general point of view, at a certain amount of the introduced phase shift, this phase layer must exhibit special features in focusing of different harmonics. In the present work, the phase shift was chosen to provide specific ”resonance” conditions for certain harmonics. Also, a wider set of harmonics was analyzed that includes the first six harmonics and thus allows to study features of the focusing process of the finite-amplitude beam in the considered scheme in more detail. Numerical simulation has shown that the action of the phase layer of the proposed type on the field of higher order harmonics is indeed selective. The results obtained in the modeling were also validated in the experiment.

It should be noted that synthesis of a layer with specified statistical properties is a separate interesting and important problem. Similar problems arise, for example, in development of random ultrasound arrays for medical applications (Gavrilov & Hand, 2000a). An essential circumstance in this situation is the necessity to take into account the technological limitations and, as a consequence, application of a pseudorandom algorithm and its optimization.

§4.2 Theoretical model and numerical algorithm: the Westervelt equation

4.2.1 The Westervelt equation

Nonlinear, diffraction and absorption effects in the focused ultrasound beam are described here using the Westervelt equation (Westervelt, 1963):

$$\frac{\partial^2 p}{\partial t^2} - c_0^2 \Delta p = \frac{\varepsilon}{\rho_0 c_0^2} \frac{\partial^2 p^2}{\partial t^2} + \frac{\delta}{c_0^2} \frac{\partial^3 p}{\partial t^3}. \tag{4.1}$$

In the retarded system of coordinates the equation can be written in the form (see Appendix. B):

$$\frac{\partial^2 p}{\partial \tau \partial z} = \frac{c_0}{2} \Delta p + \frac{\varepsilon}{2\rho_0 c_0^3} \frac{\partial^2 p^2}{\partial \tau^2} + \frac{\delta}{2c_0^3} \frac{\partial^3 p}{\partial \tau^3}. \tag{4.2}$$

Here p is the acoustic pressure, z is the spatial coordinate along the beam axis, $\tau = t - z/c_0$, t is time, $\Delta p = \partial^2 p/\partial x^2 + \partial^2 p/\partial y^2 + \partial^2 p/\partial z^2$, x and y are spatial coordinates lateral to z; ρ_0, c_0, ε and δ are the density, ambient sound speed, nonlinearity coefficient, and absorption coefficient of the medium, respectively. The values of physical parameters in the the Eq. (4.1) were chosen to correspond to water: $\rho_0 = 1000$ kg/m^3, $c_0 = 1486$ m/s, $\varepsilon = 3.5$, $\delta = 4.33 \cdot 10^{-6}$ m^2/s. Equation (4.2), which governs the propagation of nonlinear waves in a thermoviscous medium in the positive direction of the z axis, was widely used in many studies to simulate weakly nonlinear and weakly focused fields generated by diagnostic ultrasound transducers (Zemp *et al.*, 2003, Varslot & Taraldsen, 2005). Note that, unlike the widely used Khokhlov-Zabolotskaya equation (Khokhlova *et al.*, 2006, Jing & Cleveland, 2007), Eq. (4.1) does not assume that the diffraction angles are small. In this work, the characteristic dimensions of the studied inhomogeneities are of few wavelengths long; therefore, the diffraction effects must be taken into account more accurately, than using parabolic approximation.

For the convenience of the numerical solution, the Eq. (4.2) was rewritten in terms of dimensionless variables as following:

$$\frac{\partial^2 P}{\partial\theta\partial Z} = \frac{1}{2k_0 z_l}\Delta P + \frac{N}{2}\frac{\partial^2 P^2}{\partial\theta^2} + A\frac{\partial^3 P}{\partial\theta^3}. \tag{4.3}$$

Here $P = p/p_0$, p_0 is normalization pressure, $\theta = \omega\tau$, ω is a fundamental angular frequency, the spatial coordinates $Z = z/z_l$, $X = x/z_l$, $Y = y/z_l$ are normalized to the wavelength of the fundamental frequency $z_l = \lambda = 2\pi/k_0$, $k_0 = \omega/c_0$. The Eq. (4.3) includes two dimensionless parameters: a nonlinear coefficient N and absorption coefficient A:

$$N = \frac{\beta\omega z_l p_0}{\rho_0 c_0^3} = \frac{z_l}{z_N},\ A = \frac{\delta\omega^2 z_l}{2c_0^3} = \frac{z_l}{z_A}. \tag{4.4}$$

These coefficients are inversely proportional to nonlinear z_N and absorption z_A characteristic lengthes, respectively:

$$z_N = \frac{\rho_0 c_0^3}{\beta\omega p_0},\ z_A = \frac{2c_0^3}{\delta\omega^2}. \tag{4.5}$$

In the following, the intermediate equations will be given for non-normalized pressure p and simulations results – for dimensionless variable P.

The Eq. (4.2) will be used in the next chapter 5 to model three-dimensional nonlinear fields generated by two-dimensional multi-element phased arrays, which are used in therapeutic applications of high intensity focused ultrasound (HIFU). In spite of using almost the same methods to solve the Eq. (4.2), the modeling of HIFU impose more numerical difficulties which are primarily due to strong nonlinear effects and to formation of shock waveforms in the focus. Also, great dimensions of the array in comparison to the wavelength at fundamental frequency increase numerical burden. Thus, certain important optimizations of the algorithm are needed which will be discussed in the next chapter. Here only the basic version of the algorithm is reported which is sufficient to calculate the propagation of the weakly nonlinear beam.

4.2.2 Numerical algorithm

First-order operator splitting

The method of fractional steps with the operator splitting of the first order, used in the previous chapters 1 and 3, was also employed here to separate the nonlinear, diffraction and absorption physical effects over the grid step along the coordinate z. According to the method, the Eq. (4.2) was divided into simpler equations for diffraction,

$$\frac{\partial^2 p}{\partial \tau \partial z} = \frac{c_0}{2} \Delta p, \tag{4.6}$$

nonlinearity,

$$\frac{\partial p}{\partial z} = \frac{\beta}{2\rho_0 c_0^3} \frac{\partial p^2}{\partial \tau} \tag{4.7}$$

and absorption,

$$\frac{\partial p}{\partial z} = \frac{\delta}{2c_0^3} \frac{\partial^2 p}{\partial \tau^2}. \tag{4.8}$$

The nonlinear, diffraction and absorption effects were evaluated sequentially one after another on each step Δz along the wave propagation coordinate z. The simulation was performed entirely in the spectral domain and the solution to Eq. (4.2) was represented in the form of a finite Fourier series expansion as following (Bessonova *et al.*, 2009):

$$p(\tau, x, y, z) = \sum_{n=-N_{\max}}^{n=N_{\max}} p_n(x, y, z) \exp(-in\omega\tau). \tag{4.9}$$

Because the nonlinear effects were assumed to be sufficiently weak, the typical calculations used $N_{\max} = 8$ and the first six harmonics were then analyzed.

Nonlinearity and absorption operators

The nonlinear operator was calculated at each node of the mesh on the transverse spatial coordinates using the fourth order Runge-Kutta method. The set of nonlinear coupled equations for the harmonic amplitudes in the Fourier series expansion (4.9) was solved (Khokhlova *et al.*, 2002):

$$\frac{\partial p_n}{\partial z} = \frac{in\beta\omega}{\rho_0 c_0^3} \left(\sum_{k=1}^{N_{\max}-n} p_k p_{n+k}^* + \frac{1}{2} \sum_{k=1}^{n-1} p_k p_{n-k} \right), \tag{4.10}$$

where p_n^* denotes the complex conjugate harmonic amplitude.

The absorption term was calculated in the frequency-domain using an exact solution for each harmonic:

$$p_n(x, y, z + \Delta z) = p_n(x, y, z) \exp(-\Delta z \omega_n^2 \delta / 2c_0^3), \tag{4.11}$$

where ω_n is the angular frequency of the n-th harmonic. Another types of absorption and dispersion relations are allowed in the algorithm, for example, characteristic for biological tissues (Hill *et al.*, 2002). It should be noted, that weak absorption in water did not have an noticeable effect on the results under the conditions considered here.

Diffraction operator and angular spectrum method

The diffraction operator (4.6) was calculated for each of the harmonics by the angular spectrum method using 2D FFTs in spatial coordinates (Zemp *et al.*, 2003, Varslot & Taraldsen, 2005, Christopher & Parker, 1991b). According to this method, complex pressure amplitude of the n-th harmonic in the plane (x, y) at the distance z is expanded by fast Fourier transform into a two-dimensional spectrum $\widehat{p}(k_x, k_y, z)$ over spatial frequencies (k_x, k_y). The angular spectrum components $\widehat{p}(k_x, k_y, z + \Delta z)$ at the next step in the propagation distance were calculated by multiplying the spectrum by the corresponding phase factor (Appendix B):

$$\widehat{p}(k_x, k_y, z + \Delta z) = \widehat{p}(k_x, k_y, z) \exp\left[i\Delta z\sqrt{(k_n^2 - k_x^2 - k_y^2)} - i\Delta z k_n\right], \qquad (4.12)$$

where $k_n = n\omega/c_0$ is the wavenumber of the n-th harmonic. The phase factor is also called as the transfer function or the propagator for a particular harmonic component (Goodman, 1996). Note also that the angular spectrum method can be easily modified to calculate the diffraction effects in a parabolic approximation by replacing the phase factor as follows:

$$\widehat{p}(k_x, k_y, z + \Delta z) = \widehat{p}(k_x, k_y, z) \exp\left[-i\Delta z(k_x^2 + k_y^2)/(2k_n)\right]. \qquad (4.13)$$

The inverse FFT gives the pressure field at the next step $z + \Delta z$.

Evaluation of the diffraction operator using the angular spectrum method is a much more computationally effective alternative to the direct summation of the Rayleigh integral due to the use of the FFT (Christopher, 1997, Zemp *et al.*, 2003). However, the angular spectrum method has certain limitations. First, the method assumes that the angular spectrum components of the pressure field propagate only in the forward half space (in this case, in the positive direction of the z axis) and, thereby, backscattering to the backward half space is ignored. However, if the backscattering is weak, it can be assumed that the wave field is described accurately enough (Varslot & Masoy, 2006).

Another limitation of the angular spectrum method is related to the fact that the finite spatial window for the field $p_n(x, y, z)$ and periodic boundary conditions over the coordinates x and y are used. In the case of the square region, its size $L = L_x = L_y$ determines the maximal finite sampling step $\Delta k = 2\sqrt{2}\pi/L$ in the spatial frequency domain along the radial direction $k = \sqrt{k_x^2 + k_y^2}$. The propagator in the Eq. (4.12) depends on the spatial frequencies in an oscillating manner. The frequency of these oscillations is tending to infinity as $\sqrt{k_x^2 + k_y^2} \to k_0$. Thus, sampling with a nonzero step Δk in spatial frequency domain unavoidably produce aliasing error which appears as artificial waves coming from the periodical boundaries of the physical domain. To suppress these artificial waves, at each step in the propagation distance, the amplitudes of spectral components were set to zero beyond a circle of radius $k_{\max}$, i.e., in the region $k_x^2 + k_y^2 > k_{\max}^2$

(Zemp *et al.*, 2003). The radius of the circle for each harmonic was defined by the relation $k_{\max} = k_n/\sqrt{z^2\Delta k^2/\pi^2 + 1}$, which correspond to cut-off of the spatial frequencies that cannot adequately be represented sampling the spectrum with the step size Δk. Thus, the accuracy of calculation of the diffraction operator becomes somewhat lower, since the parts of angular spectrum propagating in the intervals of angles between the vector $\vec{k}$ and the z axis from $\arcsin k_{\max}/k_0$ to $90°$ are excluded. Nevertheless, in many practically important cases, when the angle of focusing of the transducer is not extremely high, this solution proves to be sufficiently accurate (Wu *et al.*, 1997).

When arriving at the phase layer, the field of each harmonic was multiplied by a phase factor determined by the phase layer:

$$p_n^{scr}(x, y, z) = p_n(x, y, z)\exp\left[in\phi(x, y)\right],\ n = 1, \ldots 8, \tag{4.14}$$

where the function $\phi(x, y)$ describes phase variations in the layer at the fundamental frequency $(n = 1)$. The quantities $p_n^{scr}(x, y, z)$ and $p_n(x, y, z)$ are harmonic fields after and before the phase layer, respectively.

The x- and y-axis dimensions of the spatial window in simulations were $L_x = L_y = 143.4$ mm, and steps were $dx = dy = 0.14$ mm (1024×1024 points). Zeroing of the propagator at these parameters yields the maximum diffraction angle of $36°$ at the distance $z = 72$ mm, while the angular half-aperture of the transducer, used in simulations is $15°$ about. Thus, the parameters of numerical algorithm were chosen correctly. The propagation step was $dz = 0.5$ mm; calculations were performed up to the geometrical focus of the transducer. The accuracy of the algorithm was tested *via* comparison with the analytical solution for the linear field of the focused circular piston radiator on the axis. The relative error was less than 1%.

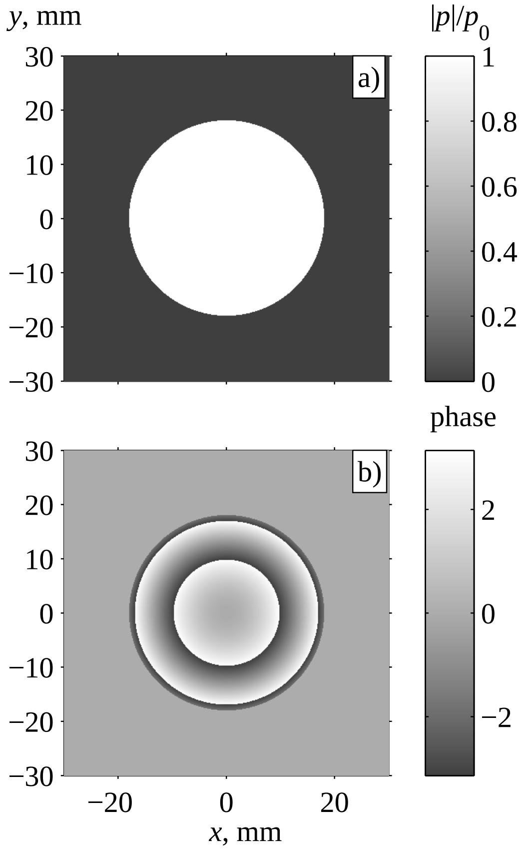

Figure 4.2: The pressure magnitude in the plane $z = 0$ in the case of circular focused piston.

4.2.3 Boundary conditions

A circular focused piston transducer was used (Fig. 4.2) as the boundary condition in the plane $(x, y, z = 0)$ for a theoretical analysis of the problem (§4.3-4.4). The radius was set as $R = 18$ mm, the focal distance as $F = 70$ mm, amplitude of the acoustic pressure at the surface of the transducer – $p_0 = 0.45$ MPa, the phase was set to $k_0\sqrt{x^2 + y^2}/2F$ to produce focusing. In the given conditions the difference between the field calculated from the plane piston and from the curved spherical cup of the

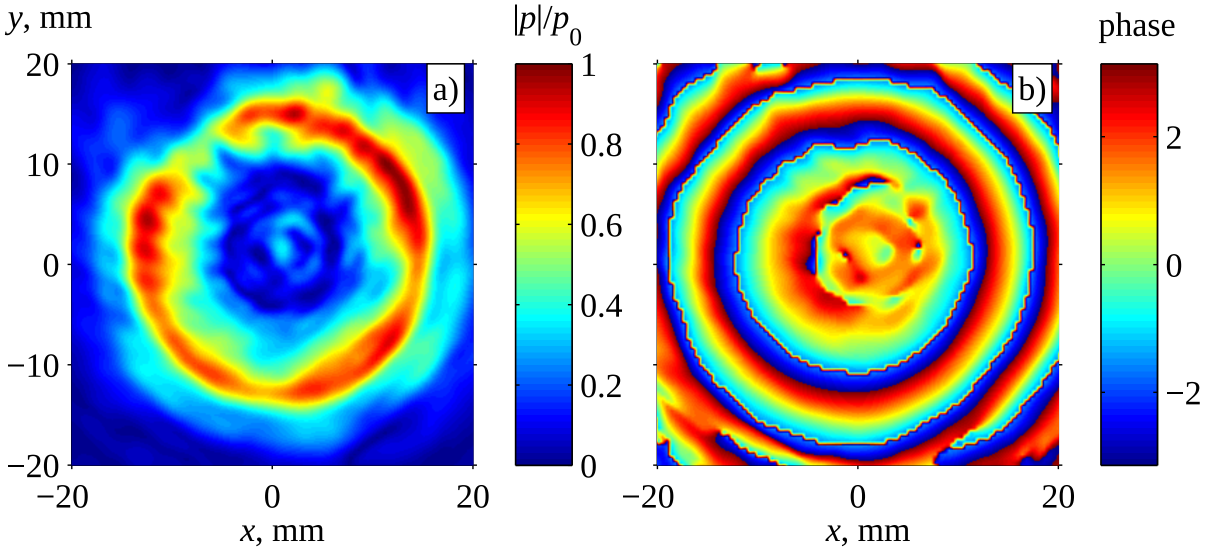

Figure 4.3: The amplitude (a) and phase (b) in the source plane $z = 0$ mm, obtained using the acoustic holography method.

same radius is less than 2%, so it is acceptable to use of the plane circular piston as the boundary condition.

For comparison between the theory and the measurements the boundary condition was modified to better simulate the experiment. The amplitude and phase distributions in the source plane $z = 0$ were obtained using the acoustic holography method (Sapozhnikov *et al.*, 2003) at a low excitation voltage applied to the transducer, which provided linear wave propagation conditions. It was assumed that, in the further measurements, this distribution remains unchanged at the higher transducer excitation levels. These amplitude and phase distributions are shown in Fig. 4.3a and Fig. 4.3b, respectively. It is seen from the amplitude distribution, that the central part of the source does not radiate ultrasound. Such radiation pattern is consistent with the source design, shown below in the photo in the Fig. 4.13c. The source is composed from two piezoelectric plates, one of which has big diameter and operates at 1.1 MHz frequency; the second smaller plate is in the center and has operating frequency of 6.6 MHz. The high frequency plate hides the central part of the big plate and thus prevent the ultrasound radiation from this zone. Ultrasound focusing was achieved using an acoustic lens. The magnitude of the source pressure distribution in the calculations was chosen such that, in the homogeneous medium, the agreement between the theoretical and experimental axial and focal distributions of the first and second harmonics was the best. The focal distance of the real transducer was equal to 72 mm.

4.2.4 Focusing quality criterion

Various parameters of the acoustic field are of interest in studies of the nonlinear beam propagation: harmonic amplitudes, peak pressures, intensity, overall power of the beam. In this work, such parameter as a degree of the focusing degradation (or conservation) after passing the phase layer will be studied. To determine the degree to which the phase layer maintains or destroys the focusing, an energy criterion similar to that introduced in studies (Tabei *et al.*, 2003, Yan, 2004)

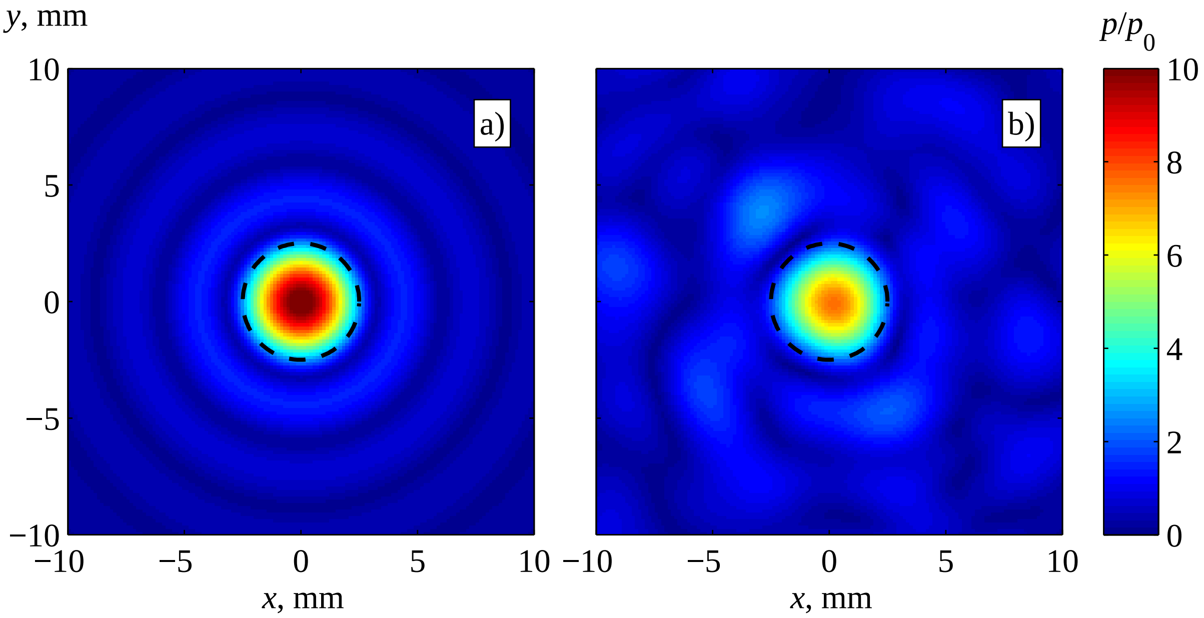

Figure 4.4: An illustration to definition of the focusing quality criterion for the first harmonic: the magnitude of the harmonic in the focal plane $z = F$ without the phase layer in the beam path (a) and with it (b). The focal area is defined from the *undisturbed* focal distribution at the -6 dB level from its the maximum value.

was used. The parameter relies on calculation of the portion of the beam energy concentrated within the main focal maximum at frequency of the each harmonics (Fig. 4.4). However, there are some differences between the definitions. In the present work a ratio α_n of the beam power at the frequency of the n-th harmonic within the main focal maximum, W_n, to the total beam power, W_{0n}, at the same frequency, was calculated ($\alpha_n = W_n/W_{0n}$), rather than to the total power outside the focal maximum, $W_{0n} - W_n$, as it was done in (Tabei *et al.*, 2003, Yan, 2004). The normalized quantity

$$Q_n = \frac{\alpha_n^{scr}}{\alpha_n^0} \,, \tag{4.15}$$

where α_n^{scr} is calculated in the presence of the layer (Fig. 4.4b), and α_n^0 – without it (Fig. 4.4a), characterizes the degree to which the n-th harmonic of the beam remains focused after it passes through the layer. The size of the central focal region was estimated from the *undisturbed* focal distribution at the -6 dB level from its maximum value, by analogy with procedures established for determining the space-averaged focal intensity (Hill *et al.*, 2002). In the Fig. 4.4 the focal region is marked by a dashed circle. The total destruction of the focal region corresponds to $Q_n \to 0$; focusing without the phase layer is characterized by $Q_n = 1$. The focusing quality Q_n was calculated for the first six harmonic components of the beam.

The established focusing quality criterion has a simple geometrical sense. The criterion gives an information whether or not the focus maintains its regular form, but it does not provide knowledge about the power and intensity within the focal region at the frequency of each harmonics. Additionally, the criterion has a low value in case, if the focal maximum maintains its form, but it

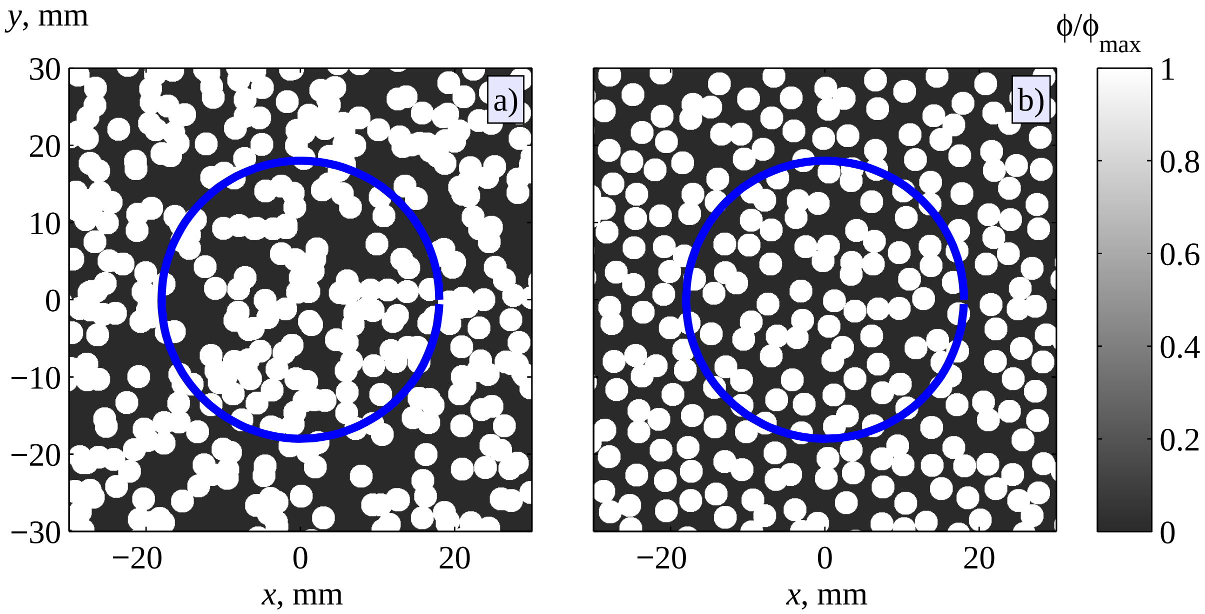

Figure 4.5: Examples of two phase layers: one of the layers is characterized by totally random positions of the circular elements (a), in the second one the elements were randomly moved from centers of a triangular grid (b). The cover ratio is equal to 0.5 for both screens, the diameter of circles $d = 3$ mm. Blue circles show dimensions of the transducer.

is slightly moved away from the initial centered position. Studies on energetic characteristics of the beam for each harmonic component are subject of another research.

4.2.5 Theoretical model of the phase layer

A special phase layer model was developed to selectively change the focusing quality of different harmonics in the beam. The proposed phase layer consists of a great number of identical circular regions of diameter d randomly distributed on a plane that introduce a fixed phase shift $\phi_{\max}$. This means that the phase shift in an arbitrary point on the plane (x, y) is either zero or $\phi_{\max}$. One more important characteristic of the phase layer is a cover ratio equal to the phase averaged over the plane, $\bar{\phi} =< \phi(x, y) >$, divided by the maximal phase shift: $\eta = \bar{\phi}/\phi_{\max}$. A prototype of the proposed phase layer model was first found in the experimental part of the study (Yan, 2004). Here, an idea to set the "resonant" phase shifts, equal to $180°$ or $360°$ for certain harmonics, was explored. It will be shown below, that such phase shifts lead to destruction of the focusing for some harmonics and maintain focusing quality for the others.

Two methods to spread the circles of the phase shift $\phi_{\max}$ over the layer plane were considered. In the first method coordinates x and y of the circles centers were independent random numbers (Fig. 4.5a), uniformly distributed in the given rectangle area. The phase shift in domains of intersections of the circles is supposed to be equal $\phi_{\max}$. The desired cover ratio η was adjusted by an average number of the circles per area unit. In the numerical simulations this phase layer does not impose difficulties in use. However, in the experiment, due to technical limitations of fabrication process, a condition of no intersection of the circles was necessary. To solve this problem the second method to spread the circles was proposed.

The second method imposed a mesh of equilateral triangles of side $D = d\sqrt{\pi/\sqrt{3}}$ over the surface (Fig. 4.6) and further displacements of the circle centers from the mesh nodes within a specified circle in an independent random manner. In Fig. 4.6, the circle area where the central circle was moved randomly is shown by dashed line and the similar area of the neighbor circle – by dash-dotted line. The radius of the circle for the random displacement of the centers to ensure non overlapping should be less than $0.5(D-d)$. However, using this radius, very arranged distribution of the circles was produced. So, the radius was set to $1.25(D-d)$ to increase random scattering of the circles, retaining, nevertheless, low probability of overlapping. An example of the resulting phase layer is shown in Fig. 4.5b, which demonstrates more arranged structure than the layer in Fig. 4.5a.

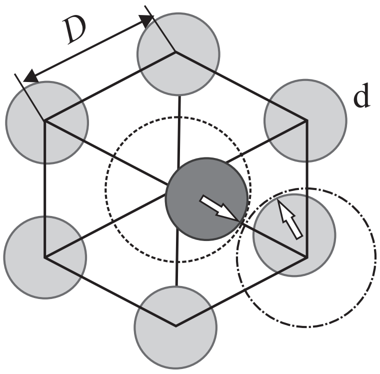

Figure 4.6: The method of random displacement of the circles to produce negligible overlap.

The cover ratio η for the given value of the triangles side D was equal to 0.5. This cover ratio value is important because in a series of preliminary simulations based on the linear model it was shown that, other conditions being the same, the maximum distortions of the focusing were achieved when the ratio of the circles surface to the layer surface was equal to 0.5. This proportion was used in all further nonlinear simulations. It was also verified that distortions of the focusing increase with the phase shift $\phi_{\max}$ in the circles and achieve their maximum at $\phi_{\max} = 180°$. The diameter of the circles also has an influence on the focusing quality. As the diameter d of the circles grows, distortion of the focusing decreases and a variance of the results over individual realization increases. Effect of the layer positioning along the beam axis was also considered. Naturally, closer position of the layer to the transducer results in the lower focusing quality. For example, for the layer parameters $\phi_{\max} = 180°$ and $d = 3$ mm, the focusing quality Q_1 is lower than 10% up to $z_{\mathrm{p}} = 0.8F$ position of the phase layer. Further approaching of the phase layer to the focus results in rapid growth of Q_1, and in the limit of $z_{\mathrm{p}} \to F$, the Q_1 is going to the unit.

Both models of the phase layer did not show a great differences concerning the focusing quality criterion. The phase layer model corresponding the example given in the Fig. 4.5a was used in the most of numerical simulations reported below. The other model, Fig. 4.5b, was use in the simulations performed for a more detailed comparison between the theory and the experiment. This phase layer model was also employed to fabricate physical realizations of the layer. Of course, other methods to spread the circles over the surface are possible, but they were not considered here.

Simulations were performed for different positions of the layer on the beam axis and for different values of the phase shift introduced by the layer inhomogeneities. Below, the most representative results for the cases of the $180°$ and $90°$ phase shifts at the fundamental frequency are provided.

§4.3 Modeling results: selective destruction of focusing of odd harmonics behind 180° phase layer

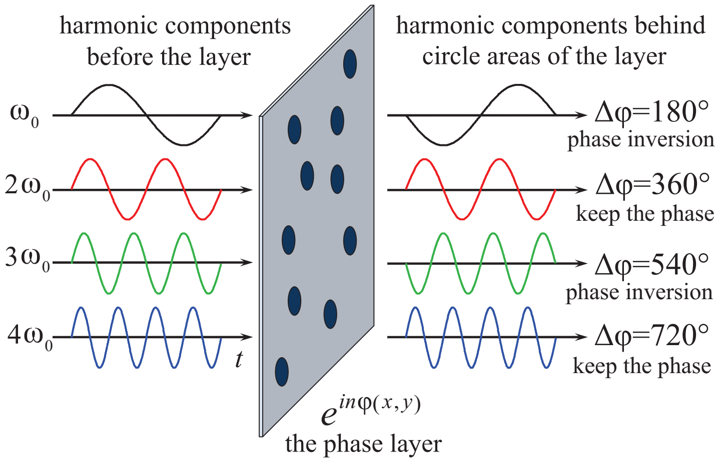

Figure 4.7: An illustration to explanation of phase distortions introduced by the 180° phase layer.

Main principle of phase distortions, introduced by the 180° phase layer is explained in Fig. 4.7. Initially, different harmonics in the beam propagate in phase. After passing the layer, the beam components beyond the circle inhomogeneities change their phase of the fundamental and other odd harmonics frequencies by the angle equivalent to 180°. The phase of the second and other even harmonics is changed by the angle equivalent to zero phase shift (360°, 720°, *etc*). In a further propagation, highly disturbed wave front of the fundamental and odd harmonics will lead to destruction of their focusing. On the contrary, even harmonics should be focused well.

Examples of focal distributions of pressure magnitudes for the first 6 harmonics, obtained in simulations with 180° phase layer are shown in Fig. 4.8. The layer position on the axis was

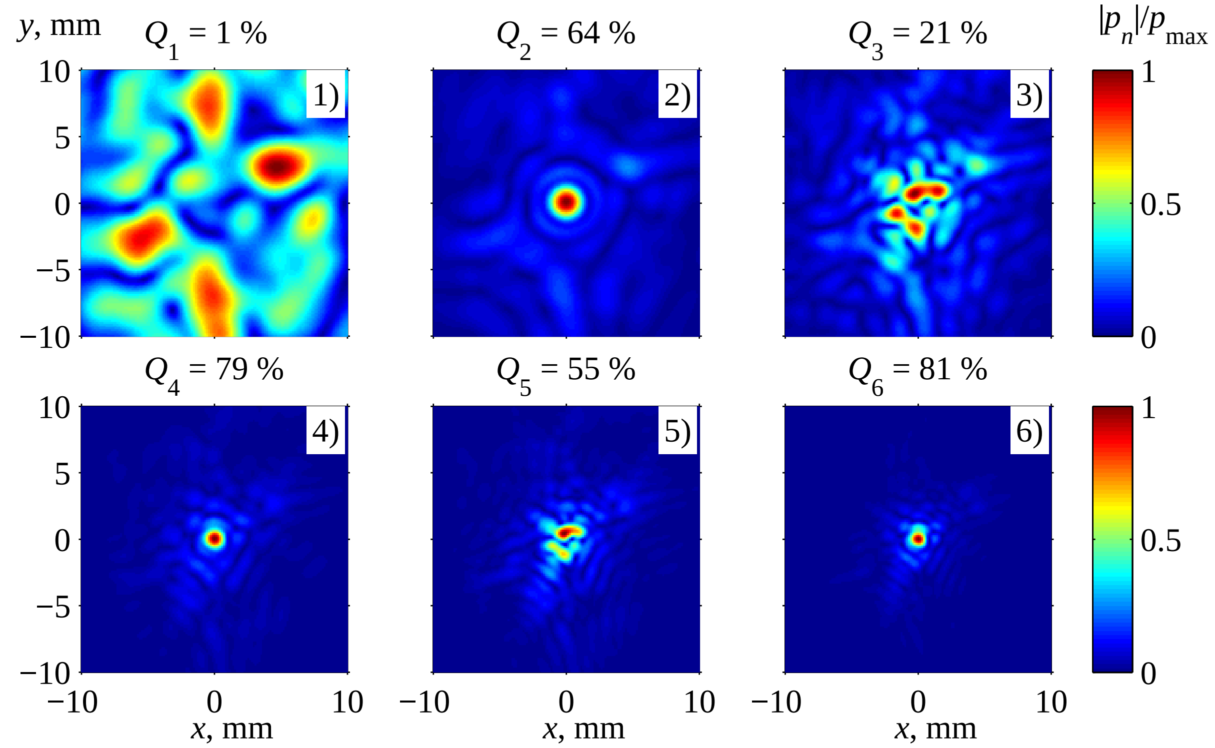

Figure 4.8: Spatial distributions of the pressure magnitude of the first 6 harmonics (number in the corner) in case of the 180° phase layer ($d = 3$ mm) placed at $z_{\mathrm{p}} = 0.5F = 35$ mm distance from the source. The focusing quality Q_n is given at the top of each image. The characteristic feature of the example is low focusing quality of the odd harmonics and high quality of even harmonics.

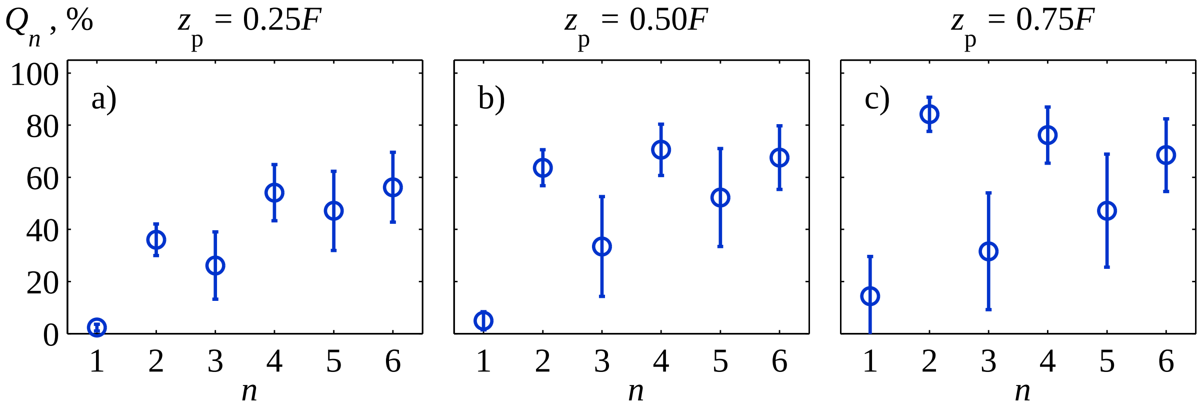

Figure 4.9: Mean values of the focusing quality Q_n for the first 6 harmonics in a case of the 180° phase layer placed at distances $z_{\mathrm{p}} = 0.25F$ (a), $z_{\mathrm{p}} = 0.50F$ (b), and $z_{\mathrm{p}} = 0.75F$ (c) from the source. Averaging was done using 10 realizations, error bars correspond to standard deviations.

$z_p = 0.5F$. As it was expected, the characteristic feature of this example is high distortion of the beam at the fundamental and odd harmonics frequencies ($Q_1 = 1\%$, $Q_3 = 21\%$, $Q_5 = 55\%$). In the focal distributions of these harmonics several random spread peaks are observed. At the same time, focusing of the even harmonics is essentially less disturbed ($Q_2 = 64\%$, $Q_4 = 79\%$, $Q_6 = 81\%$). The main central peak is almost intact, only background noise is introduced by the phase layer.

In Fig. 4.9 calculated mean values of Q_n are shown (circles) as well as standard deviations (error bars) obtained from statistical analysis of 10 realizations. The simulations were performed for three positions of the layer on the axis: $z_{\mathrm{p}} = 0.25F$ (a), $z_{\mathrm{p}} = 0.50F$ (b), and $z_{\mathrm{p}} = 0.75F$ (c). The statistical data confirms conclusions obtained from one realization: the even harmonics have better focusing quality than the odd ones.

The data presented in the Fig. 4.9 shows, that as the index n of a harmonic increases, the differences of Q_n parameter values between the even and the odd harmonics decreases due to increasing of the focusing quality of the odd harmonics. This recovery of the focusing of the higher harmonics can be explained as a result of nonlinear interactions that continue after passing the layer, but less efficiently in comparison to the propagation of the undisturbed beam. For example, well focused field of the second harmonic can interact with the scattered field of the fundamental frequency, partially recovering the focusing of the third harmonic. On the other hand, the direct effect of the 180° phase layer on the focusing destruction of the higher harmonics, i.e. without taking into account the nonlinear interactions, is smaller than on the fundamental component. This is because to the fact that beam's cross section at the frequencies of harmonics is decreasing for higher harmonic numbers. So, the effective diameter of circle inhomogeneities increases relative to the cross section, and, as it was mentioned above, the other conditions being the same, the distortions decrease if the diameter increases. Also, it is seen from the Fig. 4.9a that placing the phase layer close to the source results in lower focusing quality of all harmonics: the odd ones are more destructed and Q_n of the even ones is lower in comparison to the case when the phase layer is placed closer to the focal plane (Fig. 4.9 b and c). When the layer is close to the source

($z = 0.25F$), the amplitudes of the harmonics are still low. As a consequence, a superposition of the weak undisturbed field of the odd harmonics with the field generated from strongly disturbed beam on the fundamental frequency leads to lowering quality of these odd harmonics.

§4.4 Modeling results: focusing distortions of the second harmonic behind $90°$ phase layer

In analogy to the Fig. 4.7, the principle of phase distortions introduced by the $90°$ phase layer is explained in Fig. 4.10. After passing the layer, the fundamental component changes its phase by $90°$ beyond the circle inhomogeneities. The phase of the second harmonic is changed by $180°$. The fourth harmonic does not change its phase, since the angle of $360°$ is equivalent to zero shift. Under these phase modulations, the focusing of the fundamental component should be disturbed to some extent; the strongest destruction is introduced for the second harmonic, and fourth harmonic should maintain high focusing quality. However, more complex distortion results are observed due to the nonlinear interactions between the harmonics. The effect depend on the phase layer position along the beam axis.

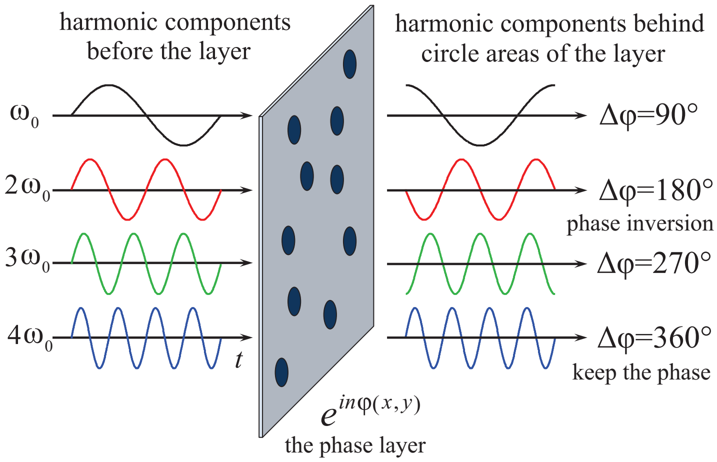

Figure 4.10: Phase distortions introduced by the $90°$ phase layer.

As mentioned above, the $90°$ case is of interest because it may reduce efficiency of the cascade processes of energy transfer to higher spectrum components due to the random defocusing and violation of interaction coherence between the first and second harmonics. The strong effect of modulating action of the layer on the second harmonic must be observed when the amplitude of the incidence wave onto the layer is already relatively high, i.e., when the layer is placed close enough to the focal point. On the other hand, if the layer is too close to the focus, the distortions will be lower, because the distance passed by the phase modulated wave from the layer to the focal point becomes shorter and because the effective circle diameter increases relative to the beam's cross section. So there should be some distance, where the modulating action of the layer on the focusing quality of the second harmonic is most efficient.

In Fig. 4.11 calculated mean values of Q_n are shown (circles) for the same positions of the phase screen as in the Fig. 4.9. It is interesting that even such a relatively high phase shift as $90°$ does not destroy focusing of the fundamental harmonic completely: the quality falls to the level of about $50 - 60\%$ for all layer positions represented in the Fig. 4.11.

When the layer is placed close to the source ($z_\mathrm{p} = 0.25F$, Fig. 4.11a), the harmonics are generated mostly behind the layer in the field of the distorted wave of the fundamental frequency.

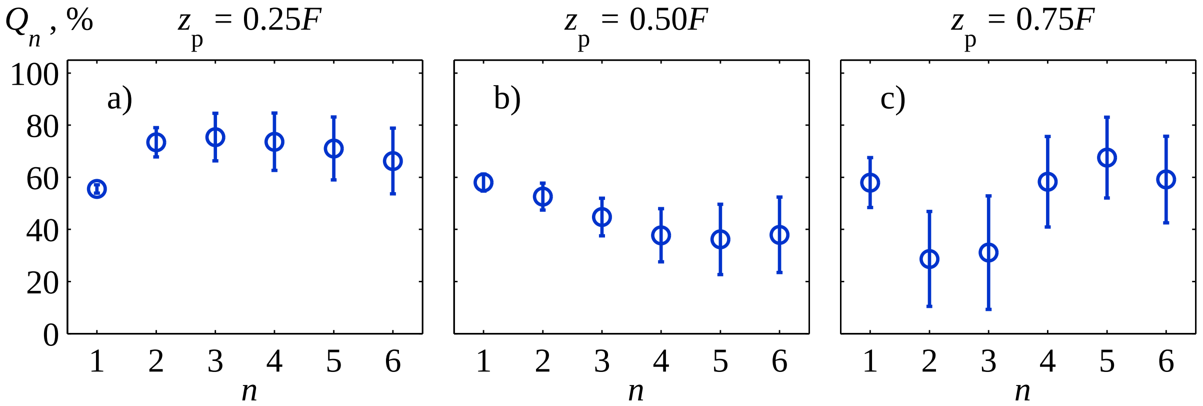

Figure 4.11: Mean values of the focusing quality Q_n for the first 6 harmonics in a case of the 90° phase layer placed at distances $z_\mathrm{p} = 0.25F$ (a), $z_\mathrm{p} = 0.50F$ (b), and $z_\mathrm{p} = 0.75F$ (c) from the source. Averaging was done using 10 realizations, error bars correspond to standard deviations.

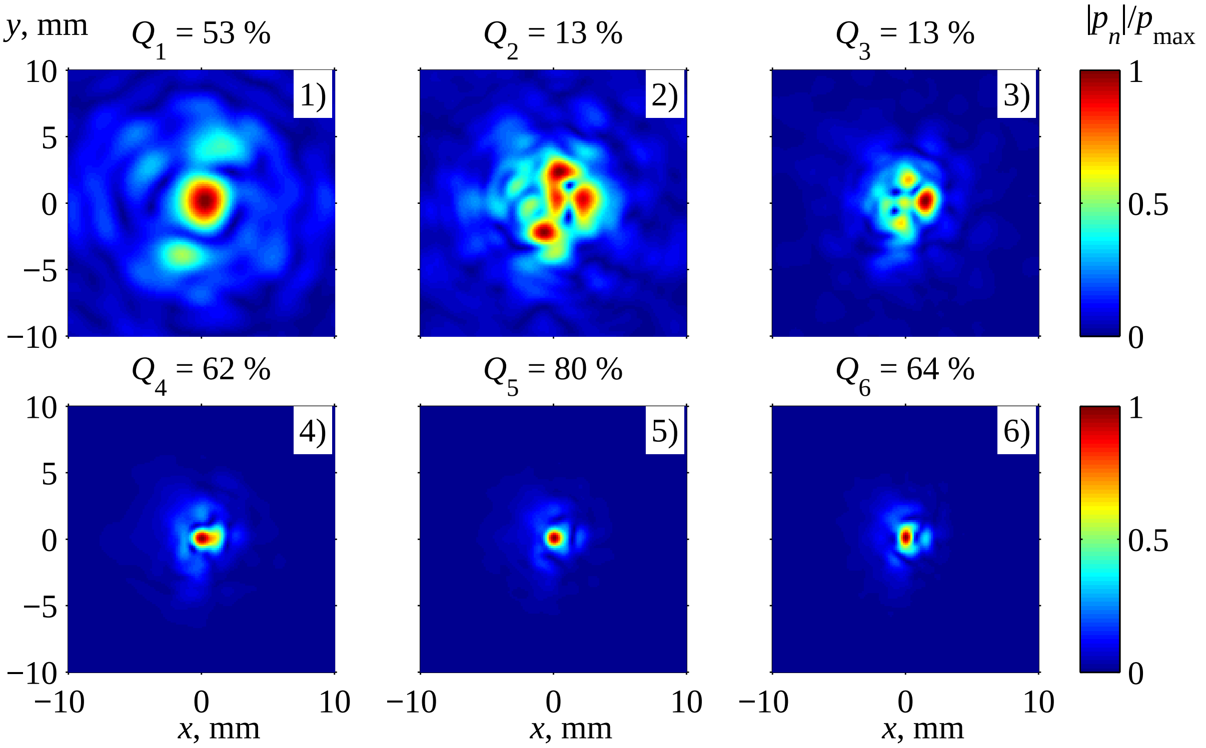

Figure 4.12: Spatial distributions of the pressure magnitude in the focal plane for the first 6 harmonics (number is given in the corner) in a case of the 90° phase layer ($d = 3$ mm) placed at $z_\mathrm{p} = 0.75F = 52.5$ mm distance from the source. The focusing quality Q_n is given at the top of each image.

The amplitude of the second harmonic at the layer is low, and random inversion of its phase does not produce a noticeable effect. It is seen that focusing of the higher harmonics is maintained better than focusing of the first harmonic ($Q_n > Q_1$ at $n > 1$). Thus, the assumption that conditions may exist under which the higher order harmonics are focused in the medium with inhomogeneities better than the fundamental component is corroborated by numerical simulations done for this layer position.

When the layer is positioned halfway between the transducer and its focal plane ($z_\mathrm{p} = 0.50F$, Fig. 4.11b), the amplitude of the second harmonic when passing the layer is already sufficiently high. Its strong modulation results in violation of the in-phase condition necessary for the cascade energy transfer up the spectrum in the process of further beam propagation. Thus, focusing of the higher-order harmonics appears to be destroyed stronger than that of the fundamental frequency component.

As the layer is moved further toward the focal point ($z_\mathrm{p} = 0.75F$, Fig. 4.11c), the amplitudes of not only the second, but also of the higher-order harmonics are sufficiently high and, therefore, the effect of random phase modulation of these harmonics can be observed in the focal plane. For the considered position of the phase layer, simulations predict an especially rapid decrease in the parameter Q_n for the second and third harmonics. On the contrary, for the fourth harmonic, Q_n is high, which is explained by the zero phase shift ($360°$ is equivalent to $0°$) at this frequency. Examples of focal distributions of the first 6 harmonics for the considered case are shown in Fig. 4.12. The relatively high focusing quality is observed at the fundamental frequency and very high quality for the 4-6 harmonics ($Q_4 = 62\%$, $Q_5 = 80\%$ and $Q_6 = 64\%$). On the contrary, the focusing of the second and third harmonics is strongly disturbed ($Q_2 = Q_3 = 13\%$).

§4.5 Experiment

The cases of resonant distortion of the field of the harmonics behind the layers of $180°$ and $90°$ phase shifts, considered theoretically above were compared with the experiment. Below, the experimental setup will be described, the results of the measurements are reported and comparison of the focusing quality parameter Q_n with numerical simulations, adopted to the experimental conditions, are provided.

4.5.1 Experimental setup and measurement methods

A simplified diagram of the experiment is shown in Fig. 4.1 and an overall view on the experimental setup is presented in Fig. 4.13a. A piezoelectric ultrasound transducer with a diameter of 36 mm, focal distance of 72 mm, and resonance frequency of 1.1 MHz, was placed in a water-filled tank. Ultrasound pulse parameters: duration of 25 periods (23 μs) and repetition frequency of 100 Hz were set by the Tektronix AFG-3102 generator. The output from the generator was fed to a special amplifier, which increased the amplitude of the excitation tone-bursts applied to the transducer up to 60 V. This amplification was necessary to provide efficient generation of harmonics of up to the sixth order as a result of propagation of the ultrasound beam to the focal plane. For the chosen parameters, in the absence of the layer, a positive peak pressure of 2.4 MPa was measured at the focus and the beam intensity at the focus was $140\ \mathrm{W/cm^2}$. The acoustic pressure was measured using a GEC-Marconi wideband membrane hydrophone with the membrane diameter of 100 mm and diameter of the active zone 0.5 mm (Fig. 4.13b). Irregularity of the hydrophone frequency response in the frequency range from 1 to 7 MHz was less than 3 dB. The hydrophone was scanned in the focal plane of the transducer using a Velmex BiSlide automatic positioning system. In most of the experiments, a region of 50×50 mm was scanned with the step size of 1 mm. When necessary, an additional scanning mesh was used in the central focal region with step size of 0.2

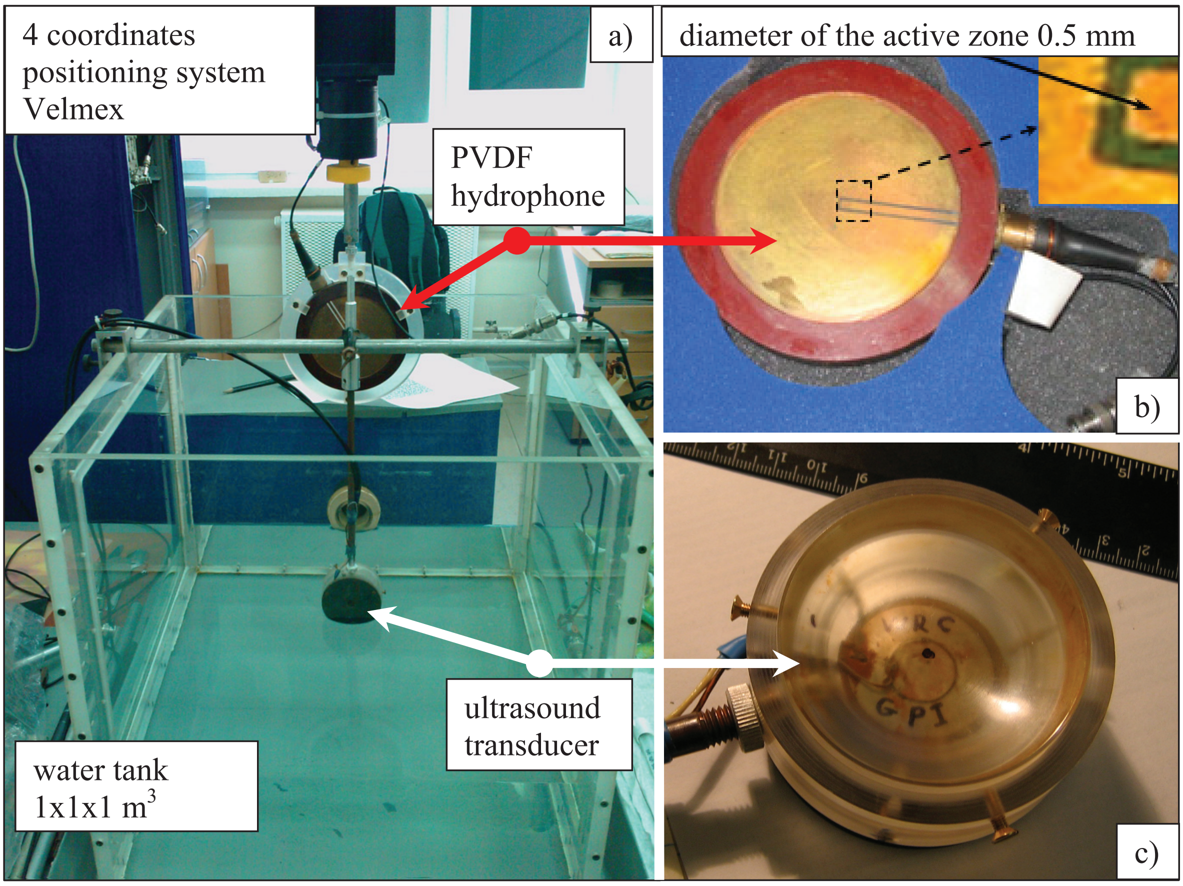

Figure 4.13: An overall view on the experimental setup (a) and photographs of PVDF hydrophone (b) and of transducer (c).

mm. The signal received by the hydrophone was transferred through a wideband preamplifier to a Tektronix TDS 340A oscilloscope. At each point, the measured signal was averaged over 16 samples and then Fourier analyzed to calculate complex pressure amplitudes p_n of the first six harmonics.

To calculate Q_n, the region was found in the focal field distribution of each n-th harmonic in the absence of the layer, where the pressure magnitude was not less than -6 dB of its central maximum. In this region, a sum of squares of absolute values of the complex amplitudes $|p_n|^2$ was calculated over the measurement mesh, which is proportional to the power W_n of the harmonic in the focal region. The quantity W_{n0}, proportional to the total power of the harmonic, was calculated through a similar summation over the entire measurement area. In this procedure, $|p_n|$ that did not exceed the noise amplitude were set to zero. Next, Q_n was calculated from the above relationships (sec. 4.2.4, Eq. 4.15).

4.5.2 Physical realization of the phase layer

The phase-modulating layer was placed between the transducer and the focal point perpendicular to the transducer axis. As in the study (Yan, 2004), the layer was prepared as polyethylene plate with identical cylindrical cavities following the theoretical model (sec. 4.2.5). The plate was 4.4 mm thick, and the cavity diameter was $d = 3$ mm. This diameter was chosen as a compromise between

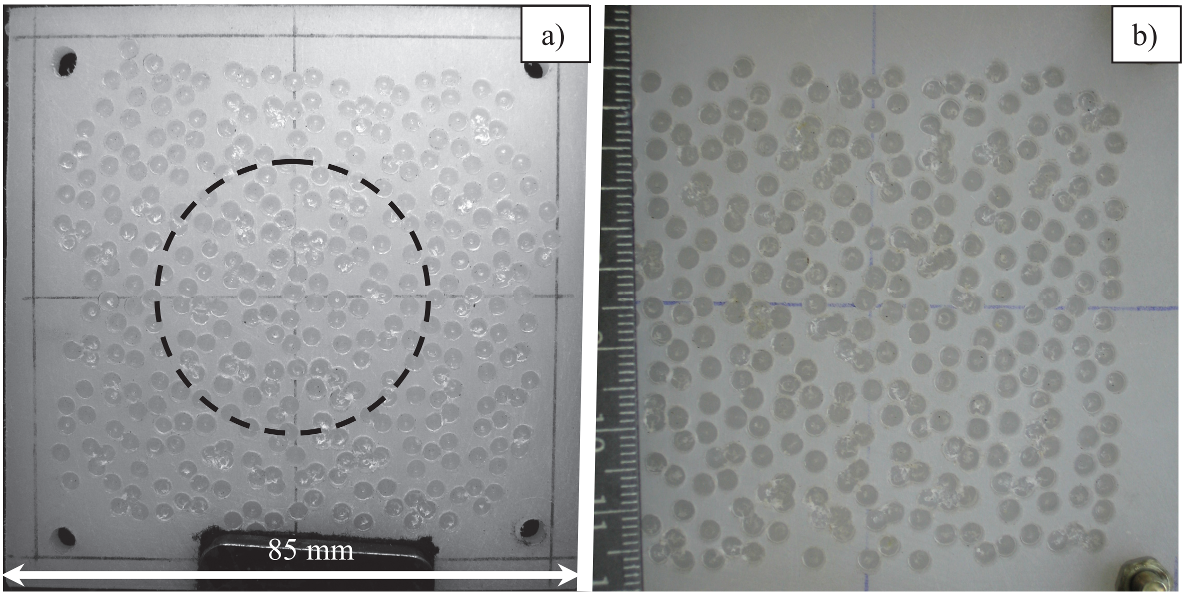

Figure 4.14: Images of the 90° – (a) and the 180° – (b) phase layers fabricated from low-density polyethylene. The dashed circle indicates the diameter of the source.

the number of cavities reasonable in fabrication and the desire to achieve significant focusing distortions in the experiments. The layer was fabricated of low-density polyethylene (PE-LD). The velocity of the longitudinal waves in the layer was $c_{\mathrm{pe}} = 1950 \pm 50\ \mathrm{m/s}$, the density was $\rho_{\mathrm{pe}} = 920\ \mathrm{kg/m^3}$ (Selfridge, 1985), and the acoustic impedance was $c_{\mathrm{pe}}\rho_{\mathrm{pe}} = 1.80 \pm 0.05 \times 10^6\ \mathrm{kg/m^2 s}$. The closeness of the polyethylene and water impedances ($c_{\mathrm{w}}\rho_{\mathrm{w}} = 1.49 \times 10^6\ \mathrm{kg/m^2 s}$) provided good acoustic matching of these two media.

Absorption of ultrasound in the layer was measured over the frequency range from 1 to 7 MHz using a wideband version of insert/substitution method (Gong *et al.*, 1989). For the 1-6 harmonics the absorption was $50\ \mathrm{m^{-1}}$, $120\ \mathrm{m^{-1}}$, $180\ \mathrm{m^{-1}}$, $250\ \mathrm{m^{-1}}$, $320\ \mathrm{m^{-1}}$, and $390\ \mathrm{m^{-1}}$, respectively. Note, that allowance for absorption in the layer in the simulations negligibly affected the results provided below. The wave transmission coefficient (in terms of the acoustic pressure) measured for a 4.4-mm-thick flat polyethylene plate at 1.1 MHz and at normal incidence in water was 0.8. However, in the simulations transmission losses were not taken into account.

In the experiments two phase layers fabricated from the same realization were used: with 1.4 ± 0.1 mm and 2.8 ± 0.1 mm deep cylindrical cavities, which corresponded to the phase shifts of the fundamental component on the layer inhomogeneities of $90°$ and $180°$ with an error less than 8% and 4%, respectively. The photo of $90°$ phase layer is shown in Fig. 4.14a and the photo of $180°$ layer – in Fig. 4.14b. The dashed circle shows the dimensions of the transducer.

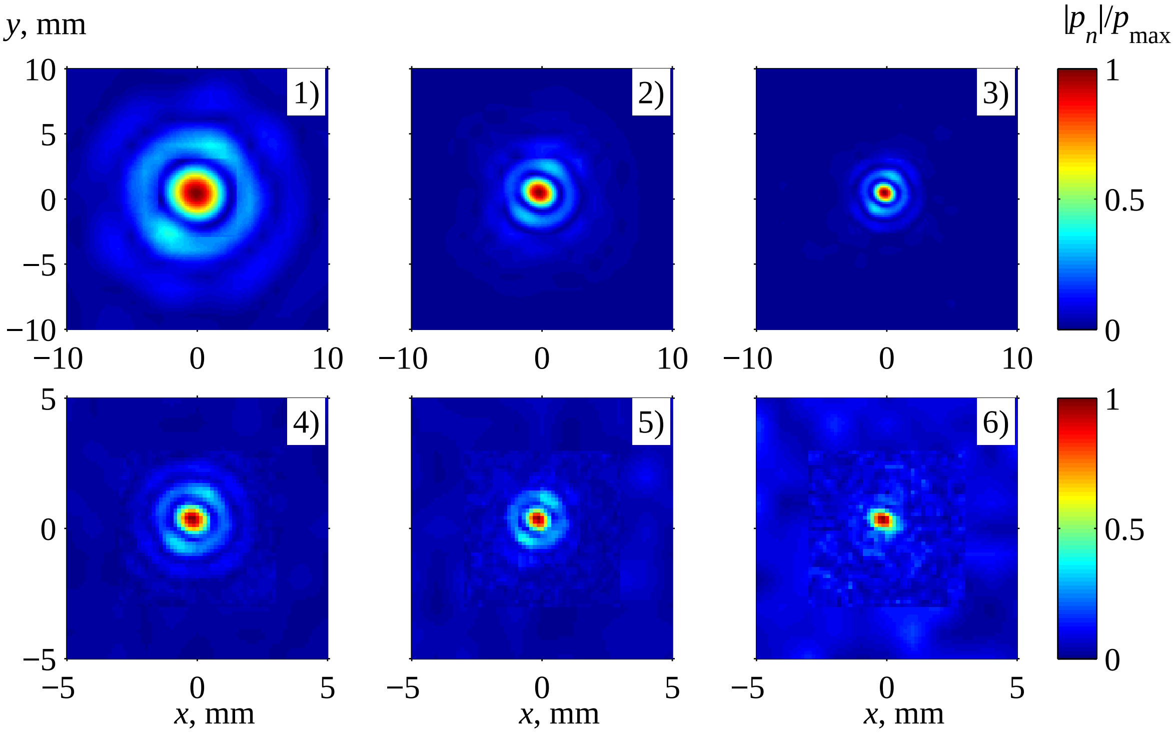

Figure 4.15: Pressure magnitudes of the first 6 harmonics in the focal plane (the number is in the corner), measured without the phase layer. The amplitudes are normalized on their peak values $p_{\max}$, equal to 2000, 420, 150, 55, 28 and 14 kPa, respectively.

4.5.3 Experimental results and discussion

Acoustic field without a phase layer

The focal distributions of the first 6 harmonics measured without the phase layer are shown in Fig. 4.15. The scale of a lower row of the figures (4-6 harmonics) is two times greater in comparison to the higher row. Here experimental data from two measurement series were used: one with large scanning step of 1 mm and second with smaller scanning step of 0.2 mm. Both data sets were interpolated on the common grid with step sizes $dx = dy = 0.14$ mm, which are equal to those used in the simulations. Usual narrowing of focal distributions is observed. For example, the size of the central maximum at -6 dB threshold is 4.1 mm, 2.2 mm 1.5 mm, 1.2 mm, 1.2 mm and 1.2 mm respectively for 1-6 harmonics. The harmonics focal distributions are normalized to their maximal values which are equal to 2000, 420, 150, 55, 28 and 14 kPa, respectively from the first to sixth harmonic. Measurements of the higher harmonics are difficult due to their small amplitude and small size of the focal spot. Thus, noticeable noise can be seen in the distributions of the 4-6 harmonics. This noise will complicate the experimental data analysis when the phase layer will be placed on the beam path, since, in general, magnitudes of the harmonics will be 5-10 lower in comparison to the case without the phase layer. Remember, that in this case without the phase layer, focusing quality of all harmonics has highest possible value $Q_n = 100\%$, $n = 1, 2, \ldots, 6$.

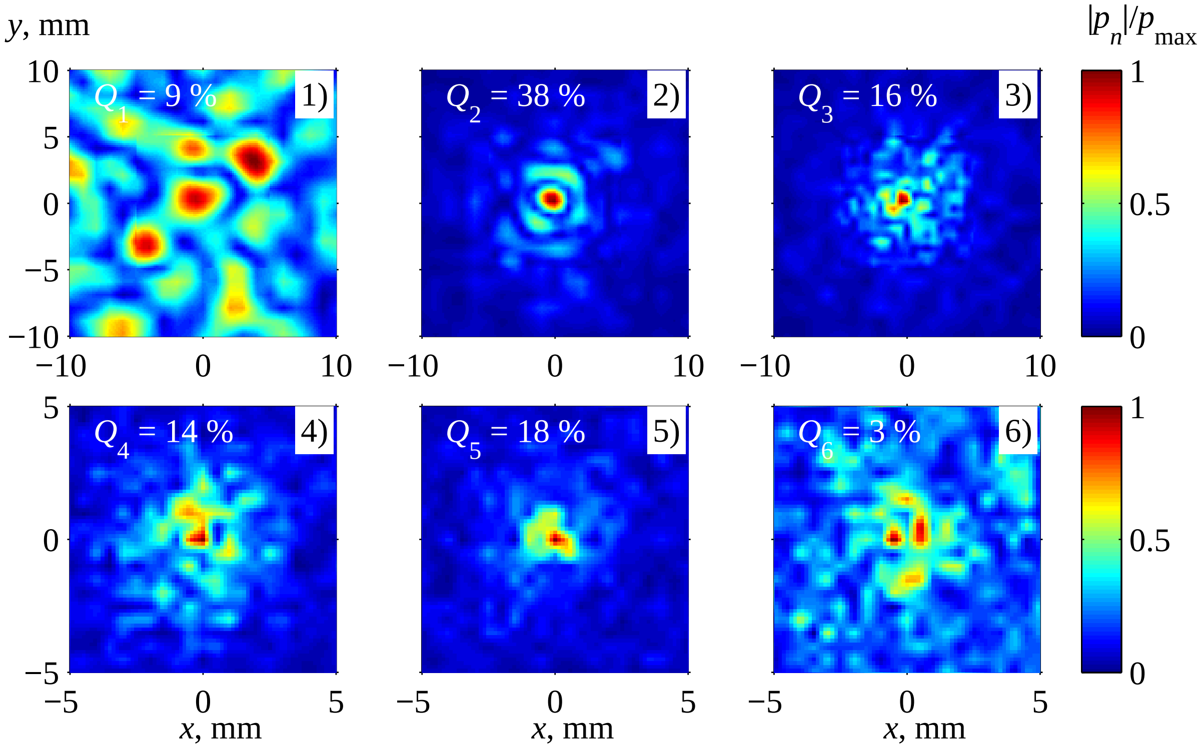

Figure 4.16: Pressure magnitudes of the first 6 harmonics measured in the focal plane (number in the corner). The 180° phase layer was placed at the distance from the source $z_\mathrm{p} = 0.5F = 36$ mm. The amplitudes are normalized on their peak values p_max, equal to 450, 76, 16, 3.0, 2.5 and 0.6 kPa, respectively.

Acoustic field behind the 180° phase layer

The measured amplitudes of the 1-6 harmonics in the focal plane in the case when the 180° phase layer is placed at the distance from the source $z_\mathrm{p} = 0.5F = 36$ mm, are presented in Fig. 4.16. The experiment demonstrates that focusing of the first harmonic is removed almost completely with the relatively low focusing quality of $Q_1 = 9\%$. Several random peaks are clearly seen in the amplitude distribution of this harmonic. On the contrary, focusing of the second harmonic is maintained in accordance with the theory predictions (§4.3): the focusing quality $Q_2 = 38\%$ is relatively high in comparison with quality of other measured harmonics. Processing and analysis of harmonics with higher numbers is complicated due to significant noise. However, visually one can say, that focusing of the 3-th and 4-th harmonics is destroyed, but the 5-th harmonic is well focused.

Figure 4.17 shows the experimental (color markers) and theoretical (black markers) behavior of the criterion Q_n as a function of the index n of the harmonic for the 180° phase layer positioned at the distances $z_\mathrm{p} = 0.25F = 18$ mm (a), $z_\mathrm{p} = 0.50F = 36$ mm (b) and $z_\mathrm{p} = 0.71F = 51$ mm (c). Different type of the color markers corresponds to different realizations of the phase layer obtained by moving it parallel in the (x, y) plane. Qualitative agreement between the experiment and simulations, which predict dips at even harmonics, is observed for the first three harmonics. The effect is more remarkable for the middle (b) and far (c) positions of the phase layer on the axis. Nevertheless, the experimental focusing criterion for the second harmonic did not agree quantitatively with the theoretical predictions. For harmonics higher than the third one, the measured Q_n are much lower than the simulated values. It can be also observed, that in comparison with the

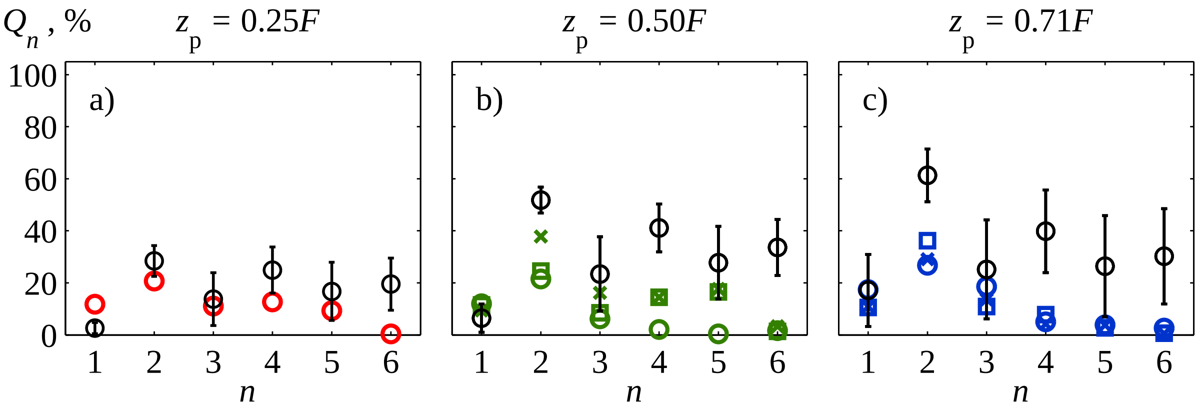

Figure 4.17: Comparison of the focusing quality criterion Q_n for the first six harmonics with the 180° phase layer placed at the distances $z_{\mathrm{p}} = 0.25F = 18$ mm (a), $z_{\mathrm{p}} = 0.50F = 36$ mm (b) and $z_{\mathrm{p}} = 0.71F = 51$ mm (c): experimental data (color markers) and simulations results (black markers). Different type of the color markers corresponds to different realizations of the phase layer obtained by moving it parallel in the (x, y) plane.

case of the piston source (Fig. 4.9), realistic boundary conditions and absorption in the layer led to some smearing of "resonant" focusing destruction effect. Nevertheless, the shown theoretical and experimental data demonstrated the possibility, in principle, to selectively destroy the focusing of the harmonic which was affected by the 180° phase shifts in the layer (the first harmonic in the considered case), and to preserve the focusing of another harmonic which phase was turned by a whole period 360° (the second harmonic).

The differences between the experiment and the simulations can be explained by low accuracy and noisy measurements of small amplitude harmonics. Another possible source of the disagreement may be the presence of harmonic components excited directly by the radiator due to insufficient linearity of the laboratory power amplifier. Also, the simulations were done with idealized infinitely thin phase layer model, but in the experiment reverberation effects can play some role due to finite thickness of the layer and imperfect matching of water and polyethylene impedances. The accuracy of cavities depth control in manufacturing process can also affect the experimental results.

Acoustic field behind the 90° phase layer

Spatial distributions of pressure magnitudes of the 1-6 harmonics in the focal plane, measured in the case of the 90° phase layer, are presented in Fig. 4.18. For the shown case, the layer was placed at the distance from the source $z_{\mathrm{p}} = 0.71F = 51$ mm. High focusing quality of the fundamental frequency ($Q_1 = 73\%$) and of the fourth harmonic ($Q_4 = 42\%$) is observed. At the same time, the second and third harmonics have relatively low focusing quality criterion of the 30% about. The measured data is in agreement with the theory (§4.4) since the second harmonic lost its focusing due to 180° phase shift on inhomogeneities, and the fourth harmonic kept the focusing since the obtained 360° phase shift is equivalent to zero. The 5-th and the 6-th harmonics are also distinguishable in this example. However, most likely due to the noise, data processing algorithm yields low Q_n values for these harmonics.

Comparison of the experimental (color markers) and theoretical (black markers) behavior of the criterion Q_n as a function of the index n of the harmonic for the $90°$ phase layer is shown in Fig. 4.19 for the same distances as in the Fig. 4.17. The focusing quality for the layer placed close to the focus ($z_\mathrm{p} = 0.71F = 51$, Fig. 4.19c) mm have been discussed above. In the middle position of the layer (Fig. 4.19b), the experiment also follows the theory: focusing quality of all harmonics is low due to strong second harmonics degradation and violation of the in-phase condition necessary for the cascade energy transfer to higher harmonics. In the closest position of the phase layer to the source (Fig. 4.19a), in agreement with the theory, the focusing quality of the

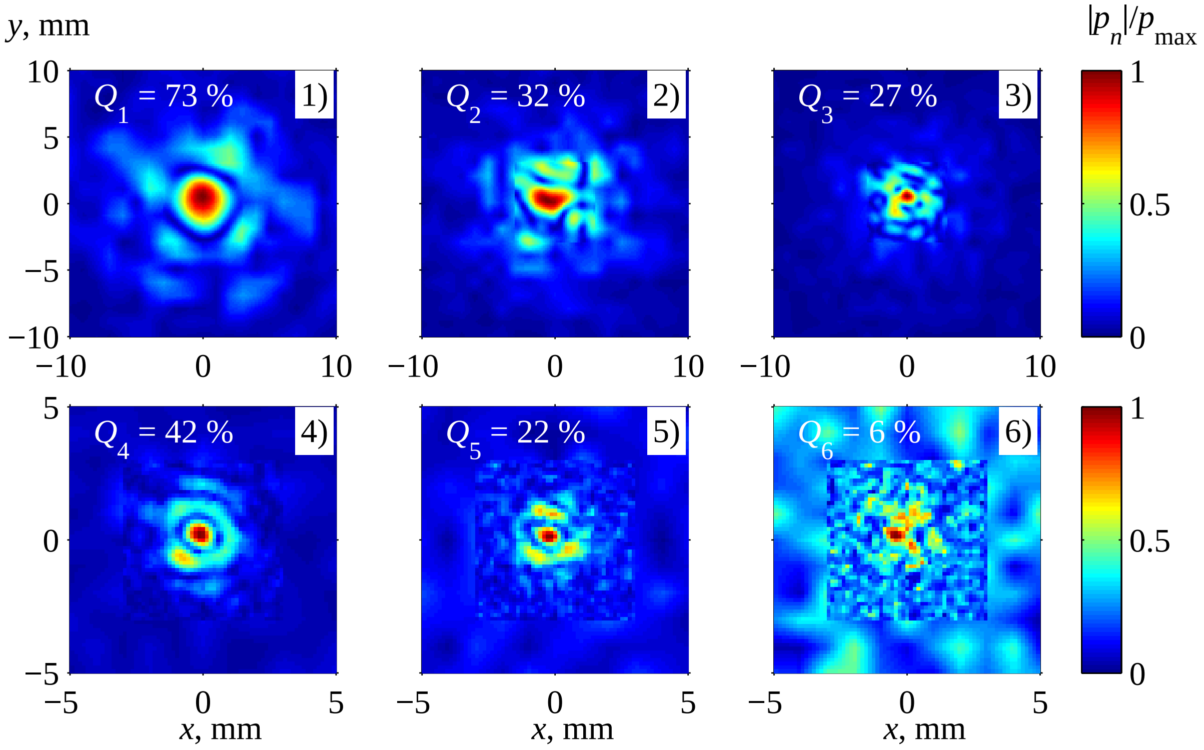

Figure 4.18: Pressure magnitudes of the first 6 harmonics in the focal plane (number in the corner), measured in a case of the $90°$ phase layer. The layer was placed at the distance from the source $z_\mathrm{p} = 0.71F = 51$ mm. The amplitudes are normalized on their peak values p_max, equal to 1260, 100, 26, 9.3, 3.6 and 1.4 kPa, respectively.

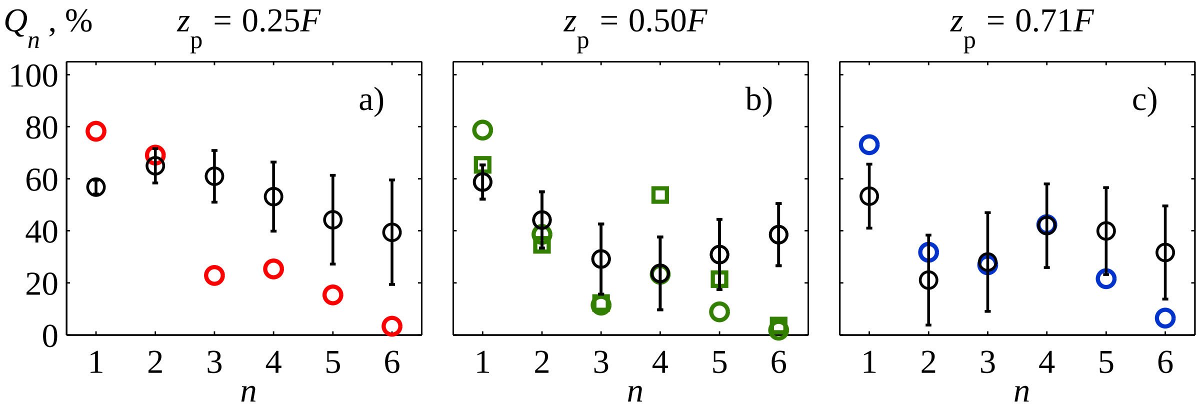

Figure 4.19: Comparison of the focusing quality criterion Q_n for the first six harmonics with the $90°$ phase layer placed at the distances $z_\mathrm{p} = 0.25F = 18$ mm (a), $z_\mathrm{p} = 0.50F = 36$ mm (b) and $z_\mathrm{p} = 0.71F = 51$ mm (c): experimental data (color markers) and simulations results (black markers). Different type of the color markers correspond to different realizations of the phase layer obtained by moving it parallel in its own plane.

second harmonic is high, since its field was produced by slightly distorted fundamental field on a long propagation path until the focus. For the harmonics higher than the third one, experimental Q_n values are low. However, the detailed analysis of the focal distributions has shown that it is due to slight deviation of the central maximum rather than due to its strong destruction.

§4.6 Conclusions

In this chapter focusing of finite-amplitude ultrasound beam behind the phase layer of special configurations was considered theoretically and experimentally. The phase layer which consists of a great number of identical circular regions with fixed phase shift and randomly distributed in a plane was proposed to control the focusing of different harmonics of the beam. It is demonstrated that, choosing the value of the phase shift in the layer equal to $180°$, this system can selectively destroy focusing of the fundamental harmonic and of the closest odd harmonics, keeping relatively high focusing quality for the even ones. In case of the $90°$ phase layer it is shown that when the layer is placed near the transducer, focusing of the higher-order harmonics is advantageous. Better focusing of harmonics also occurs in case of arbitrary inhomogeneities, which does not destroy significantly the focusing of the fundamental component. Thus, the obtained results justify the Tissue Harmonic Imaging method, available in many modern diagnostic ultrasound devices. Also, depending on the position of the $90°$ phase layer along the axis, focusing of higher-order harmonics can be destroyed. For example, when the layer is near the focal point, focusing of the second harmonic is strongly degraded, since it was exposed to the $180°$ phase shift. So, the possibility to destroy the focusing at certain harmonics and to preserve focusing at others using the inhomogeneous phase layer with ”resonant” phase shifts was established. The layer can also be tuned to destroy focusing of other harmonics, for example, $60°$ phase shift can be used to destroy the third harmonic.

Chapter 5

Simulation of three-dimensional nonlinear fields of ultrasound therapeutic arrays

§5.1 Introduction

An increasing number of current high intensity focused ultrasound (HIFU) noninvasive surgical devices rely on using two-dimensional multi-element phased arrays with the elements distributed over a segment of a spherical surface (Pernot *et al.*, 2003, Hynynen *et al.*, 2006, Quesson *et al.*, 2006, Hand *et al.*, 2009). Each element of such an array is controlled independently, which makes it possible to electronically steer the focus in space, to create a complex field configuration in the form of several foci, and to minimize the heating of acoustic obstacles (for instance, ribs) while maintaining high intensities at the focus (Quesson *et al.*, 2006, Hand *et al.*, 2009, Gavrilov & Hand, 2000b, Gavrilov, 2003, Bobkova *et al.*, 2010). The abilities of arrays can also be utilized to improve the quality of focusing in inhomogeneous tissue using time reversal methods, as well as to trace the region of treatment, which shifts due to respiration (Pernot *et al.*, 2003, Pernot *et al.*, 2004).

Numerical experiment is an important tool in characterizing pressure fields created by HIFU radiators, in developing exposure protocols, and in predicting corresponding HIFU-induced biological effects in tissue (Canney *et al.*, 2008, Bessonova *et al.*, 2009). Intensity levels at the focus of HIFU radiators can reach several tens of thousands of $\mathrm{W/cm^2}$, causing nonlinear propagation effects. Nonlinear effects can result in formation of weak shocks in the ultrasound waveform, which fundamentally changes the efficiency of ultrasound thermal action on tissue and can lead to new biological effects of a non-thermal nature (Burov *et al.*, 2002, Canney *et al.*, 2010).

Nonlinear propagation effects in focused ultrasound fields with account for the formation of shocks have been studied in detail for axially symmetric beams (Canney *et al.*, 2008, Bessonova *et al.*, 2009, Canney *et al.*, 2010, Tavakkoli *et al.*, 1998). Three-dimensional problems in parabolic approximation have been solved for beams radiated from diagnostic ultrasound transducers, i.e., for the case of weak focusing and weak nonlinear effects (Khokhlova *et al.*, 2006, Jing & Cleveland, 2007). Recently, new methods for diagnostic ultrasound simulation were developed, which correctly take into account the nonlinear and diffraction effects in case of high-angle steering of a beam (Huijssen & Verweij, 2010). However, no results have been reported yet on modeling nonlinear effects in three-dimensional fields of multi-element HIFU arrays with account for the formation of shocks. Several difficulties are combined at once in this problem: the complex diffraction structure of the near field and large focusing angles requiring the use of accurate diffraction models and a fine spatial numerical grid. In addition, strong nonlinear effects require large number of harmonics to be included in the simulations or a fine temporal grid. For simulation in a three-dimensional geometry with allowance for generation of shock fronts, in general, significant expenditures of RAM and computer time are required, which exceed the capabilities of modern SMP computers, i.e., multiprocessor computers with shared memory.

In this chapter, a numerical solution was obtained for the first time for the nonlinear field of a therapeutic array in the presence of high amplitude shocks. An algorithm was developed that economizes RAM, making it possible to perform such calculations on SMP computers. As an example, numerical modeling was performed for an array with a frequency of 1.2 MHz, consisting of 256 elements with a radius of 3.3 mm, distributed over a spherical cup with a radius of 64 mm and an opening for a diagnostic transducer with a radius of 9 mm, focusing distance of 120 mm, and intensity of up to $10\ \mathrm{W/cm}^2$ at the radiating elements (Quesson *et al.*, 2006, Kreider *et al.*, n.d.).

§5.2 Numerical algorithm to model strongly focused acoustic fields with shocks

5.2.1 The Westervelt equation

The field of the array was simulated according to the Westervelt equation (Westervelt, 1963):

$$\frac{\partial^2 p}{\partial t^2} - c_0^2 \Delta p = \frac{\varepsilon}{\rho_0 c_0^2}\frac{\partial^2 p^2}{\partial t^2} + \frac{\delta}{c_0^2}\frac{\partial^3 p}{\partial t^3}. \tag{5.1}$$

The description of the Eq. (5.1) was provided in the previous chapter in sec. 4.2. The same transformations of the Eq. (5.1) were done: the equation was rewritten in the retarded system of coordinates and in the dimensionless variables (Eq. 4.3). In this chapter, calculations were performed for water, and the corresponding physical parameters in Eq. (5.1) were as follows: $\rho_0 = 1000\ \mathrm{kg/m}^3$, $c_0 = 1500\ \mathrm{m/s}$, $\varepsilon = 3.5$, $\delta = 4.33 \cdot 10^{-6}\ \mathrm{m^2/s}$. The origin of the coordinates corresponded to the center of a spherical segment where individual elements of the array were located so that the point $x = 0$, $y = 0$, $z = F$ corresponded to the geometric focus of the array.

5.2.2 Boundary condition to the model

To solve the Westervelt equation (4.2), written in the evolution form in terms of the z coordinate, it is necessary to set boundary conditions at some initial plane $(x, y, z = z_0)$. Since the elements of the array are distributed on the surface of a spherical cup, the field was first calculated on the plane 2 cm from the center of the array using the Rayleigh integral. This plane is located near the edge of the array cup, which is at a distance of z = 1.85 cm from the array center. The Rayleigh

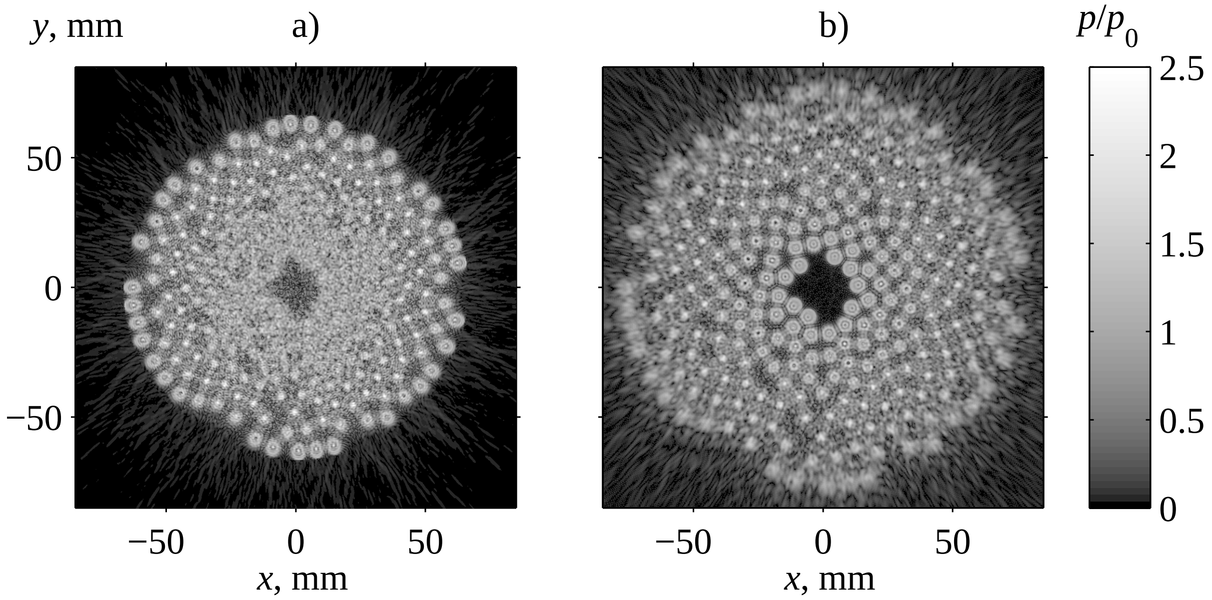

Figure 5.1: Spatial distributions of dimensionless pressure amplitude p/p_0 calculated in a plane $(x, y, z = 20\ \mathrm{mm})$ near the edge of the radiator (a) and in a plane $(x, y, z = 0\ \mathrm{mm})$ – ”virtual” source (b). Here, $p_0 = \rho_0 c_0 u_0$, where u_0 is the amplitude of the vibration velocity at the surface of the array element.

integral is

$$p(\vec{r}) = -i\rho_0 c_0 \frac{k}{2\pi} \int_S \frac{u(\vec{r}\,') \exp\left(ik|\vec{r} - \vec{r}\,'|\right)}{|\vec{r} - \vec{r}\,'|} dS', \tag{5.2}$$

where $k = \omega/c_0$ is the wavenumber, $\omega = 2\pi f$, f is the ultrasound frequency, and $u(\vec{r}\,')$ is the complex amplitude of the vibration velocity of the radiator surface S.

To perform numerical calculations of the Rayleigh integral the surface of the radiator was fragmented on triangles as follows. A local coordinate system in the vicinity of each radiating element was introduced in a plane tangent to the array surface. In the plane a rectangular grid with steps $\lambda/20$ and $\lambda/20$ was defined to fully cover a projection of the element. Each square of the grid was partitioned on two right-angled triangles. Then the coordinates of triangle vertices were projected on the spherical cup. After this procedure the integration is straightforward according to Eq. (5.2): vector $\vec{r}\,'$ points to center of mass of a triangle on the transduce surface, $\vec{r}$ points to the target point where the pressure is calculated, and it is accepted that if the center of mass of a triangle is inside of an element circle, then $u(\vec{r}\,')$ is equal to u_0, else $u(\vec{r}\,')$ is set zero. Elementary surface area dS' is the surface of the triangle in this case.

Figure 5.1a shows the complex diffraction structure of the pressure field created by the 256 elements in the given plane $(x, y, z = z_0)$. In order to account for nonlinear effects in the near field of the array, this boundary condition was then carried back to plane $(x, y, z = 0)$, tangential to the center of the spherical array surface. Back propagation was performed with the Rayleigh integral calculated using the angular spectrum method, described in previous chapter in sec. 4.2.2. Figure 5.1b shows the distribution of the ”virtual” sources obtained in this plane. Numerical solutions were calculated using both boundary conditions; the differences observed between the simulation results for nonlinear pressure fields are discussed below further in sec. 5.4.2.

5.2.3 Numerical algorithm

Second-order operator splitting

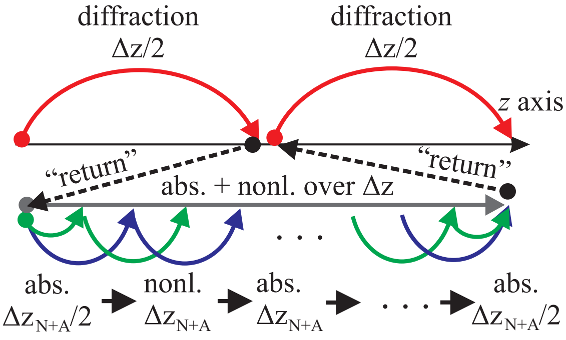

Figure 5.2: Diagram of the method of fractional steps with the operator splitting procedure over the one step Δz.

The numerical solution to the Eq. (4.2) was calculated sequentially, passing from a plane $(x, y, z = z_1)$ to a plane $(x, y, z = z_1 + \Delta z)$ with a step of Δz, following the method of fractional steps with the operator splitting procedure of the second order (Tavakkoli *et al.*, 1998,Zemp *et al.*, 2003,Varslot & Taraldsen, 2005). As for splitting procedure of the first order, the Eq. (4.2) was divided into simpler equations for diffraction (4.6), nonlinearity (4.7), and absorption (4.8). With known pressure distribution in the plane $(x, y, z = z_1)$, combining in a certain way the solutions to these equations consequentially one after another, a solution to Eq. (4.2) was obtained in the plane $(x, y, z = z_1 + \Delta z)$ with the second-order accuracy, i.e., with the error in approximation at each step $O(\Delta z^3)$ and on the entire calculation path along the z coordinate, $O(\Delta z^2)$ (Tavakkoli *et al.*, 1998, Varslot & Taraldsen, 2005). In this work, the version of the splitting method was applied in which each step over the coordinate z begins and ends with the diffraction operator calculated over a half-step of the grid. If one denotes the action of the diffraction operator over the step Δz as $\Gamma_{D,\Delta z}$, the combined action of the nonlinearity and absorption operators as $\Gamma_{N+A,\Delta z}$, and the action of all operators as $\Gamma_{D+N+A,\Delta z}$, then the scheme of applying the splitting method can be represented as follows:

$$p(\tau, x, y, z + \Delta z) = \Gamma_{D+N+A,\Delta z} p(\tau, x, y, z) = \Gamma_{D,\Delta z/2} \Gamma_{N+A,\Delta z} \Gamma_{D,\Delta z/2} p(\tau, x, y, z). \tag{5.3}$$

The graphic representation of the scheme over the one step Δz is shown in Fig. 5.2 where diffraction steps over $\Delta z/2$ are illustrated by red arc arrows. "Return" black dashed arrows show transmission of the numerical data from the output of the diffraction operator $\Gamma_{D,\Delta z/2}$ to the input if the absorption-nonlinear operator $\Gamma_{N+A,\Delta z}$ and *vice versa*. The diffraction half-steps $\Gamma_{D,\Delta z/2}$ of two adjacent steps $\Gamma_{D+N+A,\Delta z}$ were combine into the one step $\Gamma_{D,\Delta z}$. As the distance of z changed and the amplitudes of high-frequency components of the wave spectrum increased, the step size Δz was varied to ensure the required accuracy of the solution.

The combined action of the nonlinearity and absorption operators $\Gamma_{N+A,\Delta z}$, Eq. (5.3), was calculated using the same fractional step algorithm of the second-order:

$$\Gamma_{N+A,\Delta z} = \Gamma_{A,\Delta z_{N+A}/2} \Gamma_{N,\Delta z_{N+A}} \Gamma_{A,\Delta z_{N+A}} \dots \Gamma_{A,\Delta z_{N+A}/2}. \tag{5.4}$$

Unlike diffraction splitting, substeps Δz_{N+A} of the step Δz were introduced to increase accuracy of the simulations (Zemp *et al.*, 2003). In Fig. 5.2 absorption substeps are shown by green arc arrows and nonlinearity substeps – by blue arrows. The "return" arrows between absorption and nonlinear operators are not shown in the figure. The number of the substeps Δz_{N+A} within the step Δz was varied as the distance of z changed and usually was augmented in vicinity of the focus by several times in comparison to the beginning of the simulation.

Simulations were performed using the advantages of both the frequency and temporal representations of the acoustic field. In the frequency domain, the solution to Eq. (4.2) was represented in the form of a finite Fourier series expansion (4.9). The transition between the spectral and temporal representations of the solution (4.9) was carried out using fast Fourier transform (FFT) realized in the FFTW library. FFT calculation was performed in relatively small blocks, i.e., simultaneously for some relatively small number of waveforms (several hundred) taken at adjacent points along the x axis. This method made it possible to substantially increase the efficiency of calculations comparing to the method when single FFTs are calculated for each spatial point, sequentially one after another.

Diffraction operator

The diffraction operator (4.6) was calculated for the amplitudes of each harmonic similarly as in the previous chapter 4 using the angular spectrum method with several optimizations. The first, in the relation for the radius of the cut-off circle for the spatial spectrum of each harmonic $k_{\max} = k_n/\sqrt{z_{\text{prop}}^2 \Delta k^2/\pi^2 + 1}$, the common propagation distance z for all harmonics was changed to the propagation distance z_{prop}, which was different for each harmonic due to their gradual inclusion in the calculations. Here $\Delta k = 2\sqrt{2}\pi/L$ is the maximal step over the radial direction in the spatial frequency domain in the case of a square region of size L. The second, an artificial absorption quadratic with frequency was introduced in the layer adjacent to the boundaries of the spatial domain, which helps to reduce the waves coming from the periodical boundaries of the calculation domain. Absorption coefficient ν at the fundamental frequency increased according to the law $\nu = \nu_0[(x - x_1)/l_x]^2$, where x_1 is the coordinate of the beginning of the layer, l_x is the width of the layer, and ν_0 is the maximum absorption at the boundary. Typical values of the parameters of the layer were as follows: $\nu_0 = 1.6\ \text{mm}^{-1}$ and $\Delta x = 10\ \text{mm}$. More sophisticated method to decrease numerical reflections on the domain boundary, the PML (Berenger, 1994), can be applied under the angular spectrum method (Yasumoto & Ishihara, 2002). However, from a numerical point of view it is resource-demanding and was not considered here.

Nonlinearity and absorption operators

The nonlinear operator (4.7) was calculated using two algorithms. At small distances from the radiator, the integration was performed in a frequency domain using the fourth order Runge-Kutta method for the set of nonlinear coupled equations for the harmonic amplitudes (4.10). Since the number of operations in this algorithm is proportional to the squared number of harmonics $N_{\max}$, it is quite efficient when a relatively small number (several tens) of harmonics are considered. To shorten the calculation time, additional harmonics were introduced into the algorithm gradually, as the wave spectrum broadened with increasing propagation distance z. A threshold amplitude of the last harmonic in the spectrum was set to 10^{-6}. Reduction of the number of harmonics was also provided in the algorithm if the last harmonic amplitude falls below the threshold.

When the steepness of the wave profile exceeded a quantity that corresponds to a plane, initially sinusoidal wave at the distance equal to 0.1 from the shock formation distance $z_{\mathrm{sh}} = c_0^3\rho_0/\beta p\omega$, the nonlinear algorithm was changed to a conservative time-domain Godunov-type scheme. This scheme makes it possible to simulate the evolution of waveforms containing shocks having only two to three grid points at the shock front (Kurganov & Tadmor, 2000, Averiyanov, 2008). When calculating nonlinearity using this algorithm the fractional substep of nonlinear and absorption operators Δz_{N+A} was additionally partitioned to a number of smaller substeps Δz_{nonl} in order to feet a condition:

$$\Delta z_{\mathrm{nonl}} \leq 0.1\rho_0 c_0^3 \Delta\tau/\beta p_{\mathrm{sh}}, \tag{5.5}$$

where p_{sh} is the shock amplitude, $\Delta\tau = 0.5/fN_{\max}$ is the time step, $N_{\max}$ is the number of harmonics. As it was shown in the study (Averiyanov, 2008), fulfilment of this criterion is necessary to obtain stable and accurate solutions.

The absorption was calculated similarly as in the previous chapter using an exact solution for each harmonic, Eq. (4.11), where Δz step should be replaced by Δz_{N+A} substep.

5.2.4 Optimization of calculations and parallelism of the algorithm

Numerical resources requirements

Numerical simulations of three-dimensional nonlinear acoustic fields using the numerical method presented above are computationally intensive requiring long time of calculations and large volume of RAM. These requirements increase significantly when the acoustic fields with shock fronts are considered. In this case a high-resolution numerical grid in both the temporal and spatial coordinates should be used (Bessonova *et al.*, 2009, Tavakkoli *et al.*, 1998). Data arrays become excessively large and the problem cannot be solved on conventionally available multiprocessor SMP computers, whose RAM, as a rule, does not exceed 32 GB, although at that time expensive systems with 256 Gb of memory or more can be found. With a calculation region for the field of the array in transverse coordinates of 25×25 cm, a size of the grid steps of $dx = dy = 0.05$ mm, 500 harmonics included in calculations, as well as single accuracy in the representation of floating point numbers, the size of data arrays for describing the pressure field is about 90 GB. Working with such arrays is not a problem for cluster systems; however, development of a parallel algorithm for a cluster using MPI technology is more difficult than for an SMP computer. In this work, the algorithm was optimized in such a way that it can be used for calculation on multiprocessor machines with an overall RAM of several tens of GB, for example, 32 or 48.

Echelon-type data storage

It was possible to optimize the algorithm because nonlinear effects in strongly focused fields of HIFU systems are significant only in the proximity of the focal region. In this region, it is necessary to include a large number of harmonics in calculations. However, much smaller number of harmonics can be used beyond the focus region both along and transverse to the beam axis. A similar approach of limiting the number of harmonics outside of the beam region containing shocks was employed in simulating nonlinear effects in the near field of an axially symmetric radiator (Khokhlova *et al.*, 2002).

Figure 5.3 schematically illustrates the method in the case of three regions with different number of harmonics. The harmonics, starting from the first through n_1, are kept in calculations in region no. 1 of size L_1; from $n_1 + 1$ through n_2, in region no. 2 of size L_2. A specific number of harmonics in each region varies for each calculation. Such a method of data allocation is named here as echelon-type, and the regions themselves – echelons. As shown in the figure, the dimensions of each echelon L_i are multiples of the dimensions of the smallest echelon L_3; i.e., the entire computational region is divided into squares outlined in the figure by dotted lines. This partitioning of the domain was chosen in order to effectively and uniformly implement the nonlinear algorithms inside the squares with the application of stream data processing and efficient RAM accessing. The size of each echelon was determined using the formula $L_k = L_1(2N - 2k + 1)/(2N - 1)$, where k is the echelon number and N is the overall number of echelons. This data arrangement provided the differentiation for the allocation of harmonics in space, saving of the resources of RAM by a factor of tens as well as maintaining the calculations efficiency.

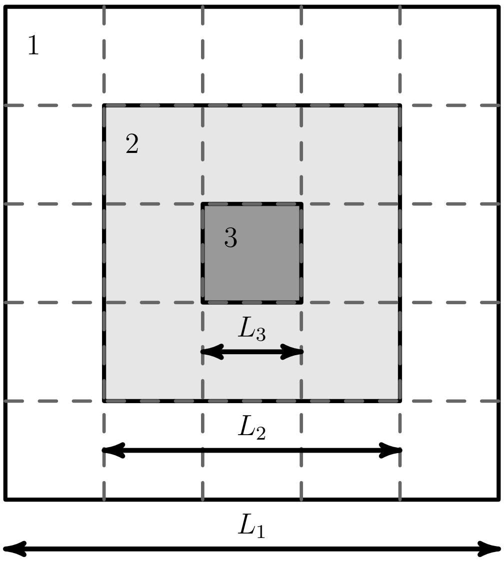

Figure 5.3: Geometry of echelon storage of the 2D data arrays. Three echelons are shown in the figure in white (no. 1), gray (no. 2), and by dark-gray (no. 3). In the central echelon (no. 3), the maximum number of harmonics is included in calculations; in the boundary echelon (no. 1), the minimum number. The dashed lines divide squares, in which parallel calculations of the nonlinearity and absorption operators are performed.

The code was written in FORTRAN 95 intending to parallel computations. In calculation of two-dimensional FFTs for the diffraction substep, parallel computing was performed using an internal ability of the FFTW library. The remaining substeps were parallelized using OpenMP technology. Calculations were performed within one node of the SKIF-MSU supercomputer Chebyshev. The node contains 8 processor cores (2 quad-core processors) and 8, 16, or 32 GB of RAM. The nodes with small amount of memory (8 and 16 GB) where used to calculate the cases with weak nonlinearity, and the nodes with 32 GB – to calculate the most intensive cases. Overall, the performance of the parallel computations was six times faster in comparison to sequential execution of the code.

5.2.5 Artificial absorption

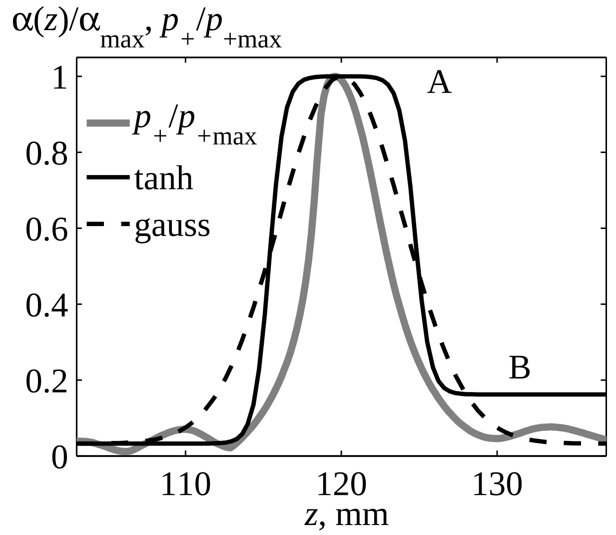

Figure 5.4: An example of the artificial absorption $\alpha(z)$, given by the Eq. 5.6 along the z axis (black solid line), peak positive pressure – gray solid line, and a possible gaussian dependence of the artificial absorption – dashed line. The simulation case corresponds to $I_0 = 5\ \mathrm{W/cm}^2$(see sec. 5.4.3). All curves are normalized here to their maximal values.

When shock fronts develop in the pressure waveform, strong gradients appear in the transverse spatial field structure as well. These spatial gradients can cause artificial oscillations in the numerical solutions. Using smaller spatial steps leads to decreasing of the oscillations. With given computational resources the parameters of the algorithm were optimized by varying the echelon configuration to achieve the minimum transverse steps $dx = dy = 0.025$ mm and maximum number of harmonics in the central echelon $N_{\max} = 500$. However, such steps were not sufficient to accurately capture the spatial gradients mentioned above and to eliminate considerable oscillations of magnitude $10 - 20\%$ from peak positive pressure.

To eliminate the oscillations, an additional artificial absorption was introduced in the algorithm locally around the focus where shocks were present (Bessonova *et al.*, 2009). In the cited work the gaussian function centered in the geometric focus of the radiator was used to govern localization of the absorption along the z axis. In the present model better localization was necessary, since in some cases high artificial absorption in the focus is unavoidable that can lead to remarkable attenuation of the amplitude but not only to the shock front smoothening. Therefore, the artificial absorption coefficient α was chosen according to the following dependence on the axial coordinate:

$$\alpha(z) = a_1 + 0.5(A-1)\left[\tanh\left(\frac{z-z_1}{\Delta z_1}\right) - a_2 \tanh\left(\frac{z-z_2}{\Delta z_2}\right)\right]. \qquad (5.6)$$

Here, parameter A determines the increase in the absorption coefficient near the focus in comparison to the absorption coefficient in water. Coefficients $a_1 = (1+B)/2$ and $a_2 = 1+(1-B)(A-1)$ are expressed in terms of the parameter B, which determines an increase in the absorption coefficient postfocally. Geometric parameters z_1 and z_2 determine the size of the region of increased absorption, and parameters Δz_1 and Δz_2 – the width of transition regions to the values of absorption coefficients A and B. An example of the artificial absorption dependence (5.6) taken from one simulation reported below (sec. 5.4.3) is shown in Fig. 5.4 by dashed line. The absorption is normalized in the figure by its maximal value and is shown with the normalized peak positive (solid gray line) along the axis z. It is seen form the figure, that the chosen dependence provides well localization of the absorption around the focus, while possible gaussian curve (dashed line) have unnecessary ”tails” before and beyond the focus. The values of parameters in the formula (5.6) were chosen for each individual case of calculations to completely eliminate oscillations in the numerical solutions with shocks. Comparison of simulations results for axially symmetric HIFU transducer with the data from other studies (Bessonova *et al.*, 2009) showed, that the used values of artificial absorption did not significantly attenuate the solutions (§5.3).

5.2.6 Parameters of the numerical algorithm

In this work simulations were performed for nonlinear pressure field generated by a multi-element array over clinically relevant power outputs. The intensities at the radiating elements were $I_0 = 1$, 2, 2.5, 5, and 10 $\mathrm{W/cm}^2$; linear focusing of ultrasound was considered as well. Simulations for the linear case and for $I_0 = 1\ \mathrm{W/cm}^2$ were performed on the spatial grid with steps of $dx = dy = 0.05$ mm in transverse coordinates and a number of grid points of $N_x = N_y = 5000$. For the remaining cases, the steps were $dx = dy = 0.025$ mm and a number of grid points was $N_x = N_y = 10000$. Thirteen echelons were chosen, and the maximum number of harmonics was distributed over the echelons in the following way: from the 1st through the 6th, $N_{\max} = 14$; from the 7th through the 9th, $N_{\max} = 40$; from the 10th to the 13th, $N_{\max} = 100$, 200, 300, and 500, respectively. The size of the array data including technical arrays was close to 32 GB. The distribution of harmonics over echelons provided 16 times economy in RAM.

Pressure field of the array was calculated starting from the initial plane $z_0 = 0$ mm or from the plane $z_0 = 20$ mm to a distance of $z = 1.3F = 156$ mm depending on the boundary conditions used. The step Δz along the array axis was 0.1875 mm in the segment from the initial plane to $z = 0.8F$, 0.125 mm in segment $[0.8F\ \ 0.9F]$, 0.0625 mm in $[0.9F\ \ 1.1F]$; and 0.125 mm in $[1.1F\ \ 1.3F]$. The number of substeps Δz_{N+A} for the nonlinearity and absorption operators increased from one in the first segment to six in the area around the focus $[0.9F\ 1.1F]$.

The values of artificial absorption parameter in the equation (5.6) were 2.5, 5, 20, and 40 for intensities of 2, 2.5, 5, and 10 $\mathrm{W/cm}^2$, respectively, which ensured about 7 points per shock front in the focus. The values of the geometric parameters in the equation (5.6) were close to $0.96F$ and $1.03F$ for z_1 and z_2, and $0.01F$ for Δz_1 and Δz_2. The calculation time for these parameters of the code was several hours in case of weak nonlinear effects and up to 1-2 days in case of developed shocks.

§5.3 Validation of the numerical algorithm and comparison with known solutions

The accuracy of the numerical solutions obtained with the new algorithm was examined by comparing the simulation results with known analytical solutions or numerical simulations performed using other methods. For each of the operators (4.6), (4.7) and (4.8) governing a particular physical effect, the results were compared with known analytical solutions. A test of the complete

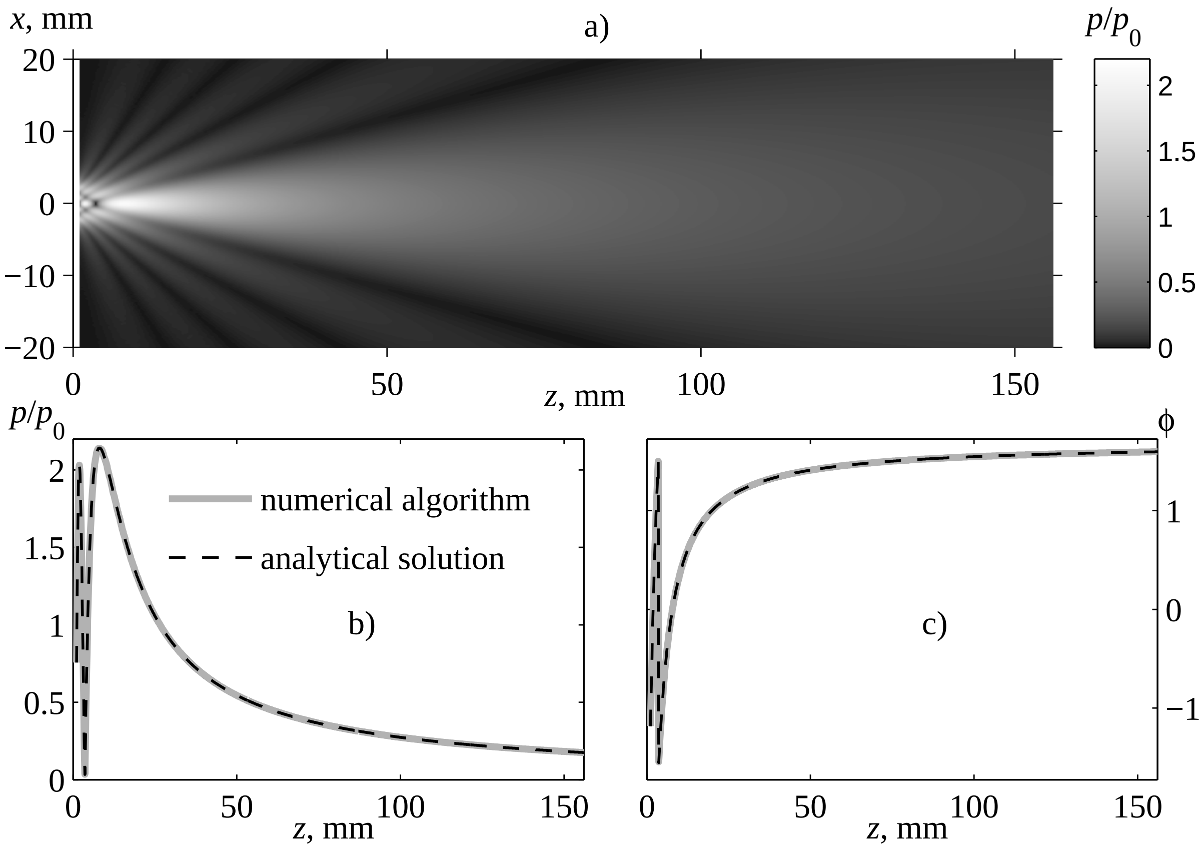

Figure 5.5: Pressure amplitude distribution p/p_0 for a single array element, calculated numerically in a linear approximation in the axial plane of the element (a). Results of linear numerical calculations (solid gray curves) for the pressure amplitude (b) and phase (c) along the element axis in comparison to an analytic solution (thin dashed curves).

algorithm, failing the existence of general analytical solution, was performed by comparison with known modeling results of other studies obtained in a parabolic approximation for nonlinear fields of axially symmetric radiators (Filonenko & Khokhlova, 2001, Bessonova *et al.*, 2010).

The diffraction algorithm was tested by calculating the linear field from a single focused piston element of the array (Fig. 5.5a) and comparing it with known analytic solutions for the axial field. Figure 5.5 shows the results of simulations (solid curves) and analytic solutions (dashed curves) for the pressure amplitude Fig. 5.5b and phase Fig. 5.5c on the axis of the element. The comparison shows very good agreement of the results, the curves nearly coincide, and the maximum deviation between them does not exceed 0.5%.

The algorithm (4.10) for calculating nonlinear term (4.7) was tested by comparing the simulated propagation curves for harmonic amplitudes with the Bessel-Fubini solution for nonlinear propagation of a plane, initially harmonic wave up to the shock formation distance (Rudenko & Soluyan, 1977). The deviation from the analytic solution was obtained at a level of 10^{-6}. At longer distances, when shocks were present, the simulations obtained using Godunov-type time-domain scheme were compared with the analytic solution for sawtooth waves (Rudenko & Soluyan, 1977, Rudenko, 1995). When 500 harmonics were included in simulations, the shock amplitude in the numerical solution was different from the exact solution by less that 0.3%.

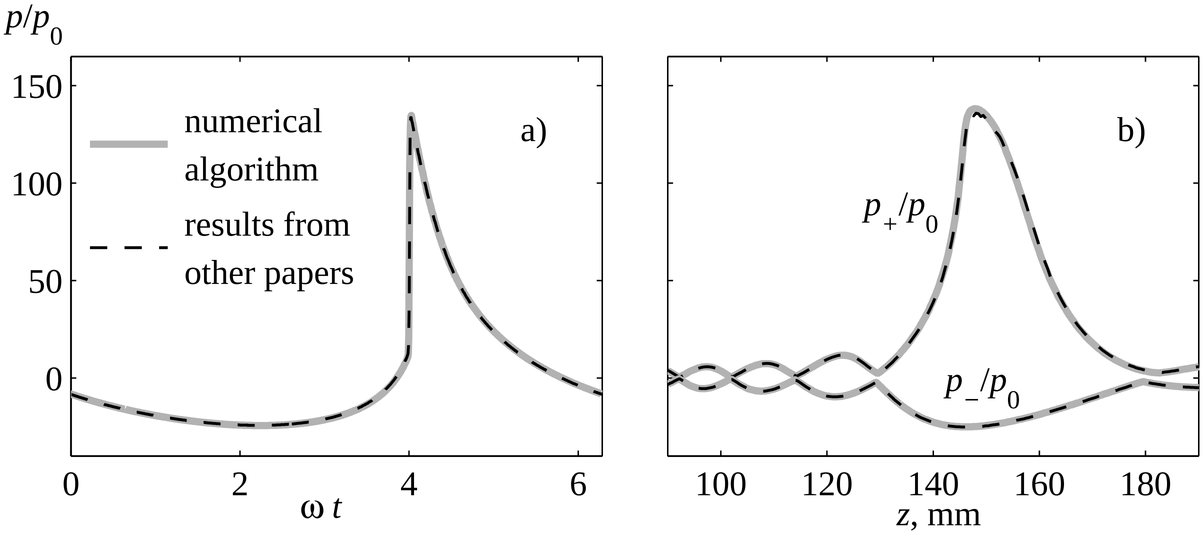

Figure 5.6: Comparison of the modeling results for nonlinear field of an axially symmetric radiator. The results were obtained in the parabolic approximation using the new algorithm (solid gray curves) and calculations performed with other algorithms (thin dashed curves): pressure waveforms at the geometric focus (a); positive p_+/p_0 and p_-/p_0 negative peak pressures along the beam axis (b). Nonlinear parameter $N = 0.25$, linear focusing gain $G = 40$.

Complete testing of the algorithm was performed by comparison of numerical solutions for an axially symmetric single element focused radiator. The solutions were obtained using the new algorithm with account for diffraction in parabolic approximation (4.13) and analogous calculations performed using other numerical schemes based on the Khokhlov-Zabolotskaya-Kuznetsov (KZK) equation (Canney *et al.*, 2008, Bessonova *et al.*, 2009, Filonenko & Khokhlova, 2001, Bessonova *et al.*, 2010). The corresponding boundary condition in the three-dimensional algorithm was set at $z = 0$ in the form of a round piston with the phase $k_0\sqrt{x^2 + y^2}/2F$. For comparison, a radiator with an operational frequency of 1.7 MHz, a radius of 41.1 mm, and a focusing distance of 150 mm, was considered. The parameters of the radiator were chosen identical to those of the HIFU transducer considered in the earlier publication (Filonenko & Khokhlova, 2001). The linear focusing gain of the radiator was $G = \omega R^2/2c_0F = 40$ and the output intensity level was chosen such that the nonlinearity coefficient $N = F\beta p_0\omega/c_0^3\rho_0 = 0.25$ corresponded to the case considered in (Bessonova *et al.*, 2010). The initial pressure amplitude near the radiator was 0.15 MPa, and the linear estimate of intensity at the focus was $1200\ \mathrm{W/cm}^2$. Figure 5.6 shows a comparison of the pressure waveforms at the focus (a) and the peak pressure distributions along the beam axis (b) obtained with the new numerical algorithm (solid curves) and in the previously cited study (Bessonova *et al.*, 2010) (dashed curves). The results of modeling demonstrate very good agreement with less than 1% difference.

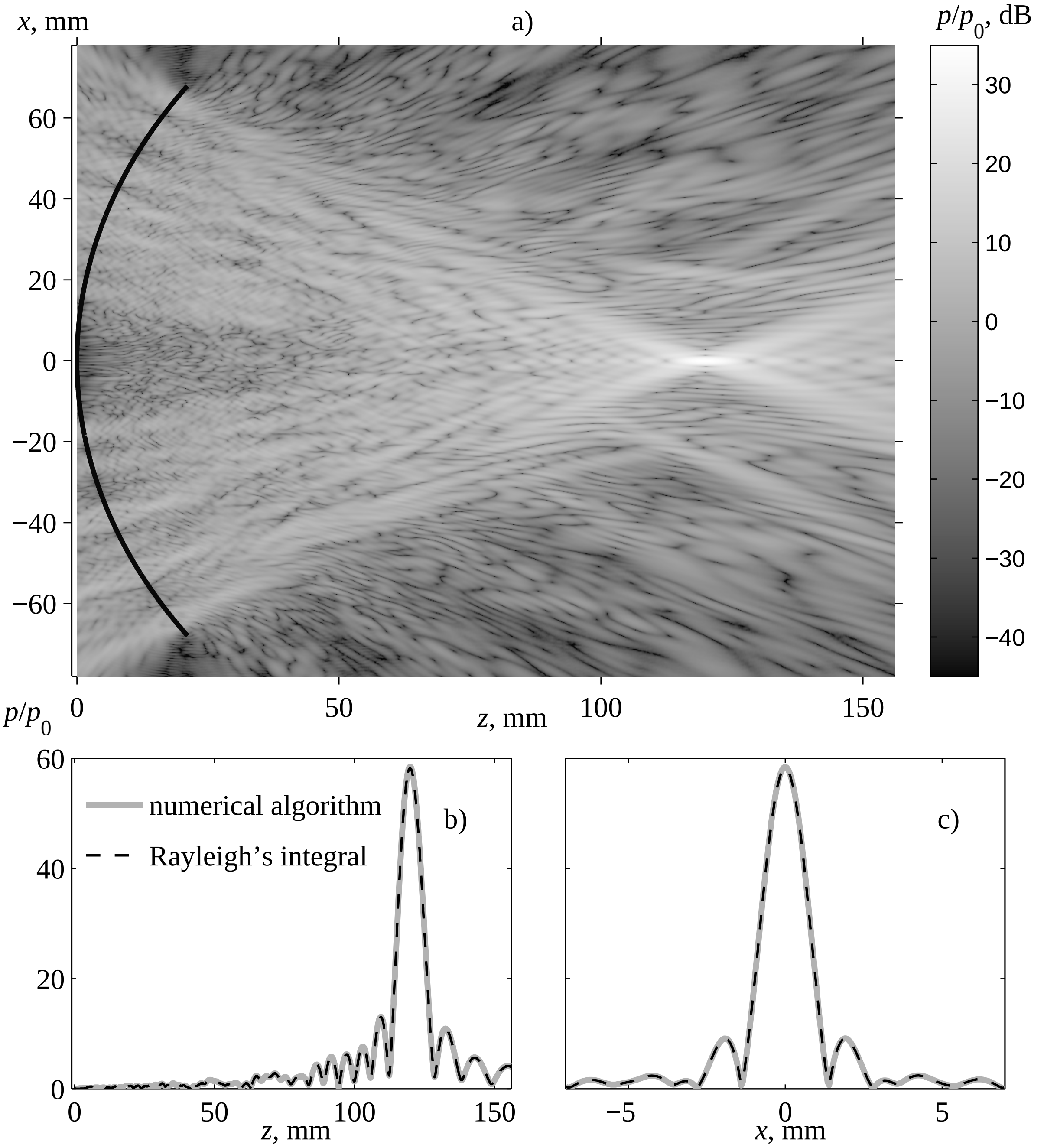

Figure 5.7: Pressure amplitude distribution p/p_0 in the axial plane (x, z), calculated numerically in the linear approximation with the new algorithm (a). The black line denotes the position of the spherical cup where the elements are located (the scale of the x axis is compressed by a factor of 1.5 in relation to the scale of the z axis). Comparison of the results calculated with the new algorithm (solid gray curves) and the Rayleigh integral (dotted curves) for the linear field of the array: pressure amplitude p/p_0 on the axis (b) and in the focal plane along the x axis (c).

§5.4 Nonlinear-diffraction effects in the field of multi-element array

5.4.1 Linear field of the array

The results of modeling the array field in the linear approximation are shown in Fig. 5.7. Figure 5.7a shows the distribution of the pressure amplitude in the axial plane of the array (x, z). The amplitude scale is shown in dB relative to the initial pressure amplitude p_0. Complex diffraction pattern of the field in this axial cross section of the beam results from the multi-element structure of the array and randomized distribution of its elements. However, the pressure distribution in the focal region is nearly regular because the pressures from all the elements of the array are combined in phase close to the focus. Figure 5.7b shows the pressure amplitude along the axis of the array in a linear scale (solid curve). The results of calculating the field directly with the Rayleigh integral (dotted line) are also presented for comparison. Both curves nearly coincide; the difference between them does not exceed 0.5%. The linear pressure gain in the geometric focus of the array is $G = p_F/p_0 = 58.46$ (58.22 for the Rayleigh integral). This value agrees well with the quantity obtained by summation of pressures at the focus from all array elements, $p_F/p_0 = 256\widehat{p}_F/p_0 = 58.37$, where $\widehat{p}_F/p_0 = 0.228$ is the normalized pressure at the focus in the field of one element (Fig. 5.5). This simple estimate is an indirect validation of the algorithm for calculating the diffraction term. Figure 5.7c shows the pressure distributions in the focal plane along the x axis, also calculated using the two methods. The curves are practically indistinguishable from each other. From the results of linear simulations one can determine the dimensions of the focal region of the beam: the size along the beam axis z at a level of 6 dB is 9.7 mm, and the size in the transverse direction, 1.7 mm. The pressure amplitude in the side lobes does not exceed 16% of the amplitude at the focus, and intensity in the side lobes – 2.6% of the intensity in the focus. So, linear field of the array was modeled very accurately, the results demonstrated that array has high focusing gain and low level of side lobes.

5.4.2 Effect of the boundary condition on nonlinear propagation

In modeling nonlinear equation (4.1) with the boundary condition given on the plane $z = 20$ mm, nonlinear effects are not taken into account in the propagation path from the radiator to the given plane. In order to account for nonlinear effects in this region, a method that was previously proposed for modeling ultrasound fields of diagnostic radiators was employed (Christopher, 2006). The field calculated with the Rayleigh integral near the edge of the radiator (on the plane $z = 20$ mm) was back propagated to the plane $(x, y, z = 0)$ using Eq. (4.12) with $-\Delta z$ instead of Δz. In the linear approximation, calculations of the field of the array with such a boundary condition evidently yield the same result as with the boundary condition given on the plane $(x, y, z = 20\ \mathrm{mm})$. In further nonlinear calculations, the boundary condition was set on the plane $z = 0$ (Fig. 5.1b). While propagating between the two planes, the nonlinear operator (4.7) was applied only in the volume bounded by the surface of the radiator cup. The conditions on choosing the volume can be written in the form $z > F - \sqrt{F^2 - x^2 - y^2}$, when $x^2 + y^2 \le R^2$, and $z = F - \sqrt{F^2 - R^2}$, when $x^2 + y^2 > R^2$. The results of calculation using such an algorithm have shown that at intensities of 1, 2, 2.5, 5, and 10 $\mathrm{W/cm}^2$, the peak positive pressure in the geometric focus increases by 2, 5, 7, 1, and 0.1 %, respectively, in comparison to the case where nonlinear effects were not taken into account inside the spherical segment of the array. These results demonstrate that the discrepancies in solutions obtained with boundary conditions set on the two planes are mainly pronounced at moderate intensities of 2 and 2.5 $\mathrm{W/cm^2}$. It will be shown below that at these intensities the shock front is beginning to form at the focus. The difference of two solutions produced using two different boundary conditions is consistent with the study (Bessonova *et al.*, 2009) where it is shown, that the coefficient of nonlinear amplification of the peak positive pressure is growing rapidly if the initial amplitude increases in some range of moderate intensities. Thus in this range of the intensities, small variation of the initial intensity leads to great variation of the peak positive pressure in the focus. The the case of "virtual" sources considered here additional augmentation of harmonics amplitudes is due to a greater propagation distance rather due to increasing of excitation amplitude on fundamental frequency. Further results presented in the work were obtained only with account for nonlinear propagation inside the volume confined by the surface of the array.

5.4.3 Nonlinear field of the array

Figure 5.8 shows the waveforms in the center of the curvature of the array that were simulated at different initial intensities on the array elements. The intensity values are indicated by numbers given near the curves: 1, 2, 2.5, 5, and 10 $\mathrm{W/cm^2}$; index 0 corresponds to the case of linear focusing. The waveforms were shifted in time relative to each other in order to better distinguish the curves.

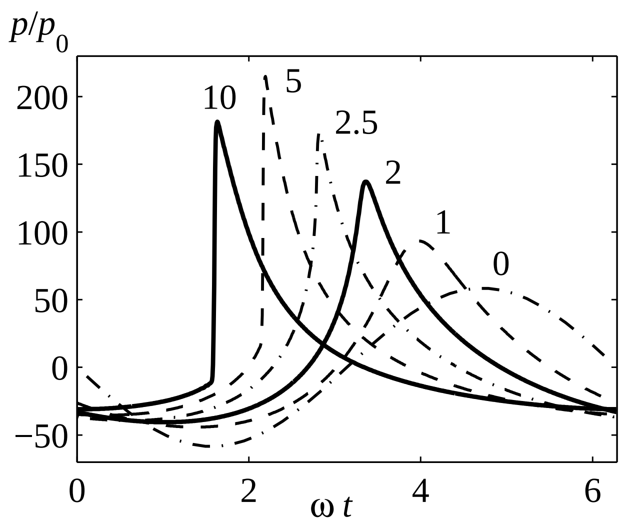

Figure 5.8: Dimensionless pressure waveforms in the geometric focus of the array $(x = 0, y = 0, z = F)$, calculated at different initial intensity levels on array elements: 1, 2, 2.5, 5, and 10 $\mathrm{W/cm^2}$ (numbers next to the curves); 0 – linear focusing of the field.

The sequence of waveforms illustrates typical distortion of the focal wave profiles that follows the strengthening of nonlinear effects (Bessonova *et al.*, 2009). First, when nonlinear effects are weak (1 $\mathrm{W/cm^2}$), insignificant distortion of the waveform occurs without formation of a shock front. The focusing gain increases for the peak positive pressure and decreases for the peak negative pressure in comparison to the linear one because of the diffraction phase shift between the harmonics. The change in the focusing gain for the peak pressures caused by nonlinear effects can be described by a correction indices K_{P+} and K_{P-} which are the ratio of dimensionless pressures p_+/p_0 and p_-/p_0 at the focus in nonlinear and linear beams (Bessonova *et al.*, 2009). For initial intensity of 1 $\mathrm{W/cm^2}$ the correction index for the peak positive pressure is 1.6, for the peak negative pressure 0.76. With an increase in initial intensity (2.5 $\mathrm{W/cm^2}$), a shock front begins to form at the focus and the focusing gain for the peak positive pressure further increases (a correction index of 3). At intensity of 5 $\mathrm{W/cm^2}$, a high amplitude shock is developed near the focus and the correction index for the peak positive pressure reaches its maximum value of 3.7. At even higher

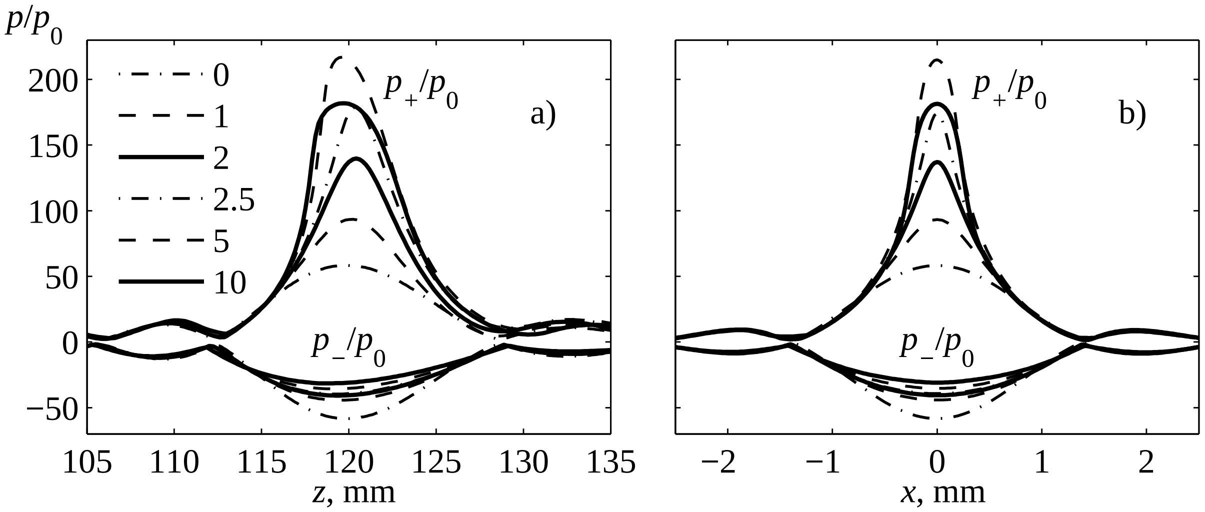

Figure 5.9: Distributions of dimensionless positive p_+/p_0 and negative p_-/p_0 peak pressures along the axis of the array (a) and in the focal plane along the x axis (b) at various initial intensities: 0 – linear focusing (dotted line); the remaining numerals next to the curves correspond to intensities on the array elements, measured in $\mathrm{W/cm^2}$.

initial intensity (10 $\mathrm{W/cm^2}$), the shock front forms prefocally and, since strong nonlinear absorption of the wave energy occurs at the shocks, the correction index for the peak positive pressure decreases to a value of 3.1. The main characteristics such as peak positive and negative pressures, intensity ($I = \sum_{n=1}^{N_{\max}} 4|p_n|^2/2\rho_0 c_0$) and corresponding nonlinear correction indices are reported in the Table 5.1.

I_0, $\mathrm{W/cm^2}$	1	2	2.5	5	10
K_{P+}	1.6	2.35	3.0	3.7	3.1
K_{P-}	0.76	0.70	0.67	0.61	0.53
p_+, MPa	16.2	33.6	47.7	83.2	100.0
p_-, MPa	-7.7	-9.9	-10.8	-13.7	-17.0
K_I	1.09	1.22	1.31	1.48	1.24
I, $\mathrm{W/cm^2}\times 10^4$	0.37	0.83	1.12	2.53	4.24

Table 5.1: Nonlinear amplification indices K_{P+}, K_{P-} and K_I of the peak pressures and intensity in the focus and values of positive p_+ and negative p_- peak pressures in Pa and intensity I in $\mathrm{W/cm^2}$ for different initial intensities at the array elements.

Shown in the Fig. 5.9 the dependencies of the positive p_+/p_0 and negative p_-/p_0 peak pressures along the axis z (Fig. 5.9a) and in the focal plane along the axis x (Fig. 5.9b). In addition to the effect of nonlinear amplification in p_+/p_0 and a monotonic decrease in p_-/p_0 focusing gains, the effect of a shift of the spatial maximum is observed. The shift is away from the radiator at moderate intensities (2 and 2.5 $\mathrm{W/cm^2}$) and towards the radiator at high (5 and 10 $\mathrm{W/cm^2}$) (Bessonova *et al.*, 2009). At intensity levels considered here the shift was approximately 0.5 mm in both directions. With an increase in the initial intensity to a value at which the focusing gain for the peak positive pressure reaches its maximum and begins to decrease (5 $\mathrm{W/cm^2}$), narrowing of the focal region is observed in both the longitudinal and transverse directions. After the focusing gain passes through

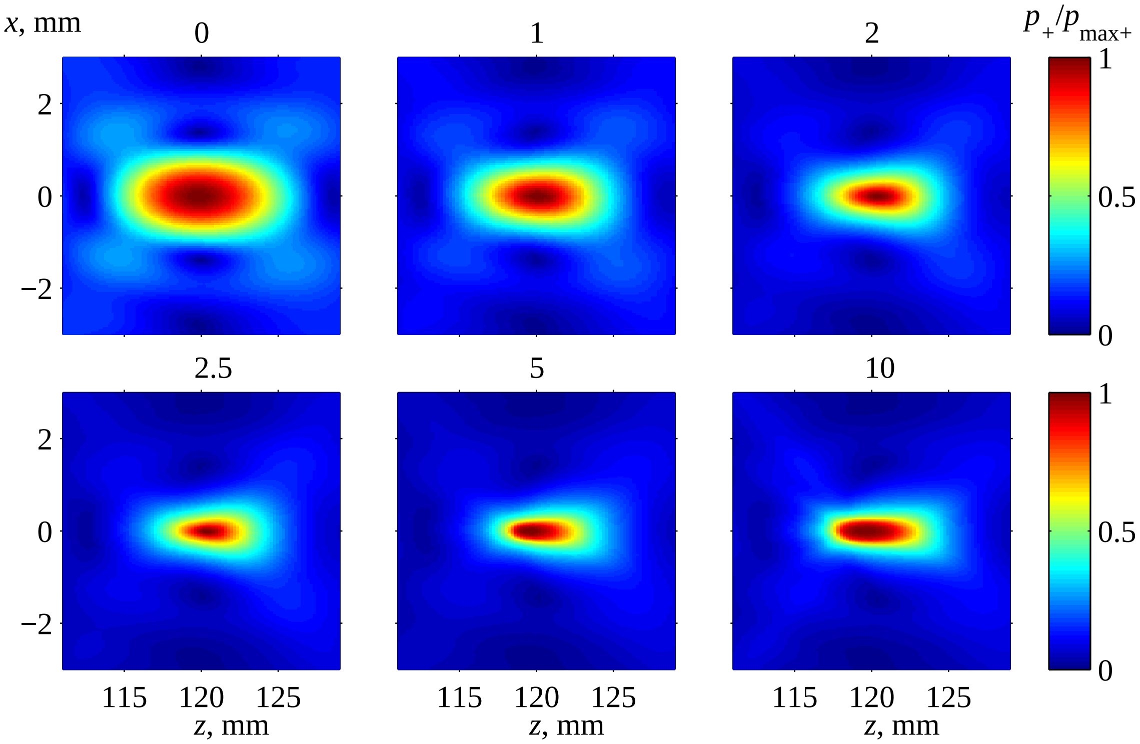

Figure 5.10: Normalized at their maximum distributions of peak positive pressures $p_+/p_{\max+}$ in a plane (x, z) near the focus for different initial intensities at the elements 1, 2, 2.5, 5 and 10 $\mathrm{W/cm^2}$. Scale of the x axis is stretched 3 times in comparison to the z axis.

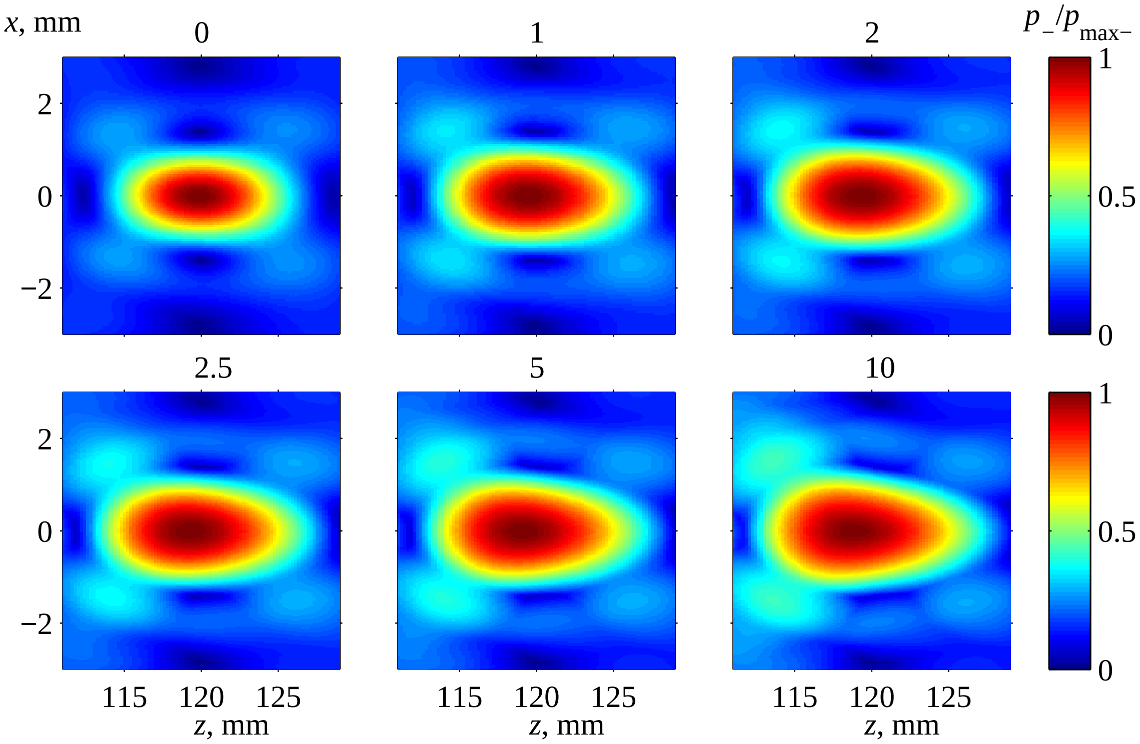

Figure 5.11: Normalized at their maximum distributions of peak negative pressures $p_-/p_{\max-}$ in a plane (x, z) near the focus for different initial intensities at the elements 1, 2, 2.5, 5 and 10 $\mathrm{W/cm^2}$. Scale of the x axis is stretched 3 times in comparison to the z axis.

a maximum, the focal region begins to widen. The width of the focal region at a level of 6 dB for intensities of 1, 2, 2.5, 5, and 10 $\mathrm{W/cm^2}$ in the longitudinal direction is 7.5, 6.0, 5.3, 5.3, and 6.2 mm, respectively; in the transverse direction, 1.2, 0.8, 0.7, 0.6, and 0.7 mm.

Spatial distributions of peak positive and peak negative pressures near the focus in the axial plane (x, z) are shown in Fig. 5.10 and Fig. 5.11, respectively. The peak pressure is normalized to its maximal value. The x axis in the figures is 3 times stretched in comparison to the z axis. Narrowing and broadening of p_+ distributions with increasing the intensity and monotonic broadening of p_- are clearly seen.

§5.5 Method of an equivalent source

5.5.1 Theory of the method

Despite the fact that the simulations of three-dimensional field of an array radiator became now possible, there are several reasons to have faster and simpler methods to calculate nonlinear fields of the 2D therapeutic arrays. First, three-dimensional modeling discussed in previous sections is time and memory consuming. It is not possible to obtain the characteristic of the array in a wide range of initial intensities within reasonable time. Second, already at the design stage of the array there is a need to calculate the nonlinear field. So the number of configurations for which calculations should be done is growing rapidly: scheme of elements distribution over the surface, diameter of the elements, operating frequency, maximal power. Third, the field in the focus is of great interest mainly since here the ultrasound have a targeted impact on tissue. Therefore, as a basic characteristic of the array it is sufficient to evaluate the nonlinear field only near the focus.

A possibility of faster simulations of nonlinear field of the array in the focal region is shown below and relies on the following facts. From Figures (5.7–5.11) it is seen that the acoustic field near the focus is very symmetric about the z axis. Moreover, nonlinear effects (amplification of p_+/p_0, decreasing of p_-/p_0, shocks) are observed only near the focus. In the considered case this area can be defined by intervals $[112\ \ 128]$ mm along the z axis and $[-1\ \ 1]$ mm along x and y axes. Beyond the focal area the nonlinear effects are much weaker. So one can try to approximate the field of the array by an axially symmetric field of a piston radiator in a manner that both fields match each other in the focal area. In this case the axially symmetric source is called here as an *equivalent* source or radiator. If this method works, then faster and well studied axially symmetric 1.5D models can by used to estimate the field of the array either in parabolic approximation (Bessonova *et al.*, 2009,Bessonova *et al.*, 2010,Canney *et al.*, 2008,Khokhlova *et al.*, 2002) or using simulations with the axially symmetric version of the Westervelt equation (Christopher & Parker, 1991a,Tavakkoli *et al.*, 1998). The method of an equivalent source was previously used to model a real non-ideal piston radiator in the parabolic approximation (Canney *et al.*, 2008).

It the present work two types of equivalent sources are considered. One of them will be modeled using the axially symmetric version of the Westervelt equation and the second – in the parabolic approximation. In Fig. 5.12 boundary conditions in the plane $z = 0$ for the array (a) and two equivalent sources are shown. Abbreviates interpret as: WE – Westervelt equation (b) and PE – parabolic approximation (c). For the calculations of the equivalent sources the three-dimensional algorithm was used, rather than any other programs specially adopted to the axially

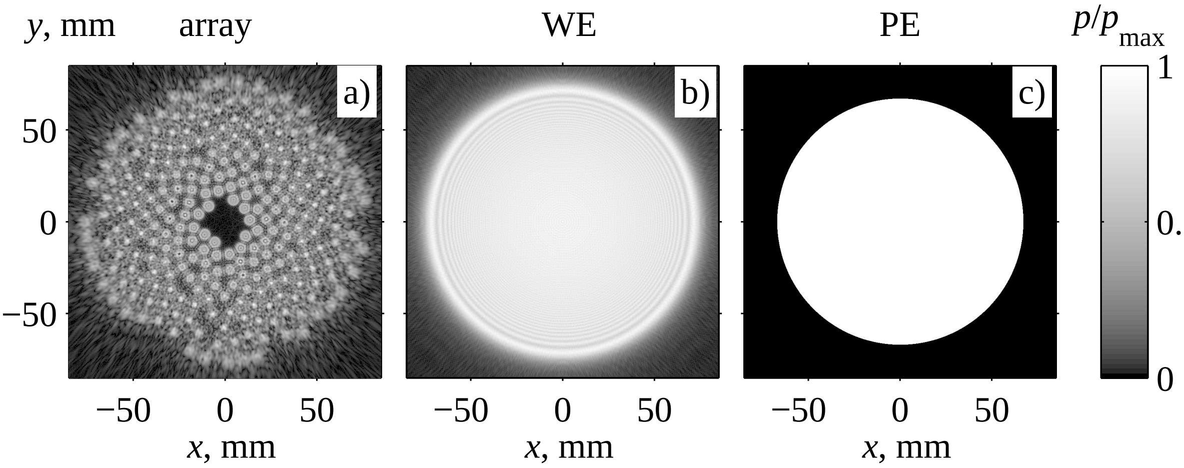

Figure 5.12: Initial pressure magnitude distributions of the array (a) and of two equivalent sources (b and c) in a plane $z = 0$, normalized at the maximum of the each distribution. Abbreviates explain diffraction models corresponding to the boundary conditions: WE – the Westervelt equation (b), PE – parabolic equation (c). Dimensionless pressure $p_{\max}/p_0$ for three cases are equal to 2.34, 1.13 and 1.00, respectively.

symmetric case. Only appropriate boundary conditions and diffraction operators (4.12) or (4.13) were imposed in 3D. However, at the same time, parabolic approximation results were verified in comparison with simulations done using specialized axially symmetric model realized in a work (Bessonova *et al.*, 2010).

5.5.2 Practical realization of the method and simulation results

Parameters of the equivalent sources were selected in case of linear beam propagation using analytical solutions available for the pressure field of the axially symmetric piton source on the axis and in the focal plane (see Appendix A). First, geometric parameters were selected and then the amplitude. A focal distance of the piston sources was equal to the focal distance of the array, and its radii R_{eqv} were varied. Difference of two normalized fields of pressure magnitude of the piston and of the array along the axes x and z was minimized to obtain the optimal piston radius. Then the excitation pressure magnitude of the piston was adjusted to feet the same pressure as in the focus of the array. A correction coefficient arises from the fact that the piston source has greater radiating surface than the array and consequently it has greater focusing gain. Denote the pressure in the focus of the piston source as $\tilde{p}_F = G_{\text{eqv}}\tilde{p}_0$ and the same quantity in the focus of the array as $p_F = Gp_0$, where G_{eqv} and G are corresponding focusing gains, and $\tilde{p}_0$ and p_0 are pressure amplitudes on the surface of the radiators. The condition $p_F = \tilde{p}_F$ gives $K_{\text{sc}} = \tilde{p}_0/p_0 = G/G_{\text{eqv}} < 1$. The ratio of the surface amplitudes of the piston and the array K_{sc} is called here as amplitude scaling coefficient. Parameters of the array and of the equivalent sources are listed in a Tab. 5.2. As seen from the data, the radii of the equivalent sources are close to the radius of the array and the differences are in focusing gains only, which are about 1.6 times greater for the piston sources.

In the Fig. 5.13 the pressure fields of the array and the equivalent sources are compared on the axis (amplitude in Fig. 5.13a and phase in Fig. 5.13b) and in the focal plane (Fig. 5.13c). Good

Source type/parameters	F, mm	R, mm	G	$K_{\rm sc}$
array	120	64	58.4	1.0
Rayleigh integral (WE)	120	64.6	94.5	0.613
parabolic approximation	120	66.9	93.8	0.620

Table 5.2: Parameters of the array and the corresponding equivalent sources.

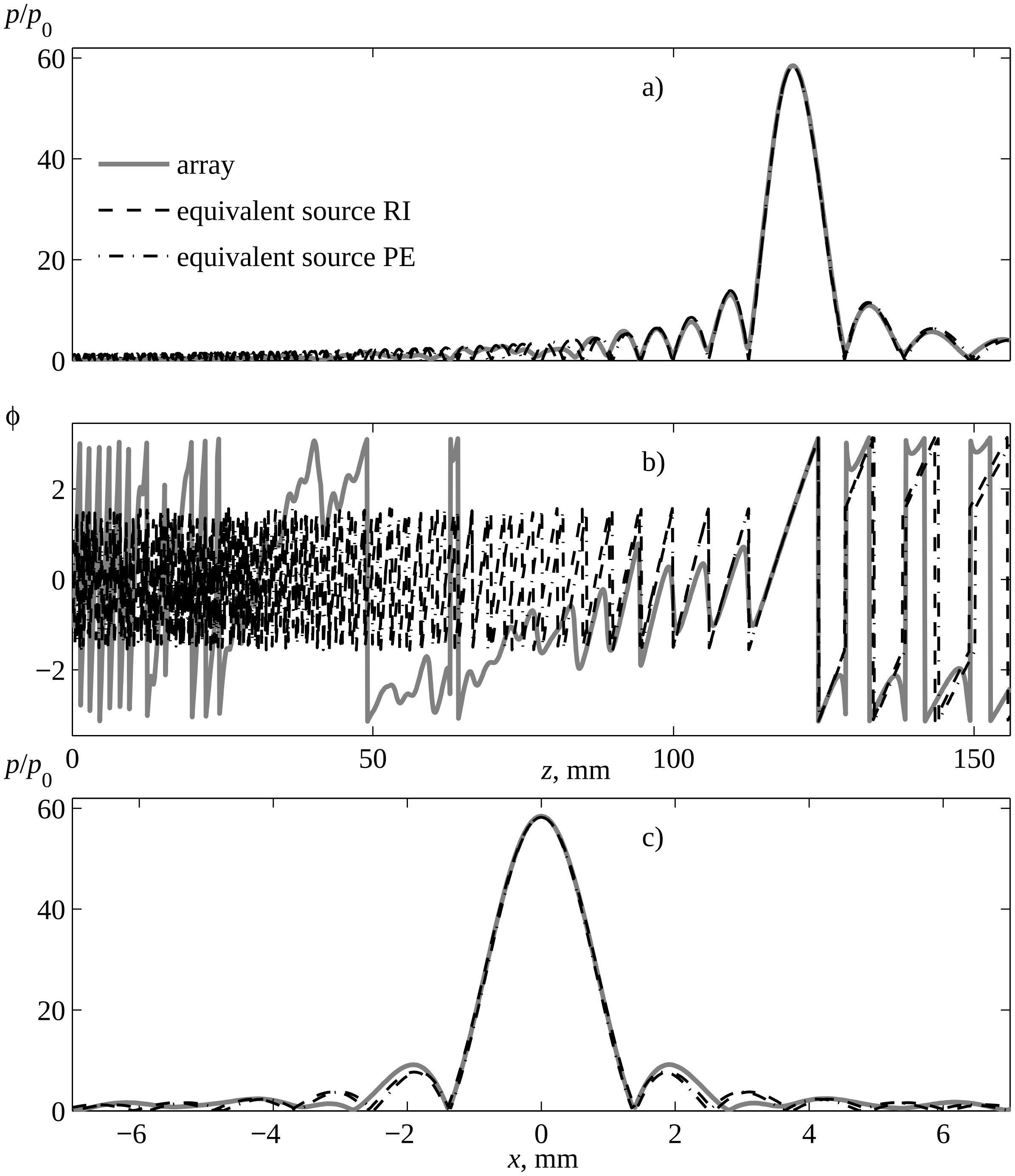

Figure 5.13: Comparison of the linear pressure field of the array (solid gray line) on the axis (a – amplitude, b – phase) and in the focal plane (c – amplitude) with analytical solutions for the fields of the equivalent sources. The Rayleigh integral results are shown by dashed lines and parabolic equation results by dash-dotted lines.

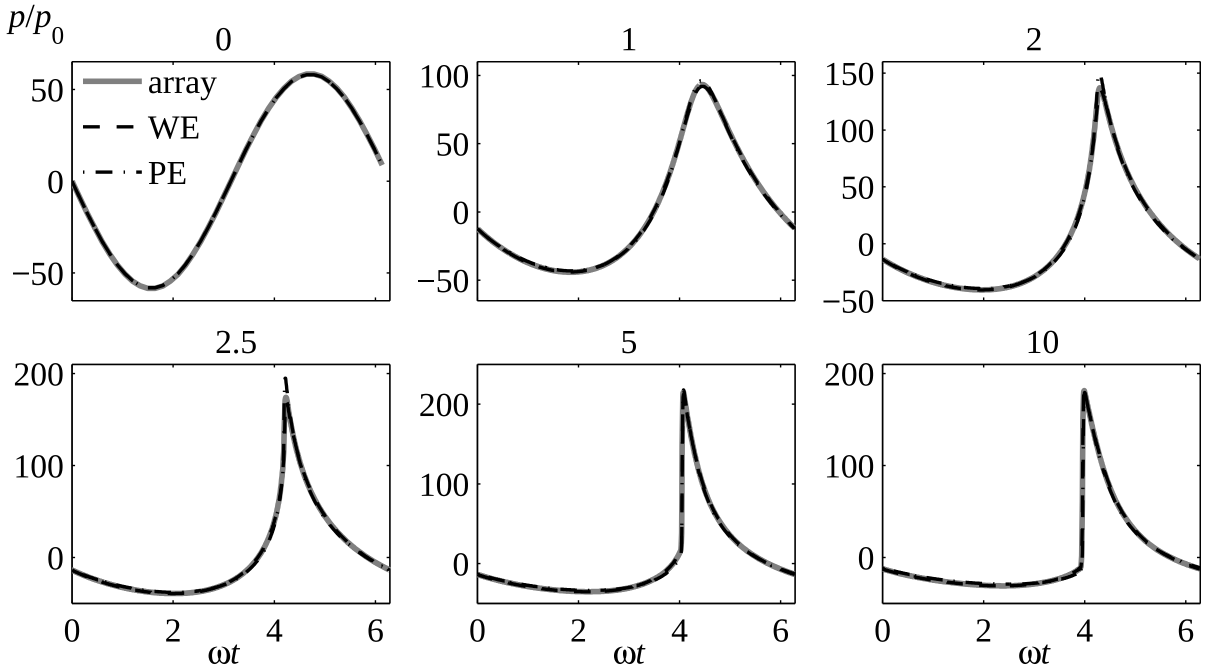

Figure 5.14: Comparison of the waveforms in the focus, obtained in modeling of the field of the array (solid gray line) and the fields of the equivalent sources: the first calculated using the Westervelt equation (dashed line) and the second in the parabolic approximation (dash-dotted line). Numbers above subfigures are the initial intensities at the elements I_0, $\mathrm{W/cm^2}$. The amplitude scale is different for different subfigures.

approximation of the array field is achieved. In longitudinal direction the fields are concide not only in the focus but also in several prefocal and postfocal maxima. In the focal plane the coincidence is observed up to the first sidelobes. Some smaller amplitude of the first sidelobes in the fields of the equivalent sources is explained by the fact that the considered piston models does not include an opening for the diagnostic transducer in the center as it takes place for the array. However, since the radius of the opening is small (9 mm) it does not introduce any significant discrepancies. If necessary, an equivalent axisymmetric source with a central opening can be considered as well.

After the selection of optimal parameters of the equivalent sources nonlinear simulations were done. In the Eq. (4.3) the normalized amplitude was set to $\tilde{p}_0$ for this case. To do the comparison between the field of the array and the equivalent sources, the calculated data of the latter should be normalized by the pressure p_0 corresponding to the array. To do this, all calculated amplitude data were multiplied on the scaling coefficient K_{sc}.

Nonlinear modeling results of the equivalent sources in comparison with the array field are presented in three figures for several excitation intensities: Fig. 5.14 – waveforms in the focus, Fig. 5.15 – peak pressures along the axis z and Fig. 5.16 – peak pressures in the focal plane along the axis x. Solid gray curves correspond to the array, the Westervelt equation (WE) equivalent source results are marked by dashed lines and parabolic equation (PE) results – by dash-dotted lines. Numbers above subfigures are intensities at the array elements measured in $\mathrm{W/cm^2}$, zero corresponds to linear propagation. The agreement between the three simulation results is very good, excluding only parabolic equation results at moderate intensities of 2 and 2.5 $\mathrm{W/cm^2}$. Quan-

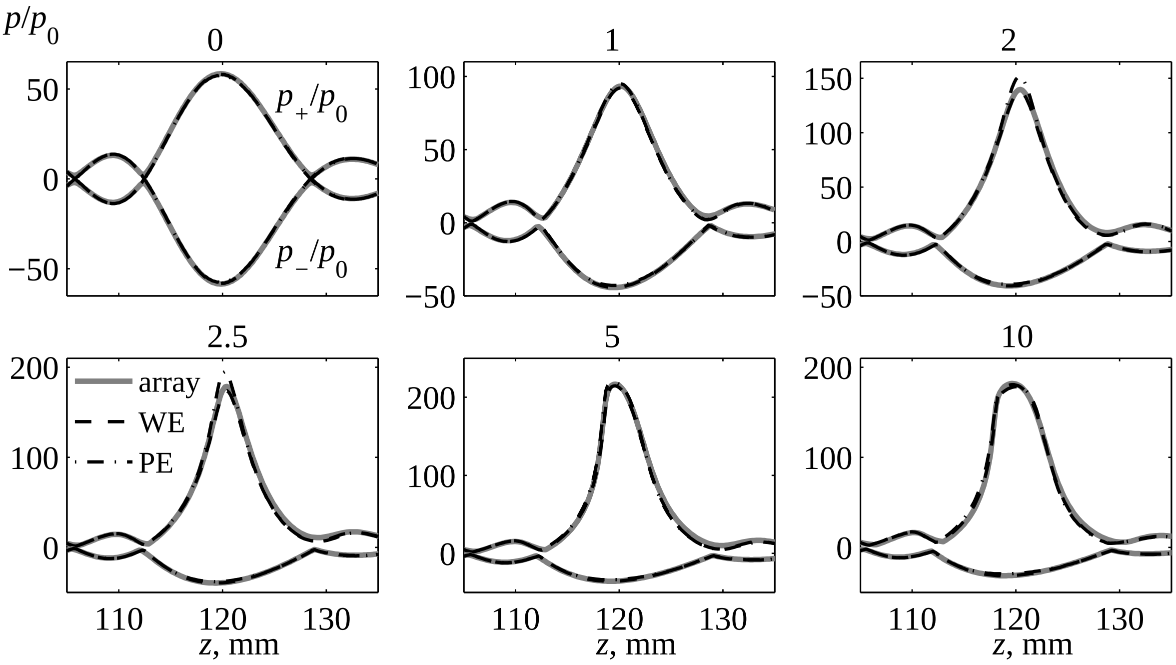

Figure 5.15: Comparison of the peak pressures along the z axis obtained in modeling of the field of the array (solid gray line) and the fields of equivalent sources. Notations are the same as in Fig. 5.14.

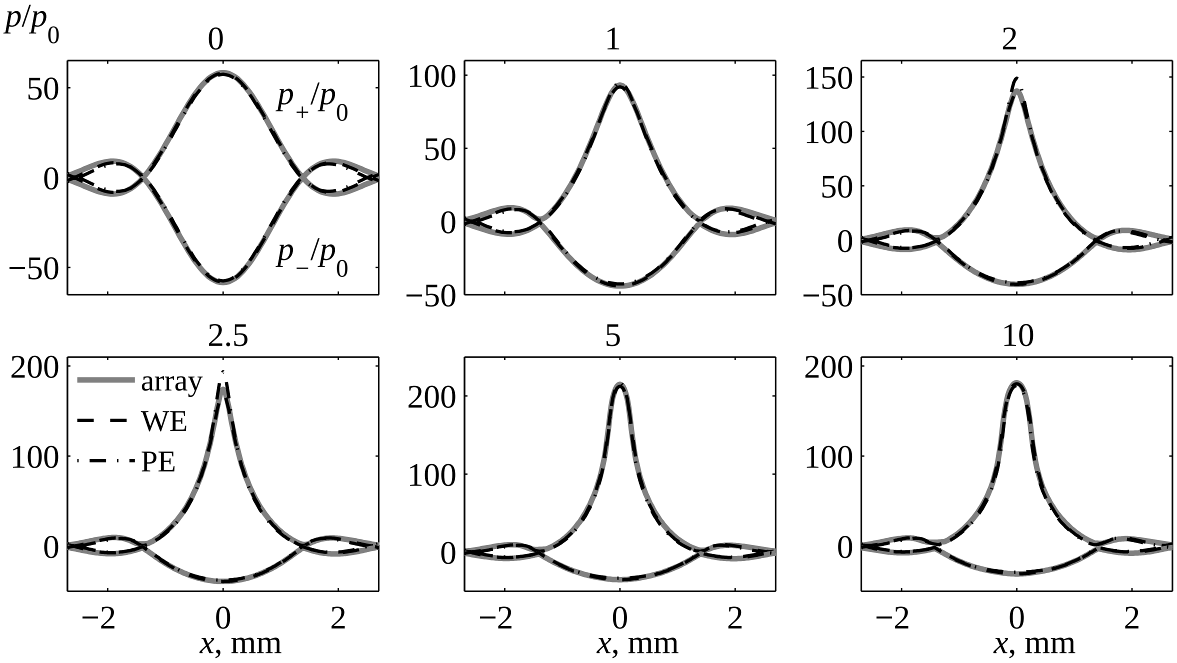

Figure 5.16: Comparison of the peak pressures in the focal plane along the x axis, obtained in modeling of the field of the array (solid gray line) and the fields of equivalent sources. Notations are the same as in Fig. 5.14.

titatively, relative differences between the peak positive pressures p_+/p_0 in the focus are shown in Fig. 5.17. Cross-markers correspond to the Westervelt equation results and circle-markers – to the parabolic equation. Overestimation of p_+/p_0 in the parabolic approximation is noticeably high as 12% at $I_0 = 2.5\ \mathrm{W/cm^2}$ intensity.

The overestimation of the peak positive pressure is explained by the same reason as the difference between nonlinear simulations of the array using two different boundary conditions (see sec. 5.4.2). Namely, in the parabolic approximation boundary conditions were set in the plane $(x, y, z = 0)$ and nonlinear effects were calculated without any limitations of the propagation volume by the surface of the spherical cup, as it was done in sec. 5.4.2. Thus, additional volume of the nonlinear interactions results in higher amplitudes of harmonics in the vicinity of the source that lead to higher p_+/p_0 in the focus. This problem of the parabolic approximation can be solved imposing the same limitation on the nonlinear interaction volume that was already discussed. Note, that this remark concerns only moderate intensity cases when the shock front in the focus begins to appear. When well-developed shock is present in the focus then the discussed difference in peak positive pressure is small (Fig. 5.17, $I_0 = 5$ and 10 $\mathrm{W/cm^2}$cases), since the correction index K_{P+} becomes much less sensitive to the excitation intensity I_0 (Bessonova *et al.*, 2009). At the same time the error in the case of the equivalent source, calculated using the Westervelt equation is small for all intensities and has maximum of -3% at $I_0 = 2.5\ \mathrm{W/cm^2}$. Most of this error of p_+ can be explained by some error of adjustment of the scaling coefficient K_{sc} which was $0.5\ \%$ smaller that it should be. This difference was amplified due to nonlinear effects, and actually, the p_+ values of the piston source are smaller than the array one.

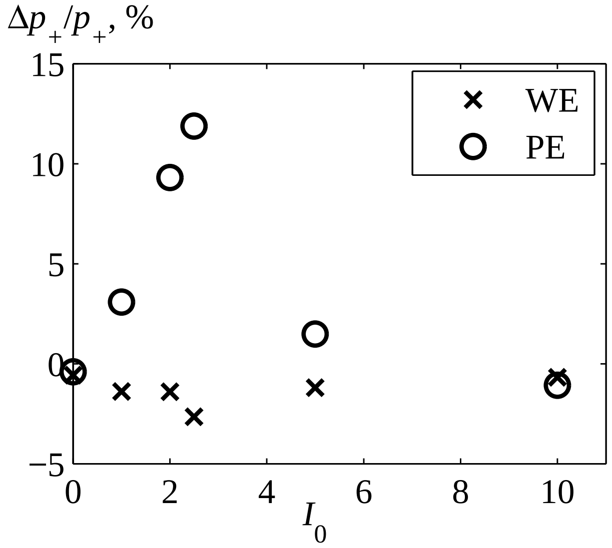

Figure 5.17: Relative difference between the peak positive pressure in the focal waveforms of the equivalent source and of the array $[p_+(eqv.) - p_+(arr.)]/p_+(arr.)$ depending on the intensity I_0. Cross markers correspond to the axisymmetric Westervelt equation, circle markers – to the parabolic equation.

Thus, in this section numeric modeling results showed that the method of the equivalent axisymmetric source can be successfully used to predict nonlinear field in the focus of the array. It is preferably to use for this purpose the axisymmetric variant of the Westervelt equation. However, the parabolic equation also can be used. In general, despite of the large enough focusing angle of the considered equivalents source ($\sin\alpha = R/F$, $\alpha = 27°$), the parabolic approximation was found to be an adequate model. Correction indices K_{P+}, K_{P-} and K_I for axisymmetric piston source modeled in parabolic approximation are already calculated for different nonlinearity coefficients and focusing gains in the paper (Bessonova *et al.*, 2009).

§5.6 Conclusions

In this chapter, a novel numerical algorithm based on the Westervelt equation was developed. The algorithm makes it possible to model three-dimensional nonlinear fields of focused ultrasound radiators including formation of shocks in the focal region. A varying number of harmonics and ”echelon-type” data storage were employed in the algorithm in order to reduce the sizes of data arrays during calculations. A parallel computation model for multiprocessor SMP computers was implemented resulting in significant acceleration of calculations. The accuracy of modeling different operators in the algorithm and the complete solution to the problem were tested by comparing the results of simulations with known analytic solutions or with the results of modeling obtained in other studies in a parabolic approximation for nonlinear axially symmetric beams. The test results have shown high accuracy of the developed algorithm. To demonstrate the abilities of the algorithm, nonlinear field of a multi-element two-dimensional phased array was simulated. It was shown that, at clinically relevant intensity levels on the array elements, high amplitude shock fronts are present in the focus of the array.

A model of an equivalent source intended to accelerate calculations of the nonlinear field of an array in the focal region was also developed. It was shown that very good approximation with an error about few percent can be obtained using the equivalent source model and simulating the field using either axially symmetric Westervelt equation or the parabolic KZK equation.

The developed algorithm can be used to solve a broad class of practically important problems of nonlinear medical acoustics. It can be applied to perform nonlinear ultrasound characterization of pressure fields of ultrasound HIFU surgical devices in water, as well as to calculate ultrasound-induced thermal effects in tissue. Generalization of the algorithm with account for smooth inhomogeneities in the propagation medium would enable more realistic simulations in soft tissues; it is also possible to model ultrasound exposures in tissue with the presence of acoustic obstacles, e.g., during irradiation through the rib cage. An important feature of the algorithm in application to HIFU is the possibility of calculating three-dimensional fields of radiators with complex spatial configuration while maintaining reasonable requirements on the currently available computing resources.

Conclusion

The general aim of the dissertation was experimental and numerical studies on propagation of nonlinear acoustic pulses and ultrasonic beams in inhomogeneous media in context of atmospherical acoustics and sonic boom problem as well as in context of diagnostic and therapeutic medical ultrasound. So several particular research branches were pursued in the dissertation.

In experimental study devoted to sonic boom propagation in turbulent atmosphere, the aim was to build an experimental setup which allows to investigate shock wave propagation in thermal turbulence. High amplitude and short duration N-waves produced by a spark source were used in the experiment. The problems of measuring the pulses using acoustical and optical methods were considered in the first chapter. The N-wave propagation in quiet air was analyzed using numerical simulations of the Burgers equation. The modeling data were compared to measurements done by a condenser microphone. A good agreement between simulations results and experimental data for peak positive pressure values and duration of the pulse was shown. However, the front shock rise time deduced from the microphone output was found to be largely overestimated because of the limitations in the frequency response of the measuring system. In order to estimate the front shock rise time more accurately, optical measurements based on a focused shadowgraphy technique were done. To interpret shadowgrams, the light propagation through refraction index inhomogeneity produced by the shock was modeled. Two light propagation models were tested: the first was based on the geometrical optics, and the second was based on the parabolic equation. It is shown that geometrical optics cannot accurately predict intensity pattern of the shadow. The rise times at different distances from the source deduced from shadowgrams using the parabolic model were shown to be in a very good agreement with the acoustical modeling results. The shortcomings of the condenser microphones were explicitly demonstrated, so acoustical measurements should be analyzed with care because the response of the measurement system has a great influence on shock rise time estimation.

In the second chapter of the dissertation the propagation of spherical N-waves of short duration and high amplitude (40 μs duration and amplitude of 1100 Pa at 20 cm from the source) in thermal turbulence was studied experimentally. The new experimental setup was built at the Graduate Engineering School of Lyon (ECL). The thermal turbulence was produced by a heating grid. The turbulent field was measured in many spatial points using thermal probes mounted on 3D positioning system. The measured spectra of fluctuations of acoustical refraction index μ were found to be well described by the von Karman spectrum of isotropy homogeneous scalar turbulence with the outer scale $L_0 = 20$ cm, the inner scale $l_0 = 5$ mm, and the mean-square $\sqrt{<\mu^2>}$

equal to 0.85% on average near the propagation path of the acoustic wave. The randomly distorted waveforms were measured in the range of propagation distances (source-microphones) from 0.4 m to 2 m and statistical distributions of most important parameters of the N-wave were investigated. Classical effects of broadening the probability distributions of the N-wave parameters (peak pressures, shock rise time, and arrival time) and trends for the mean and standard deviation with increasing propagation distance were demonstrated. For the first time the duration of the distorted N-waves was analyzed and the pulses with extreme duration 2-3 times greater than the duration in homogeneous medium were shown.

The obtained experimental data were compared with the previously reported results of the experiment on N-wave propagation in kinematic turbulence (Averiyanov, 2008). The two experiments were close in terms of the widths of the turbulent layers, the parameters of the propagating pulse, the values of the characteristic scales of the energy spectrum, while the type of turbulence was different: scalar type for thermal turbulence and vector type for kinematic turbulence. It was shown that in a case of almost the same mean square $\sqrt{<\mu^2>}$ of the refraction index, the kinematic turbulence leads to much stronger distortions of the amplitude and the shock rise time of the N-wave. In addition, the kinematic turbulence was shown to be much more efficient in terms of the appearance of strong focusing: in comparison to the case of thermal turbulence, it produces 2-3 times greater cumulative probability for the peak positive pressure to exceed two times the amplitude of the N-wave propagated in homogeneous air. Comparable distortions of the peak pressure and the shock rise time are achieved in the kinematic turbulence at much lower values of the refraction index rms $\sqrt{<\mu^2>}$ (2.5 times lower) than in the thermal turbulence.

In theoretical study of N-pulses propagation in inhomogeneous medium, the aim was to develop two-dimensional numerical model which allow to investigate nonlinear and diffraction effects on statistics of amplitude of N-wave, which wavefront was randomly modulated. In the third chapter, the model based on two-dimensional KZK equation and a model of random phase screen with Gaussian spectrum was presented. The phase screen was characterized by correlation length and by refraction length z_r, which is the propagation distance where first major focusing zones (caustics) occur. Probability distributions, mean value and standard deviation of the N-wave amplitude were obtained from the numerical solutions of the KZK equation and were presented as functions of propagation distance and nonlinear length for different correlation lengths of the phase screen. Results obtained from the KZK diffraction model were compared with analytical solutions of the nonlinear geometrical acoustics (NGA) approach. It was shown that close to the screen, up to the propagation distances of $z_r/3$, the results of the diffraction and geometric approaches agree very well. At longer distances statistical properties of the random acoustic field can be accurately described only if diffraction effects are taken into account. The effect of the spatial size of phase fluctuations on statistical distributions was considered. Large-scale phase fluctuations produce stronger focusing zones and probability distribution functions become larger. The mean amplitude becomes smaller than the plane wave amplitude. The amplitude field behind the small-scale phase screens is characterized by weak focusing in the caustics, probability distributions become narrower. The mean value is close to the amplitude of the plane wave in this case. The effect of nonlinearity on the amplitude statistics was shown to be twofold. Weak nonlinearity leads to slight enhancement of focusing effects resulting in higher probability of high amplitude waves. Strong nonlinear effects suppress amplitude fluctuations and lead to narrower probability distributions.

The problems concerning diagnostic and therapeutic applications of focused ultrasound were also considered in the dissertation. In the fourth chapter the problem of selective destruction of the harmonics fields in a finite amplitude weakly focused beam after propagation through a random phase layer of special configuration was considered using numerical simulations and experimentally. The phase layer consisted of a great number of identical circular regions with fixed phase shift and randomly distributed on a plan was used. Theoretical model for calculating the propagation of a nonlinear beam, based on the Westervelt equation, was described. The focusing quality criterion was introduced to quantify distortions of harmonic fields. The simulation results for two special cases of $180°$ and $90°$ "resonant" phase shifts at the fundamental frequency were studied theoretically. The effect of selective destruction of focusing on the fundamental frequency and odd harmonics in the case of $180°$ phase layer placed in any position along the axis was shown. The destruction of the second harmonic in the case of $90°$ layer located close to the focus was observed. When the $90°$ phase layer was placed close to the source the better focusing of the higher harmonics was shown. The experimental setup built in LEMAC laboratory in General Physics Institute of A.M. Prokhorov was described and physical realizations of the $90°$ and $180°$ phase layers were presented. The measured ultrasound fields for these two cased were compared to the simulation results and good qualitative agreement for the focusing quality of considered harmonics was found. So, the possibility to destroy the focusing at certain harmonics and to preserve focusing at others using the inhomogeneous phase layer with "resonant" phase shifts was established.

In the fifth chapter the problem of modeling three-dimensional ultrasound fields of high intensity therapeutic transducers with account for the formation of shocks was considered. A novel numerical algorithm based on the Westervelt equation was developed. A varying number of harmonics and "echelon-type" data storage were employed in the algorithm in order to reduce the sizes of data arrays in calculations. A parallel computation model for multiprocessor SMP computers was implemented resulting in significant acceleration of calculations. The algorithm was tested using comparison of the simulated fields to reported data for the case of axially symmetrical source. The test results have shown high accuracy of the developed algorithm. As an example, nonlinear field of a multi-element two-dimensional phased array was simulated. It was shown that, at clinically relevant intensity levels on the array elements, high amplitude shock fronts are present in the focus of the array. A model of an axially symmetric equivalent source intended to accelerate calculations of the nonlinear field of an array in the focus was developed. A good approximation of the array field near the focus by the field of the equivalent source with an error of few percents was demonstrated in wide range of acoustical intensities using either axially symmetric Westervelt equation or the parabolic KZK equation.

The studies reported in the dissertation open a number of possible perspectives. The problem of peak negative pressure and rear shock of the N-wave generated by spark source remains open. To accurately measure the rear shock the optical methods which are more sensitive than shadowgraphy should be applied. For example, a Mach-Zehnder laser interferometer could be used (Smeets, 1977) which application to measure the N-waves was theoretically considered by author (Yuldashev *et al.*, 2010b). The knowledge about the peak negative pressure and rear shock rise time would be helpful to improve the method of calibration of condenser microphones proposed in (Yuldashev *et al.*, 2008b).

The conclusions done in the chapter 2 about different statistics of N-wave distortions after propagation in turbulence of two different types should be validated theoretically. Despite of many theoretical studies which used geometrical acoustics to look on the problem, consecutive results of comparison of turbulence type impact on the N-wave distortions obtained using at least 2D parabolic models does not exist. Taking into account that 3D simulations of nonlinear pulse propagation are not possible for the moment, the qualitative comparison and validation of the experiment based on 2D models will be acceptable. It is also interesting to not only simulate a plane wave propagation but also to try use the waves with curved wavefront which represents radiation from a point source. It could be done using wide-angle parabolic equation (Dallois, 2000) or more sophisticated one-way propagation models which currently attract a high interest of researches (Dagrau *et al.*, 2011).

The numerical model presented in the chapter 3 can be extended using another phase screen spectra. For example, the phase screen with von Kármán spectrum could be considered to take into account multi-scale effects on N-wave random focusing. Also, several phase screens can be considered on the propagation path to simulate extended random medium. And finally, extension the model to 3D geometry may have an interest.

The theoretical studies with the phase layers done in the chapter 4 could be continued using the optimized algorithm, presented in the chapter 5. For example, it is interesting to statistically analyze not only focusing quality of harmonics but also their amplitude and power characteristics as functions of propagation distance in the presence of the layer on the path. Investigation of the influence of the layer on the focusing of the more intensive beam with a shock waveform in the focus could be also very interesting.

And finally, a number of applications of the algorithm developed in the chapter 5 to many interesting problems of the medical ultrasound could be considered. For example, it is interesting to model nonlinear ultrasound exposures in tissue irradiated through the rib cage, similarly as it was done in linear simulation using Rayleigh's integral in (Bobkova *et al.*, 2010). It would be also interesting to compare the simulations results of the array field to measurements done for the real prototype.

Appendix A

Axial and focal pressure fields of focused circular piston

§A.1 Analytic solution in parabolic approximation

The analytical solutions for the pressure field of the focused circular piston on the axis and in the focal plane can be obtained resolving the standard liner parabolic equation (Vinogradova *et al.*, 1979). On the axis of the piston, the pressure amplitude is written as following:

$$p(z) = p_0 \frac{1 - \exp\left[-iG(1-z/F)/(z/F)\right]}{1 - z/F}$$
$$p(z = F) = ip_0 G. \tag{A.1}$$

Magnitude of the pressure field thus is:

$$|p(z)| = 2p_0 \frac{\sin\left[0.5G(1-z/F)/(z/F)\right]}{1 - z/F}$$
$$|p(z = F)| = p_0 G.$$

Pressure amplitude in the focal plan is:

$$p(r) = 2p_0 G \frac{J_1(2Gr)}{2Gr}. \tag{A.2}$$

In the above equations, $G = k_0 R^2/2F$ is the linear pressure gain in the focus, F is the focal distance, R is the piston radius, p_0 is the pressure magnitude close to the source, k_0 is the wavenumber, z is the coordinate along the axis, r is the radial coordinate in a plane perpendicular to the axis, J_1 is the Bessel's function of the 1-st order.

§A.2 Analytic solution calculated using Rayleigh integral

The pressure field radiated by a spherical cup with the oscillation velocity distributed over the curved surface uniformly in the circle of radius R was calculated in (O''Neil, 1949). The following notations are introduced: $\Delta = F(1 - \sqrt{1 - R^2/F^2})$ is the depth of the cup, α is half-angle of the cap aperture which related to the dimensions as $\cos\alpha = 1 - \Delta/F$, $\sin\alpha = 1 - R/F$. Using the quantity $R_{\max}$

$$R_{\max}(z) = F\sqrt{1 + (1 - z/F)^2 - 2(1 - z/F)\cos\alpha},$$

the complex amplitude on the axis z is be written as following:

$$\begin{aligned} p(z) &= p_0 \frac{1 - \exp\left[ik_0 z - ik_0 R_{\max}(z)\right]}{1 - z/F} \\ p(z = F) &= ip_0 k_0 \Delta. \end{aligned} \tag{A.3}$$

The amplitude in the focal plane is provided by the formula:

$$p(r) = 2p_0 k_0 \Delta \frac{J_1(k_0 r \sin\alpha)}{k_0 r \sin\alpha}. \tag{A.4}$$

Appendix B

Transformation of the Westervelt equation

The Westervelt equation with thermoviscous therm in its original form can be written as following:

$$\frac{\partial^2 p}{\partial t^2} - c_0^2 \Delta p = \frac{\delta}{c_0^2} \frac{\partial^3 p}{\partial t^3} + \frac{\varepsilon}{\rho_0 c_0^2} \frac{\partial^2 p^2}{\partial t^2} \tag{B.1}$$

In the retarded system of coordinates $\tau = t - z/c_0$, $z = z$, $p(t, z, x, y) \to \tilde{p}(\tau, x, y, z)$, time and spatial derivatives are transformed as following:

$$\begin{aligned} \frac{\partial^2 p}{\partial t^2} &= \frac{\partial^2 \tilde{p}}{\partial \tau^2} \\ \frac{\partial p}{\partial z} &= -\frac{1}{c_0} \frac{\partial \tilde{p}}{\partial \tau} + \frac{\partial \tilde{p}}{\partial z} \\ \frac{\partial^2 p}{\partial z^2} &= \frac{1}{c_0^2} \frac{\partial^2 \tilde{p}}{\partial \tau^2} - \frac{2}{c_0} \frac{\partial^2 \tilde{p}}{\partial \tau \partial z} + \frac{\partial^2 \tilde{p}}{\partial z^2}. \end{aligned} \tag{B.2}$$

Substitution the corresponding derivatives in the Eq. (B.1) and renaming the variable $\tilde{p}$ back to p gives the equation:

$$\frac{\partial^2 p}{\partial \tau \partial z} = \frac{c_0}{2} \Delta p + \frac{\delta}{2 c_0^3} \frac{\partial^3 p}{\partial t^3} + \frac{\varepsilon}{2 \rho_0 c_0^3} \frac{\partial^2 p^2}{\partial t^2}, \tag{B.3}$$

which was used in chapter 4 and in chapter 5.

Let describe here the diffraction operator calculated with angular spectrum method. The diffraction operator of Eq. (B.3) for each harmonic component at angular frequency ω_n is provided by the equation:

$$\frac{\partial p_n}{\partial z} = \frac{i}{2 k_n} \left(\frac{\partial^2 p_n}{\partial z^2} + \Delta p_\perp \right). \tag{B.4}$$

Transformation of this equation to angular spectrum (spatial spectrum) gives ordinary differential equation for each component of the spectrum $\widehat{p}_n(k_x, k_y, z)$:

$$\frac{\partial^2 \widehat{p}_n}{\partial z^2} + 2 i k_n \frac{\partial \widehat{p}_n}{\partial z} - k_\perp^2 \widehat{p}_n = 0. \tag{B.5}$$

Solving this equation in the form

$$\widehat{p}_n = A \exp\left[ikz\right], \tag{B.6}$$

one can find that $k = -k_n \pm \sqrt{k_n^2 - k_\perp^2}$ following to solution of characteristic equation $k^2 + 2k_n k + k_\perp^2 = 0$. The choice of solution which corresponds to the wave traveling in positive direction of z

axis gives the diffraction transfer function (propagator) for each spatial spectrum component:

$$\widehat{p}_n(k_x, k_y, z) = \widehat{p}_n(k_x, k_y, z = 0) \exp\left[-ik_n z + \sqrt{k_n^2 - k_\perp^2}\, z\right]. \tag{B.7}$$

Appendix C

Theory and experimental evaluation of turbulence spectrum

§C.1 One and two dimensional spectra of random field

In the chapter 2 the homogeneous isotropic turbulence of scalar and vector types was discussed and formulae of energy spectrum were given (2.3 and 2.4). However, to analyze the characteristic properties of the turbulence, it is common to introduce one dimensional and two dimensional spectra (Comte-Bellot & Bailly, 2003). Moreover, in the experiment, only one dimensional spectrum can be measured, so a theoretical 1D spectrum is necessary to do comparison between experiment and theory. In this appendix the corresponding 1D and 2D spectra are discussed and the method to obtain the 1D spectra from experimental data is shown.

C.1.1 The random field of scalar-type

The definition of the one dimensional spectrum G_{1D} as a function of wavenumber k_1 is the following:

$$G_{1D}(k_1) = \iint_{-\infty}^{\infty} \Phi_{3D}(k) dk_2 dk_3 = \iint_{-\infty}^{\infty} \frac{G(k)}{4\pi k^2} dk_2 dk_3. \tag{C.1}$$

Transformation of cartesian variables to cylindrical coordinate system $dk_2 dk_3 \to 2\pi k_\perp dk_\perp$ in the integral leads to:

$$G_{1D}(k_1) = \frac{1}{2} \int_0^{\infty} \frac{G(\sqrt{k_\perp^2 + k_1^2})}{k_\perp^2 + k_1^2} k_\perp dk_\perp, \tag{C.2}$$

where $k = |\vec{k}| = \sqrt{k_1^2 + k_2^2 + k_3^2}$, and $k_\perp^2 = k_2^2 + k_3^2$. These notations will be used in the following. In literature, the Eq. (C.2) is often represented in another form (Rytov *et al.*, 1978):

$$G_{1D}(k) = \int_k^{+\infty} 2\pi k' \Phi^{3D}(k') dk' = \frac{1}{2} \int_k^{+\infty} \frac{G(k')}{k'} dk'. \tag{C.3}$$

Two dimensional spectrum G_{2D} as a function of transversal wavenumber $k_\perp$ is defined as:

$$G_{2D}(k_\perp) = 2\pi k_\perp \int_{-\infty}^{+\infty} \Phi_{3D}(k) dk_1 = 2\pi k_\perp \int_{-\infty}^{+\infty} \frac{G(k)}{4\pi k^2} dk_1. \tag{C.4}$$

The substitution $k = \sqrt{k_\perp^2 + k_1^2}$ leads to the formula:

$$G_{2D}(k_\perp) = \int_0^{+\infty} \frac{G(\sqrt{k_\perp^2 + k_1^2})}{k_\perp^2 + k_1^2} k_\perp dk_1 \tag{C.5}$$

Radially-symmetric correlation function $B(r)$ of the isotropic scalar random field can be obtained from the energy spectra using the following integral (Rytov *et al.*, 1978):

$$B(r) = \int_0^\infty 4\pi k^2 \Phi_{3D}(k) \frac{\sin kr}{kr} dk = \int_0^\infty G(k) \frac{\sin kr}{kr} dk. \tag{C.6}$$

C.1.2 The random field of vector-type

The one and two dimensional spectra of vector-type turbulence will be described below analogically as it was done for scalar-type turbulence above. Even in a case of isotropic homogenous turbulence of vector-type the spectrum of a single component, for example, u_x is anisotropic. One dimensional longitudinal spectrum of u_x component as a function of wavenumber k_1 is defined as follows:

$$E_{11}^{(1)}(k_1) = \iint_{-\infty}^{\infty} \Phi_{11}(k) dk_2 dk_3 = \iint_{-\infty}^{\infty} \frac{E(k)}{4\pi k^2} \left[1 - \frac{k_1^2}{k^2}\right] dk_2 dk_3. \tag{C.7}$$

The change of variables to cylindrical coordinate system in the integral $dk_2 dk_3 \to 2\pi k_\perp dk_\perp$ leads to:

$$E_{11}^{(1)}(k_1) = \frac{1}{2} \int_0^\infty \frac{E(\sqrt{k_\perp^2 + k_1^2})}{(k_\perp^2 + k_1^2)^2} k_\perp^3 dk_\perp. \tag{C.8}$$

Two dimensional spectrum of the same component u_x as a function of transversal wavenumber $k_\perp = \sqrt{k_2^2 + k_3^2}$ is defined as follows:

$$E_{11}^{(2,3)}(k_\perp) = 2\pi k_\perp \int_{-\infty}^{+\infty} \Phi_{11}(k) dk_1 = 2\pi k_\perp \int_{-\infty}^{+\infty} \frac{E(k)}{4\pi k^2} \left[1 - \frac{k_1^2}{k^2}\right] dk_1. \tag{C.9}$$

Substituting in the integral $k = \sqrt{k_\perp^2 + k_1^2}$ one can obtain formula:

$$E_{11}^{(2,3)}(k_\perp) = \int_0^{+\infty} \frac{E(\sqrt{k_\perp^2 + k_1^2})}{(k_\perp^2 + k_1^2)^2} k_\perp^3 dk_1. \tag{C.10}$$

One dimensional spectrum as a function of one transversal wavenumber k_2 (and similarly for the k_3) can by obtained via the formula:

$$E_{11}^{(2)}(k_2) = \frac{1}{4} \int_0^{+\infty} \frac{E(\sqrt{k_\perp^2 + k_1^2})}{(k_\perp^2 + k_1^2)^2} (k_\perp^2 + 2k_2^2) k_\perp dk_\perp. \tag{C.11}$$

Note, that this transversal one dimensional spectrum is different from the one dimensional longitudinal spectrum defined in the Eq. C.2.

C.1.3 Normalization constant of modified von Karman spectra

The normalization constant C in formulae (2.3) and (2.4) describing von Karman energy spectra of scalar and vector turbulent fields can be evaluated using the formula (Tatarskii, 1971,Comte-Bellot & Bailly, 2003):

$$C = \frac{2^{1/3}}{\pi} \frac{\Gamma(2/3)\Gamma(8/3)}{\Gamma(4/3)} \sin(\pi/3) \approx 0.7924. \tag{C.12}$$

This value of C was obtained in an assumption that the "outer" scale is much more greater than the "inner" scale of the turbulence $l_0 << L_0$. However, if the ratio of l_0 and L_0 is a finite number then a correction of C should be taken into account, which depends on l_0 value. To do that, the mean-square of refraction index should be calculated integrating energy spectra as over a whole range of wavenumbers from zero to infinity:

$$\int_0^{+\infty} G(k)dk = <\mu'^2_{\text{sc}}>, \tag{C.13}$$

$$\int_0^{+\infty} E(k)dk = \frac{3}{2} <\mu'^2_{\text{vec}}> \tag{C.14}$$

The calculated rms $<\mu'^2_{\text{sc}}>$ and $<\mu'^2_{\text{vec}}>$ will be not equal to the desired $<\mu^2>$ specified in Eq. (2.3) and Eq. (2.4). Hence, to correct this, the scalar-type spectrum Eq. (2.3) should be multiplied by $<\mu^2>/<\mu'^2_{\text{sc}}>$, and the vector-type spectrum Eq. (2.4) by $<\mu^2>/<\mu'^2_{\text{vec}}>$.

§C.2 Treatment of experimental spectra

In the theory of random process and fields it is common to do with a power spectral density defined for infinitely long realizations of the process or the field. For example, if the $U(x)$ is an one dimensional random field and $\widehat{U}(k)$ is its Fourier transform, defined as:

$$\widehat{U}(k) = \frac{1}{2\pi} \int\limits_{-\infty}^{+\infty} U(x) \exp[-ikx] dx, \tag{C.15}$$

then by definition (Rytov *et al.*, 1978) the power spectral density $\Phi(k)$ is a quantity that satisfies the equation:

$$< \widehat{U}(k')\widehat{U}^*(k'') >= \Phi(k')\delta(k' - k''). \tag{C.16}$$

The power spectral density is in relation with correlation function by Fourier transform.

In the experiment the only finite long realization $V(x)$ of the random field can be processed. Mathematically, the finite long realization can be represented as a product of the infinitely long realization by a window function $V(x) = U(x)F(x)$. Resulting spectrum of $V(x)$ is a convolution

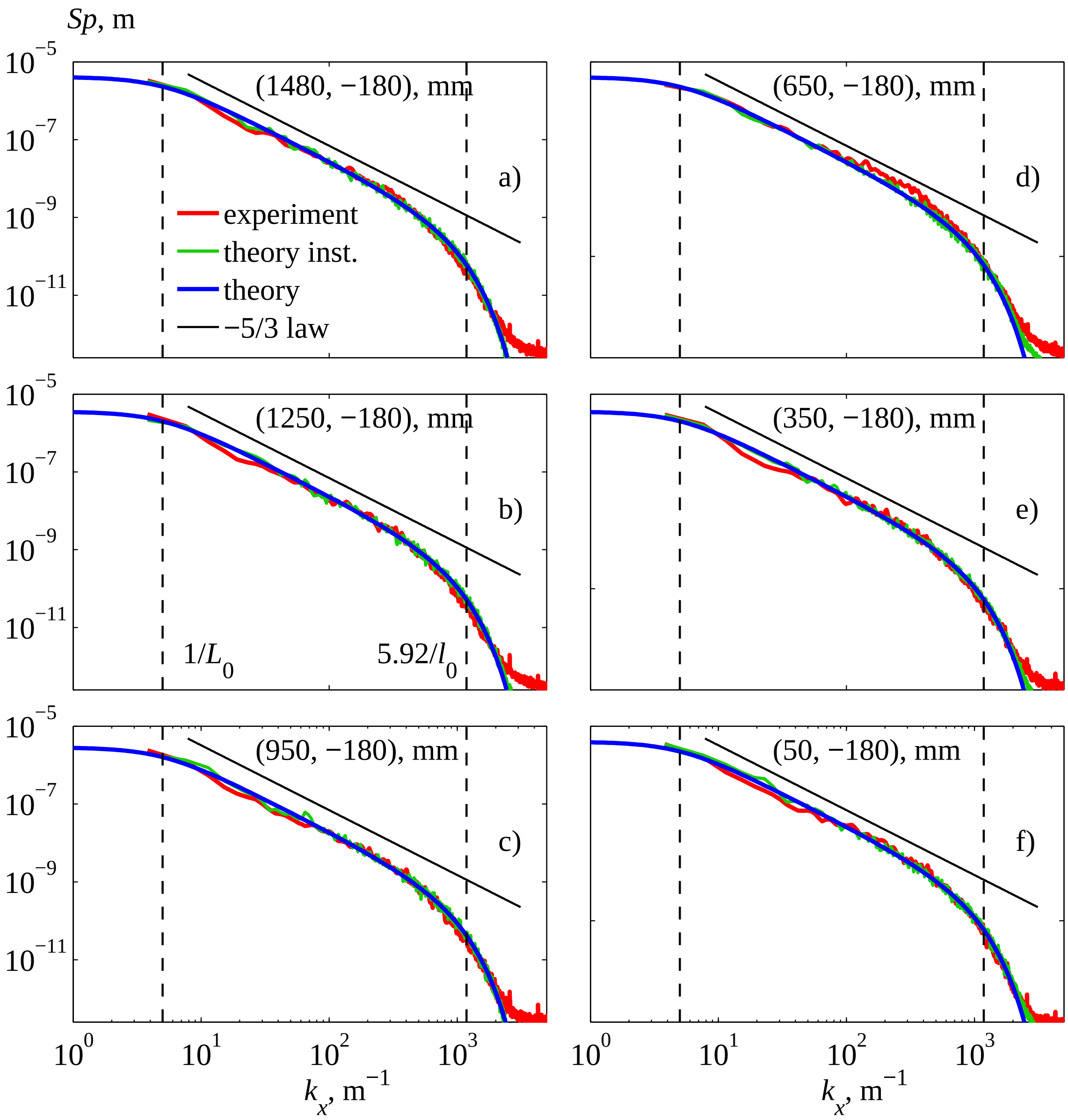

Figure C.1: Additional experimental spectra of the refraction index measured in points placed along the x axis at $y = -180$ mm. The experimental data are shown by red line, the von Karman theoretical spectrum with parameters $L_0 = 20$ cm and $l_0 = 5$ mm by blue line. Green line corresponds to the spectrum obtained from an artificial realization with the same von Karman spectrum using the processing procedure (C.23). Black line denote Kolmogorov's power law $k^{-5/3}$.

of spectra of $U(x)$ and of the window function $F(x)$:

$$\widehat{V}(k) = \int_{-\infty}^{+\infty} \widehat{U}(k_1)\widehat{F}(k - k_1)dk_1 \tag{C.17}$$

It follows from the convolution, that the averaging of power spectrum of the finite long realization is a convolution of power spectrum of infinite long realization with the square of module of the window function spectrum:

$$< \widehat{V}(k)\widehat{V}^*(k) >= \int\limits_{-\infty}^{+\infty} \Phi(k_1)|\widehat{F}(k-k_1)|^2 dk_1 \tag{C.18}$$

For a sufficiently large window, denoting the its width as X, the square of window function spectra $|\widehat{F}(k-k_1)|^2$ becomes a narrow peak concentrated around the wavenumber $k-k_1$. So in the limit of infinitely large window $X \to \infty$ one can obtain that:

$$< \widehat{V}(k)\widehat{V}^*(k) >= \Phi(k) \int\limits_{-\infty}^{+\infty} |\widehat{F}(k-k_1)|^2 dk_1, \tag{C.19}$$

or using Parseval's theorem it becomes

$$< \widehat{V}(k)\widehat{V}^*(k) >= \Phi(k)\frac{1}{2\pi} \int\limits_{-\infty}^{+\infty} F(x)^2 dx. \tag{C.20}$$

Hence, the final formula for power spectra of random process is

$$\Phi(k) = \lim_{X\to\infty} \frac{2\pi}{\int\limits_{-\infty}^{+\infty} F(x)^2 dx} < \widehat{V}(k)\widehat{V}^*(k) > . \tag{C.21}$$

In the experimental situation the window is always finite. Here beginning and the end of the window are denoted as x_1 and x_2 correspondingly. So one can calculate only approximate power spectra $\Phi_{\text{instr}}(k) \approx \Phi(k)$ which inherently includes some error of the method:

$$\Phi_{\text{instr}}(k) = \frac{2\pi}{\int\limits_{x_1}^{x_2} F(x)^2 dx} < \widehat{V}(k)\widehat{V}^*(k) >= \frac{2\pi}{\int\limits_{x_1}^{x_2} F(x)^2 dx} \int\limits_{-\infty}^{+\infty} \Phi(k_1)|\widehat{F}(k-k_1)|^2 dk_1. \tag{C.22}$$

In this case the comparison of the experimental power spectrum should be done also with this approximate spectrum $\Phi_{\text{instr}}(k)$ as well as with purely theoretical spectrum $\Phi(k)$ to verify that the windowing does not introduce noticeable error. The normalization coefficient $2\pi/\int_{x_1}^{x_2} F(x)^2 dx$ depends on the window function. For example, rectangular window of the width X gives $\int_{x_1}^{x_2} F(x)^2 dx = X$, and the Hann widows $F(x) = 0.5(1-\cos[2\pi x/X])$ gives the coefficient $3/8X$.

Discrete Fourier transform that is commonly used to process data gives Fourier coefficients $\widehat{V}_{Xn}$ of periodically continued function $V_X(x)$ over the period X. These spectral amplitudes of the periodical function are related to the continuous spectrum of the function $V(x)$ as $\widehat{V}_{Xn} = \frac{2\pi}{X}\widehat{V}(k_n)$.

So the approximate spectrum will be calculated as:

$$\Phi_{\mathrm{instr}}(k) = \frac{2\pi}{\int\limits_{x_1}^{x_2} F(x)^2 dx} \frac{X^2}{(2\pi)^2} < \widehat{V}_{Xn} \widehat{V}^*_{Xn} > \tag{C.23}$$

This is the final formula that was used to process the experimental data presented in sec. 2.4.3 of the Chapter 2. The Hann window was used in all cases and the measured realization was partitioned on 40 equal segments for the signals of 180 seconds duration and on 20 segments for 30 seconds duration. Some processed experimental spectra were presented in Fig. 2.10. Here, in Fig. C.1, additional spectra of the refraction index μ captured in measuring points placed along the x axis at $y = -180$ mm were presented and compared with theoretical von Karman spectra. The comparison shows a good agreement between theoretical spectrum and the experiment data in a whole range of inhomogeneities scales.

Appendix D

Synthèse des résultats

Introduction

La propagation des ondes non linéaires dans des mileux aléatoirement hétérogènes est un problème important pour plusieurs applications modernes de l'aéroacoustique et de l'acoustique médicale. En aéroacoustique moderne le problème de la génération et de la propagation du bruit des avions supersoniques (bang sonique) a reçu beaucoup d'attention dans le cadre des programmes de développement de transport civil supersonique. Dans le cas du bang sonique, l'onde en N associée à l'émission du bang se propage de l'avion vers le sol à travers les couches turbulentes de l'atmosphère, ce qui conduit à une distribution aléatoire du champ pression acoustique au sol. Les variations de l'amplitude et du temps de montée du choc mesurées peuvent alors être assez importantes selon des conditions atmosphériques. Et ces variations aléatoires ont un rôle important au niveau de la gêne induite par les vols en régimes supersoniques. Dans le but d'estimer l'impact environnemental on doit être capable de prédire les propriétés statistiques de ce bruit aléatoire pour différentes conditions atmosphériques.

Le problème de la propagation d'onde en N dans une atmosphère turbulente a été largement étudié théoriquement et expérimentalement. Dans les études théoriques, les premiers résultats sont liés à l'utilisation de l'approximation de l'acoustique géométrique non linéaire (NGA). Cependant cette approximation d'acoustique géométrique non linéaire ne prend pas en compte plusieurs effets importants comme la diffraction, la réfraction non linéaire; de plus cette approche NGA n'est valide que jusqu'à l'apparition des premières caustiques. Récemment plusieurs modèles numériques sur la base des équations non linéaires paraboliques de type de Khokhlov-Zabolotskaya (KZ) ont été développés. Ces modèles permettent de prendre en compte les effects de la diffraction et de non linéairité qui changent la forme d'onde en N – comme par expemple au passage de l'onde à travers des caustiques - ainsi que la stratification de l'atmosphère, l'absorption liée aux phénomènes de relaxation, les hétérogénéités spatiales dans les composantes longitudinales et transversales de vitesse du vent, l'effet de la surface de la terre. Un cas particulier important, qui représente une couche turbulente d'épaisseur finie, est constitué du modèle d'écran de phase aléatoire (random phase screen).

En utilisant l'approche NGA, des solutions analytiques ont été obtenues pour les statistiques de l'amplitude d'onde en N après le passage à travers cette couche. Dans notre travail, en utilisant la solution numérique du problème de la diffraction d'impulsions non linéaires, ces résultats ont été généralisés aux cas des écrans de phase aléatoire possédant des inhomogénéités d'échelles spatiales caractéristiques de taille différente. Notons que les distributions obtenues pour la même distance de focalisation que dans le cas d'un calcul NGA mettent en évidence l'importance des effets de diffraction.

Lors de la propagation du son dans l'atmosphère deux types d'hétérogénéités spatiales sont suceptibles de modifier la célérité du son: d'une part des inhomogénéités scalaires qui sont provoquées par des fluctuations de la température dans l'air montant de la surface chauffée et d'autre part des inhomogénéités cinématiques (vectorielles) qui sont liées aux fluctuations de la vitesse moyenne de l'air résultant de la présence des tourbillons ou plus géneralement du vent. Les spectres spatiaux des champs turbulents homogènes et isotropes sont différents selon la nature de ces fluctuations (scalaire/thermique ou vectorielle/cinématique); et, selon les estimations théoriques disponibles dans la littérature, l'effet de ces deux types de champs turbulents se traduit par des variations des statistiques des paramètres de l'onde acoustique traversant le milieu turbulent. Le problème de la propagation d'onde en N dans un écoulement turbulent (turbulence cinématique) a été étudié récemment dans une expérience modèle conduit par M.V. Averyanov (2008). Pour analyser la variation des distributions statistiques selon la nature des fluctutations (scalaire/vectorielle) une expérience modèle sur la propagation d'ondes en N dans la turbulence thermique respectant le rapport caractéristique de longueur d'onde et la taille des inhomogénéités a été réalisée dans ce travail. La comparaison des résultats expérimentaux pour les statistiques des impulsions en N non linéaires permettra de confirmer les résultats théoriques existants.

La réalisation d'une expérience modèle en laboratoire impose une mise à l'échelle. Ainsi nous utiliserons des ondes de choc assez courtes d'une durée de 30 μs à 50 μs générées classiquement par l'étincelle d'un arc électrique. L'utilisation de microphones capacitifs disponibles dans le commerce pose des problèmes de métrologie en raison de la limite de la bande fréquencielle de ces microphones dans la gamme de hautes fréquences supérieures à 100 kHz. En effet, dans ce type de mesure de signaux impulsionnels très brefs, la pression maximale et la durée d'impulsion sont déterminée assez précisément, mais le temps de montée du choc est en général très fortement surestimé. À cet égard, la recherche sur l'applicabilité d'autres méthodes et notamment optique, pour améliorer la résolution temporelle dans ces mesures de choc, qui est d'un intérêt pour pratique important, a fait l'objet d'une attention spéciale dans nos travaux. Dans la thèse la méthode d'ombroscopie a été proposée pour la détermination du temps de montée du choc.

Le problème de la propagation des ondes acoustiques non linéaires à travers un milieu hétérogène et aléatoire est également d'intérêt pour le diagnostic médical et les problèmes de contrôle non destructif. L'inhomogénéité des tissus biologiques ou plus généralement des structures des matériaux altèrent la focalisation réalisée par des méthodes ultrasonores classiques, en réduisant la résolution spatiale de l'équipement de diagnostique. Des études expérimentales et théoriques, effectuées dans ce domaine, suggèrent que sous certaines conditions la focalisation d'harmoniques dans un milieu hétérogène peut améliorer la qualité de focalisation par rapport au cas du faisceau linéaire émettant à la fréquence de cette harmonique. L'étude des conditions dans lesquelles cette focalisation non linéaire est mise en œuvre reste encore un problème théorique important. De plus, le problème de la gestion des interactions d'harmoniques dans un milieu non dispersif en «jouant» avec des inhomogénéités artificielles spécialement sélectionnés est d'un grand intérêt théorique et expérimental. Dans la thèse l'utilisation de l'écran de phase d'une configuration particulière a été proposée pour réaliser la destruction sélective des champs des certaines harmoniques du faisceau faiblement non linéaire.

Dans l'acoustique médicale, des recherches actuelles et intensives sont associées à l'utilisation des ultrasons de forte puissance focalisés pour la chirurgie non invasive (HIFU - High Intensity Focused Ultrasound). Une nouvelle classe d'équipements thérapeutique HIFU, utilisant un émetteur ultrasonore composé d'un grand nombre d'émetteurs élémentaires aléatoirement distribués sur une portion d'une surface sphérique, est en plein essor. Dans ce type d'appareil, ces émetteurs sont accordés en phase de façon électronique afin de déplacer le foyer dans l'espace, réaliser une configuration complexe du champ acoustique sous la forme de quelques foyers et minimiser l'échauffement le long du trajet du faisceau en tenant compte de la présence éventuelle d'obstacles (milieux osseux). L'intensité acoustique dans le foyer des systèmes HIFU peut augmenter jusqu'à plusieurs dizaines de milliers de watts par centimètre carré, en provoquant la formation d'onde de chocs par des effets non linéaires qui augmentent fondamentalement l'efficacité des effets thérapeutiques des ultrasons sur les tissus. La simulation numérique des champs HIFU est un outil important pour le développement de protocoles thérapeutiques et en partulier pour la prédiction des effets biologiques associés. Toutefois, à notre connaissance, la description des effets non linéaires dans les champs tridimensionnels produits par des émetteurs multi-éléments, en tenant compte de la formation d'onde de choc dans le foyer, n'a pas été faite jusqu'à présent. Dans cette thèse le développement de nouveaux algorithmes pour calculer des champs non linéaires de telles grilles multi-éléments avec l'utilisation raisonnable des ressources informatique est présenté.

Objectifs

L'objectif de cette thèse est une étude théorique et expérimentale des caractéristiques de la propagation d'impulsions non linéaires et de faisceaux ultrasonores dans les milieux aléatoires avec des inhomogénéités distribuées dans le volume ou concentrées dans une couche mince pour l'application aux problèmes de l'aéroacoustique et aux problèmes de diagnostiques et thérapeutiques. Dans cette perspective nous avons retenu les objectifs intermédiaires suivants:

1. Détermination de la précision de la méthode d'ombroscopie utilisée pour mesurer le temps de montée de l'onde de choc en N dans l'expérience modèle réalisée dans l'air. Démonstration des restrictions des microphones capacitifs modernes dans les mesures de front de choc des ondes acoustiques.
2. Étude des caractéristiques statistiques du champ acoustique dans le problème de la propagation d'ondes en N à travers une couche de turbulence thermique dans une expérience de laboratoire. Comparaison des statistiques d'amplitude d'onde en N propagée dans un champ de turbulence thermique et dans un écoulement turbulent.
3. Développement d'un modèle numérique basé sur l'équation KZK pour examiner les effets de diffraction et de non-linéairité dans le problème de la propagation d'ondes en N derrière

un écran de phase aléatoire en tenant compte du passage de l'onde par des caustiques aléatoires. Etude de l'influence des effets non-linéaires et des dimensions caractéristiques des inhomogénéités de phase sur les paramètres statistiques de l'onde en N en comparaison avec des solutions analytiques obtenues dans l'approximation d'acoustique géométrique non-linéaire.

4. Étude de la faisabilité d'une destruction sélective des champs des composantes harmoniques du signal dans un faisceau ultra-sonore faiblement focalisé d'amplitude finie après avoir traversé un écran de phase aléatoire dans le cas de notre configuration.
5. Développement d'un nouvel algorithme numérique basé sur l'équation de Westervelt afin de simuler des champs non linéaires en trois dimensions émis par des émetteurs multi-éléments focalisés, appelé aussi «grilles thérapeutiques», pour les conditions de la formation de fronts de choc dans la région focale.
6. Développement de la méthode de l'émetteur équivalent possédant une symétrie axiale pour calculer rapidement les champs tridimensionnels non linéaires émis par des grilles multi-éléments thérapeutiques (avec l'utilisation de modèles à deux dimensions basés sur les équations soit de KZK, soit de Westervelt).

Cette thèse en co-tutelle a été accomplie avec le soutien d'une bourse du Président de la Fédération de Russie, d'une bourse de thèse en cotutelle du Gouvernement Français distribuée par l'ambassade de France en Russie, d'une bourse de la Société d'Acoustique des Etats-Unis, et dans le cadre des programmes de recherche RFBR 10-02-91062-NTsNI et 09-02-01530, INTAS no. 05-1000008-7841, scientific schools RF no. NSH-4449.2006.2., Projet International de Coopération Scientifique (PICS RFBR 10-02-91062/CNRS 5603) grants, GPI RAS's Fundamentals of Acoustic Diagnostics of Artificial and Natural Media programs: ISTC (projet no. 3691) et NIH (projet no. R01EB007643).

Synthèse des résultats

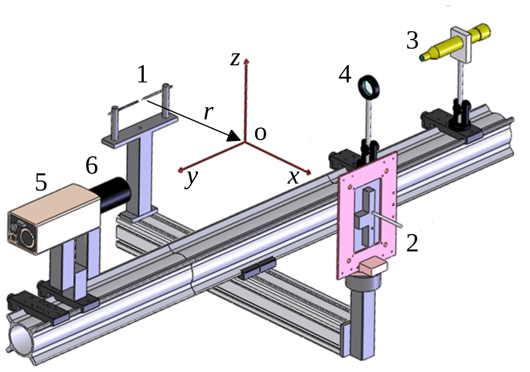

Figure D.1: Le dispositif expérimental :1 – source à étincelles, 2 – microphone bafflé, 3 – source lumière blanche, 4 – lentille de focalisation, 5 – caméra CCD, 6 – objectif de la caméra.

Dans l'introduction l'actualité du sujet de la thèse est justifiée, l'état de l'art à ce jour du problème est exposé, des objectifs généraux sont donnés et un résumé des travaux décrits par chapitres est présenté.

Premier chapitre

Le premier chapitre est consacré au problème de la détermination du temps de montée du choc des ondes en N de forte amplitude et de courte durée avec des méthodes acoustique et optique. Le §1.1 présente la bibliographie sur l'utilisation des sources à étincelles pour générer des ondes en N dans des expériences modèles d'aéroacoustique. Il est noté qu'en raison de la gamme de fréquence limitée des microphones capacitifs disponibles dans le commerce il est impossible de caractériser des chocs avec un temps de montée de moins de 3 microsecondes. Pour améliorer la résolution temporelle dans des mesures du temps de montée du choc il est proposé d'utiliser une méthode d'ombroscopie.

Dans le §1.2 nous décrivons le dispositif expérimental créé par l'auteur à l'Ecole Centrale de Lyon pour réaliser des mesures optiques et acoustiques d'onde en N sphérique propagée dans l'air au repos (Fig. D.1). Des impulsions en N ont été générées par une source à étincelles; l'amplitude de l'impulsion à une distance de 16 cm de la source était $p_0 = 1400 \pm 80$ Pa, et la demi-durée était $T_0 = 19.0 \pm 0.1$ μs. Les mesures acoustiques ont été effectuées en utilisant un microphone 1/8 inches (Brüel & Kjaer, 4138), monté dans un baffle (2). La partie optique du dispositif consistait en une source lumière (3) (Nanolite KL-L), un filtre atténuateur, une lentille convergente (4), une caméra numérique CCD (5) (Dantec dynamic, FlowSense 2M), un objectif Nikon (6). Les impulsions de lumière émises par la source Nanolite étaient d'une durée d'environ 20 ns, ce qui a permis d'obtenir des images d'ombroscopie avec une bonne résolution saptiale.

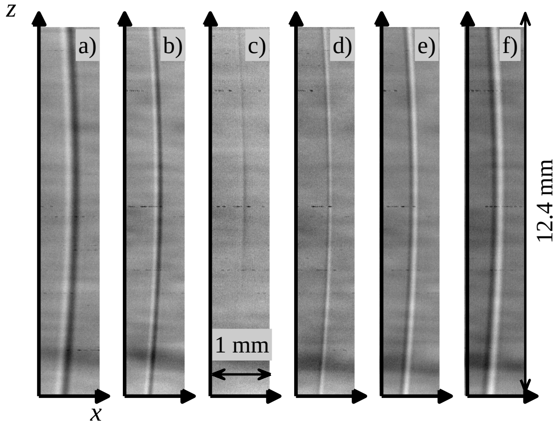

Figure D.2: images d'ombroscopie prises pour les différentes dispositions du plan d'objet sur l'axe y: y = 32 mm (a), 12 mm (b), 2 mm (c), et -4 mm (d), -13 mm (e), et -24 mm (f).

Dans le §1.3 la propagation d'une onde en N sphérique a été analysée en respectant nos conditions expérimentales typiques et ce sur la base de simulations numériques avec l'équation de Burgers, en tenant compte des processus de relaxation dans les molécules d'oxygène et d'azote. Il est montré que le temps de montée du choc, défini comme le temps, nécessaire pour que la pression sur le choc passe du niveau 0.1 au niveau 0.9 de la pression maximale, ne dépasse pas une valeur de 1 microseconde.

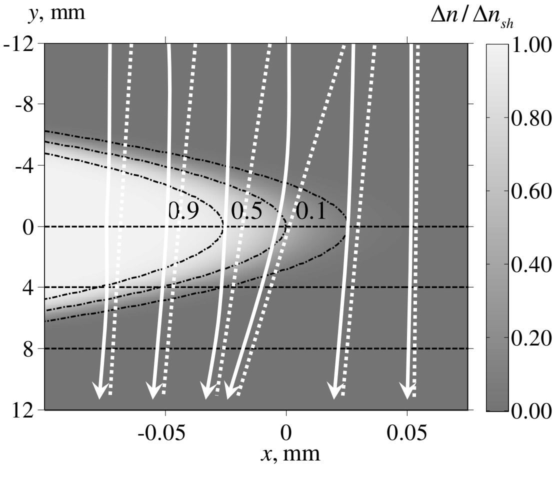

Figure D.3: Schéma de déviation des rayons optiques dans le plan xOy (flèches pleines) à cause de la propagation de la lumière à travers des inhomogénéités de l'indice de réfraction provoqués par l'onde de choc. Des lignes en pointillés représentent la formation de l'ombre «virtuelle».

Dans le §1.4 des résultats des mesures d'ondes en N avec un microphone sont montrés et la méthode de détermination de l'amplitude et de la durée des ondes en s'appuyant sur les données expérimentales est expliquée. La durée d'impulsion a été déterminée par les premiers zéros du spectre du signal, et l'amplitude - par l'allongement nonlinéaire de l'impulsion. Les résultats expérimentaux pour l'amplitude et la durée d'impulsion étaient en bon accord avec ceux calculés théoriquement. Cependant, le temps de montée obtenu dans l'expérience (3 microsecondes) a été largement surestimé par rapport à la théorie.

Dans le §1.5 l'utilisation d'une méthode d'ombroscopie pour mesurer des impulsions de choc «faible» avec un nombre de Mach acoustique inférieur à 1% est justifiée. Des images d'ombre ont été photographiées avec une caméra digitale sur un plan objet, dont la position était variable le long de l'axe optique (l'axe y sur la Fig. D.1). Les tracés de la Fig. D.2 (a-e) montrent des exemples des photographies d'ombres. Dans les images des bandes sombres et claires sont clairement distinguées, qui sont associées à la déviation des rayons lumineux sur les inhomogénéités du front de choc (Fig. D.3). L'inversion de la distribution de l'intensité de la lumière dans d'ombre est attribuée à la formation des images «virtuelles» lorsque le plan objet passe de l'autre côté du point $y = 0$. La largeur de l'ombre Δx a été calculée sur la base des images d'ombre et elle a été définie comme la distance entre les valeurs maximum et minimum d'intensité le long de l'axe x.

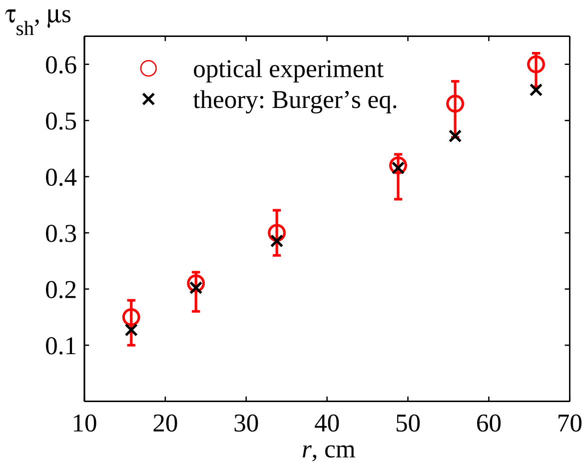

Figure D.4: Comparaison du temps de montée du choc, tel que mesuré par la méthode d'ombroscopie (marqueurs circulaires) et calculé en utilisant l'équation de Burgers (marqueurs croisillons).

Pour interpréter les images obtenues dans l'expérience, la formation d'ombre a été examinée théoriquement, en utilisant la modélisation de la propagation de la lumière à travers des inhomogénéités de l'indice de réfraction sur le front de choc à l'aide d'une équation parabolique. Selon les calculs une relation entre la largeur de l'ombre et le temps de montée a été obtenue, ce qui a permis de trouver le temps de montée qui correspond à des données expérimentales. Les résultats obtenus, en contraste avec les mesures acoustiques, sont en bon accord avec des résultats des calculs basés sur l'équation de Burgers (Fig. D.4). Dans le paragraphe §1.6 des conclusions du premier chapitre de la thèse sont présentées.

Deuxième chapitre

Le deuxième chapitre de la thèse est consacré à l'étude des différences quantitatives dans les statistiques du champ acoustique d'onde en N pour des cas de propagation dans la turbulence thermique ou cinématique. Dans le §2.1 une synthèse des résultats d'expériences de laboratoire simulant la propagation des impulsions en N dans la couche turbulente superficielle de l'atmosphère (turbulence cinématique) est donnée.

Dans le §2.2, nous montrons des spectres de von Kármán modifiés des fluctuations de l'indice de réfraction pour des champs de turbulence de types vectoriel ou scalaire. Les différences des spectres, qui conduisent aux plus fortes distorsions du champ acoustique dues aux focalisations aléatoires dans la turbulence cinématique sont discutées.

Le §2.3 décrit le dispositif expérimental qui a été réalisé à L'Ecole Centrale de Lyon, et qui permet d'examiner la propagation d'ondes en N dans une turbulence thermique. Le champ turbulent a été généré par une grille d'éléments chauffants (Fig. D.5). Une onde en N généré par l'étincelle d'un arc électrique a été propagée dans le champ turbulent et enregistrée par des microphones B&K 4138 situés à la même hauteur que la source à une distance r de celle ci. Le champ moyen et les fluctuations de la température ont été mesurés en utilisant un thermocouple de type K (chromel-alumel), et deux sondes d'anémométrie fils froids de température (Dantec 55P31).

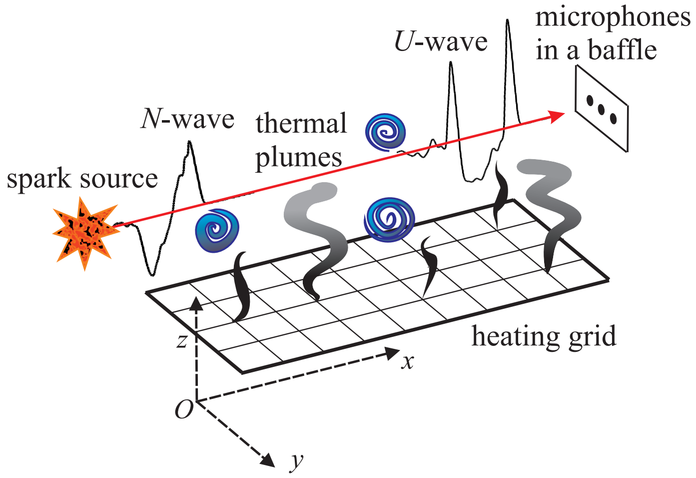

Figure D.5: Le schéma expérimental pour la propagation d'une onde sphérique en N générée par une source à étincelles dans la turbulence thermique.

Dans le §2.4 les résultats des mesures de corrélations spatiales des fluctuations de la température sont donnés, à partir desquels nous avons calculé les paramètres des fluctuations du champ turbulent: l'échelle externe de turbulence $L_0 = 20$ cm et la vitesse ascentionnelle de convection $U_{\mathrm{vert}} = 1.1$ m/s. Il est montré que les spectres expérimentaux sont bien décrits par un spectre modifié de von Kármán avec une zone inertielle type pour une turbulence homogène isotrope ayant un niveau moyen de fluctuation rms de l'indice de réfraction $\mu_{\mathrm{rms}} = 0.85$ %.

Dans le §2.5 des résultats de mesures acoustiques réalisées à des distances de 41 cm à 201 cm de la source sont présentés. Dans l'air homogène une pression de pic de 430 ± 25 Pa et positive et une durée de 43.6 ± 0.4 μs ont été mesurées à une distance r = 41 cm. Les résultats pour les ondes en N passées à travers une couche turbulente, sont donnés sous la forme des distributions statistiques, de la moyenne, de l'écart type et des valeurs maximales et minimales. Les pressions des pics positif et négatif, la durée, le temps de montée de choc et le temps d'arrivée de l'impulsion ont été analysés. Tous les paramètres analysés sont caractérisés par un élargissement considérable de la distribution statistique avec l'augmentation de la distance de la propagation. À de grandes distances de propagation (181 à 201 cm) des impulsions

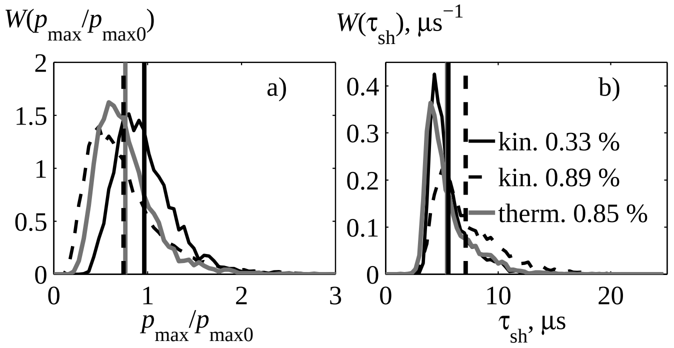

Figure D.6: Comparaison des densités de répartition de la pression maximale normalisée $p_{\mathrm{max}}/p_{\mathrm{max0}}$ (a) et du temps de montée du choc τ_{sh} (b) pour le cas de la propagation d'onde en N dans la turbulence cinématique avec $\mu_{\mathrm{rms}} = 0.89\%$ (ligne noire solide), avec $\mu_{\mathrm{rms}} = 0.33\%$ (ligne noire en pointillés) et dans la turbulence thermique (ligne grise) avec une pression de pic positif 3 à 3.5 fois supérieur, et négatifs - de deux fois plus grande que dans l'air homogène ont été observés. Cette différence est explique par l'asymétrie de déformation de la forme d'onde dans les zones aléatoires de focalisation. À de grandes distances, la durée d'impulsion peut être 2-3 fois plus élevée que dans l'air homogène, et le temps de montée du choc pour certaines peut être augmenté jusqu'à 15-20 μs. Des chocs avec un temps de montée inférieurs à 3 μs n'ont pas été enregistrés en raison des limitations en fréquence des microphones capacitifs, qui ont été discutés dans le chapitre un.

turb.	$<P_+>$	δP_+	$<\tau_{\rm sh}>$	$\delta\tau_{\rm sh}$	$P_{+,1}$,%	$P_{+,1.5}$,%	$P_{+,2}$,%
1 term., 0.85%	0.762	0.31	5.5	2.0	17.8	2.9	0.4
2 cin., 0.89%	0.743	0.40	7.1	2.8	20.1	5.1	1.3
3 cin., 0.33%	0.965	0.31	5.6	1.8	38.5	5.8	0.7

Table D.1: Comparaison des caractéristiques principales des densités de répartition de la pression maximale normalisée $P_+ = p_{\rm max}/p_{\rm max0}$ et du temps de montée du choc $\tau_{\rm sh}$. La probabilité d'observer des valeurs de $P_+ > \alpha$ est désignée comme $P_{+,\alpha}$, la moyenne statistique est $<>$ et l'écart type est δ.

Dans le §2.6 les résultats obtenus en turbulence thermique sont comparés avec la statistique des distorsions d'ondes en N dans la turbulence cinématique examinés dans la thèse de M. Averyanov (2008). Dans les deux expériences, l'épaisseur maximale de la couche turbulente (1.8 m) et l'échelle externe ($L_0 = 20$ cm) sont similaires. La Fig. D.6 compare la fonction de distribution pour la pression de pic normalisée $P_+ = p_{\rm max}/p_{\rm max0}$ (a) et pour le temps de montée de choc $\tau_{\rm sh}$ (b). Dans le tableau D.1 la moyenne et l'écart type, ainsi que la probabilité de dépassement des seuils de pression maximale normalisée de 1, 1,5 et 2 sont présentés.

Considérant les cas avec des valeurs de $\mu_{\rm rms}$ similaires on peut voir que la fonction de distribution de P_+ dans la turbulence cinématique est plus large (Fig. D.6a), c'est à dire a un écart type plus élevé (tableau D.1, lignes 1 et 2). Il est montré que dans la turbulence cinématique des probabilités de dépassement des seuils d'un et demi et du double pour la pression maximale positive sont 2-3 fois plus élevés que dans le cas de la turbulence thermique. En outre, la turbulence cinématique conduit à une diffusion du front de choc plus efficace (Fig. D.6b). Par ailleurs, le cas d'une turbulence cinématique avec $\mu_{\rm rms} = 0.33$ % , c'est-à-dire pour une intensité 2.6 fois plus faible des fluctuations turbulentes que dans la turbulence thermique, a été considéré. La largeur de la distribution du pic positif de pression déterminée par les écarts type, est la même ($\delta P_+ = 0.31$). Néanmoins, comme dans le cas précédent, la probabilité d'observer des ondes de grandes amplitudes, $P_{+,1.5}$ et $P_{+,2}$, est 2 fois plus grande dans le cas cinématique que dans le cas scalaire. Pour le temps de montée du choc les fonctions de distribution étaient très proches les unes des autres. Ainsi, un niveau comparable de distorsion de l'amplitude et du temps de montée est réalisé dans la turbulence cinématique à des valeurs $\mu_{\rm rms}$ beaucoup plus faibles (2.6 fois) que dans le cas de la turbulence thermique. Le §2.7 présente les conclusions du deuxième chapitre.

Troisième chapitre

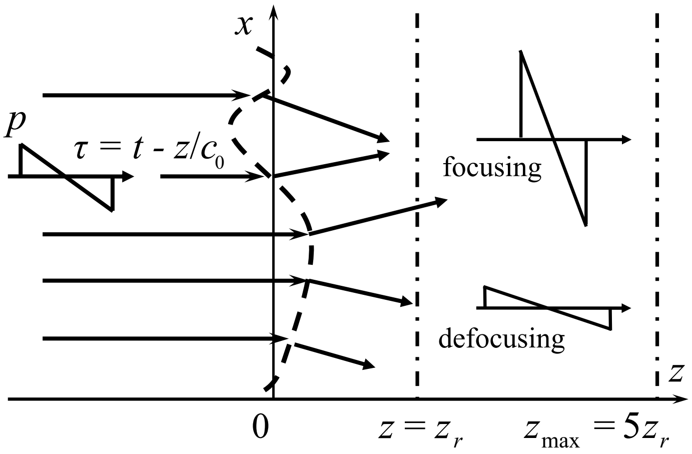

Figure D.7: Propagation d'une onde en N plane à travers un écran de phase (ligne pointillée), situé à $z = 0$. La longueur de réfraction typique de l'écran de phase est désignée comme z_r et la distance maximale dans les calculs est $z_{\max}$.

Le troisième chapitre traite d'un modèle numérique pour décrire les statistiques de l'amplitude d'ondes en N propagées à travers une couche aléatoire inhomogène (Fig. D.7). Le modèle est basé sur l'équation parabolique non linéaire KZK à deux dimensions et le milieu est modélisé par un écran de phase aléatoire (random phase screen).

Dans le §3.1 une revue est donnée sur l'utilisation de la méthode d'écran de phase aléatoire dans des problèmes de propagation des ondes linéaires et non linéaires dans des milieux hétérogènes, ainsi que sur l'utilisation de l'approximation de l'acoustique géométrique non-linéaire (NGA) pour le calcul des statistiques de l'amplitude d'ondes en N transmises. Les avantages de l'approximation parabolique sur l'approche NGA sont mis en évidence avec la prise en compte des effects de diffraction.

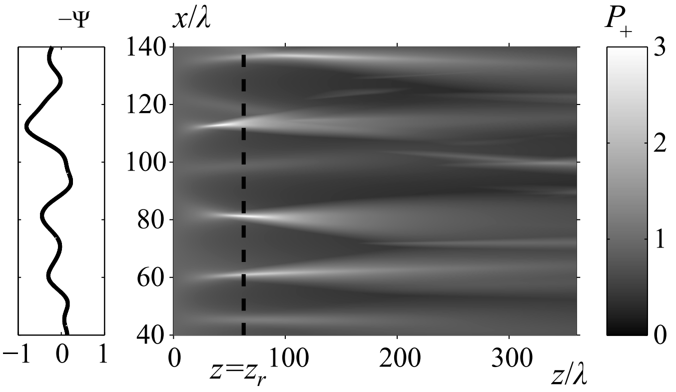

Figure D.8: Exemple de distribution de la pression de pique positive d'onde en N derrière la couche de phase $\Psi(x)$, représenté par la ligne continue sur la gauche. Des paramètres de la couche ont été choisi comme: $l/\lambda = 6$, $z_r/\lambda = 63$, la longueur non-linéaire $z_n = 8z_r$.

Dans le §3.2 un algorithme de résolution numérique de l'équation KZK dans le domaine temporel est décrit. Dans le §3.3, nous avons présenté un modèle d'écran de phase aléatoire avec un spectre gaussien pour les inhomogénéités. Les propriétés de la couche aléatoire sont alors décrites par la longueur de corrélation l, qui détermine la taille caractéristique des inhomogénéités, et la longueur de réfraction z_r, qui fixe la distance caractéristique de formation des premières caustiques. La longueur de corrélation a été choisie pour être de l'ordre de grandeur de quelques longueurs d'onde en N ; notons que ce choix est en accord avec les échelles des inhomogénéités spatiales dans l'atmosphère. La longueur non linéaire z_n est définie comme la distance à laquelle l'amplitude de l'onde en N diminue d'un facteur $\sqrt{2}$ par rapport à amplitude initiale p_0. Un exemple d'écran de phase avec $l/\lambda = 6$ est représenté dans la partie gauche de la Fig. D.8.

Dans le §3.4 les caractéristiques des distributions spatiales de la pression de pic positif normalisée ($P_+ = p_+/p_0$, Fig. D.8) pour un milieu non linéaire sont examinées. Il est montré que

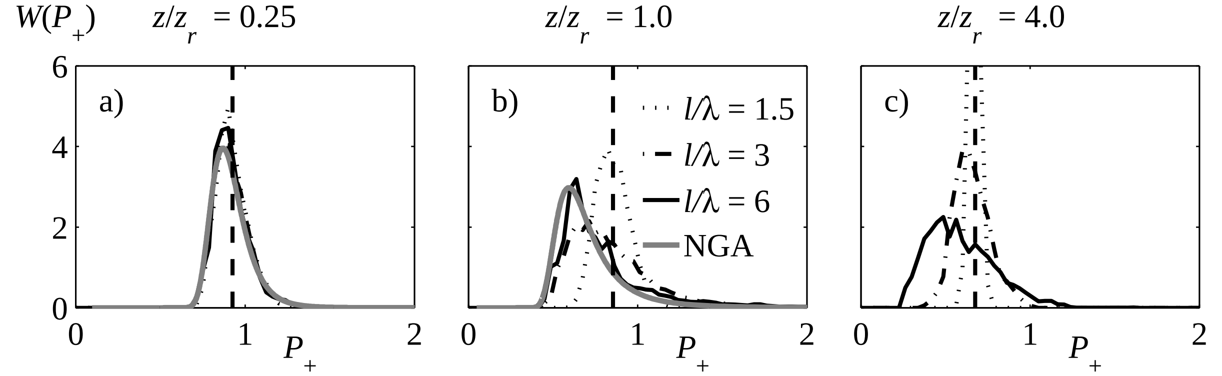

Figure D.9: Fonctions de répartition de la pression positive de pic P_+, obtenues en calculant le modèle diffractif avec des longueurs de corrélation différentes de l'écran de phase (lignes noires) et des solutions analytiques pour le modèle des rayon NGA (ligne grise). La ligne pointillée verticale montre l'amplitude d'une onde en N plane. Une comparaison est effectuée pour trois distances: $z = 0.25z_r$ (a), $z = 1.0z_r$ (b), $z = 4.0z_r$ (c) en vertu de la longueur non-linéaire: $z_n = 4z_r$.

l'amplification de la focalisation pour une faible non-linéarité et l'atténuation dans le cas d'une forte absorption non linéaire sur le front de choc sont très influencées par la taille des inhomogénéités. Des examples des formes d'onde déformées sont fournis avec la formation d'onde en U dans la région des focalisations aléatoires et d'ondes «lissées» dans les régions de défocalisation.

Dans le §3.5 nous considérons les fonctions de la distribution d'amplitude obtenues à partir des calculs basées sur l'hypothèse d'ergodicité et en utilisant des écrans de phase de grandes dimensions dans la direction perpendiculaire à l'axe de propagation. Nous avons réalisé une étude paramétrique des effets de la taille des inhomogénéités et de l'amplitude de l'onde initiale sur l'élargissement des distributions de probabilité en fonction de la distance parcourue. En comparant les résultats avec les solutions analytiques de la NGA (Fig. D.9) il est montré que l'applicabilité de la NGA est limitée à une distance d'un tiers de la longueur de réfraction. Il est à noter qu'une faible amplitude initiale conduit à un léger élargissement de la distribution d'amplitude, tandis qu'une forte amplitude initiale conduit à un resserrement des distributions autour d'une valeur moyenne à cause de l'absorption des chocs lors de la propagation. Il est montré que les modulations du front d'onde liées à l'écran de phase ont un effet significatif sur la valeur moyenne de P_+, lorsque les fluctuations de phase sont de grande échelle ($l/\lambda = 6$ dans le cas présent). Et dans ce cas la valeur moyenne de P_+ derrière un écran de phase est plus faible que dans le cas d'une onde plane. On remarque aussi que l'écart type des fluctuations de P_+ atteint un maximum à la distance d'une longueur de réfraction, là où des focalisations fortes apparaissent. Il est presque proportionnel à la taille des hétérogénéités dans l'intervalle allant de $l/\lambda = 1.5$ à $l/\lambda = 6$. Le §3.6 présente les conclusions du troisième chapitre de la thèse.

Quatrième chapitre

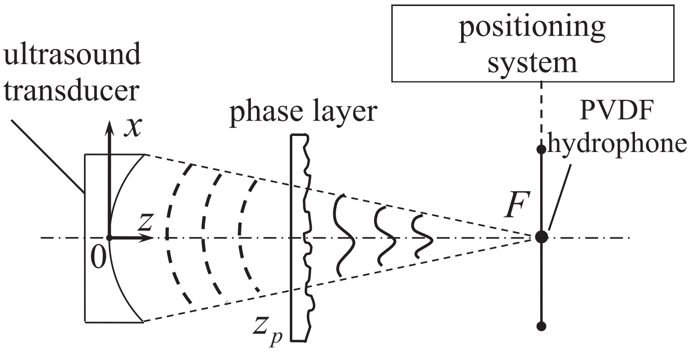

Figure D.10: Formulation du problème et le dispositif expérimental.

Le quatrième chapitre est consacré à l'étude théorique et expérimentale de la focalisation d'un faisceau ultrasonore non linéaire à travers un écran de phase physiquement réalisable pour permettre une étude expérimentale.

Le §4.1 traite de l'importance du problème de la propagation des ondes acoustiques dans les milieux aléatoirement inhomogènes représentatifs des applications en échographie médicale ou en contrôle non destructif des matériaux. Les avantages de focalisation des harmoniques supérieures dans un milieu hétérogène sont mis en exergue. Ensuite, la formulation du problème de contrôle de la focalisation des différentes harmoniques dans le faisceau utilisant un écran de phase sélectif (en fonction de la fréquence des harmoniques) situé à une distance $z = z_{\mathrm{p}}$ de la source est illustré sur la figure Fig. D.10. L'intérêt de cette configuration est de pouvoir maîtriser le degré de distorsion du champ à différentes harmoniques dans le plan focal $z = F$.

Le §4.2 décrit le modèle théorique de calcul de la propagation d'un faisceau non-linéaire, basé sur l'équation de Westervelt en utilisant la formulation avec le temps retardé τ:

$$\frac{\partial^2 p}{\partial\tau\partial z} = \frac{c_0}{2}\left(\frac{\partial^2 p}{\partial x^2}+\frac{\partial^2 p}{\partial y^2}+\frac{\partial^2 p}{\partial z^2}\right)+\frac{\beta}{2\rho_0 c_0^3}\frac{\partial^2 p^2}{\partial\tau^2}+\frac{\delta}{2c_0^3}\frac{\partial^3 p}{\partial\tau^3}. \tag{D.1}$$

Dans l'équation ci-dessus, p est la pression acoustique, z est une direction privilégiée alignée avec l'axe du faisceau, $\tau = t - z/c_0$, t est le temps, x et y sont les coordonnées spatiales transversales à la coordonnée z; ρ_0, c_0, β et δ sont respectivement la densité, la vitesse du son, le coefficient de non linéarité et le coefficient d'absorption du milieu. Par rapport à l'équation de Khokhlov-Zabolotskaya-Kuznetsov, dans l'équation (D.1) on ne fait pas l'hypothèse sur les petits angles de diffraction (i.e on ne fait pas l'approximation paraxiale).

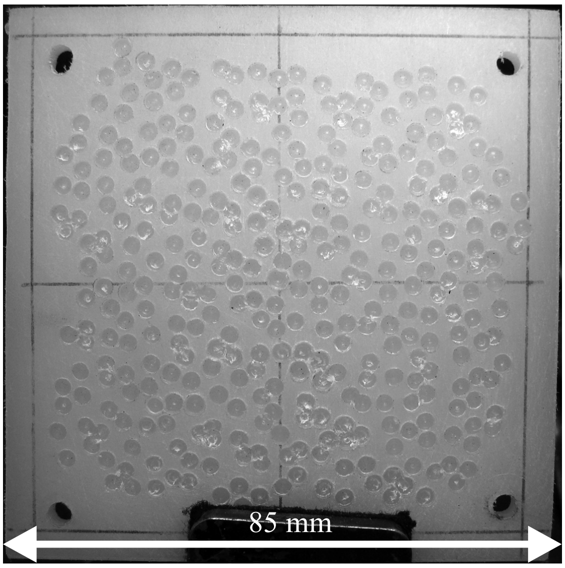

Figure D.11: Photo d'un écran de phase expérimental.

Ensuite, un algorithme numérique basé sur une méthode de pas fractionnés adaptée aux différents effets physiques pris en compte est présenté. L'équation (D.1) a été décomposée en équations plus simples pour la diffraction, la non-linéarité et l'absorption, qui ont été résolues une par une à chaque pas spatial le long de l'axe z. La répartition frontière de la pression, correspondant à une source focalisée, a été spécifiée dans le plan $z = 0$. La modélisation des harmoniques temporelles a été effectuée dans le domaine spectral. Pour calculer l'opérateur non-linéaire un système d'équations pour les amplitudes des harmoniques a été résolu. L'opérateur de diffraction pour chacune des harmoniques a été calculé par la méthode du spectre angulaire en utilisant une transformée de Fourier rapide (FFT) sur les coordonnées spatiales en deux dimensions. Pour l'analyse des répartitions de pression dans le plan focal, un critère de qualité pour chaque n-ièm harmonique a été introduit: $0 \leq Q_n \leq 1$, dont les valeurs faibles correspondent à la la suppression de la focalisation, et les valeurs élevés à la conservation de la focalisation.

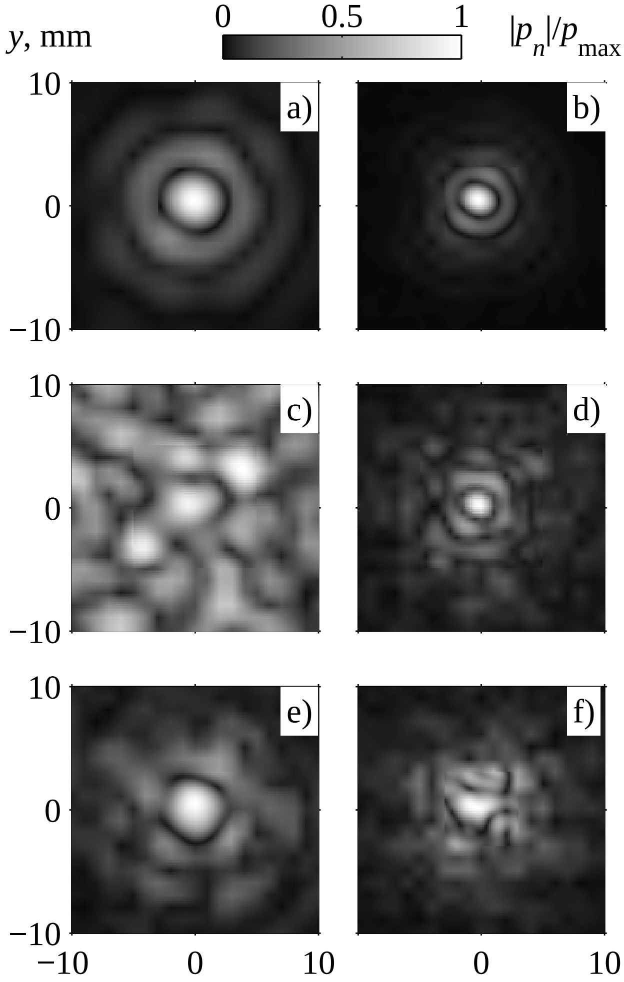

Figure D.12: Amplitude de la première (à gauche) et deuxième (à droite) harmoniques dans le plan focal, mesurées en l'absence d'une couche de phase (a, b), en présence d'une couche de 180° (c, d) et en présence d'une couche de 90° (e, f)

La section suivante décrit un modèle théorique d'écran de phase, constitué d'un ensemble des zones circulaires identiques et aléatoirement distribuées dans le plan et ayant une phase fixe égale à $\varphi_{\max}$. Il est à noter que le degré maximal de distorsion du faisceau a été obtenu en remplissant à moitié la surface du plan par des cercles et en choisissant une phase de $\varphi_{\max} = 180°$. L'exemple d'une réalisation de la couche de phase, faite en polyéthylène, est montré dans la Fig. D.11.

Dans le §4.3 et le §4.4, nous discutons des résultats de simulation numérique pour les cas de déphasage de 180° et de 90° à la fréquence fondamentale. Nous montrons la possibilité de la destruction sélective de la focalisation sur la fréquence fondamentale et les harmoniques impaires dans le cas de l'écran de phase de 180°. L'effet est expliqué par le fait que dans des sections du front d'onde, situées derrière des inhomogénéités circulaires, la phase à ces fréquences est imposée à un angle égal ou équivalent à 180°. La phase de la seconde harmonique et des autres harmoniques paires, dans les mêmes sections du front d'onde est changée à un angle multiple de 360°, ce qui est équivalent à l'absence de décalage de phase.

Dans le cas de l'écran de phase de 90°, la destruction de la focalisation du second harmonique est observée en plaçant l'écran de phase près du foyer, ce qui s'explique par le fait qu'après l'écran de phase le champ acoustique du second harmonique a une phase fixée à 180°. Lorsqu'on place un écran de phase de 90° proche de la source, on obtient la meilleure focalisation des harmoniques supérieures. Ceci est une conséquence de la génération des champs de ces harmoniques résultants des interactions non linéaires dans un champ de la fréquence fondamentale légèrement déformée.

Le §4.5 montre le dispositif expérimental, qui a été utilisé pour les mesures du champ ultrasonore de transducteur focalisé après avoir traversé des couches de phase de $180°$ et $90°$ (Fig. D.11) faites de polyéthylène. L'expérience a été menée par l'auteur dans le General Physics Institute of Russian Academy of Science A.M. Prokhorov. Les résultats des mesures sont présentés sur la Fig. D.12 à savoir: les distributions d'amplitude de la première (a) et de la deuxième (b) harmoniques dans le plan focal mesurées en l'absence d'écran de phase, avec un écran de phase de $180°$ (c, d) et avec un écran de phase de $90°$ (e, f). Pour un écran de phase de $180°$ les résultats expérimentaux montrent une destruction presque complète de la focalisation de premier harmonique. Au contraire, le 2-ème harmonique, en accord avec les calculs numériques, a une qualité de focalisation relativement élevée. Pour un écran de phase de $90°$ on peut apprécier la haute qualité de focalisation de la fréquence fondamentale, tout en notant que la focalisation de la second harmonique est très faible. Ainsi, les résultats obtenus expérimentalement sont en bon accord qualitatif avec les prédictions théoriques. Dans le §4.6 les conclusions du quatrième chapitre sont présentées.

Cinquième chapitre

Le cinquième chapitre traite du problème de la modélisation en trois dimensions des champs des émetteurs ultrasonores de forte puissance en présence des fronts de choc dans la région focale qui sont utilisés en chirurgie.

Dans le §5.1 les principales capacités des émetteurs constitués d'un grand nombre des émetteurs élémentaires sont discutées, ce qui les rend d'usage prometteur dans des nombreuses applications biomédicales. À titre d'exemple, une grille d'émetteurs avec une fréquence de 1.2 MHz est considérée ; elle est composé de 256 éléments d'un rayon de 3.3 mm situés sur une cuvette sphérique de longueur focale de 120 mm et de rayon de 64 mm avec une intensité acoustique par élément pouvant atteindre jusqu'à 10 $\mathrm{W/cm^2}$.

Les simulations numériques à réaliser imposent des exigences élevées (temps de calculs, taille de mémoire) sur les ressources informatiques à mettre en œuvre et ceci pour plusieurs raisons : i) la grande taille de

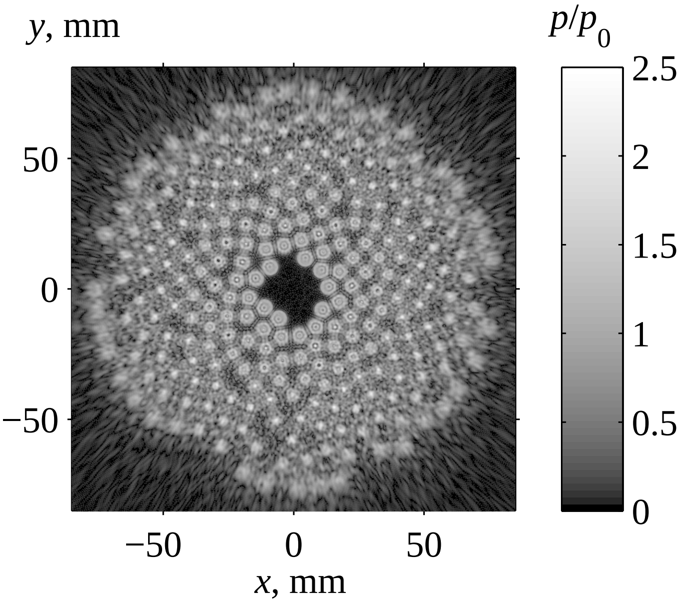

Figure D.13: Amplitude normalisée du champ initial p/p_0 dans le plan $(x, y, z = 0 \text{ mm})$. La pression de normalisation est $p_0 = \rho_0 c_0 u_0$, où u_0 est l'amplitude de la vitesse vibratoire à la surface d'un élément de la grille.

l'émetteur (jusqu'à 100 longueurs d'onde de la fréquence fondamentale) définit une grande fenêtre spatiale, ii) la focalisation sur un grand-angle nécessite l'utilisation d'un modèle de diffraction plus précis que l'approximation parabolique, iii) pour décrire les irrégularités du champ proche et aussi la zone focale de petite taille des pas spatiaux fins du schéma numérique sont nécessaires, iv) enfin, les effets non-linéaires forts nécessitent de prendre en compte soit un grand nombre d'harmoniques du spectre soit une maille temporelle très fine.

Dans le §5.2 un algorithme numérique de résolution de l'équation de Westervelt en trois dimensions (D.1) pour modéliser des champs des grilles ultrasonores est décrit. Une méthode de fractionnement d'équation suivant les facteurs physiques a été utilisée dans l'algorithme. Dans cette méthode de deuxième ordre de précision, pour trouver le champ $p(\tau, x, y, z + \Delta z)$ à chaque étape Δz les opérateurs de la diffraction, de la non-linéarité et de l'absorption ont été calculés comme suit:

$$p(\tau, x, y, z + \Delta z) = \Gamma_{D,\Delta z/2}\Gamma_{N+A,\Delta z}\Gamma_{D,\Delta z/2}p(\tau, x, y, z), \tag{D.2}$$

où l'action de l'opérateur de la diffraction pour une étape Δz est notée comme $\Gamma_{D,\Delta z}$, et l'action cumulée des opérateurs de l'absorption et de la non linéairité est notée comme $\Gamma_{N+A,\Delta z}$. Ce dernier opérateur a été calculé par la même méthode de fractionnement au second ordre, mais avec une subdivision du pas Δz en quelques pas plus petits. La modélisation a été effectuée en utilisant les avantages des représentations spectrale et temporelle du champ acoustique.

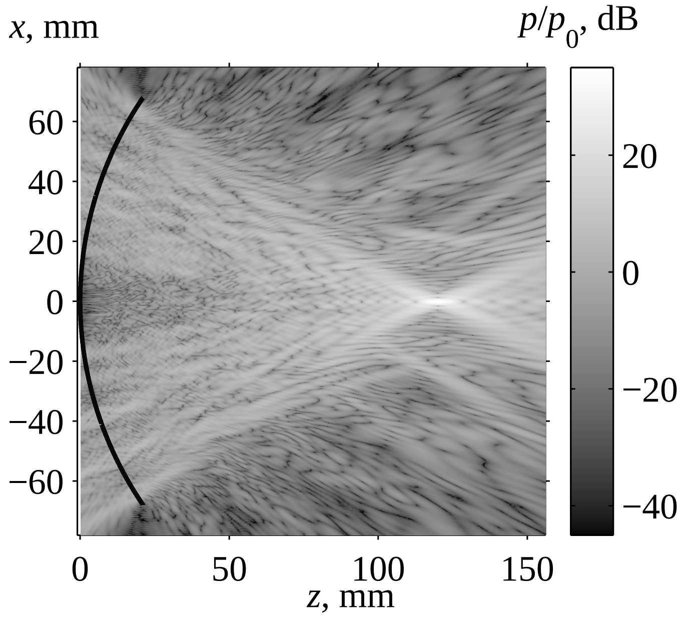

Figure D.14: Répartition de l'amplitude de pression p/p_0 dans le plan (x, z) sur l'axe de la grille, calculée numériquement dans l'approximation linéaire. La ligne noire indique la position de la surface sphérique du transducteur.

L'étape de diffraction a été calculée pour chacun des harmoniques par la méthode du spectre angulaire, l'absorption est prise en compte dans la représentation spectrale à l'aide d'une solution analytique. L'opérateur non-linéaire pour les distances à la source courtes a été calculé dans la représentation spectrale, et en cas de formation de choc un schéma temporel conservatif de type Godounov a été prévu dans l'algorithme.

Une caractéristique clef de notre algorithme est de garder en mémoire des champs des harmoniques de type «échelon» uniquement proche du foyer acoustique, pour lequel un grand nombre d'harmoniques est indispensable pour avoir une bonne précision. En dehors des zones de focalisation seule une dizaine d'harmoniques est prise en compte. Cette approche a permis de réduire la taille mémoire d'un facteur 10 à 20.

Dans le §5.3 les résultats d'un test complet de l'algorithme sont présentés en comparant les résultats des calculs avec des données connues de la littérature pour des émetteurs axisymétriques.

La précision de l'algorithme de 0.5-1% est indiquée. Dans le §5.4 les résultats de simulation pour la grille constituée de 256 éléments sont présentés. La Fig. D.14 montre la répartition de l'amplitude de pression dans le plan de l'axe de l'émetteur (x, z) dans le cas d'une modélisation linéaire. La Fig. D.15 montre les résultats de la simulation non linéaire pour des formes d'ondes dans le foyer géométrique obtenues avec des intensités d'ultrasons sur un élément dans une gamme allant de 1 à 10 $\mathrm{W/cm^2}$. Nous voyons qu'à des niveaux d'intensité qui peuvent être réalisés dans des équipements médicaux modernes, l'onde avec le front de choc est formée dans le foyer.

Dans le §5.5, nous présentons une méthode de source équivalente axisymétrique, par laquelle nous pouvons simplifier le calcul des champs non-linéaire des grilles ultrasonores thérapeutiques dans la région focale. La méthode est basée sur les hypothèses suivantes.

Les effets non linéaires dans les champs de forte amplitude issus des grilles ne se manifestent largement qu'en région focale, région qui est suffisamment symétrique autour de l'axe z. Par conséquent, la grille de géométrie complexe peut être remplacée dans une première étape par un émetteur à symétrie axiale, tel que le champ linéaire donne une bonne approximation dans la région focale du champ acoustique issu de la grille ; dans une deuxième étape on effectue le calcul non linéaire avec l'émetteur équivalent à symétrie axiale retenu afin d'avoir le champ acoustique dans le foyer. Les résultats des calculs non linéaires montrent que le champ d'un tel émetteur équivalent, calculé sur la base de l'équation de Westervelt ou de l'approximation parabolique correspond au foyer au champ acoustique issue de la grille avec une précision de 3%. Dans le §5.6 les conclusions du cinquième chapitre sont présentées.

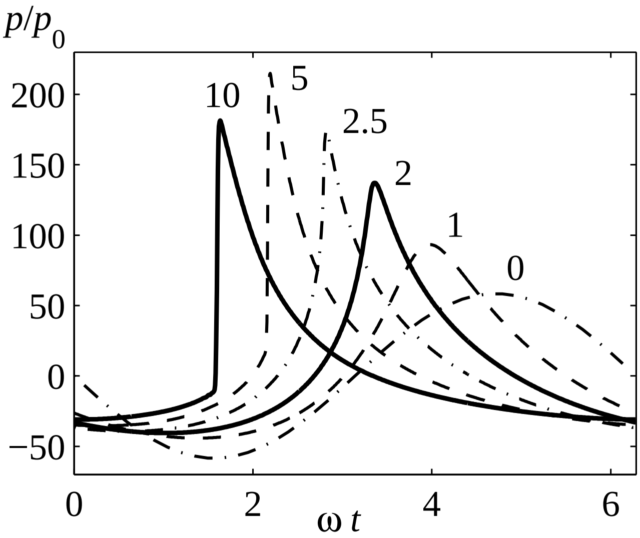

Figure D.15: Des formes d'ondes de pression adimensionnels au foyer géométrique de la grille à des niveaux d'intensité sur les éléments 1, 2, 2,5, 5 et 10 $\mathrm{W/cm^2}$ dans des simulations non linéaire; 0 – la simulation linéaire.

L'annexe présente un résumé des formules pour le champ d'un transducteur axisymétrique sur l'axe et dans le plan focal, la transformation de l'équation de Westervelt dans le système des coordonnées avec le temps retardé et une méthode pour obtenir le spectre des fluctuations de la turbulence à partir des données expérimentales. A la fin de la thèse les principaux résultats et conclusions sont présentés.

Conclusions

1. Un dispositif expérimental d'ombroscopie a été réalisé. Des mesures dans l'air du temps de montée du choc d'onde en N non linéaire sont effectuées avec une méthode d'ombroscopie en utilisant la simulation de la diffraction de la lumière sur les inhomogénéités de l'indice

de réfraction générées par le choc pour interpréter les images. Il est montré que la méthode proposée permet d'obtenir une résolution temporelle du temps de montée du choc (0.15 microseconde) de plus d'un ordre de grandeur meilleure par rapport aux mesures en utilisant les microphones capacitifs à large bande (3 microsecondes).

2. La propagation d'impulsions en N de grande amplitude et de courte durée (une amplitude de 1100 Pa et une durée 40 microsecondes à 20 cm de la source) dans la turbulence thermique a été étudié expérimentalement. Il est montré qu'à échelles spatiales caractéristiques et intensité des fluctuations de l'indice de réfraction identiques, la turbulence cinématique conduit à des focalisations aléatoires plus marquées, des fluctuations du pic positif de la pression plus élevées et une disparition du choc plus importante, par rapport au cas de la turbulence thermique.
3. L'influence de l'effet de la diffraction et des effets non linéaires sur les statistiques du champ d'onde en N derrière un écran de phase aléatoire a été étudié numériquement avec l'équation KZK en prenant compte le passage de l'onde à travers des caustiques. Il est montré qu'en changeant l'échelle spatiale des fluctuations de phase, les effets de diffraction entraînent des différences importantes dans les statistiques du champ acoustique derrière l'écran de phase, qui ne sont pas décrites dans l'approximation de l'acoustique géométrique non-linéaire.
4. Les caractéristiques de focalisation des harmoniques d'un faisceau ultrasonore d'amplitude finie derrière un écran de phase aléatoire ont été étudié numériquement et expérimentalement. La possibilité d'une destruction sélective de la focalisation de l'harmonique fondamentale et des harmoniques impaires a été montrée dans le cas d'un déphasage de $180°$ introduit par l'écran de phase.
5. Un algorithme numérique basé sur l'équation de Westervelt a été élaboré ; il permet de modéliser des champs acoustiques non-linéaires en trois dimensions produits par des émetteurs ultrasonores focalisés de géométrie complexe, en tenant compte de la formation de fronts de choc dans la région focale. L'expérience numérique pour une grille phasé multi-éléments à deux dimensions a été faite. Il a été montré que des ondes de choc de grand amplitude (jusqu'à 80 MPa) se forment dans la région focale avec des niveaux d'intensité ultrasonore typiques pour des applications de cet équipement dans la chirurgie.
6. Un modèle de source équivalente axisymétrique pour calculer des effets non linéaires dans la région focale des grilles multi-éléments thérapeutiques a été proposé. Il a été montré que la simulation basée sur les équations KZK ou Westervelt avec des conditions frontières imposées sous la forme d'un émetteur équivalent permet de décrire le champ non-linéaire de la grille dans la région focale avec une erreur qui ne dépassant pas 2-3%.

References

Alauzet, F., & Loseille, A. 2010. High-order sonic boom modeling based on adaptive methods. *J. Comput. Phys.*, **229**(3), 561–593.

Almgren, M. 1986. Acoustic boundary layer influence on scale model simulation of sound propagation: Experimental verification. *J. Sound Vib.*, **110**, 247–259.

Ames, W. F. 1992. *Numerical methods for partial differential equations*. Academic, San Diego, 3rd ed.

Andreev, V.G., Vasil'eva, O.A., Rudenko, O.V., & Lapshin, E.A. 1985. *Akust. Zh.*, **31**(12).

Averiyanov, M., Khokhlova, V., Sapozhnikov, O., Blanc-Benon, Ph., & Cleveland, R. 2006. Parabolic equation for nonlinear acoustic wave propagation in inhomogeneous moving media. *Acoust. Phys.*, **52**(6), 623–632.

Averiyanov, M., Blanc-Benon, P., Cleveland, R. O., & Khokhlova, V. 2011. Nonlinear and diffraction effects in propagation of N-waves in randomly inhomogeneous moving media. *J. Acoust. Soc. Am.*, **129**(4), 1760–1772.

Averiyanov, M. V. 2008. *Non linear diffraction effects in propagation of sound waves through turbulent atmosphere: experimental and theoretical studies*. Ph.D. thesis, Ecole Centrale de Lyon / Moscou State University, ECL 2008-18.

Averiyanov, M. V., Yuldashev, P. V., Khokhlova, V. A., Ollivier, S., & Blanc-Benon, P. 2007. Nonlinear propagation of spark-generated N-waves in relaxing atmosphere: laboratory-scaled experiments and theoretical study. *In:* 13^{th} *AIAA/CEAS Aeroacoustics Conference, AIAA-2007-3676*.

Averkiou, M.A., Roundhill, D.N., & Powers, J.E. 1997. A new imaging technique based on the nonlinear properties of tissues. *Pages 1561–1566 of: IEEE Ultrasonics Symp.*, vol. 2.

Bailey, M.R, Khokhlova, V.A., Sapozhnikov, O.A., Kargl, S.G., & Crum, L.A. 2003. Physical mechanisms of the therapeutic effect of ultrasound (A review). *Acoust. Phys.*, **49**(4), 369–388.

Bass, H.E., Raspet, R., Chambers, J.P., & Kelly, M. 2002. Modification of sonic boom waveforms during propagation from the source to the ground. *J. Acoust. Soc. Am.*, **111**(1).

Batchelor, G.K. 1999. *The theory of homogeneous turbulence*. Cambridge.

Berenger, J.-P. 1994. A perfectly matched layer for the absorption of electromagnetic waves. *J. Comput. Phys.*, **114**(2), 185–200.

Bessonova, O., Khokhlova, V., Bailey, M., Canney, M., & Crum, L. 2009. Focusing of high power ultrasound beams and limiting values of shock wave parameters. *Acoust. Phys.*, **55**(4), 463–473.

Bessonova, O., Khokhlova, V., Canney, M., Bailey, M., & Crum, L. 2010. A derating method for therapeutic applications of high intensity focused ultrasound. *Acoust. Phys.*, **56**(3), 354–363.

Blanc-Benon, P., Juvé, D., & Comte-Bellot, G. 1991. Occurrence of caustics for high-frequency acoustic waves propagating through turbulent fields. *Theoretical and Computational Fluid Dynamics*, **2**, 271–278.

Blanc-Benon, P., Juvé, D., Ostashev, V.E., & Wandelt, R. 1995. On appearance of caustics for plane sound-wave propagation in moving random media. *Waves in Random Media*, **5**, 183–199.

Blanc-Benon, P., Lipkens, B., Dallois, L., Hamilton, M. F., & Blackstock, D. T. 2002. Propagation of finite amplitude sound through turbulence: Modeling with geometrical acoustics and the parabolic approximation. *J. Acoust. Soc. Am.*, **111**(1 Pt. 2), 487–498.

Blanc-Benon, P., Ollivier, S., Attenborough, K., & Qin, Q. 2005. Laboratory experiments to study N-waves propagation: effects of turbulence and/or ground roughness. *Pages 651–654 of: 17^{th} International Symposium on Nonlinear Acoustics, Manchester, UK*, vol. 838.

Blokhintsev, D. I. 1981. *Acoustics of moving inhomogeneous media*. Moscow : Science.

Bobkova, S., Gavrilov, L., Khokhlova, V., Shaw, A., & Hand, J. 2010. Focusing of high intensity ultrasound through the rib cage using a therapeutic random phased array. *Ultrasound. Med. Biol.*, **36**(6), 888–906.

Brekhovskikh, L.M. 1974. *Ocean Acoustics*. Moscow: Science.

Brysev, A., Krutyansky, L., Pernod, P., & Preobrazhensky, V. 2004. Nonlinear ultrasonic phase-conjugate beams and their application in ultrasonic imaging. *Acoust. Phys.*, **50**(6), 623–640.

Brysev, A.P., Bunkin, F.V., Krutyansky, L.M., & Klopotov, R.V. 2005. Acoustic imaging of object in phase inhomogeneous medium using phase conjugation of higher harmonic of ultrasound beam. *Phys. Wave Phenomena*, **13**(2), 81–86.

Burov, V.A., Dmitrieva, N.P., & Rudenko, O.V. 2002. Nonlinear ultrasound: breakdown of microscopic biological structures and nonthermal impact on a malignant tumor. *Biokhim. Biofiz. Mol. Biol.*, **383**(1), 101–104.

Candel, S. M. 1977. Numerical solution of conservation equations arising in linear wave theory - Application to aeroacoustics. *Journal of Fluid Mechanics*, **83**, 465–493.

Canney, M., Khokhlova, V., Bessonova, O., Bailey, M., & Crum, L. 2010. Shock-induced heating and millisecond boiling in gels and tissue due to high intensity focused ultrasound. *Ultrasound in Medicine and Biology*, **36**(2), 250–267.

Canney, M.S., Bailey, M.R., Crum, L.A., Khokhlova, V.A., & Sapozhnikov, O.A. 2008. Acoustic characterization of high intensity focused ultrasound fields: A combined measurement and modeling approach. *J. Acoust. Soc. Am.*, **124**(4), 2406–2420.

Christopher, P.T. 1997. Finite amplitude distortion-based inhomogeneous pulse echo ultrasonic imaging. *IEEE Trans. Ultrason. Ferroelctr. Freq. Control.*, **44**(1), 125–139.

Christopher, P.T. 2006. Algorithm for the nonlinear propagation of acoustic beams from phased arrays and nonplanar sources. *IEEE Trans. Ultrason. Ferroelectr. Freq. Control.*, **53**(11), 2188–2192.

Christopher, P.T. 2009. Tissue harmonic depletion imaging. *IEEE Trans. Ultrason. Ferroelctr. Freq. Control.*, **56**(1), 225–230.

Christopher, P.T., & Parker, K.J. 1991a. New approaches to nonlinear diffractive field propagation. *J. Acoust. Soc. Am.*, **90**(1), 488–499.

Christopher, P.T., & Parker, K.J. 1991b. New approaches to the linear propagation of acoustic fields. *J. Acoust. Soc. Am.*, **90**(1), 507–521.

Cleveland, R.O., Hamilton, M.F., & Blackstock, D.T. 1996. Time-domain modeling of finite-amplitude sound in relaxing fluids. *J. Acoust. Soc. Am.*, **99**(6), 3312–3318.

Comte-Bellot, G., & Bailly, C. 2003. *Turbulence*. France:CNRS.

Cotté, B., & Blanc-Benon, P. 2009. Time-domain simulations of sound propagation in a stratified atmosphere over an impedance ground. *J. Acoust. Soc. Am.*, **125**(5), EL202–EL207.

Coulouvrat, F. 2002. Sonic boom in the shadow zone: A geometrical theory of diffraction. *J. Acoust. Soc. Am.*, **111**(1), 499–508.

Coulouvrat, F. 2008. Parabolic approximation in ray coordinates for high-frequency nonlinear waves in a inhomogeneous and high speed moving fluid. *Wave Motion*, **45**(6), 804–820.

Couture, O., Aubry, J-F., Montaldo, G., Tanter, M., & Fink, M. 2008. Suppression of tissue harmonics for pulse-inversion contrast imaging using time reversal. *Phys. Med. Biol.*, **53**(19), 5469–5480.

Cowan, G.R., & Hornig, D.F. 1950. The experimental determination of the thickness of a shock front in a gas. *J. Chem. Phys.*, **18**, 1008–1018.

Crum, L., & Hynynen, K. 1996. Sound therapy. *Physics world*, **August**, 28–33.

Dagrau, F., Rénier, M., Marchiano, R., & Coulouvrat, F. 2011. Acoustic shock wave propagation in a heterogeneous medium: A numerical simulation beyond the parabolic approximation. **130**(1), 20–32.

Dallois, L. 2000. *Propagation des ondes acoustiques dans les milieux en mouvement: extension grand angle de l'approximation parabolique*. Ph.D. thesis, L'Ecole Centrale de Lyon.

Davy, B. A., & Blackstock, D. T. 1971. Measurements of the refraction and diffraction of a short N-wave by a gas-filled soap bubble. *J. Acoust. Soc. Am.*, **49**(3B), 732–737.

Dubrovskii, A.N., Khokhlova, V.A., & Rudenko, O.V. 1996. Fluctuation characteristics of a sonic boom after passing through randomly inhomogeneous layer. *Acoust. Phys.*, **42**(5), 550–554.

Elmer, K.R., & Joshi, M.C. 1994. Varability of measured sonic boom signatures: volume 1 - technical report. *NASA Contracor Report 191483*, **1**.

Fidell, S., Silvati, L., & Pearsons, K. 2002. Relative rates of growth of annoyance of impulsive and non-impulsive noises. *J. Acoust. Soc. Am.*, **111**(1), 576–585.

Filonenko, E., & Khokhlova, V. 2001. Effect of acoustic nonlinearity on heating of biological tissue by high-intensity focused ultrasound. *Acoust. Phys.*, **47**, 468–475.

Gainville, O. 2008. *Modélisation de la propagation atmospherique des ondes infrasonores par une méthode de trace de rayons non linéaire*. Ph.D. thesis, L'Ecole Centrale de Lyon, ECL 2008-07.

Ganjehi, L., Marchiano, R., Coulouvrat, F., & Thomas, J.-L. 2008. Evidence of wave front folding of sonic booms by a laboratory-scale deterministic experiment of shock waves in a heterogeneous medium. *J. Acoust. Soc. Am.*, **124**(1), 57–71.

Gavrilov, L. 2003. Two-dimensional phased arrays for surgical applications: Multiple focus generation and scanning. *Acoust. Phys.*, **49**(5), 508–515.

Gavrilov, L., & Hand, J. 2000a. Two-dimensional phased arrays for surgery: Movement of a single focus. *Acoust. Phys.*, **46**(4), 390–399.

Gavrilov, L.R., & Hand, J.W. 2000b. A theoretical assessment of the relative performance of spherical phased arrays for ultrasound surgery and therapy. *IEEE Trans. Ultrason. Ferroelec. Freq. Contr.*, **41**(1), 125–139.

Gong, X.F., Zhu, Z.M., Shi, T., & Huang, J.H. 1989. Determination of acoustic nonlinearity parameter in biological media using FAIS and ITD methods. *J. Acoust. Soc. Am.*, **86**(1), 1–5.

Goodman, J. W. 1996. *Introduction to Fourier optics*. 2ed., McGraw-Hill.

Greene, E.F., Cowan, G.R., & Hornig, D.F. 1951. The thickness of shock fronts in argon and nitrogen and rotational heat capacity lags. *J. Chem. Phys.*, **19**, 427–434.

Grillon, V., Meynial, X., & Polack, J.D. 1996. What can auralisation in small scale models achieve. *Acta Acust.*, **82**, 362–364.

Gusev, V., & Rudenko, O. 2006. Statistical characteristics of an intense wave behind a two-dimensional phase screen. *Acoust. Phys.*, **52**(1), 24–35.

Hand, J.W., Shaw, A., Sadhoo, N., Rajagopal, S., Dickinson, R.J., & Gavrilov, L.R. 2009. A random phased array device for delivery of high intensity focused ultrasound. *Physics in Medicine and Biology*, **54**(19), 5675–5693.

Hargather, M.J., & Settles, G.S. 2007. Optical measurement and scaling of blasts from gram-range explosive charges. *Shock Waves*, **17**(4), 215–223.

Hill, C., Bamber, J., & Haar, G. T. 2002. *Physical principles of medical ultrasonics*. 2nd edn. Wiley.

Hilton, D.A., Hubbard, H.H., Huckel, V., & Maglieri, D.J. 1964. Ground measurements of sonic-boom pressures for the altitude range of 10,000 to 75,000 feet. *NASA-TR-R-198 tech. report*, **1**.

Hirama, M., Ikeda, O., & Sato, T. 1982. Adaptive ultrasonic array imaging system through an inhomogeneous layer. *J. Acoust. Soc. Am.*, **71**(1), 100–109.

Hoff, L. 2002. Acoustic characterization of contrast agents for medical ultrasound imaging. *Page 230 of: Kluwer Academic Publishers*.

Hugon-Jeanin, Y. 1992. *Simulation numérique de la propagation d'ondes acoustique en milieu turbulent*. Ph.D. thesis, L'Ecole Centrale de Lyon, ECL 92-37.

Huijssen, J., & Verweij, M.D. 2010. An iterative method for the computation of nonlinear, wide-angle, pulsed acoustic fields of medical diagnostic transducers. *J. Acoust. Soc. Am.*, **127**(1), 33–44.

Hynynen, K., McDannold, N., Clement, G., Jolesz, F.A., Zadicario, E., Killiany, R., Moore, T., & Rosen, D. 2006. Pre-clinical testing of a phased array ultrasound system for MRI-guided noninvasive surgery of the brain-A primate study. *European Journal of Radiology*, **59**(2), 149–156.

Jing, Y., & Cleveland, R. 2007. Modeling the propagation of nonlinear three-dimensional acoustic beams in inhomogeneous media. *J. Acoust. Soc. Am.*, **122**(3), 1352–1364.

Karweit, M., Blanc-Benon, P., Juvé, D., & Comte-Bellot, G. 1991. Simulation of the propagation of an acoustic wave through a turbulent velocity field: A study of phase variance. *J. Acoust. Soc. Am.*, **89**(1), 52–62.

Karweit, M.J., & Blanc-Benon, P. 1993. Arrival-time variance for acoustic propagation in 3D random media: the effect of lateral scales. *C.R. Acad. Sci. Paris*, **316**(2), 1695–1702.

Khokhlova, V., Ponomarev, A., Averkiou, M., & Crum, L. 2006. Nonlinear pulsed ultrasound beams radiated by rectangular focused diagnostic transducers. *Acoust. Phys.*, **52**(4), 481–489.

Khokhlova, V.A., Kashcheeva, S.S., Averkiou, M.A., & Crum, L.A. 2000. Effect of selective absorption on nonlinear interactions in high intensity acoustic beams. *Pages 151–154 of: In: Nonlinear Acoustics at the Turn of the Millennium (Proc. 15th International Symposium on Nonlinear Acoustics, Goettingen, Germany, 1999), ed. W. Lauterborn and T. Kurz, Am. Inst. of Phys.*

Khokhlova, V.A., Souchon, R., Tavakkoli, J., Sapozhnikov, O.A., & Cathignol, D. 2002. Numerical modeling of finite-amplitude sound beams: Shock formation in the near field of a cw plane piston source. *J. Acoust. Soc. Am.*, **110**(1), 95–108.

Krasilnikov, V. A. 1998. Linear and nonlinear sound propagation in turbulent and inhomogeneous media. *Acoust. Phys.*, **44**(4), 481–490.

Kravtsov, Y. A., & Orlov, Y. I. 1990. *Geometrical optics of inhomogeneous media*. Berlin, GR: Springer-Verlag.

Kreider, W., Sapozhnikov, O., Khokhlova, V., Farr, N., Bailey, M., Kaczkowski, P., Partanen, A., & Brazzle, D. Acoustic measurements and holographic reconstruction of the Philips MR-guided HIFU source. *Page 79 of: In: Program and Abstract Book "Current and Future Applications of MR-guided Focused Ultrasound", 2nd International Symposium, 17-20 October 2010, Washington DC, USA.*

Kurganov, A., & Tadmor, E. 2000. New high-resolution central schemes for nonlinear conservation laws and convection-diffusion equations. *J. Comput. Phys.*, **160**(1), 241–282.

Leatherwood, J.D., & Sullivan, B.M. 1992. Subjective loudness response to simulated sonic booms. *Pages 151–170 of: High-Speed Research: Sonic Boom, (SEE N92-33874 24-05)*, vol. 1.

Leatherwood, J.D., Sullivan, B.M., Shepherd, K.P., McCurdy, D.A., & Brown, S.A. 2002. Summary of recent NASA studies of human response to sonic booms. *J. Acoust. Soc. Am.*, **111**(1), 586–598.

Lee, R.A., & Downing, J.M. 1991. Sonic Boom produced by United states Navy aircraft: measured data, AL-TR-1991-0099. *Biodynamic Environment Branch, Biodynamics and Bioengenineering Division, Armstrong Laboratory,Wright-Patterson Air Force Base, Ohio.*

Leissing, T. 2009. *Propagation d'ondes non linéaires en milieu complex – Application à la propagation en environment urbain.* Ph.D. thesis, Université Paris-Est.

Li, F, Gong, X, Hu, K, Li, C, & Wang, Z. 2006. Effect of ribs in HIFU beam path on formation of coagulative necrosis in goat liver. *AIP Conference Proceedings*, **829**(1), 477–480.

Lipkens, B. 1993. *Experimental and theoretical study of the propagation of N-waves through a turbulent medium.* Ph.D. thesis, The university of Texas at Austin.

Lipkens, B. 2002. Model experiment to study sonic boom propagation through turbulence. Part III: Validation of sonic boom propagation models. *J. Acoust. Soc. Am.*, **111**(1 Pt.2), 509–519.

Lipkens, B., & Blackstock, D.T. 1998a. Model experiment to study sonic boom propagation through turbulence. Part I: Model experiment and general results. *J. Acoust. Soc. Am.*, **103**(1), 148–158.

Lipkens, B., & Blackstock, D.T. 1998b. Model experiment to study sonic boom propagation through turbulence. Part II: Effect of turbulence intensity and propagation distance through turbulence. *J. Acoust. Soc. Am.*, **104**(3 Pt.1), 1301–1309.

Liu, D.-L., & Waag, R.C. 1994. Correction of ultrasonic wavefront distortion using backpropagation and a reference waveform method for time-shift compensation. *J. Acoust. Soc. Am.*, **96**(2), 649–660.

Loubeau, A., Sparrow, V.W., Pater, L.L., & Wright, W.M. 2006. High-frequency measurements of blast wave propagation. *J. Acoust. Soc. Am.*, **120**(3), EL29–EL35.

Mach, E., & Salcher, P. 1887. Photographische fixierung der dunch projectile in der luft eingeleiteten Vorgänge. *Sitzungsb. Akad. Wiss. Wien*, **95**, 764–780.

Maglieri, D.J., Sotchcott, V.E., & Keefer, T.N. 1992. A summary of XB-70 sonic boom signature data for flights during March 1965 through May 1966. *NASA Contracor Report 189630.*

Marchiano, R., Coulouvrat, F., Baskar, S., & Thomas, J.-L. 2007. Experimental evidence of deviation from mirror reflection for acoustical shock waves. *Phys. Rev. E*, **76**(5), 056602.

Martin, J.M., & Flatte, Stanley M. 1988. Intensity images and statistics from numerical simulation of wave propagation in 3-D random media. *Appl. Opt.*, **27**(11), 2111–2126.

Mast, T.D., Hinkelman, L.M., Orr, M.J., Sparrow, V.W., & Waag, R.C. 1997. Simulation of ultrasonic pulse propagation through the abdominal wall. *J. Acoust. Soc. Am.*, **102**(2), 1177–1190.

Merzkirch, W. 1974. *Flow visualization.* Academic Press, New York and London.

Musatov, A.G., Rudenko, O.V., & Sapozhnikov, O.A. 1992. Nonlinear refraction and absorption phenomena due to powerful pulses focusing. *Acoust. Phys.*, **38**(3), 502–510.

Niedzwiecki, A., & Ribner, H.S. 1978. Subjective loudness of N-wave sonic booms. *J. Acoust. Soc. Am.*, **64**(6), 1617–1621.

Nock, L., Trahey, G.E., & Smith, S.W. 1989. Phase aberration correction in medical ultrasound using speckle brightness as a quality factor. *J. Acoust. Soc. Am.*, **85**(5), 1819–1833.

Ollivier, S., & Blanc-Benon, Ph. 2004. Model experiment to study acoustic N-wave propagation through turbulence. *Pages AIAA2004–2921 of:* 10^{th} *AIAA/CEAS Aeroacoustics Conference, Manchester, UK.*

O"Neil, H.T. 1949. Theory of focusing radiators. *J. Acoust. Soc. Am.*, **21**(5), 516–526.

Ostashev, V. E. 1997. *Acoustics in moving inhomogeneous media*. Ed. E&Fn Spon, London.

Ostashev, V.E. 1994. Sound propagation and scattering in media with random inhomogeneities of sound speed, density and medium velocity. *Waves in Random Media*, **4**(4), 403–428.

Panda, J. 1995. Wide angle light scattering in shock-laser interaction. *AIAA Journal*, **33**, 2429–2431.

Panda, J., & Adamovsky, G. 1995. Laser light scattering by shock waves. *Phys. Fluids*, **7**, 2271–2279.

Pernot, M., Aubry, J.-F., Tanter, M., Thomas, J.-L., & Fink, M. 2003. High power transcranial beam steering for ultrasonic brain therapy. *Phys. Med. Biol.*, **48**(16), 2577–2589.

Pernot, M., Tanter, M., & Fink, M. 2004. 3-D real-time motion correction in high-intensity focused ultrasound therapy. *Ultrasound. Med. Biol.*, **30**(9), 1239–1249.

Picaut, J., & Simon, L. 2001. A scale model experiment for the study of sound propagation in urban areas. *Appl. Acoust.*, **62**(3), 327–340.

Picaut, J., Pollès, T. Le, L'Hermite, P., & Gary, V. 2005. Experimental study of sound propagation in a street. *Appl. Acoust.*, **66**(2), 149–173.

Pierce, A. D. 1981. *Acoustics: an introduction to its physical principles and applications*. New York: McGraw-Hill Book Co.

Plotkin, K. J. 2002. State of the art of sonic boom modeling. *J. Acoust. Soc. Am.*, **111**(1), 530–536.

Qin, Q., & Attenborough, K. 2004. Characteristics and application of laser-generated acoustic shock waves in air. *Appl. Acoust.*, **65**(4), 325–340.

Quesson, B., Merle, M., Ḱohler, M.O., Mougenot, C., Roujol, S., De Senneville, B.D., & Moonen, C.T. 2006. A method for MRI guidance of intercostal high intensity focused ultrasound ablation in the liver. *Med. Phys.*, **37**(6), 2533–2540.

Rachlin, D. 1990. Direct estimation of aberrating delays in pulse-echo imaging systems. *J. Acoust. Soc. Am.*, **88**(1), 191–198.

Rudenko, O. V., & Soluyan, S. I. 1977. *Theoretical foundations of nonlinear acoustics*. New York: Consultants Bureau.

Rudenko, O.V. 1995. Nonlinear sawtooth-shaped waves. *Physics-Uspekhi*, **38**(9), 965–989.

Rudenko, O.V. 2006. Giant nonlinearities in structurally inhomogeneous media and the fundamentals of nonlinear acoustic diagnostic techniques. *Physics-Uspekhi*, **49**(1), 69–87.

Rudenko, O.V. 2007. Nonlinear waves: some biomedical applications. *Physics-Uspekhi*, **50**(4), 359–367.

Rudenko, O.V., & Enflo, B.O. 2000. Nonlinear N-wave propagation through a one-dimensional phase screen. *Acta Acustica united with Acustica*, **86**(2), 229–238.

Rudenko, O.V., & Sapozhnikov, O.A. 2004. Self-action effects for wave beams containing shock fronts. *Physics-Uspekhi*, **47**(9), 907–922.

Rytov, S.M., Kravtsov, Y.A., & Tatarskii, V.I. 1978. *Introduction to statistical radiophysics (in russian)*. Moskva: Nauka.

Sapozhnikov, O., Pishchal'nikov, Yu., & Morozov, A. 2003. Reconstruction of the normal velocity distribution on the surface of an ultrasonic transducer from the acoustic pressure measured on a reference surface. *Acoust. Phys.*, **49**(3), 354–360.

Sarvazyan, A., Rudenko, O., Swanson, S., Fowlkes, J., & Emelianov, S. 1998. Shear wave elasticity imaging: a new ultrasonic technology of medical diagnostics. *Ultrasound in Med. and Biol.*, **24**(9), 1419–1435.

Selfridge, A.R. 1985. Approximate material properties in isotropic materials. *IEEE transactions on sonics and ultrasonics*, **SU-32**(3), 381–394.

Settles, G. S. 2001. *Schlieren and shadowgraph techniques: visualizing phenomena in transparent media*. Springer-Verlag, Heidelberg.

Shlenov, S.A., & Kandidov, V.P. 2004. Filament beaming in propagation of femtosecond laser impulse through turbulent atmosphere. Part 1. Method. *Atmos. Ocean. Opt.*, **17**(8), 565–571.

Smeets, G. 1977. Laser interference microphone for ultrasonics and nonlinear acoustics. *J. Acoust. Soc. Am.*, **61**(3), 872–875.

Tabei, M., Mast, T.D., & Waag, R.C. 2002. A k-space method for coupled first-order acoustic propagation equations. *J. Acoust. Soc. Am.*, **111**(1), 53–63.

Tabei, M., Mast, T.D., & Waag, R.C. 2003. Simulation of ultrasonic focus aberration and correction through human tissue. *J. Acoust. Soc. Am.*, **113**(2), 1166–1176.

Tatarskii, V. I. 1971. *The effects of the turbulent atmosphere on wave propagation*. Moscow: Nauka.

Tavakkoli, J., Cathignol, D., Souchon, R., & Sapozhnikov, O.A. 1998. Modeling of pulsed finite-amplitude focused sound beams in time domain. *J. Acoust. Soc. Am.*, **104**(4), 2061–2072.

ter Haar, G. 2001. High intensity focused ultrasound for the treatment of tumors. *Echocardiography*, **18**(4), 317–322.

Tillett, J.C., Daoud, M.I., Lacefield, J.C., & Waag, R.C. 2009. A k-space method for acoustic propagation using coupled first-order equations in three dimensions. *J. Acoust. Soc. Am.*, **126**(3), 1231–1244.

Tjotta, J.N., Tjotta, S., & Vefring, E.H. 1991. Effects of focusing on the nonlinear interaction between two collinear finite amplitude sound beams. *J. Acoust. Soc. Am.*, **89**(3), 1017–1027.

Uscinski, B.J. 1977. *The elements of wave propagation in random media*. New-York: McGraw-Hill.

Vaezy, S., Martin, R., & Crum, L. 2001. High intensity focused ultrasound: a method of hemostasis. *Echocardiography*, **18**(4), 309–315.

Varslot, T., & Masoy, S.E. 2006. Forward propagation of acoustic pressure pulses in 3D soft biological tissue. *Modeling Identification and Control*, **27**(3), 181–200.

Varslot, T., & Taraldsen, G. 2005. Computer simulation of forward wave propagation in soft tissue. *IEEE T. Ultrason. Ferr.*, **52**(9), 1473–1482.

Varslot, T., Masoy, S.E., & Angelsen, B. 2007. Aberration and second harmonic imaging. *IEEE Trans. UFFC*, **54**(3), 470–479.

Vinogradova, M. B., Rudenko, O. V., & Suhorukov, A. P. 1979. *Teorija voln*. Nauka.

Vorontsov, A.M., Paramonov, P.V., Valley, M.T., & Vorontsov, M.A. 2008. Generation of infinitely long phase screens for modeling of optical wave propagation in atmospheric turbulence. *Waves in Random and Complex Media*, **18**(1), 91–108.

Wasier, J. 1999. *Etude expérimentale des effects d'une frontière sur la propagation des ondes acoustique à travers d'une turbulence thermique*. Ph.D. thesis, L'Ecole Centrale de Lyon, ECL 99-46.

Westervelt, P.J. 1963. Modeling the propagation of nonlinear three-dimensional acoustic beams in inhomogeneous media. *J. Acoust. Soc. Am.*, **35**(4), 535–537.

Willshire, Jr. W. L., & Devilbiss, D.W. 1992. Preliminary results from the White Sands Missle Range sonic boom. *High-speed research: sonic boom*, **1**, 137–149.

Wojcik, G., Mould, J., Ayter, S., & Carcione, L. 1998. A study of second harmonic generation by focused medical transducer pulses. *Pages 1583–1588 of: In proc. of ultrasonics symposium, Sendai, Japan, 5-8 oct.*

Wright, W.M. 1983. Propagation in air of N-waves produced by sparks. *J. Acoust. Soc. Am.*, **73**(6), 1948–1955.

Wright, W.M., & McKittrick, J.L. 1967. Diffraction of spark-produced acoustic impulses. *Am. J. Phys.*, **35**(2), 124–128.

Wright, W.M., & Medendorp, N.W. 1968. Acoustic radiation from a finite line source with N-wave excitation. *J. Acoust. Soc. Am.*, **43**(5), 966–971.

Wu, P., Kazys, R., & Stepinski, T. 1997. Optimal selection of parameters for the angular spectrum approach to numerically evaluate acoustic fields. **101**(1), 125–134.

Yan, X., & Hamilton, M.F. Angular spectrum decomposition analysis of second harmonic ultrasound propagation and its relation to tissue harmonic imaging. *In: The 4th Int. Workshop on Ultrasonic and Advanced Methods for Nondestructive Testing and Material Characterization, June 19, 2006 at UMass Dartmouth, N. Dartmouth, MA - Proceedings published in www.ndt.net.*

Yan, Xiang. 2004. *Statistical model of beam distortion by tissue inhomogeneities in tissue harmonic imaging*. Ph.D. thesis, The University of Texas at Austin.

Yasumoto, K.and Watanabe, K., & Ishihara, J. 2002. Numerical analysis of optical waveguides with the use of fourier-series expansion method combined with perfectly matched layer. *Microw. and Opt. Tech. Lett.*, **34**(6), 182–188.

Yuldashev, P.V., Averiyanov, M.V., Khokhlova, V.A., Sapozhnikov, O.A., Ollivier, S., & Blanc-Benon, P. 2008a. Nonlinear propagation of spark-generated N-waves in atmosphere: theoretical and experimental assessment of the shock front structure. *Pages 565–570 of: Proc. of Acoustics'08 Paris Congress, Paris, 27 June–4 July.*

Yuldashev, P.V., Aver'yanov, M.V., Khokhlova, V.A., Ollivier, S., & Blanc-Benon, P. 2008b. Nonlinear spherically divergent shock waves propagating in a relaxing medium. *Acoust. Phys.*, **54**(1), 32–41.

Yuldashev, P.V., Krutyansky, L.M., Khokhlova, V.A., Brysev, A.P., & Bunkin, F.V. 2010a. Distortion of the focused finite amplitude ultrasound beam behind the random phase layer. *Acoust. Phys.*, **56**(4), 467–474.

Yuldashev, P.V., Averiyanov, M.A., Khokhlova, V.A., Sapozhnikov, O.A., Ollivier, S., & Blanc-Benon, P. 2010b. Measurement of shock N-waves using optical methods. *Page CD of: 10ème Congrès Français d'Acoustique, Lyon, 12-16 avril.*

Yuldashev, P.V., Bryseva, N.A., Averiyanov, M.V., Blanc-Benon, P., & Khokhlova, V.A. 2010c. Statistical properties of nonlinear diffracting N-wave behind a random phase screen. *Acoust. Phys.*, **56**(2), 158–167.

Yuldashev, P.V., Ollivier, S., Averiyanov, M.V., Sapozhnikov, O.A., Khokhlova, V.A., & Blanc-Benon, P. 2011. Nonlinear propagation of spark-generated N-waves in air: modeling and measurements using acoustical and optical methods. *J. Acoust. Soc. Am.*, **128**(6), 3321–3333.

Zemp, R.J., Tavakkoli, J., & Cobbold, R.S. 2003. Modeling of nonlinear ultrasound propagation in tissue from array transducers. *J. Acoust. Soc. Am.*, **113**(1), 139–152.

Zhang, S., Yin, L., & Fang, N. 2009. Focusing ultrasound with an acoustic metamaterial network. *Phys. Rev. Lett.*, **102**(19), 194301.